Aerodynamics of nonslender delta wings

Vardaki, Eleni

Award date:
2006

Awarding institution:
University of Bath

AERODYNAMICS OF NONSLENDER DELTA WINGS

Eleni Vardaki

A thesis submitted for the degree of Doctor of Philosophy

University of Bath

Department of Mechanical Engineering

2006

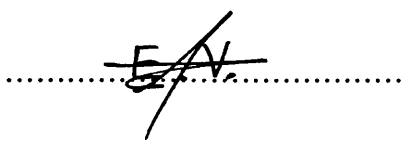

ProQuest LLC
789 East Eisenhower Parkway
P.O. Box 1346
Ann Arbor, MI 48106-1346

ABSTRACT

An experimental investigation was undertaken to understand the aerodynamics of nonslender delta wings. Particular emphasis was placed on the vortex breakdown phenomenon, the control of the vortices in the post-stall region focusing on vortex reformation, and rolling oscillations of various amplitudes and frequencies. Additionally a number of different rolling manoeuvres were investigated. Flow visualisation techniques along with PIV and LDV measurements were implemented for the completion of this project. Different nonslender delta wings, including rigid, flexible, simple and cropped planforms with different sweep angles and thicknesses, were used. All the experiments were conducted in a water tunnel facility.

Rigid and flexible wings of varying thicknesses and flexibility, and a sweep angle of 50°, were investigated with the main purpose of discovering the effect of flexibility on the flowfield. Small amplitude and high frequency rolling motions were used to simulate the vibrations observed on flexible delta wings. Parametric effects, such as different sweep angles (40° and 30°), different planform shapes such as cropped wings, and pitching motions were also investigated to accumulate information on the behaviour of the flowfield. Finally, large amplitude and low frequency rolling manoeuvres of both rigid and flexible delta wings were studied.

Flexibility creates a beneficial effect on the flowfield, by promoting earlier reformation of the vortices, at an incidence where breakdown has already occurred on the rigid wing. A combination of the results presented here with experiments undertaken in a wind tunnel, proves that it is not the flexibility *per se* that reenergises the flow, but antisymmetric vibrations of the leading edge observed on flexible wings. Small amplitude oscillations followed, in order to verify these results, with very interesting findings, including flow reattachment, vortex reformation and delay in the vortex breakdown location. In the study of the parametric effects, the same response was observed when wings with different sweep angles or planform shapes were undergoing oscillatory motions. Interestingly enough, earlier reattachment and vortex reformation was also observed in symmetric perturbations. The large amplitude manoeuvres gave insight into the effect of the effective sweep angle and sideslip, and the advantages these provide for the flowfield over a nonslender delta wing.

DEDICATED TO MY PARENTS,
ΜΙΧΑΛΗ ΚΑΙ ΣΤΕΛΛΑ

ΑΦΙΕΡΩΝΕΤΑΙ ΣΤΟΥΣ ΓΟΝΕΙΣ ΜΟΥ,
ΜΙΧΑΛΗ ΚΑΙ ΣΤΕΛΛΑ

ACKNOWLEDGEMENTS

First of all, I would like to thank my supervisor, Ismet, for all his help and support during this three and a half year long project. The valuable discussions on the complicated, but at the same time highly exciting, subject of the unsteady aerodynamics over nonslender delta wings was part of my daily routine with Ismet, which proved to be the most powerful tool in order to complete this project. Apart from the aerodynamics discussion, Ismet has been very supportive and understanding in every difficult moment I have had in my life during these three and a half years.

A big thanks goes to all the technicians (Dave, Roland, Les, Tony, Eric and I can go on forever....) and the instrumentation people (Vijay, Steve , Colin and Paul), who gave me their full support and helped throughout this project, and for always being nice to me, even if sometimes I could be annoying..... Special thanks to Roland for being a perfectionist and making my models look as good and accurate as the drawings I gave him and to Les for always helping me out when needed. Nothing would have been done without their valuable help.

Many thanks to all my office mates, old and new. First of all Gordon for being a friend from the very first day, for his help and long discussions over delta wings, for giving answers to all my questions and obviously for the long distractions and comments! To my Greek housemates, Panagiotis, who apart from an annoying housemate has always been a good friend and has helped a lot during difficult times in my PhD, and Giota, my best friend, who had always something good to say to make my day and has always been there for me. Thanks also to everyone else in the office Dave, Zhijin, Paul, Charbel, Anna, Colin, Steve, James, Sam for the long hours of office football, inventing office games or continuously suggesting a break for food or drink. I wouldn't be able to finish my thesis without you!!! Thank you.

A big thanks to my parents in Greece for their constant moral support and help and to my boyfriend, Bernardo, for always being there when needed, and for always being supportive when times were difficult and stressing for me. Thank you for proof reading my thesis and for correcting my Greeklish!!!

Finally, I would like to thank Dr Michael Carley for his suggestions on my thesis and his valuable help on Matlab throughout my PhD.

Many thanks to all!!!!!!!

CONTENTS

ABSTRACT i
ACKNOWLEDGEMENTS iii
CONTENTS iv
LIST OF FIGURES vii
LIST OF TABLES xiv
NOMENCLATURE xv
ABBREVIATIONS xvii

CHAPTER 1: INTRODUCTION 1

1.1 BACKGROUND 1
1.2 LITERATURE REVIEW 3
1.2.1 Introduction 3
1.2.2 Vortical Flows over Delta Wings and the Effect of Different Parameters 3
1.2.2.1 Introduction 3
1.2.2.2 Slender Delta Wings 3
1.2.2.3 Nonslender Delta Wings 9
1.2.3 Vortex Breakdown 12
1.2.3.1 Types of Vortex Breakdown 13
1.2.3.2 Parameters Affecting the Vortex Breakdown Phenomenon 15
1.2.3.3 Oscillations of the Vortex Breakdown 17
1.2.3.4 Flow Properties Affected by the Breakdown Phenomenon 18
1.2.3.5 Models and Theories Introduced for the Explanation of Aerodynamic Characteristics and for the Vortex Breakdown Phenomenon 19
1.2.4 Manoeuvring Delta Wing Aerodynamics 22
1.2.4.1 Introduction 22
1.2.4.2 Rolling Manoeuvre 22
1.2.4.3 Pitching Manoeuvre 24
1.2.4.4 Wing Rock 24
1.2.5 Flexible Nonslender Delta Wings 26
1.3 OBJECTIVES 27
1.4 FIGURES CHAPTER 1 29

CHAPTER 2: EXPERIMENTAL APPARATUS 39

2.1 INTRODUCTION 39
2.2 WATER TUNNEL FACILITY 39
2.3 MODELS 40
2.4 INSTRUMENTATION 41
2.4.1 Introduction 41
2.4.2 Rolling Mechanism 41
2.4.3 Flow Visualisation 42
2.4.4 Particle Image Velocimetry (PIV) 43

2.4.5 Laser Doppler Velocimetry (LDV) 45
2.4.6 Argon-Ion laser 46
2.5 FIGURES CHAPTER 2 47

CHAPTER 3: EXPERIMENTAL PROCEDURES 59

3.1 INTRODUCTION 59
3.2 OVERVIEW OF EXPERIMENTAL PROCEDURES 59
3.3 DATA ACQUISITION AND ANALYSIS 59
3.3.1 Flow Visualisation Images and Vortex Breakdown Location 60
3.3.2 PIV Data 61
3.3.2.1 Hart Correlation 62
3.3.3 Calculation of Flow Quantities 62
3.3.3.1 Vorticity and Circulation 62
3.3.4 Additional Parameters 64
3.3.4.1 Spanwise Bending Flexibility 64
3.3.5 LDV Data 65
3.4 DATA QUALITY AND VALIDATION 65
3.4.1 Delta Wing Models 65
3.4.2 Vortex Breakdown Location 66
3.4.3 Rolling Mechanism Control 66
3.4.4 PIV 67
3.4.5 Flow Quantities 68
3.4.6 LDV 68
3.5 FIGURES CHAPTER 3 70

CHAPTER 4: FLEXIBLE NONSLENDER DELTA WINGS 72

4.1 INTRODUCTION 72
4.2 EFFECT OF FLEXIBILITY AT LOW/MODERATE INCIDENCES 72
4.3 EFFECT OF FLEXIBILITY IN THE POST-STALL REGION 74
4.4 CIRCULATION 75
4.5 FIGURES CHAPTER 4 77

CHAPTER 5: SMALL AMPLITUDE OSCILLATIONS OF NONSLENDER DELTA WINGS 87

5.1 INTRODUCTION 87
5.2 EFFECT OF SMALL AMPLITUDE OSCILLATIONS 88
5.2.1 Introduction 88
5.2.2 Laser Induced Flow Visualisation 88
5.2.3 Laser Doppler Velocimetry (LDV) Measurements 90
5.2.4 Dye Flow Visualisation Results 95
5.2.5 PIV Results 98
5.3 FIGURES CHAPTER 5 101

CHAPTER 6: PARAMETRIC EFFECTS 127

6.1 INTRODUCTION 127
6.2 SWEEP ANGLE EFFECT 128
6.3 PLANFORM SHAPE EFFECT 129
6.4 EFFECT OF SYMMETRIC EXCITATION 131
6.5 FIGURES CHAPTER 6 132

CHAPTER 7: LARGE AMPLITUDE MANOEUVRES OF NONSLENDER DELTA WINGS 145

7.1 INTRODUCTION 145
7.2 LARGE AMPLITUDE MANOEUVRES OF RIGID DELTA WINGS 145
7.3 LARGE AMPLITUDE MANOEUVRE OF FLEXIBLE DELTA WINGS 154
7.4 ADDITIONAL MEASUREMENTS ON ROLLING MANOEUVRES 156
7.5 FIGURES CHAPTER 7 159

CHAPTER 8: CONCLUSIONS 191

8.1 INTRODUCTION 191
8.2 REVIEW AND CONCLUDING REMARKS 191
8.3 RECOMMENDATIONS FOR FUTURE WORK 193

CHAPTER 9: REFERENCES 195

CHAPTER 10: LIST OF PUBLICATIONS 204

LIST OF FIGURES

CHAPTER 1

FIGURE 1.1: QUALITATIVE DIAGRAM OF THE LIFT COEFFICIENT C_L VERSUS THE ANGLE OF ATTACK, A. 29

FIGURE 1.2: VARIATIONS OF DELTA WING PLANFORMS (ANDERSON, JR. J. D.-2001). 29

FIGURE 1.3: SCHEMATIC OF THE SUBSONIC FLOWFIELD OVER A DELTA WING (ANDERSON, JR. J. D.-2001). 30

FIGURE 1.4: SCHEMATIC OF THE VORTICAL FLOW OF A DELTA WING (TOP); STREAMLINE PATTERN ON THE SURFACE OF THE WING (BOTTOM) (VISSER AND WASHBURN-1994). 30

FIGURE 1.5: A) CONTOURS OF INSTANTANEOUS VORTICITY MAGNITUDE THROUGH THE VORTEX CORE ON THE EVOLUTION OF VORTICAL STRUCTURES WITH INCREASING RE; B) EVOLUTION OF THE SHEAR LAYER STRUCTURE WITH INCREASING RE AS AN ISOSURFACE OF AXIAL VORTICITY (VISBAL AND GORDNIER-2003). 31

FIGURE 1.6: A) CONTOURS OF INSTANTANEOUS AXIAL VORTICITY AT SEVERAL CROSSFLOW PLANE ALONG THE WING AT $Re = 25{,}000$; B) $Re = 50{,}000$ (VISBAL AND GORDNIER-2003). 31

FIGURE 1.7: COMPUTATIONAL SIMULATIONS SHOWING DOUBLE VORTEX STRUCTURES (GORDNIER AND VISBAL-2003). 32

FIGURE 1.8: EXPERIMENTAL CROSSFLOW VORTICITY MEASUREMENTS SHOWING DOUBLE VORTEX STRUCTURES (TAYLOR *ET AL.*-2003). 32

FIGURE 1.9: FLOW VISUALISATION OF LEADING EDGE VORTICES OVER A $\Lambda = 50°$, AT $\alpha = 5°$ (TAYLOR *ET AL.*-2003). 32

FIGURE 1.10: SURFACE STREAMLINE PATTERN AND PRESSURE COEFFICIENT AT $\alpha = 5°$, PS: PRIMARY SEPARATION; PA: PRIMARY ATTACHMENT; SS: SECONDARY SEPARATION; SA: SECONDARY ATTACHMENT (GORDNIER AND VISBAL-2003). 33

FIGURE 1.11: SURFACE STREAMLINE PATTERN AND PRESSURE COEFFICIENT AT $\alpha = 10°$, PS: PRIMARY SEPARATION; PA: PRIMARY ATTACHMENT; SS: SECONDARY SEPARATION; SA: SECONDARY ATTACHMENT TS: TERTIARY SEPARATION; TA: TERTIARY ATTACHMENT (GORDNIER AND VISBAL-2003). 33

FIGURE 1.12: SURFACE STREAMLINE PATTERN AND PRESSURE COEFFICIENT AT $\alpha = 15°$, PS: PRIMARY SEPARATION; PA: PRIMARY ATTACHMENT; SS: SECONDARY SEPARATION; SA: SECONDARY ATTACHMENT TS: TERTIARY SEPARATION; TA: TERTIARY ATTACHMENT (GORDNIER AND VISBAL-2003). 34

FIGURE 1.13: VELOCITY MAGNITUDE IN THE VORTEX CORE PLANE (TAYLOR & GURSUL-2004B) 34

FIGURE 1.14: VORTEX BREAKDOWN OVER A DELTA WING. BOTH SPIRAL AND BUBBLE TYPE ARE PRESENT (LAMBOURNE AND BRYER-1961). 35

FIGURE 1.15: BUBBLE AND SPIRAL FORMS OF VORTEX BREAKDOWN (LEIBOVICH-1978). 35

FIGURE 1.16: BUBBLE TYPE VORTEX BREAKDOWN (SARPKAYA-1971A)..... 36
FIGURE 1.17: SPECTRUM OF UNSTEADY FLOW PHENOMENA OVER RIGID SLENDER DELTA WINGS (MENKE *ET AL.*-1999). 36
FIGURE 1.18: COMPARISON OF LIFT GENERATED BY DIFFERENT DELTA WINGS (TAYLOR AND GURSUL-2004A). 37
FIGURE 1.19: VISUALISATION OF LEADING EDGE DEFORMATION FOR 1MM FLEXIBLE WING AT $\alpha = 25°$ TAYLOR AND GURSUL-2004A)..... 37
FIGURE 1.20: FINITE ELEMENT MODAL SOLUTION FOR 1MM WING TAYLOR AND GURSUL-2004A). 38

CHAPTER 2

FIGURE 2.1: PHOTO OF EIDETICS MODEL 1520 WATER TUNNEL (COURTESY ROLLING HILLS RESEARCH CORPORATION). 47
FIGURE 2.2: SCHEMATIC PICTURE OF EIDETICS MODEL 1520 WATER TUNNEL (COURTESY ROLLING HILLS RESEARCH CORPORATION). 47
FIGURE 2.3: RIGID, 50° SWEEP ANGLE MODEL. 49
FIGURE 2.4: RIGID, 40° SWEEP ANGLE MODEL. 50
FIGURE 2.5: RIGID, 30° SWEEP ANGLE MODEL. 50
FIGURE 2.6: RIGID, 50° SWEEP ANGLE MODEL WITH CAVITY. 51
FIGURE 2.7: OVERVIEW OF EXPERIMENTAL SETUP. 52
FIGURE 2.8: PRINCIPAL DIMENSIONS OF CROPPED MODEL WITH $\Lambda = 50°$. 53
FIGURE 2.9: PRINCIPAL DIMENSIONS OF CROPPED MODEL WITH $\Lambda = 40°$. 54
FIGURE 2.10: PRINCIPAL DIMENSIONS OF CROPPED MODEL WITH $\Lambda = 30°$. 55
FIGURE 2.11: PRINCIPAL DIMENSIONS OF CROPPED MODEL WITH $\Lambda = 20°$. 56
FIGURE 2.12: PRINCIPAL DIMENSIONS OF CROPPED MODEL WITH $\Lambda = 10°$ 57
FIGURE 2.13: PRINCIPAL DIMENSIONS OF CROPPED MODEL (SQUARE PLATE) WITH $\Lambda = 0°$. 58

CHAPTER 3

FIGURE 3.1: SCHEMATIC OF CALCULATION OF THE VORTEX BREAKDOWN LOCATION. 70
FIGURE 3.2: EXPLANATION OF THE MEASUREMENT OF THE WAKE DISTANCE, Δy_w, ON A $\Lambda = 40°$ DELTA WING. 70
FIGURE 3.3: SCHEMATIC OF CALCULATION OF THE DISTANCE BETWEEN WAKES..... 70
FIGURE 3.4: CONTOURS OF MAGNITUDE OF TIME-AVERAGED VELOCITY IN A PLANE THROUGH THE VORTEX CORE IN (A) WATER TUNNEL; AND (B) WIND TUNNEL EXPERIMENTS, $\alpha = 15°$ (VARDAKI *ET AL.*-2005)..... 71

CHAPTER 4

FIGURE 4.1: EFFECT OF SPANWISE FLEXIBILITY, λ, ON $\Lambda = 50°$ DELTA WINGS AT $\alpha = 15°$ 77

FIGURE 4.2: CROSS FLOW VORTICITY MEASUREMENTS AT $x/c = 0.8$ AND $\alpha = 15°$ FOR DIFFERENT SPANWISE FLEXIBILITY. 78
FIGURE 4.3: CROSS FLOW VELOCITY MEASUREMENTS AT $x/c = 0.8$ AND $\alpha = 15°$ FOR DIFFERENT SPANWISE FLEXIBILITY. 79
FIGURE 4.4: EFFECT OF SPANWISE FLEXIBILITY, λ, ON $\Lambda = 50°$ DELTA WINGS AT $\alpha = 20°$. 80
FIGURE 4.5: CROSS FLOW VORTICITY MEASUREMENTS AT $x/c = 0.8$ AND $\alpha = 20°$ FOR DIFFERENT SPANWISE FLEXIBILITY. 81
FIGURE 4.6: CROSS FLOW VELOCITY MEASUREMENTS AT $x/c = 0.8$ AND $\alpha = 20°$ FOR DIFFERENT SPANWISE FLEXIBILITY. 82
FIGURE 4.7: EFFECT OF SPANWISE FLEXIBILITY, λ, ON $\Lambda = 50°$ DELTA WINGS AT $\alpha = 25°$. 83
FIGURE 4.8: CROSS FLOW VORTICITY MEASUREMENTS AT $x/c = 0.8$ AND $\alpha = 25°$ FOR DIFFERENT SPANWISE FLEXIBILITY. 84
FIGURE 4.9: CROSS FLOW VELOCITY MEASUREMENTS AT $x/c = 0.8$ AND $\alpha = 25°$ FOR DIFFERENT SPANWISE FLEXIBILITY. 85
FIGURE 4.10: VARIATION OF NORMALISED CIRCULATION WITH WING SPANWISE FLEXIBILITY, FOR DIFFERENT INCIDENCES. 86

CHAPTER 5

FIGURE 5.1: COMPARISON BETWEEN STATIC AND DYNAMIC INSTANTANEOUS (*TOP HALF*) AND TIME AVERAGE (*BOTTOM HALF*) LASER INDUCED FLOW VISUALISATION IMAGES IN CROSSFLOW PLANE AT $x/c = 0.8$, FOR $\Delta\phi = 1°$ AND AT $\alpha = 15°$ AND $\alpha = 20°$ 101
FIGURE 5.2: DETAILED COMPARISON BETWEEN STATIC AND DYNAMIC INSTANTANEOUS (*TOP HALF*) AND TIME AVERAGE (*BOTTOM HALF*) LASER INDUCED FLOW VISUALISATION IMAGES IN CROSSFLOW PLANE AT $x/c = 0.8$, FOR $\Delta\phi = 1°$ AND AT $\alpha = 15°$ AND $\alpha = 20°$. 102
FIGURE 5.3: INSTANTANEOUS (*LEFT SIDE*) AND TIME AVERAGE (*RIGHT SIDE*) LASER INDUCED FLOW VISUALISATION IMAGES IN CROSSFLOW PLANE AT $x/c = 0.8$, $\alpha = 25°$, FOR DIFFERENT DIMENSIONLESS FREQUENCIES AND $\Delta\phi = 1°$. 103
FIGURE 5.4: DETAILED INSTANTANEOUS (*LEFT SIDE*) AND TIME AVERAGE (*RIGHT SIDE*) LASER INDUCED FLOW VISUALISATION IMAGES IN CROSSFLOW PLANE AT $x/c = 0.8$, $\alpha = 25°$, FOR DIFFERENT DIMENSIONLESS FREQUENCIES AND $\Delta\phi = 1°$. 104
FIGURE 5.5: MEAN AND RMS VELOCITY MEASUREMENTS AT $x/c = 0.7$ AND AT $y/s = 0$, FOR $\alpha = 25°$, FOR DIFFERENT DIMENSIONLESS FREQUENCIES AND $\Delta\phi = 1°$. 105
FIGURE 5.6: MEAN AND RMS VELOCITY MEASUREMENTS AT $x/c = 0.7$ AND AT $y/s = 0.5$, FOR $\alpha = 25°$, FOR DIFFERENT DIMENSIONLESS FREQUENCIES AND $\Delta\phi = 1°$. 106

FIGURE 5.7: MEAN AND RMS VELOCITY MEASUREMENTS AT $x/c = 0.7$ AND AT $y/s = 0.5$, FOR $\alpha = 25°$, FOR DIFFERENT AMPLITUDES AND $f_r = 1$... 107
FIGURE 5.8: MEAN AND RMS VELOCITY CONTOURS AT $x/c = 0.7$, $\alpha = 25°$, $\Delta\phi = 5°$ AND $f_r = 1$ 108
FIGURE 5.9: EFFECT OF DIMENSIONLESS FREQUENCY, f_r, ON $\Lambda = 50°$ DELTA WING AT $\alpha = 25°$ UNDER SMALL AMPLITUDE $(\Delta\phi = 5°)$ ROLLING MOTION. 109
FIGURE 5.10: VARIATION OF THE MEAN BREAKDOWN LOCATION AS A FUNCTION OF THE DIMENSIONLESS FREQUENCY, f_r, FOR DIFFERENT INCIDENCES... 112
FIGURE 5.11: VARIATION OF THE MEAN BREAKDOWN LOCATION AS A FUNCTION OF THE DIMENSIONLESS FREQUENCY, f_r, AT $\alpha = 25°$, UNDER DIFFERENT AMPLITUDE ROLLING MOTION. 114
FIGURE 5.12: VARIATION OF THE MEAN BREAKDOWN LOCATION AS A FUNCTION OF THE DIMENSIONLESS FREQUENCY, f_r, AT $\alpha = 25°$, FOR DIFFERENT RE... 114
FIGURE 5.13: EFFECT OF DIMENSIONLESS FREQUENCY, f_r, ON $\Lambda = 50°$ DELTA WING AT $\alpha = 25°$ UNDER SMALL AMPLITUDE $(\Delta\phi = 1°)$ ROLLING MOTION. 115
FIGURE 5.14: POSITIONS OF THE WING, AS SEEN FROM THE BACK DURING THE OSCILLATORY MOTION, AT 0.25 TIME INTERVALS OF THE CYCLE AT DIFFERENT TIMES. 117
FIGURE 5.15: MAGNITUDE OF VORTICITY IN A CROSSFLOW PLACE $(x/c = 0.8)$ FOR STATIONARY AND SMALL AMPLITUDE $(\Delta\phi = 5°)$ ROLLING MOTION, AT $\alpha = 25°$. 118
FIGURE 5.16: VARIATION OF NORMALISED CIRCULATION OF VORTICAL FLOW IN A CROSSFLOW PLANE AT $x/c = 0.8$ AS A FUNCTION OF A DIMENSIONLESS FREQUENCY, AT $\alpha = 25°$. 120
FIGURE 5.17: MAGNITUDE OF VORTICITY IN A CROSSFLOW PLACE $(x/c = 0.8)$ FOR STATIONARY AND SMALL AMPLITUDE $(\Delta\phi = 1°)$ ROLLING MOTION, AT $\alpha = 25°$. 121
FIGURE 5.18: VARIATION OF NORMALISED CIRCULATION OF VORTICAL FLOW IN A CROSSFLOW PLANE AT $x/c = 0.8$ AS A FUNCTION OF A DIMENSIONLESS FREQUENCY, AT $\alpha = 25°$. 123
FIGURE 5.19: NEAR-SURFACE STREAMLINE PATTERNS FOR DIFFERENT DIMENSIONLESS FREQUENCIES, AT $\alpha = 25°$, FOR $\Delta\phi = 5°$ 124
FIGURE 5.20: VARIATION OF NORMALISED PRESSURE GRADIENT AS A FUNCTION OF THE CHORD LENGTH, $\alpha = 25°$ FOR DIFFERENT DIMENSIONLESS FREQUENCIES AND FOR $\Delta\phi = 5°$ 125

CHAPTER 6

FIGURE 6.1: EFFECT OF DIMENSIONLESS FREQUENCY, $f_r = 0$ (*RIGHT SIDE*), $f_r = 1.2$ (*LEFT SIDE*) ON $\Lambda = 40°$ DELTA WING AT DIFFERENT INCIDENCES UNDER SMALL AMPLITUDE $(\Delta\phi = 5°)$ ROLLING MOTION. 132

FIGURE 6.2: VARIATION OF THE BREAKDOWN LOCATION AND THE WAKE DISTANCE AS A FUNCTION OF THE DIMENSIONLESS FREQUENCY AT $\alpha = 15°$ ON A $\Lambda = 40°$ DELTA WING. 133
FIGURE 6.3: VARIATION OF THE MEAN WAKE DISTANCE AS A FUNCTION OF THE DIMENSIONLESS FREQUENCY, AT DIFFERENT INCIDENCES, FOR A $\Lambda = 40°$ DELTA WING. 133
FIGURE 6.4: EFFECT OF DIMENSIONLESS FREQUENCY, $f_r = 0$ (*RIGHT SIDE*), $f_r = 1.2$ (*LEFT SIDE*) ON $\Lambda = 30°$ DELTA WING AT DIFFERENT INCIDENCES UNDER SMALL AMPLITUDE $(\Delta\phi = 5°)$ ROLLING MOTION. 134
FIGURE 6.5: VARIATION OF THE MEAN WAKE DISTANCE AS A FUNCTION OF THE DIMENSIONLESS FREQUENCY, AT DIFFERENT INCIDENCES, FOR A $\Lambda = 30°$ DELTA WING. 135
FIGURE 6.6: EFFECT OF DIMENSIONLESS FREQUENCY, ON A $\Lambda = 50°$ CROPPED DELTA WING AT $\alpha = 25°$ UNDER SMALL AMPLITUDE $(\Delta\phi = 5°)$ ROLLING MOTION. 136
FIGURE 6.7: VARIATION OF THE MEAN WAKE DISTANCE AND THE BREAKDOWN LOCATION AS A FUNCTION OF THE DIMENSIONLESS FREQUENCY, AT $\alpha = 25°$, FOR A $\Lambda = 50°$ CROPPED AND SIMPLE DELTA WING. 138
FIGURE 6.8: EFFECT OF DIMENSIONLESS FREQUENCY, ON A $\Lambda = 40°$ CROPPED DELTA WING AT DIFFERENT INCIDENCES UNDER SMALL AMPLITUDE $(\Delta\phi = 5°)$ ROLLING MOTION. 139
FIGURE 6.9: EFFECT OF DIMENSIONLESS FREQUENCY, ON A $\Lambda = 30°$ CROPPED DELTA WING AT DIFFERENT INCIDENCES UNDER SMALL AMPLITUDE $(\Delta\phi = 5°)$ ROLLING MOTION. 140
FIGURE 6.10: EFFECT OF DIMENSIONLESS FREQUENCY, ON A $\Lambda = 20°$ CROPPED DELTA WING AT DIFFERENT INCIDENCES UNDER SMALL AMPLITUDE $(\Delta\phi = 5°)$ ROLLING MOTION. 141
FIGURE 6.11: EFFECT OF DIMENSIONLESS FREQUENCY, f_r, ON $\Lambda = 50°$ DELTA WING AT $\alpha = 25°$ UNDER SMALL AMPLITUDE $(\Delta\alpha = 1°)$ PITCHING MOTION. 142
FIGURE 6.12: VARIATION OF THE MEAN BREAKDOWN LOCATION AS A FUNCTION OF THE DIMENSIONLESS FREQUENCY, AT $\alpha = 25°$, UNDER SMALL AMPLITUDE PITCHING AND ROLLING MOTION. 144

CHAPTER 7

FIGURE 7.1: COMPARISON BETWEEN STATIC (*LEFT SIDE*) AND DYNAMIC CASE (RIGHT SIDE, $f_r = 0.01$) FLOW VISUALISATION IMAGES AT $\alpha = 15°$ FOR $\phi_{max} = 30°$ 159
FIGURE 7.2: COMPARISON BETWEEN STATIC (*LEFT SIDE*) AND DYNAMIC CASE (RIGHT SIDE $f_r = 0.15$) FLOW VISUALISATION IMAGES AT $\alpha = 15°$ FOR $\phi_{max} = 30°$ 160
FIGURE 7.3: CROSS FLOW STATIC VORTICITY MEASUREMENTS AT $x/c = 0.8$ AND $\alpha = 15°$ FOR DIFFERENT ROLL ANGLES. 161

FIGURE 7.4: VARIATION OF THE VORTEX BREAKDOWN POSITION, X_{BD}/c, WITH THE ROLL ANGLE, FOR DIFFERENT CASES OF THE WING MOTION, AT $\alpha = 15°$ AND FOR $\phi_{max} = 30°$ 162
FIGURE 7.5: COMPARISON BETWEEN STATIC (*LEFT SIDE*) AND DYNAMIC CASE (RIGHT SIDE, $f_r = 0.01$) FLOW VISUALISATION IMAGES AT $\alpha = 15°$ AND FOR $\phi_{max} = 40°$ 163
FIGURE 7.6: COMPARISON BETWEEN STATIC (*LEFT SIDE*) AND DYNAMIC CASE (RIGHT SIDE $f_r = 0.15$) FLOW VISUALISATION IMAGES AT $\alpha = 15°$ AND FOR $\phi_{max} = 40°$ 164
FIGURE 7.7: VARIATION OF THE VORTEX BREAKDOWN POSITION, X_{BD}/c, WITH THE ROLL ANGLE, FOR DIFFERENT CASES OF THE WING MOTION , AT $\alpha = 15°$ AND FOR $\phi_{max} = 40°$ 165
FIGURE 7.8: COMPARISON BETWEEN STATIC (*LEFT SIDE*) AND DYNAMIC CASE (RIGHT SIDE, $f_r = 0.01$) FLOW VISUALISATION IMAGES AT $\alpha = 20°$ AND FOR $\phi_{max} = 30°$ 166
FIGURE 7.9: COMPARISON BETWEEN STATIC (*LEFT SIDE*) AND DYNAMIC CASE (RIGHT SIDE $f_r = 0.15$) FLOW VISUALISATION IMAGES AT $\alpha = 20°$ AND FOR $\phi_{max} = 30°$ 167
FIGURE 7.10: VARIATION OF THE VORTEX BREAKDOWN POSITION, X_{BD}/c, WITH THE ROLL ANGLE, FOR DIFFERENT CASES OF THE WING MOTION, $\alpha = 20°$ AND FOR $\phi_{max} = 30°$ 168
FIGURE 7.11: COMPARISON BETWEEN STATIC (*LEFT SIDE*) AND DYNAMIC CASE (RIGHT SIDE $f_r = 0.01$) FLOW VISUALISATION IMAGES AT $\alpha = 20°$ AND FOR $\phi_{max} = 40°$ 169
FIGURE 7.12: COMPARISON BETWEEN STATIC (*LEFT SIDE*) AND DYNAMIC CASE (RIGHT SIDE $f_r = 0.15$) FLOW VISUALISATION IMAGES AT $\alpha = 20°$ AND FOR $\phi_{max} = 40°$ 170
FIGURE 7.13: VARIATION OF THE VORTEX BREAKDOWN POSITION, X_{BD}/c, WITH THE ROLL ANGLE, FOR DIFFERENT CASES OF THE WING MOTION , AT $\alpha = 20°$ AND FOR $\phi_{max} = 40°$ 171
FIGURE 7.14: COMPARISON BETWEEN STATIC AND DYNAMIC VORTICITY IN A CROSSFLOW PLANE AT $x/c = 0.8$ AND $\alpha = 20°$ OVER A CYCLE. 172
FIGURE 7.15: VARIATION OF NORMALISED CIRCULATION WITH THE ROLL ANGLE FOR THE COUNTER-CLOCKWISE VORTEX OVER A CYCLE , FOR THE STATIC AND DYNAMIC CASE AT $\alpha = 20°$ AND $x/c = 0.8$ 175
FIGURE 7.16: COMPARISON BETWEEN STATIC (*LEFT SIDE*) AND DYNAMIC CASE (*RIGHT SIDE*) FLOW VISUALISATION IMAGES AT $\alpha = 25°$ FOR $\phi_{max} = 30°$ 176
FIGURE 7.17: COMPARISON BETWEEN STATIC AND DYNAMIC VORTICITY IN CROSSFLOW PLANE AT $x/c = 0.8$ AND $\alpha = 25°$ OVER A CYCLE. 179

FIGURE 7.18: COMPARISON BETWEEN STATIC AND DYNAMIC VORTICITY IN CROSSFLOW PLANE AT $x/c = 0.8$ AND $\alpha = 20°$ OVER A CYCLE FOR $\lambda = 9$ 182
FIGURE 7.19: VARIATION OF NORMALISED CIRCULATION WITH THE ROLL ANGLE FOR THE COUNTER-CLOCKWISE VORTEX OVER A CYCLE , FOR THE DYNAMIC CASE, $f_r = 0.15$, AT $\alpha = 20°$ AND $x/c = 0.8$ FOR THE RIGID AND A FLEXIBLE WING. 185
FIGURE 7.20: COMPARISON BETWEEN STATIC AND DYNAMIC VORTICITY IN CROSSFLOW PLANE AT $x/c = 0.8$ AND $\alpha = 20°$ OVER A CYCLE FOR $\lambda = 21.3$ 186
FIGURE 7.21: INSTANTANEOUS LASER INDUCED FLOW VISUALISATION IMAGES IN CROSSFLOW PLANE FOR DIFFERENT ROLL ANGLES AT $x/c = 0.8$, FOR STATIONARY (*LEFT SIDE*) AND DYNAMIC CASE (*RIGHT SIDE*) AT $\alpha = 22.5°$ 189
FIGURE 7.22: TIME AVERAGE LASER INDUCED FLOW VISUALISATION IMAGES IN CROSSFLOW PLANE FOR DIFFERENT ROLL ANGLES AT $x/c = 0.8$, FOR STATIONARY (*LEFT SIDE*) AND DYNAMIC CASE (*RIGHT SIDE*) AT $\alpha = 22.5°$ 190

LIST OF TABLES

CHAPTER 1

TABLE1.1: STATISTICS OF LIFT ENHANCEMENT AND STALL DELAY OVER FLEXIBLE DELTA WINGS WITH VARYING SWEEP ANGLES. COLUMN (A): C_{LMAX} OF FLEXIBLE WHEN COMPARED WITH C_{LMAX} OF RIGID (TAYLOR *ET AL.*-2005)..... 38

CHAPTER 2

TABLE 2.1: SPECIFICATIONS OF THE EIDETICS MODEL 1520 WATER TUNNEL (COURTESY ROLLING HILLS RESEARCH CORPORATION)..... 48
TABLE 2.2: DIMENSIONS FOR THE LOW SWEEP MODELS..... 48

CHAPTER 3

TABLE 3.1: MATERIAL PROPERTIES AND SPANWISE BENDING FLEXIBILITY FOR THE FLEXIBLE AND RIGID WINGS..... 71

NOMENCLATURE

Latin Symbols

b	Wing Span	[mm]
c	Chord Length	[mm]
C_L	Lift Coefficient	
C_{Lmax}	Maximum Lift Coefficient	
C_{Lp}	Potential Flow Lift Coefficient	
C_{Lv}	Vortex Lift Coefficient	
C_P	Pressure Coefficient	
d	Diameter	[mm]
E	Elastic Modulus	[N/m^2]
f	Frequency	[Hz]
f_D	Doppler Frequency	[Hz]
f_r	Non-dimensional or Reduced Frequency	
q_∞	Free Stream Dynamic Pressure	[N/m^2]
Re	Reynolds Number	
s	Local Semispan	[mm]
St	Strouhal Number	
t	Thickness	[mm]
T	Temperature	[°C]
u	Velocity in Streamwise Direction	[m/s]
U_∞	Free Stream Velocity	[m/s]
U_{mean}	Mean Velocity	[m/s]
U_{rms}	Root Mean Square Velocity	[m/s]
v	Velocity in Lateral Direction	[m/s]
w	Velocity in Vertical Direction	[m/s]
x	Streamwise Dimension	[m]
y	Lateral Dimension	[m]
z	Vertical Dimension	[m]

Greek Symbols

α	Angle of Attack	[°]
α_{stall}	Stall Angle	[°]
Γ	Circulation	[m^2/s]
γ	Leading Edge Bevel Angle	[°]
$\Delta\alpha$	Amplitude of Pitching Motion	[°]
$\Delta\phi$	Amplitude of Rolling Motion	[°]
δ_f	Fringe Spacing	[m]
Δt	Time Difference	[s]
Δy, Δx	Distance in the respective axis	[mm]
Δy_w	Distance Between Wakes	[mm]
λ	Spanwise Bending Flexibility	
λ_f	Wavelength of the Light	[m]
Λ	Wing Sweep Angle	[°]
ν_∞	Kinematic Viscosity of the Mean	
ν	Poisson's Ratio	
ξ	Vorticity	[rad/s]
ρ_∞	Density on the Mean	[kg/m^3]
ϕ	Roll Angle	[°]
ϕ_{max}	Maximum Amplitude of Manoeuvre	[°]
ϕ_{start}	Roll Angle at which the Manoeuvre Starts	[°]
X_{BD}	Breakdown Location	[mm]
ω	Angular Velocity	[rad/s]
$\omega c/U_\infty$	Non-Dimensional Vorticity	

ABBREVIATIONS

3D	Three-Dimensional
AR	Aspect Ratio
ASCII	American Standard Code for Information Interchange
CCD	Charge Coupled Device
CFD	Computational Fluid Dynamics
CSV	Comma Separated Value
DPIV	Digital Particle Image Velocimetry
FFT	Fast Fourier Transform
FPS	Frames Per Second
K-H	Kelvin-Helmholtz
LCO	Limit Cycle Oscillation
LDV	Laser Doppler Velocimetry
MAV	Micro Air Vehicle
PC	Personal Computer
PMT	PhotoMultiplier Tube
RMS	Root Mean Square
UAV	Unmanned Air Vehicle
UCAV	Unmanned Combat Air Vehicle

CHAPTER 1: INTRODUCTION

1.1 Background

A delta wing aircraft is defined as having "swept-back wings that give it a triangular appearance", as provided by the Oxford Dictionary. Its use was pioneered by Alexander Lippisch in Germany and Boris Ivanovich Cheranovsky in the USSR prior to World War II (Iowa State University, e-Library-2000), and since then it has been widely used in the aerospace industry due to its ability to generate a higher lift force coefficient than plain wing configurations, at high angles of attack. Additionally, at high incidence a delta wing presents better stability and control characteristics than a plain wing. These reasons have made it more popular and more attractive to the aerospace industry, especially for military purposes, where high manoeuvrability at high incidences is required. A good comparison between delta wings and plain wings, for the purposes of lift generation, is given in the qualitative diagram in Figure 1.1, where it is evident that a delta wing can maintain its lift at considerably higher incidences.

There are several variations in the shape of delta wings used in modern aircraft such as simple, cropped, notched or double delta wings, as shown in Figure 1.2. Two different types of delta wings, based on their sweep angles are predominant in aerodynamics and have attracted the attention of the author in this thesis: slender and nonslender delta wings. Nonslender delta wings are defined as wings with sweep angles of less than 55°.

The flow pattern over delta wings at high angles of attack is vortex dominated. Vortices are created due to the difference in pressure between the two surfaces of the wing, which consequently forces the flow around the leading edge to curl up from the bottom surface to the top. When the leading edge is swept and sharp, the vortex sheet which is created over the wing adds continually to the vorticity, and finally forms a pair of very strong and stable, counter-rotating leading edge vortices, such as the ones shown in Figure 1.3. These vortices create a strong suction force on the top surface near the leading edges, which enhances the lift produced and at the same time explains why the lift coefficient is still increasing at angles of attack where

conventional wing planforms would have stalled. The velocity values near the vortex core are quite high, whereas the static pressure in the vortex core is low, which generates the vortex-induced lift, or vortex lift, on the delta wings, as Polhamus (1971), Wentz and Kohlman (1971), Gad-el-Hak and Blackwelder (1985), Lee and Ho (1990), and Cipolla and Rockwell (1998) and many other researchers have reported. The vortex lift is extremely important for delta wings, especially at high angles of attack, since it is their main source of lift generation.

However, as the angle of attack is increased, the vortices undergo a sudden expansion, which is known as vortex breakdown or vortex bursting. The mechanism that lies behind this phenomenon has been studied extensively (since the late 1950's) and many explanations have been provided for its occurrence. However, what is not yet fully understood is why the vortex core's axial and circumferential velocities undergo a rapid deceleration. The result of this is that the axial flow stops, a stagnation point on the centre line of the vortical structure is encountered and large-scale fluctuations occur. Due to the fact that the vortices are an important factor in the lift production, an attempt has been made to preserve them over the wing or delay their breakdown, and various techniques have been proposed to reduce the adverse effects of the vortex breakdown phenomenon on aircraft performance.

Existing and future Unmanned (Combat) Air Vehicles (UAV/UCAV's) and Micro Air Vehicles (MAV's) have received extensive attention in the aerospace industry, increasing interest in manoeuvring delta wing aerodynamics. A great effort has been made to give explanations for unsteady manoeuvring phenomena such as pitching, rolling and wing rock. Both experimental measurements and numerical simulations have been used to assess the capabilities of different aircraft configurations performing extreme manoeuvres at high incidences. Additionally, flexible delta wings have been a popular subject in the literature recently and their study has proven useful, providing insight into new aerodynamic aspects.

This thesis begins with a literature review of both slender and nonslender delta wings and focuses on the flowfield developed over them, the vortex breakdown phenomenon, and the unsteady aerodynamics of manoeuvring wings, and continues with a review of flexible wings and phenomena associated with them, followed by the objectives of this study. Experimental apparatus and procedures are discussed in the following chapters. The results of this research are separated into four chapters. The first deals with the effect that flexibility has on the flowfield of a delta wing. This is followed by a chapter on rigid delta wings under dynamic conditions, where the results of experiments with small amplitude and high frequency oscillations are presented. Other parametric effects such as small amplitude pitching motion, different sweep angles, and planform shapes are discussed in the third chapter of results. Dynamic, large amplitude rolling manoeuvres on both rigid and flexible delta wings are presented in the last chapter of results. Finally, a summary of the main conclusions and recommendations for future research along with the references used and the author's publications are presented in the last chapters of this thesis.

1.2 Literature Review

1.2.1 Introduction

This chapter reviews the relevant literature for both slender and nonslender delta wing aerodynamics. There is a large amount of information and research on slender delta wings, but the same cannot be said for nonslender wings, particularly in manoeuvring aerodynamics. As a result of this, an extensive literature review is provided on slender delta wings, including phenomena like vortex breakdown and manoeuvring aerodynamics. Due to the fact that the whole project was based on the study of the unsteady aerodynamics of manoeuvring nonslender delta wings, the same effort has been made to collect information on these, and to present the available literature.

1.2.2 Vortical Flows over Delta Wings and the Effect of Different Parameters

1.2.2.1 Introduction

As previously mentioned, a delta wing has the remarkable characteristic of maintaining lift at high angles of attack where plain wing configurations have already stalled. In addition, better aircraft stability and control characteristics are demonstrable. The flowfield over a delta wing is vortex dominated, and an extended view and analysis are given in this section. Slender delta wings are initially discussed with a focus on the different types of flow that appear over the wing, followed by the unsteadiness of the flowfield and the interactions between the vortices that have been observed, and finishing with the various parameters that affect the flowfield in general. A separation in the analysis and description of the flowfield between slender and nonslender delta wings is necessary, as the differences between them are distinct. However, there are also similarities which are worth mentioning. Emphasis is placed on the differences encountered between slender and nonslender delta wings when the same parameter is applied on both configurations.

1.2.2.2 Slender Delta Wings

A delta wing set at an incidence to the free stream will generate two counter-rotating leading edge vortices. Their strength and their breakdown location depend on various parameters, such as the sweep angle, the incidence and the Reynolds number. As shown in Figure 1.3, the flow approaching the delta wing forces the boundary layer to separate, forming a free shear layer, and thus creating a primary vortex inboard of the leading edge on the suction side of the wing. This separated flow loops over the wing and then reattaches along the primary attachment line. The amount of vorticity that rolls up to create a vortex depends mainly on the condition of the boundary layer at the leading edge prior to separation, as it is the local curvature which determines

the pressure gradient (Lee and Ho-1990). Additionally it is this vorticity balance between diffusion and convection which will determine the state of the vortices. The flow over a wing with sharp leading edges will separate at a specific point (right at the sharp edge) producing a high suction region, whereas on a wing with rounded tips separation can occur at different points depending on the curvature of the edge (ellipse, semi-circular) and the flow conditions (Re).

A secondary vortex, with the opposite sign of vorticity, forms underneath the primary one, and also reattaches on its own reattachment line (Figure 1.3). In the area inboard of the two leading edge vortices, the surface streamlines starting from the vertex of the wing remain attached, and the flow is virtually undisturbed along the chord length. Continuous feeding of vorticity from the shear layer along the leading edge preserves the vortical structures over the delta wing, and thus the lift force. Leading edge vortices on slender delta wings can generate very strong axial velocities and their maximum can be as large as four or five times the free stream velocity.

The vortical flowfield developed over a slender delta wing has a conical shape. Evidence of this conical flow is provided by the linear increase in the vortex strength beginning at the apex and moving downstream, plus the increase in circulation with the incidence, for measurements on a fixed location on the wing (Visser and Nelson-1993). However, other approaches (Nelson and Pelletier-2003) associate the velocity flowfield with the leading edge vortex, as a superposition of a jet flow and a vortical flow.

A better understanding of the vortical flowfield and the parameters affecting it was considered necessary. This resulted in numerous studies where different types of flow were identified and more interestingly the same type of flow could be characterised by different regions and hence different characteristics. Three different regions were identified, according to Erickson (1982) and Visser and Washburn (1994), on the flowfield over a slender delta wing. The first area is identified as the inviscid flow outside the surface boundary layer, the free shear layer and the vortex core. Potential flow equations can be assumed for this area, and from these equations, the location of the vortex core, the vortex sheet and hence the lift of the wing can be established. The second region describes the boundary layer flow near the wing, which is dominated by viscous effects and is responsible for the generation of the secondary vortex. The third is the vorticity inside the vortex core and the vortex sheet hence provides information on the internal structure of the vortical flow (Erickson-1982). However, a different classification of the three areas is presented by Visser and Washburn (1994). These are: the area inboard of the primary attachment line, the area between the primary attachment and the secondary separation, and the area outboard of the secondary separation. The first region is dominated by attached potential flow, the second by primary vortices and the third by secondary vortices. Below the vortices and on the forward part of the wing, a laminar boundary layer occurs, which later transitions to a turbulent profile (Figure 1.4).

After analysing the flowfield from a macroscopic point of view, where different flow patterns and regions were identified, a more detailed examination of the flowfield

revealed that there is some form of interaction between the primary and the secondary vortices, which consequently received a lot of attention. This was attributed to the fact that it could possibly affect the overall behaviour of the flowfield and potentially change its dynamics.

Four repetitive stages of interaction were observed by Shih and Ding (2002): primary vortex induction with secondary vortex ejection, the effect of the ejection process on the primary vortex, the weakening of both vortices, and finally the reconnection of the primary vortex to the shear layer. In a more detailed description of the flowfield on a 60° sweep angle delta wing, at 50% of its chord, the secondary vortex exists and is located directly below the primary vortex. As time passes, the secondary vortex is ejected and moves upwards, closer to the primary. The tendency of the secondary vortex to displace the primary one by moving it upwards and inwards was also indicated by Visser and Washburn (1994). Note that this displacement is larger when the boundary layer underneath the vortex is laminar. A turbulent layer is capable of resisting the adverse pressure gradient, and so can remain attached for a longer period of time and separate closer to the leading edge. This movement affects the primary vortex, and interrupts the feeding of vorticity through the shear layer; both the primary vortex and the secondary vortices are thus weakened. The final stage of this process, allowed by the weakening of the secondary vortex, is represented by the reconnection of the shear layer with the primary vortex, which in turn resumes the feeding of vorticity. The last event reenergizes the primary vortex, and the cycle of primary/secondary interaction is repeated. No external perturbations are required to sustain this cyclic interaction.

It has been documented that the dynamics of the main vortex is different from that of the shear layer, with the maximum swirl velocity being 3.5 times bigger than the free stream (Menke and Gursul-1997). Additionally, since the strength of the vortices increases with the incidence, and therefore the swirl velocity increases, it was deemed necessary to see if the interaction between the opposite sign vortices is the cause of the large fluctuations observed in velocity. For this reason a splitter plate was placed between the two and the measurements recorded showed that the velocity profile did not change considerably. Only a slight shift in the position of the vortex core towards the leading edge was observed (Menke and Gursul-1997) leaving the interaction between the two vortices not responsible for the large fluctuations.

A deeper analysis and examination of the shear layer, which is responsible for the creation of the vortices, is required due to the importance of the structures that appear in the outer periphery of the primary vortices. For this reason a number of researchers have focused on the mechanisms that appear in the shear layer and provided explanations for their existence.

One of the explanations is that the primary vortices are the result of a series of small discrete vortices, which rotate around each other and at the same time move downstream. Gad-el-Hak and Blackwelder (1985) suggested that the small vortices shed from the leading edge rotate around each other and pair up to finally form a

large vortex. This phenomenon was attributed to Kelvin-Helmholtz (K-H) instability[1] of the two-dimensional (2D) shear layer. Although this was observed by many authors (Gordnier and Visbal-1994 and Ozgoren *et al.* 2002) a second type of instability was also documented, which is steady, and creates small scale vortices around the primary vortex (Riley and Lowson-1998, Payne *et al.*-1988 and Mitchell and Molton-2002). As a result, levels of vorticity may be classified according to their physical origin, arising from both vortex breakdown and leading edge instabilities.

Further research into the shear layer confirmed the existence of spatially stationary vortical substructures (Washburn and Visser-1994). The size and the rate of generation of these substructures depend on the wing sweep angle and the angle of attack. The substructures are co-rotating, and when the angle of attack is increased, they appear more elongated and stretched. Additionally, when the incidence is increased, the shear layer extends much further around the vortex, before creating substructures. Consequently, the reduction in the sweep angle creates a stronger primary vortex, hence increasing the generation frequency of the substructures and decreasing their size. The vortical substructures seem to be independent of changes in Re and are believed to exist due to the instability in the shear layer following a helical path around the vortex core.

Apart from the small scale structures identified in the periphery of the shear layer and around the vortex, unsteadiness in the nature of the leading edge vortices and pressure fluctuations were also observed by various researchers, including Gordnier and Visbal (1994), Gursul (1994) and Menke and Gursul (1997). Gordnier and Visbal (1994) attributed the unsteadiness to K-H instability whereas Gursul (1994) found that the source of these fluctuations is the helical mode instability and not vortex shedding, although velocity fluctuations in the wake show oscillations. It is generally believed that the flow downstream of the breakdown has much larger velocity fluctuations than the flow upstream. Gad-el-Hak and Blackwelder (1985) demonstrated that shear layer vortices due to the K-H instability exist in the separated shear layer. However, on the other hand, Menke and Gursul (1997) found that large velocity fluctuations, therefore unsteadiness, could not be produced by the shear layer instabilities. A simple model proposed that these fluctuations are due to random displacements in the vortex core and not to the interaction between the opposite leading edge vortices.

A large amount of literature has been dedicated to the parameters that affect the flowfield and the vortices in it. Both numerical simulation and experimental studies have been undertaken in view of the effects that different parameters have in the flowfield. The importance of these studies underlies firstly the identification of these parameters and secondly the fact that a minor variation can significantly alter the flowfield and along with it its aerodynamic characteristics. One of the parameters and its effect, which has received a lot of attention, is the Reynolds number.

[1] The Kelvin-Helmholtz instability is a classical example of hydrodynamic instability, which occurs when two fluids with different velocity, are separated by a surface across which the tangential velocity has a discontinuity.

A numerical study (Gordnier and Visbal-1994) pointed out a strong dependence of the flowfield on Re. At high Re (900,000) small-scale shear-layer vortices are formed and shed from the leading edge. On the other hand, the flowfield at low Re (50,000) is governed by primary and secondary vortices along with a series of small-scale vortical structures in the shear layer. The difference lies in the fact that at high Re the small-scale vortical structures are formed and shed from the leading edge of the delta wing, whereas at low Re they form further away from the leading edge, along the vortex sheet. This reduces their interaction with the secondary separation and with the wing surface. Note that Re seemed to have no effect on the unsteadiness of the flowfield, since it was present at both low (50,000) and high (900,000) Re.

A recent series of computations provided insight into the evolution of the flowfield over a range of low Reynolds numbers (Visbal and Gordnier-2003). At Re = 6,000 a steady shear layer without any substructures is present. Unsteady substructures appear at a higher Re (50,000), which then move closer to the apex, and surround the vortex core. The evolution of the instantaneous flowfield structure with increasing Re is seen in Figure 1.5. Although the range of Re covered is relatively small the complexity appearing in the vortex system was quite dramatic. The origin of the shear layer substructures moves progressively closer to the wing apex and ends up covering the whole wing at the highest Re simulated (Figure 1.5). Near their onset the vortical substructures are very coherent. However, as they move further downstream on the delta wing surface, they undergo a process of secondary instability and break up into discrete vortices, which in turn follow helical paths around the primary vortex. Downstream of this region, the instantaneous shear-layer representation is characterised by the existence of helical substructures that co-rotate around the primary vortex (Figure 1.6). This suggests that the so-called unsteady and stationary substructures are not two separate phenomena, but different representations of the same shear layer transitional process (Visbal and Gordnier-2003). The formation of the unsteady substructures is attributed to the onset of unsteady boundary layer separation and the ejection of vorticity on the wing. Hence, this unsteadiness arises naturally and it is not induced by any freestream perturbation.

In contradiction to the aforementioned numerical simulations, variations in the free stream velocity have changed the flowfield and introduced new features to it. Flow visualisation by Lowson (1991) has shown that at low speeds the flow is laminar, but as the speed is increased, unsteady effects emerge, generating vortical structures within the shear layer before it develops into fully turbulent flow. Interestingly enough, there are differences in the vortex locations when comparing results from experiments undertaken in water and wind tunnels. The vortex locations encountered in water tunnel experiments are slightly inboard and upward from the wing, which is believed to be due to the effects of larger laminar secondary separation or possible spanwise camber effects. Instabilities in the shear layer were also reported, and a forcing frequency was found and attributed to the tunnel motor cooling fan (Lowson-1991) contrary to Visbal and Gordnier (2003) where the unsteadiness appears naturally and the dominant frequencies calculated could not possibly be due to any external perturbations.

Additional studies (Visser and Washburn-1994) of the flowfield below the vortices and on the forward part of the wing showed that a laminar boundary layer occurs, which later transitions to a turbulent profile (Figure 1.4). An increase in Re, the incidence or the apex angle (decrease in the sweep angle) moves the transition point towards the apex. In concurrence with Shih and Ding (2002), an upstream transition (an increase in Re) moves the entire primary vortex downwards and outwards, contributing to the reduction in size of the secondary vortex. Other than that, the flowfield remains unchanged. Additionally, knowledge of the transition point provides useful tools for the estimation of the vortex circulation. Consequently an increase in any of these parameters (Re, incidence or apex angle) results in an increase in the circulation. Hence, the indication of a critical transitional Reynolds number, based on the velocity at the surface of the wing and the attached flow length, has been confirmed by Visser and Washburn (1994).

Another aspect of the flowfield which is also influenced by changes in Re is the aerodynamic characteristics of a slender delta wing, as presented by Traub *et al.* (1998) for $Re = 2\times10^4$ to 6×10^4. Increasing Re for a given angle of attack results in an increase in the lift force, but not beyond a specific value. The lift force is decreased for Re higher than the threshold value, which is noticeable around the maximum lift. A conclusion of the flow visualisation experiments, is that the secondary separation line moves outboard as Re increases, but again only for a limited part of the range tested. There seems to be a transition point in the flowfield estimated between $Re = 2\times10^4$ and 4×10^4, and a critical Re, which was confirmed by further experiments in the same range.

Other parameters that affect the flowfield and have been documented are the changes in the anhedral or dihedral angle of a wing. Additionally, different leading edge profiles and changes in the sweep angle seem to create great variations in the vortical flowfield.

The effects of anhedral and dihedral on a 75° sweep angle delta wing were documented experimentally by Traub (2000b). The lift force was found to change considerably, with the lift increasing for anhedral and decreasing for dihedral. As a result, anhedral is more beneficial and efficient for a wider range of applications. Small variations in anhedral angle augment the lift, although a great increase in the strength of the leading edge vortices is not evident. However, the total vortex circulation increases with increasing anhedral. Another advantage of the implementation of anhedral is the displacement of the vortex trajectory inboard and closer to the wing surface. Dihedral not only moves the vortex trajectory closer to the wing surface, but it also displaces it towards the apex. Moreover both angles seemed to introduce no adverse effects on the stability of the aircraft and the vortex breakdown characteristics.

The effect of different leading edge profiles on the flowfield of a 70° delta wing has been explored by Kegelman and Roos (1989). The common and widespread belief that the leading edge shape does not significantly affect the flowfield, provided that the wing is thin and the leading edge sharp (for example Earnshaw and Lawford-1964, Wentz and Kohlman-1971 and Payne *et al.*-1988), was proven to be incorrect.

Different separation lines appeared on the flowfield of various leading edge profiles along with different lift coefficients at the same incidences. The lift characteristics are determined by the strength of the leading edge vortex and the vorticity being fed near the leading edge.

Taking into consideration that the vortex induced lift plays a very important role in the performance of aircraft, Hemsch and Luckring (1990) underlined the effect that the sweep angle has on the vortical lift and the leading edge vortex strength. An increase in the sweep angle decreases the vortex lift and strength, which is something extremely important if high manoeuvrability and agility at high incidences is required. This conclusion gives rise to the need for low sweep delta wings to be studied, and initiates the development of wings with high angle of attack performance, by tailoring the sweep angle, the camber, and the leading edge profile.

1.2.2.3 Nonslender Delta Wings

The aerodynamic issues associated with nonslender delta wings appear to be even more complicated than those related to slender wings. This is enhanced by the fact that it is only recently that interest in these flows has arisen. As mentioned previously, extensive investigation has been undertaken for almost all the aerodynamic aspects of slender delta wings whereas the same cannot be claimed for the nonslender ones. A recent review article on nonslender delta wings provided by Gursul *et al.* (2005), gives a detailed and complete overview of the available literature on nonslender delta wings and the wide range of phenomena that appear in their flowfield.

There are many similarities between slender and nonslender wings in the way the flow is formed over them. Separation of the boundary layer creates a leading edge vortex. A secondary vortex of the opposite sign of vorticity emerges between the separated shear layer and the wing surface. In a closer observation of the shear layer that forms the primary vortex at upstream locations, a series of vortical substructures is detected for nonslender wings, (Gad-el-Hak and Blackwelder-1985, Ol and Gharib-2001, Ol-2001 and Ol and Gharib-2003) which are shed and convect downstream around the primary vortex. At downstream locations, these substructures become more diffused and break into small, fine, unsteady structures. These vortical substructures are present in the flowfield of both nonslender and slender wings (Gordnier and Visbal-2003 and Taylor *et al.*-2003).

However, there are some very distinct differences in the vortical flow topology between the two types of delta wing, and in the way the flow is affected by various parameters, as was first observed by Earnshaw and Lawford (1964). The vortex core could easily be identified for the whole range of slender delta wings tested, whereas in some of the nonslender wings tested (for example for a $\Lambda = 45°$ wing) it could not be found at all. This was explained by assuming that the vortex breakdown point was very close to the wing apex. Yaniktepe and Rockwell (2004) pointed out that a circular region of vorticity, a classical vortex core, cannot be seen on a $\Lambda = 38.7°$ wing. At relatively low angles of attack, instantaneous patterns of concentrated

vorticity can be identified, whereas at higher incidences, these patterns change more to both small-scale and large-scale concentrations, thus giving a good explanation of the unsteadiness observed in the flowfield. Furthermore, the primary vortices on a nonslender delta wing are created closer to the wing surface and a stronger interaction between the primary vortices, the surface boundary layer, and the secondary vortices is expected (Gursul *et al.*-2002 and Gursul-2004).

Both computational simulations (Gordnier and Visbal-2003) and experiments (Taylor *et al.*-2003) have identified a unique characteristic only observed in nonslender delta wings: the appearance of a second vortical structure with the same sign of vorticity as the primary one observed outboard of the primary vortex, resulting finally in the appearance of a dual vortical structure (see Figure 1.7 and 1.8). This dual structure was attributed to the interaction between the primary shear layer and the secondary flow (Gordnier and Visbal-2003). At the same time, the first experimental data (Taylor *et al.*-2003) on this dual vortex structure considered it a result of the primary vortex being split into two by boundary layer vorticity. This unique characteristic of nonslender delta wings exhibits great sensitivity to Re, the angle of attack and the sweep angle, as it is only observed at low values of these parameters.

Computational simulations by Gordnier and Visbal (2003) at a range of incidences and Re ($\alpha = 5°$ to 15°, $Re = 10{,}000$ to 50,000), identified that even at low angles of attack and low Re the separated shear layer forms a coherent vortex. At the same time, experimental evidence for $Re = 13{,}000$ have shown that there is a distinct vortical structure at an angle of attack as low as $\alpha = 2.5°$ (Taylor *et al.*-2003) (see Figure 1.9). As the incidence is increased, the size of the vortical flow region becomes larger, and the core of the primary vortex moves further away from the wing surface. The effect of Re is quite noticeable. At low Re (10,000), the flow presents strong viscous influences. There is no distinct vortical structure, and only a thick shear layer is observed (Gordnier and Visbal-2003). Experimental data also confirm that a very weak and loose vortical structure, with vorticity distributed around the shear layer is seen at low Re, but increasing Re resulted in the formation of a compact structure (Taylor *et al.*-2003) along with the development of a clear dual vortical structure. A further increase results in additional stretching of the vortices (Gordnier and Visbal-2003).

However, movement of the vortex trajectory inboard, toward the centreline of the wing, was observed with a reduction in Re and an increase in the incidence (Ol and Gharib-2001, Gordnier and Visbal-2003 and Taylor *et al.*-2003). At $\alpha = 20°$ the reattachment line approaches the centreline of the wing, but a further increase results in the reattachment failing. However, experiments in a wind and water tunnel have suggested that there is very little change in the structure of the vortices for $Re \geq 25{,}000$ for a 50° sweep angle delta wing (Taylor *et al.*-2003) contrary to the observations made for slender configurations (Lowson-1991).

A very detailed view of the flow features over a nonslender delta wing for a range of incidences is considered necessary in order to enhance our understanding of it and at the same time point out the differences observed on nonslender delta wings.

Numerical simulations performed by Gordnier and Visbal (2003) provide a very clear view of the flowfield represented by the streamline pattern, as shown in Figure 1.10, at a low incidence $(\alpha = 5°)$. The primary attachment (PA) line lies outboard of the symmetry plane, whereas inboard of this line, the streamlines are roughly aligned with the free stream velocity. The primary attachment line is positioned outboard of the wing centreline and moves closer to the symmetry plane with increasing angles of attack (See Figures 1.10, 1.11 and 1.12). This underlies one of the differences in the flowfield between slender and nonslender delta wings. It is evident that the location of the attachment line is a function of both the incidence and the sweep angle. The secondary separation and attachment are observed between the primary attachment line and the leading edge. The dual structure mentioned earlier remains distinct only at low incidences $(\alpha = 5°)$. At $\alpha = 10°$, only remnants of it appear and a more substantial secondary flow structure becomes visible, followed by a tertiary flow with the same sign of vorticity as the primary one (Figure 1.11). A further increase in the incidence $(\alpha = 15°)$ gives the flowfield a vortical structure which resembles more that of a slender wing (Figure 1.12).

Three distinct regions were identified inside the flowfield of low sweep delta wings; apart from the shear layer that leads to the formation of the primary vortex there is the wake region and reattachment region, where a strong adverse pressure gradient can cause bursting of the wall layer (Honkan and Andreopoulos-1997). In the area below the reattachment region the gradual decrease in the local vorticity is apparent, which is associated with the reduction in the mean velocity. Emphasis is also placed on the wake and its characteristics. The most important feature of it is the mean velocity defect which is associated with the secondary vortex. Hence, the secondary vortex has a wakelike mean velocity profile whereas the primary's is jetlike. A noticeable and noteworthy difference between the primary and the secondary vortex is their strength. The vorticity in the secondary vortex is a third of that of the primary.

Another interesting feature of the flow over nonslender delta wings is that, analogously to slender delta wings, the vortical structure may have a "wakelike" axial velocity profile at low incidences $(\alpha = 10°)$ or a "jetlike" axial velocity profile with increasing incidences $(\alpha = 15°)$ (Figure 1.13; Taylor and Gursul-2004b). Earlier three-dimensional (3D) Particle Image Velocimetry (PIV) crossflow measurements (Ol-2001, Ol and Gharib-2001, and Ol and Gharib-2003), employed on both slender and nonslender delta wings, provided evidence of the "jetlike" profile on a delta wing with $\Lambda = 65°$, and the "wakelike" profile on one with $\Lambda = 50°$. At low angles of attack, that is less than 10°, the flowfield of the $\Lambda = 50°$ was similar to that of the $\Lambda = 65°$ wing. That corresponds to similarities in the geometry of the shear layer, the presence of the primary vortex and the axial velocity distribution. However, higher incidences presented a divergence in the nature of the two flowfields, mainly because of the diffusion and collapse of the leading edge vortex under the increasing incidence. As the sweep angle progressively becomes lower, the flowfield behaves less like that of a slender wing. In the slender wing the axial velocity identifiable with the primary vortex increases with increasing incidence (from nearly the same as the freestream at $\alpha = 5°$ to almost twice that amount at $\alpha = 20°$). However, in the

nonslender one at low incidences ($\alpha = 5°$ and below) the value of the axial velocity in the primary leading edge core never exceeds that of the freestream (Ol-2001). Interestingly enough, by $\alpha = 20°$ the velocity magnitude outboard of the leading edge vortex and inboard of the shear layer is nearly zero, indicating an almost stagnant flow, which is attributed to the effect of the Reynolds number.

Another parameter which can be classified as one of the most important since significant changes can take place in its presence, is the leading edge profile. A thorough investigation undertaken by Miau *et al.* (1995) identified the different flow topologies. In a series of flow visualisation and velocity measurements on a $\Lambda = 50°$ delta wing with different leading edge profiles, the windward bevelling was found to present the most well structured flow characteristics, ensuring the condition for a sharp leading edge separation and a very well organised vortical structure. The trajectory of the shear layer moves further away from the wing, which enables the formation of an organised vortical structure. On the other hand, in the leeward profile, the vortical structure characteristics could hardly be discerned. The trajectory in this case remains close to the wing surface at the leading edge, resulting in a very weak vortical pattern. Consequently, the windward leading edge profile presented the most favourable characteristics for the formation of a leading edge vortex and thus is the one most commonly used.

Although the flowfield and the creation of the vortices on a nonslender and slender wing can be distinctively different, they both share one phenomenon with its adverse effects: breakdown. As expected, though, differences also appear in the presence of breakdown for the two different types of wing and are discussed in the following section.

1.2.3 Vortex Breakdown

As the angle of attack is increased, the vortices undergo a sudden expansion, which is called vortex breakdown or vortex bursting. The vortex breakdown phenomenon is characterised by the abrupt structural change of the vortex core, which is followed by a deceleration and reversal of the axial flow, divergence of the stream surfaces, instabilities and finally turbulent flow. Computational simulations of the breakdown process on a slender delta wing in subsonic flow showed that the vortex core encounters a rapid deceleration followed by an increase in the adverse axial pressure gradient (Kumar-1998). Werle (1960) was the first to observe the vortex breakdown phenomenon in 1954 in a water tunnel facility. The vortex breakdown is an unsteady phenomenon, which has adverse effects on the performance of delta wings (lift loss, unstable pitching and rolling moment behaviour, buffeting and time lags in the aircraft motion) and this is why researchers have focused on investigating it experimentally, numerically and theoretically (see for example Lowson-1964, Cummings *et al.*-2003 and Greenwell and Nangia-2003). A significant reduction in the axial vorticity magnitude takes place in the presence of vortex breakdown, and the spiralling direction of the flow upstream is reversed.

A different explanation of the breakdown phenomenon, the adverse effect it has on the flowfield and the models developed in order to explain it, need to be addressed for slender and nonslender delta wings. However, a description of the structure of the phenomenon, the parameters affecting it, the varying types and aspects of it when encountered either on its own, in a vortex tube, or over a lifting surface such as delta wings, are necessary to improve our understanding.

As already mentioned an issue regarding the vortex breakdown phenomenon is related to the devices used to produce a vortex and consequently the breakdown. Jaworski (1996) provides a good review of the literature regarding devices other than delta configurations, which have been used in order to simulate the vortex breakdown phenomenon. The big difference between these devices, such as a vortex tube, and delta wings, is that they generate "confined" vortices, while a delta wing generates "free" vortices. Although "free" vortices interact with the delta wing surface, they are not confined by it in the same way as those generated by the device, and, as such, a comparison between them is not effective, acceptable or applicable. However, the study of breakdown in a tube vortex could yield important information relevant to understanding both types of flow (Lambourne and Bryer-1961).

Hence, a distinction between confined and free vortices is necessary, given that the structure is different (Escudier-1988). A vortex generated by a highly swept wing varies significantly along its length, which is the main structural characteristic of a free vortex. On the other hand, the confined vortex, or a vortex in a tube, is highly axisymmetrical, has a confined radius and is normally subjected to negligible variations. A basic aspect of vortical flows is that the diameter of the vortex core decreases with increasing Re, in the same way that the thickness of the boundary layer decreases with increasing swirl velocity. Additionally, the breakdown at high swirl velocities occurs at lower Re than breakdown at low swirl velocities.

One of the most important observations for the breakdown occurring on swirling flows in a cylindrical tube (Harvey-1962) is that the flow after breakdown did not degenerate into an unsteady random motion, as on delta wings, but instead kept a well organised form, and under suitable conditions, a vortex could be restored. Low swirl angles gave a classical vortex whereas higher swirl angles gave a general core region with reversed flow thus providing the key conclusion that the breakdown phenomenon is the "bridging" of the two fundamental types of rotating flow.

1.2.3.1 Types of Vortex Breakdown

Although extensive research on every aspect of the vortex breakdown provides a great deal of advantages since a large amount of details is provided, thus enhancing our knowledge, it has also been a cause of controversies between researchers. A typical issue concerning the vortex breakdown phenomenon is whether there is just one type of vortex breakdown and all the variations are just a different form of the phenomenon or whether there are many different types. A large number of authors (for example Lambourne and Bryer-1961, Sarpkaya-1971a, 1971b, Escudier-1988, Delery-1994 and Lucca-Negro and O'Doherty-2001) refer to this issue and present

their work to support and sometimes establish their point of view on the vortex breakdown types. The two major types of vortex breakdown that predominate in the literature are the spiral or S-type and the bubble or B-type. The bubble type of breakdown is characterised by a stagnation point on the swirl axis followed by an oval shaped, nearly symmetric bubble. The spiral type is characterised by a rapid deceleration in the flow, followed by an abrupt kink, at which point the flow takes the form of a spiral (Payne *et al.*-1988). Lambourne and Bryer (1961) published this widely used, extraordinary dye flow visualisation photograph of a 65° sweep delta wing in a water tunnel, Figure 1.14, where the two different types of vortex breakdown can be seen at the same time on the wing surface, only to amplify the controversies about the breakdown phenomenon. However, it is widely accepted that the bursting in the leading edge vortices was related to the deceleration of the axial flow, expansion of the vortex around a stagnation point on the centreline of the vortex core, low total pressure within the vortex core, and adverse pressure gradient along the axis.

These two forms of breakdown were identified by Hall (1972). In the spiral form the filament of the fluid does not spread symmetrically from the stagnation point onwards but displays a spiralling form, hence the name. In the bubble type, the part forward of the stagnation point fills up and a bluff bubble of almost symmetric shape is created. Pictures of these two types of breakdown can be seen in Figure 1.15. Evidence that the two distinct types of breakdown are, in fact, different were provided by Leibovich (1984). The stagnation point was found to be on the vortex axis, followed by a region of reversed axial flow in both types of vortex breakdown. Moreover, in both forms, the flow downstream of the vortex breakdown is wakelike, while the flow upstream is jetlike. The same observation was acquired by flow visualisation over the flowfield on a delta wing at low Re, where the core flow is transformed from jetlike to a wakelike flow (Payne *et al.*-1988). However, the difference in the core expansion, where the core downstream is larger than that upstream in all forms but is significantly larger for the bubble form than the spiral form, provides one of the supporting reasons for distinguishing the two forms. The second reason, which assigns two different forms, is associated with the discontinuity observed in the transition from one form to another.

In spite of the extensive information given about the vortex breakdown phenomenon, there is still doubt expressed by many authors, including Delery (1994), Harvey (1962) and Leibovich (1978) amongst others, on the physical reality of the number of different types, and the nature of the phenomenon. A photo is provided with the two distinct types appearing at the same time on a delta wing (Figure 1.14). Escudier (1988) supports the viewpoint that the axisymmetric or bubble form is the basic form that appears in a flow and the spiral form is the consequence of the instability of the bubble form. The flow velocity in the breakdown bubble is extremely low. On the other hand, Lucca-Negro and O'Doherty (2001) claim that the spiral breakdown occurs before the bubble one, which is the final form that occurs in the flow. Contrary to the common belief that the spiral breakdown is associated with a stagnation point, a computational analysis of the 3D field showed that no 3D stagnation point exists (Gordnier-1997). Spiral breakdown was predominant for most of the calculations. However, a distinctive difference between the spiral and bubble

breakdown, which appear to alternate in the flow, was the existence of a stagnation point at the head of the bubble breakdown (Gordnier-1997). Visualisation of both vortex breakdown types proved that they seem to transform randomly from one to another (Payne *et al.*-1988). For the leading edge vortices, the direction of the spiral has been observed to be opposite to that of the upstream vortex. The vortex breakdown position oscillates along the vortex axis making the instability over the wing an even more critical point. Measurements on velocity profiles showed that the core velocity was three times the freestream velocity, before breakdown.

Although Lowson (1964) identified two different types of breakdown, "thistle" and "helical", on a stationary and a moving slender delta wing, they were found to reform into one another. However, in some cases only one type was observed. Oscillations of the breakdown location were observed, and when breakdown moved forwards, the "thistle" type appeared, and when moving backwards, the "helical" was seen. The dynamic experiments revealed that the final form of breakdown is not related in any way to the original disturbance and it is the pressure gradient which plays an important role in the final position of the vortex breakdown location.

In contradiction to the findings of other researchers, Sarpkaya (1971a, 1971b) reported that three types of stationary vortex breakdown are observed; the double helix breakdown, the spiral breakdown (followed by turbulent mixing) and the axisymmetric breakdown (followed by a core thicker than the one that appears in the spiral case and eventually turbulent mixing). The type and location of the breakdowns were found to be dependent on Re and the circulation of the flow. Both stationary and travelling vortex breakdowns were examined in a water tank facility. For Re between approximately 1000 and 2000, the forms of breakdown that can be observed are single or double spiral. There is a region defined by certain Reynolds numbers in which only the spiralling type of breakdown exists. The axisymmetric type of breakdown evolves from a double helix, or from a spiral, or directly from an axisymmetric swelling of the vortex core. One of the most impressive bubble type breakdown photographs provided by Sarpkaya (1971a) is that in Figure 1.16, where the bubble is very well defined.

1.2.3.2 Parameters Affecting the Vortex Breakdown Phenomenon

This section deals with the parameters that affect the vortex breakdown phenomenon and its location. However, a reference to the necessary conditions that need to be satisfied for the occurrence of the breakdown phenomenon is required.

For the breakdown to take place the swirl angle has to be large enough that the flow along the axis of the vortex core can decelerate and diverge (Hall-1972). Another condition is the positive or adverse pressure gradient in the axial direction. Any change in the pressure gradient can have well-defined effects and will affect the vortex breakdown either by promoting or degrading it. Another constraint regularly associated with breakdown and closely related to the adverse pressure gradient is the divergence of the flow in the vortex core immediately upstream of the breakdown. This can cause breakdown when the pressure gradient is not sufficient as it produces

an adverse axial pressure gradient in the interior of the vortex core. A balance between the magnitude of swirl, the pressure gradient and the degree of divergence in the flow will define if the vortex breakdown occurs, and if it does, where. The greater the adverse pressure gradient or the degree of divergence in the flow, the less the swirl that is needed for the vortex core to break down (Hall-1972).

Apart from the conditions that have to be satisfied for the occurrence of the breakdown phenomenon, a number of different parameters affect its position, and hence the aerodynamic characteristics. For this reason a lot of work has been dedicated to the detection of all these parameters.

Although a combination of criteria needs to be fulfilled in order for the vortex breakdown phenomenon to appear, it is a mistake to think that this very complicated phenomenon will be solely determined by the adverse pressure gradient and the swirl angle (Delery-1994). One parameter that has a significant effect on the vortex breakdown phenomenon is the angle of attack. Increasing the angle of attack on slender delta wings promotes the vortex breakdown, and its position moves closer to the apex. Interestingly, for a sweep angle of less than 75°, the appearance of the vortex breakdown depends on both the sweep angle and the incidence, whereas when the sweep angle is more than 75° it is only dependent on the incidence.

Validation of Delery's (1994) observations was previously acquired through measurements on 60° and 68° sweep delta wings (Hummel and Srinivasan-1967), which proved that the increase in the sweep angle at high angles of attack, moves the breakdown position further downstream. Furthermore, this increase results in the loss of a certain amount of lift and drag, as well as nose-down pitching moment which is attributed to the fact that the vortex breakdown mainly influences the rear part of the wing. The reduction in drag is due to the decrease in lift and, consequently, induced drag. Interestingly enough, the angle of attack at which the onset of the unfavourable effects of the breakdown on the overall forces and moments occurs on slender wings, coincides with the incidence at which the location of the vortex breakdown crosses the trailing edge.

Lambourne and Bryer (1961) also reached the conclusion that an increase in both the sweep angle and incidence results in movement of the breakdown position closer to the trailing edge. However, an increase in Re does not seem to affect the burst location greatly, at least for delta wings with a sharp leading edge. On the other hand, small disturbances, such as differences in pressure distribution along the vortex, seem to dramatically affect the vortex breakdown position. It has been mentioned in section 1.2.3 that a great difference in the vortex breakdown and its characteristics is observed between vortices developed in vortex tubes and over delta wings. Hence, the effect of changing the free stream velocity in a vortex tube is directly opposite to those of a leading edge vortex. When the flow was decelerated in the tube, the vortex breakdown location moved upstream.

The implementation of a static roll angle can also affect the location of the vortex breakdown (Pelletier and Nelson-2000). The rolling wing creates an effective angle of attack and sideslip angle, which changes the effective sweep angle for both sides

of the wing. As the wing rolls, the breakdown location for the leeward side of the wings propagates downwards towards the trailing edge, while the breakdown location for the windward side propagates upstream, closer to the apex of the wing. The leeward side is considered to be the side rolling upwards.

Another parameter which can significantly contribute in controlling and determining the breakdown location is the geometry of the wing, and in particular, the apex, which is believed to be of major importance (Lowson and Riley-1995). The strength of the vorticity originating from the apex is directly affected by the variation in the shape, as it causes differences in the vorticity distribution at the centre of the core. Consequently, the stability of the fluid can be seriously affected by changes in the vorticity gradient. An increase in the wing thickness and a decrease in the angle normal to the leading edge (chamfer or bevel angle), moves the vortex breakdown position further upstream, closer to the apex.

Apart from the geometry of the apex which can have a considerable impact on the vortex breakdown phenomenon, the leading edge profile might also influence it (Kegelman and Roos-1989). In a series of sharp windward, sharp with varying leading edge camber and blunt leading edge profiles that have been tested, the vortex burst trajectories for the wings with the sharp windward leading edges showed an earlier onset on the breakdown but coincided with those having a blunt edge at higher angles of attack. However, note that the burst point crossed the trailing edge at essentially the same angle for all the wings tested. The trailing edge might also have some influence since it affects the adverse pressure gradient at the trailing edge.

1.2.3.3 Oscillations of the Vortex Breakdown

Apart from the aforementioned parameters which seem to contribute considerably to the variations observed in the burst location, an extensive literature has been devoted to studying the unsteadiness observed in the breakdown phenomenon along the axis of the vortices, the flow that follows this unsteadiness, and how this is affected by changes in the sweep angle, the incidence or the Re (Lowson-1964, Payne *et al.*-1988, Fisher *et al.*-1990, Lowson and Riley-1995, Menke and Gursul-1997, Menke *et al.*-1999, Yavuz *et al.*-2004, Klute *et al.*-2005 and many others).

Oscillations of the breakdown location along the axial direction were observed in a flowfield simulation of a 65° delta wing under static roll angles undertaken by Gordnier (1997). Fluctuations of up to 10% of the chord length have been observed at incidences where the breakdown location had crossed the trailing edge (Lowson-1964 and Fisher *et al.*-1990). Oscillations in the breakdown location were observed, even at low Re, and became larger as the angle of attack or the sweep angle was increased. Additionally, it was observed that the oscillations present a form of antisymmetric motion for the breakdown location for the left and right vortex (Menke and Gursul-1997). The possibility for these oscillations to be related to K-H instability or helical mode instability was discarded since the dominant frequencies observed for the oscillations of the breakdown were much lower (Menke *et al.*-1999). The spectrum of unsteady flow phenomena over delta wings as a function of

the dimensionless frequency is shown in Figure 1.17. It was found that the fluctuations observed in the breakdown locations originate from the fluid dynamics phenomenon and not from vibrations or other disturbances caused by the facility, since variation was observed with changes in the angle of attack and the sweep angle. To enhance the fact that the unsteadiness observed is a fluid dynamics phenomenon, the free-stream velocity and the chord length were varied only to be followed by variations in the dominant frequency. Moreover these oscillations become larger and more coherent as the time-average breakdown locations of the two vortices get closer, which takes place as the incidence or sweep angle is increased. However, strong dependence on Re was found, with the frequency being lower at lower Re.

However, Ol and Gharib (2003) stated that the interaction between the leading edge vortices and their breakdown process increases when reducing the sweep angle. Their results for the 50° delta wing, which reported that the breakdown location is around the midchord of the wing, showed that the flow appears to be separated with the presence of K-H instability. Additionally, great unsteadiness was observed during an increase in the angle of attack, and the vortices move in the streamwise direction. Due to the decrease in the value of the axial velocity with the increasing angle of attack, it can be assumed that the secondary leading edge vortex breakdown precedes that of the primary, a fact confirmed by experimental data.

1.2.3.4 Flow Properties Affected by the Breakdown Phenomenon

Although the intriguing phenomenon of breakdown is affected by a number of different parameters and presents great unsteadiness, as discussed in the previous sections, there is a number of flow properties which are significantly influenced by the breakdown phenomenon, such as vorticity and circulation. It has been noted that changes in the incidence, the sweep angle or the sideslip, affect the stability of the vortex by the changing the vorticity balance (Lee and Ho-1990).

Although spanwise vorticity and circulation distributions remain unchanged at each chordwise location in the region just before the breakdown occurs, the vorticity distribution was found to be entirely altered, with maximum values of vorticity being predominant (Nelson and Visser-1990). The majority of the vorticity for the pre-breakdown state is confined to the subcore region of the vortex. Additionally the value of the azimuthal vorticity remains almost constant in the pre-breakdown region and becomes negative once breakdown occurs. As far as the circulation is concerned, it seems that the distributions are similar for each vortex before the breakdown, and grow linearly in the chordwise direction after the breakdown. Since the increase in the vortex strength is inevitably followed by breakdown and the circulation continues to increase after the breakdown, it is concluded that it is not just the total amount of circulation that determines the breakdown but the concentration of that circulation in combination with the direction of the axial vorticity (Visser and Nelson-1993).

Five distinct layers of vorticity could be detected at low angles of attack, where breakdown does not exist (Ozgoren *et al.*-2002). All of them exhibit small-scale concentrations of azimuthal vorticity. At high angles of attack the vortex breakdown

occurred within the two inner layers. Large values of circulation followed the breakdown phenomenon. An interesting observation is that the vortex breakdown region presented the same form of instability over a wide range of Re, and is hence relatively insensitive to it. Two different criteria were identified for the onset of the breakdown. The first involves the change in sign of the azimuthal vorticity, and the second the occurrence of a stagnation point along the centreline of the vortex. Peak levels of vorticity fluctuations are related to these criteria. The sign of vorticity prior to the breakdown is positive, whereas after it, the sign becomes negative (Ozgoren *et al.*-2002 and Klute *et al.*-2005).

1.2.3.5 Models and Theories Introduced for the Explanation of Aerodynamic Characteristics and for the Vortex Breakdown Phenomenon

A number of different models and theories have been introduced in order to explain the breakdown phenomenon, mainly because loss of stability follows it along with the creation of a turbulent wake. Furthermore, prediction of the aerodynamic characteristics has received a lot of attention, due to the fact that aircraft stability is one of the basic aspects that needs to be taken into account in aircraft design.

Explanations of the breakdown phenomenon include the quasi-cylindrical and boundary layer approximations[2], the hydrodynamic instability[3], and the existence of the critical state[4] in the phenomenon (Hall-1972). A critical state exists when a force or a moment presents a discontinuity which results in a discrete change in the equilibrium response (Grismer and Jenkins-1997). It is accepted that there is a transition in the state of the flow, from supercritical upstream of the breakdown to subcritical downstream. By increasing the swirl velocity, the breakdown position moves upwards until the entire flow is practically subcritical. The velocity within the breakdown bubble is extremely low, thus confirming the existence of a stagnation point (Escudier-1988). An extensive review of the theories related to the explanation of the vortex breakdown phenomenon is beyond the scope of this dissertation. For extended discussions of the various theories the reader is directed to the review articles of Hall (1972), Leibovich (1978, 1984), Escudier (1988), Delery (1994) and Benjamin (1962, 1967). A thorough study of the vortex breakdown phenomenon and hydrodynamic instability is given by Gursul (2003) in his review article. What is generally accepted is that the breakdown phenomenon is a wave propagation

[2] The idea that lies behind this theory is that the pressure gradient and the axial velocity are appreciably high before the breakdown, which actually corresponds to a failure of the quasi-cylindrical approximation. Hence the location of the breakdown is predicted when these values become large, which is similar to the separation point of a boundary layer.

[3] Vortex breakdown with a stagnation point in the axial flow is a direct consequence of hydrodynamic instability according to Ludwieg (1970). After establishing the conditions for instability the spiral disturbances under suitable circumstances may induce an asymmetry in the core, which could lead to stagnation, hence breakdown. Obviously this explanation cannot be applied to axisymmetric forms of breakdown.

[4] Two flow states are defined: the subcritical, where small disturbances may propagate upstream and the supercritical, where they can not. The breakdown of the vortex will appear at the point of transition.

phenomenon[5], with a strong analogy to shocks in gas dynamics. Based on that concept, a good understanding of the phenomenon of vortex breakdown is possible.

As previously mentioned, the vortex breakdown phenomenon is responsible for many adverse effects on the aerodynamic characteristics of aircraft and their performance, one of which is lift loss. Greenwell and Nangia (2003) developed a physical model that predicts the magnitude and the rate of burst-induced lift loss, and suggested that the interaction between the leading edge flow and the rotating vortex results in a reduction of the vorticity shed in the flow, hence a reduction in vortex lift. The basic mechanism provides answers to why the breakdown phenomenon has such a large impact on the aerodynamic characteristics, and why it is so dependent on the wing sweep angle. The helical nature of the vortex has a very strong impact on the vorticity shedding, thus affecting the aerodynamic features of the aircraft while the sweep angle regulates the rate of vorticity shedding.

Although several existing theoretical models are intended to predict the location of the vortex breakdown (Lee and Ho-1990, Erickson-1982, Wentz and Kohlman-1971 and many others) a new criterion proposed by Gursul (1995) was introduced: the variation of $\Gamma/U_{\infty}x$, which is related to the rate at which vorticity is fed in at the leading edge, or to the rate of increase in circulation in the streamwise direction. Note that this parameter does not depend on the distance since the circulation is assumed to increase linearly.

Furthermore, a method to calculate the angle of attack at which vortex breakdown occurs for various slender delta wings with sharp leading edges was documented by Rusak and Lamb (1999). Prediction of the vortex breakdown location along a delta wing as a function of the angle of attack and the swirl ratio (maximum circumferential velocity over maximum axial velocity) was achieved. The swirl ratio reached a critical average value where the vortex breakdown took place, thus providing a universal criterion for the appearance of the phenomenon. It should be mentioned that their results present more consistency with experimental results for more slender (highly swept) delta wings. The reason lying behind this is probably the fact that the model which their theory is based on is limited to axisymmetric swirling flow. However, since the leading edge vortices are formed much closer to the wing surface in nonslender delta wings, there is a greater degree of interaction, thus the vortex deviates from axisymmetry. Traub's (1996) analytical expression for the location of the vortex breakdown showed that increasing the sweep angle, increases the incidence at which breakdown occurs. The range of incidences required for the breakdown location to move from the trailing edge to the apex, is approximately from 20° to 25°.

One of the most important and still commonly used theories introduced for the prediction of the aerodynamic characteristics of an aircraft was that of Polhamus (1971), which made use of the leading edge suction analogy to develop a method that

[5] An infinitesimal wave is considered, in which the azimuthal and axial wave numbers are included, and propagates along the vortex core. The waves are directed upstream or downstream and critical states are encountered.

would predict the lift and induced drag characteristics for a sharp edged delta wing, as well as for many other different configurations, such as arrow or double delta wings. Since the vortical flow induces reattachment and the Kutta condition can be applied at the trailing edge, it is assumed that the total lift coefficient consists of a potential flow term, C_{L_P} and a vortex-lift term, C_{L_V}. The analogy indicates that the vortex induced lift is relatively independent of the AR for a certain range, but is quite sensitive to changes in the angle of attack. The potential-flow lift term, C_{L_P}, can be calculated using linear lifting-surface theory, with attached flow over the leading edge. The vortex lift term, C_{L_V}, is equated to the suction developed along the leading edge, as calculated by thin wing linear lifting surface theory. Thus the total lift is given as:

$$C_L = C_{L_P} + C_{L_V} = K_P \cdot \sin\alpha \cdot \cos^2\alpha + K_V \cdot \sin^2\alpha \cdot \cos\alpha,$$

where K_P and K_V can be obtained as a function of the Aspect Ratio (AR). By increasing the AR of the delta wing (or decreasing the sweep angle), the potential flow term remains virtually unaffected and the vortex lift term increases only slightly. The drag due to lift parameter decreases with increasing lift coefficient. Polhamus' leading edge suction analogy predicts lift and induced drag characteristics of slender, sharp-edged, fully tapered wings, with AR ranging from 0.5 to 2.0, and angles of attack of less than 25°, thus for conditions where complete flow reattachment occurs inboard of the leading edge vortices. According to this theory, the delta wing depends, more and more on the vortex for lift as the sweep angle increases.

Based on Polhamus' (1971) leading edge suction theory, Wentz and Kohlman (1971) found that less lift is produced than the theoretical value for 60° and 65° sweep angle delta wings, but for 70° and 75° sweep angle wings, the agreement was exact and in accordance with Polhamus' theory. While the vortex breakdown produces a nose-up moment, the pitch up tendency that delta wings exhibit is not due to the breakdown phenomenon, since it occurs before the appearance of the breakdown. Finally, it was established that the drag due to lift on delta wings with full leading edge separation, is given as the streamwise component of a normal force. For sweep angles greater than 75°, the breakdown takes place at a constant angle of attack, which is attributed to a different mechanism occurring in these very slender planforms.

Using a modification of Polhamus' (1971) leading edge suction analogy Traub (1997a, 1997b) presented a method of predicting the aerodynamic characteristics (lift and drag force, and pitching moment) and the vortex breakdown position on slender wings in incompressible flow. The vortex breakdown position was calculated using an interpolating equation based on calculation of the circulation on a wing. The method allowed the prediction of these characteristics for the conceptual design of the wing for relatively high angles of attack, and is based on simplifications and assumptions, which limit its use on simple slender delta wings. However, the method displayed accuracy and good agreement with the experimental results for specific wing configurations.

In an effort to identify the effect of the anhedral or dihedral angle on the aerodynamic characteristics, Traub (1999) derived a semi-empirical method to estimate the lift force with constant anhedral or dihedral angle based on Polhamus' (1971) leading edge suction analogy. Traub's (1999) expression was combined with an empirical correction, in order to characterise changes in the effective sweep angle due to roll. Generally, the anhedral angle increases the lift, whereas the dihedral decreases it on a slender wing. The effect is quite obvious on rolling delta wings as well, where one half of the wing experiences higher vortex suction peaks and earlier breakdown than the other. The effect that the anhedral and dihedral angles have was correlated with that caused by the sweep angle. It was suggested that increasing the sweep angle for a given anhedral angle, results in a noticeable increase in the vortex lift. This, however, only occurs up to a limiting anhedral angle value of about 10°, after which a decrease in the vortex lift is noticed.

1.2.4 Manoeuvring Delta Wing Aerodynamics

1.2.4.1 Introduction

Manoeuvring delta wing aerodynamics involves pitching, rolling, yawing, plunging, heaving, unsteady freestream velocity fluctuations, and wing rock. These are fields that have been investigated by a large number of researchers. Although there is great difficulty in simulating these unsteady flows, either experimentally or computationally, there is a large number of publications which refer to manoeuvring delta wing aerodynamics, and even vortex breakdown under these manoeuvres. Both experimental and numerical means have been used to assess the capabilities of aircraft configurations performing extreme manoeuvres at high angles of attack. Although considerable literature is devoted to the aerodynamics of manoeuvrable slender delta wings, nonslender delta wings have not received the same extent of attention. However, pitching and to a certain extent wing rock for nonslender wings have been studied, whereas forced rolling is not very well documented.

For the purposes of this thesis the author focussed attention on to rolling, pitching and wing rock manoeuvres for both slender and nonslender delta wings.

1.2.4.2 Rolling Manoeuvre

This section discusses the rolling manoeuvre of slender and nonslender delta wings and it also introduces the effect of sideslip on a rolling wing.

A thorough insight into the rolling motion of a slender delta wing $(\Lambda = 80°)$ under both static and dynamic conditions is provided by numerical simulations (Gordnier and Visbal-1998). A static 45° roll angle induced on the downward leading edge side led to a displacement of the vortex inboard and towards the surface of the wing, as opposed to the vortex on the other side, which moved further away from the wing

surface. Comparisons between experimental surface oil visualisation and simulated flow showed good qualitative agreement, and both the secondary and tertiary separation lines, along with the attachment, were captured. Similar behaviour of the vortices emerges in the dynamic roll motion, with a predominant appearance of a secondary flow, which emerges underneath the port-side vortex (leading edge pointing downwards). Due to the movement of the port-side, the secondary flow is forced to diminish in size and eventually disappear. The behaviour of the vortices during the manoeuvre can be explained by considering the effective angle of attack and sideslip, or alternatively the effective sweep angle. The rolling of the delta wing leads to a reduction in the effective angle of attack, and to positive sideslip. Hence the net effect is a reduction in the strength of the vortices. Moreover, the lift coefficient drops rapidly as the wing rolls. However, little difference is observed in the lift coefficient values between the static and dynamic conditions. Contrary to that, the static roll moment coefficient presents a larger restoring moment than the dynamic, attributed to the lag in position and strength of the starboard vortex during the roll manoeuvre.

Further research into a slender delta wing, subjected to large amplitude high rate oscillatory rolling motions (Hanff and Huang-1991), exhibited highly non-linear and unsteady characteristics, as well as great dependence on the amplitude and reduced frequency. The position of the vortex core did not present any considerable differences when measured under both static and dynamic rolling loads, implying that the vortex core follows more closely the wing motion. However, the location of the breakdown location changed dramatically when dynamic effects were encountered. Hysteresis effects and delay in the breakdown location were observed. The changes in the vortex breakdown location due to axial displacement produced a highly destabilising effect on the rolling moment. One of the most revealing observations regarding the dynamic experiments is the presence of a vortex at roll angles which under stationary conditions lead to breakdown considerably forward of the trailing edge.

The effect of sideslip on a rolling slender delta wing was studied by Verhaagen and Jobe (2003). The change in sideslip moved the vortex breakdown position closer to the wing apex on the windward side, and in the opposite direction on the leeward side. Increasing the sideslip tended to increase the amplitude of the breakdown location's oscillation. Hysteresis effects in the moment and force measurements were apparent due to the changes in the sideslip. Additionally, discontinuities in the rolling moment curves indicated the existence of critical states at specific static roll angles, which had previously been confirmed by Jenkins *et al.* (1996). Consequently, if a critical state is encountered, additional time is required for the transition from one flow state to another. However, time lag can result without the existence of a critical state. The effect of the roll rate on the critical state transients proved to be insignificant when a slender delta wing was tested under harmonic rolling oscillations (Grismer and Jenkins-1997).

Although there is a great amount of literature related to the rolling manoeuvre of slender wings, the same cannot be claimed for nonslender wings. To the author's knowledge the rolling manoeuvre of nonslender wings is not documented.

1.2.4.3 Pitching Manoeuvre

Another manoeuvre which has received a lot of attention in both slender and nonslender configurations is pitching.

A description of the flowfield over a slender delta wing involved in a pitching manoeuvre is documented by Nelson and Pelletier (2003). During pitch up, the breakdown delays the motion of the wing, allowing it to achieve higher lift coefficients than in the static case. There is a delay in the reestablishment of the leading edge vortices during the pitch down motion. The hysteresis loop which is being created during the pitching motion depends on the dimensionless frequency of the motion and its amplitude.

The effect of the pressure gradient on the vortex breakdown phenomenon was studied utilising a slender wing $(\Lambda = 70°)$ undergoing pitching motion (Gursul and Yang-1995). Unsteady pressure measurements showed that the pressure fluctuations, induced by the breakdown, provide an indication of the phase delay between the motion of the wing and the breakdown location. The maximum fluctuation does not occur at the maximum incidence but at a smaller angle, as the wing pitches down. The pressure field for the pitching wing appeared to be delayed compared to the quasi-steady case. This phase delay increased with increasing dimensionless pitching frequency, but was completely insensitive to variations in Re. Similar observations were found at smaller incidences where breakdown was absent, confirming that the time delays in the breakdown location were due to the external pressure gradient generated by the wing.

More recently the pitching manoeuvre in nonslender wings has attracted the attention of researchers. Cummings *et al.* (2003) carried out experimental measurements, as well as numerical simulations, on a pitching UCAV, which had a 50° leading edge sweep. The UCAV used (Boeing 1301) was not the optimum aerodynamic configuration, but presented interesting characteristics that are worth mentioning. One of these was that despite the use of a rounded leading edge profile, the leading edge vortices were clearly developed at $\alpha = 10°$, and the vortices enhanced the lift up to $\alpha = 25°$. Note that the vortices were very wide compared to their height, possibly due to the round leading edges. Furthermore, the wing continued to maintain lift in the post stall region even though vortex breakdown had occurred. The pitching characteristics of the wing were quite unusual compared to the static case, in the sense that the leading edge vortex was stronger during pitch-up, resulting in a lower pressure. Thus, rather than gaining lift, a loss was recorded prior to the post stall region. During the pitch down manoeuvre more lift was recorded compared to the static case.

1.2.4.4 Wing Rock

Another thoroughly investigated phenomenon is wing rock, which arises from the unsteady behaviour of the vortical flows over wings, coupled with the rolling degree

of freedom of the aircraft. Consequently, a rolling oscillation with a limit cycle behaviour is produced at a specific angle of attack. The wing rock phenomenon is defined as the free-to-roll, self-induced limit cycle oscillation (LCO). It has been more typically observed in slender wings at high angles of attack with corresponding mean roll angle of zero (Arena and Nelson-1994), although recently both slender and nonslender wings seemed to exhibit wing rock characteristics (Gursul-2005, Gursul *et al.*-2005 and Gursul-2003). An interesting characteristic of the wing rock phenomenon is that the onset incidence at which the wing rock starts decreases when the sweep angle is increased. Several mechanisms have been suggested in order to explain the wing rock phenomenon and what sustains the motion. It has been shown that vortex breakdown is not a necessary condition for wing rock (Arena and Nelson-1994). Delery (1994) claimed that the oscillation of the vortices along their axis might be the origin of the wing rock phenomenon, which seems to interfere with the breakdown.

The static and free-to-roll dynamics of a thick, nonslender, $\Lambda = 45°$, delta wing were examined by Ueno *et al.* (1998). Apart from measuring the aerodynamic forces and moments, the effects of unsteady aerodynamics on a free-to-roll motion were measured. During the lift and rolling moment measurements, great instability and discontinuity were observed at high angles of attack, $(\alpha = 20° - 35°)$. In the free-to-roll test, unsteady phenomena like wing rock and phase lags were observed. The oscillations observed did not have constant amplitude and therefore it cannot be determined to be wing rock oscillations, given that nonslender delta wings were not supposed to present wing rock motion characteristics and that the amplitude was found to vary little in slender wings (Arena and Nelson-1994).

Although the possibility of the wing rock phenomenon existing over nonslender wings has been ignored or in some cases eliminated an interest in this area has arisen recently. After Ueno *et al.* (1998) a 45° delta wing experiencing wing rock has been experimentally investigated, in order to attain some understanding of the flow mechanism driving this complex phenomenon (Ericsson-2001). Wing rock of nonslender delta wings occurs when certain conditions are met. Limit cycle oscillations have been observed over nonslender delta wings, and are attributed to the rounded leading edge profile. Additionally, the inclination of the roll axis is high enough that the effective sweep angle and angle of attack produce dynamic stall conditions. A combination of the two above mentioned conditions results in undamped rolling motion, which terminates in limit cycle roll oscillations.

A more recent investigation (McClain *et al.*-2007) on the phenomenon of wing rock on a $\Lambda = 50°$ wing revealed multiple trim positions. Depending on the angle of attack, only nonzero roll angles or a combination of zero and nonzero angles are possible. Several equilibrium positions at nonzero angles (depending on the initial roll angle) were found in the pre-stall incidences, which is similar to the observations made for slender wings (Jenkins *et al.*-1996). However, notice that the zero roll angle is not included in these equilibrium positions. For angles of attack larger than the stall angle a variation of zero and nonzero equilibrium positions was found. Additionally, the effect of different leading edge profiles was investigated. Self-excited roll oscillations were observed for both the round edge and sharp edged

wings, with the latter having a smaller amplitude. It is worth mentioning that this confirms the first experimental study on self-excited roll oscillations for a thin wing with sharp leading edges.

1.2.5 Flexible Nonslender Delta Wings

Although nonslender delta wings have only recently received attention in the literature, an area which has captured the interest of various researchers is that of the effects of flexibility over the flowfield of a nonslender delta wing. Although most sources of unsteadiness are related to slender planforms, low sweep planforms are subjected to aeroelastic instabilities, which are strongly coupled with flexibility.

The spectral characteristics of a vibrating flexible delta wing with $\Lambda = 50°$, showed the existence of a dominant peak at $f_r = \frac{f \cdot c}{U_\infty} = 0.7$ in the post stall region, between $\alpha = 24°$ and 30°, (Taylor and Gursul-2004a). Figure 1.18 shows the lift measurements generated by different nonslender delta wings $(\Lambda = 50°)$, a flexible, a rigid and a rigid curved wing. From the lift curve for the rigid wing it is seen that stall takes place at $\alpha_{stall} = 21°$. Impressive lift enhancement was achieved though over a very thin (1mm) flexible delta wing in the post-stall region (after $\alpha = 23°$). This proves that it is the actual vibration that is responsible for the lift enhancement, since the curved wing does not exhibit similar behaviour. Hence, wing tip acceleration (and not the time average deflection in the spanwise direction) was found to be the source of the up to 45% rise in lift force, and delaying stall by 9°. However, the curved wing produced less lift, but delayed stall by 1° when compared to the rigid planar wing. Experimental data in combination with finite element analysis showed the existence of an antisymmetric mode, (see Figure 1.19 and 1.20 2nd antisymmetric mode), suggesting the existence of antisymmetric rather than symmetric shedding (1st or 2nd symmetric modes) which has previously been reported over slender delta wings (Rediniotis *et al.*-1993). Although computational simulations of a spectral analysis of the wingtip deflections of a 60° delta wing showed the first mode to be dominant, there was a clear indication and contribution of the 2nd and 3rd structural modes for angles of attack in which the vortex breakdown was on the wing (Gordnier and Visbal-2004). Vibration of the leading edges reenergises the vortices, by adding momentum to the fluid, which is subsequently carried into the wake. This allows the shear layer to remain attached for a longer period of time and at higher incidences. However, it must be noted that the dramatic increase in lift, accompanied by the hysteresis in lift around the stall angle, together with the large drop-off in lift when stalling (see Figure 1.18), may be combined to create a detrimental effect on the controllability of an aircraft.

Further research into flexible delta wings has proved that the lift enhancement phenomenon is not limited to the $\Lambda = 50°$ delta wings, but extends to a wider range of sweep angles, with the greatest lift enhancement observed on the wing with the lowest sweep angle, $\Lambda = 40°$ (Taylor *et al.*-2005). The effect of flexibility in the lift enhancement was apparent in all wings tested apart from the $\Lambda = 60°$ case. This

provides another clear indication of the fundamentally different flows that exist between slender and nonslender delta wings. Table1.1 shows the values for lift coefficient for both rigid and flexible wings, along with the increment in the stall angle. Interestingly enough, the 60° flexible wing experienced a reduction in lift when compared with the rigid one. This was attributed to the effect the spanwise dihedral camber has on the flow over the wing, which accounts to a reduction in the effective wing sweep angle and incidence. In an effort to find whether or not the antisymmetric vibration of the wing is the requirement for the production of additional lift, a half-wing flexible model was tested. Wing tip acceleration measurements suggested that this form of vibration is indeed necessary. It is clear that the flexibility results in fundamental improvement in the flow, allowing the shear layer to continue to reattach at angles at which it is not expected to, thus giving a more coherent flowfield (Taylor *et al.*-2005).

However, a numerical simulation (Attar *et al.*-2006) of a flexible wing similar to that used by Taylor and Gursul-2004a $(\Lambda = 50°)$ subjected to the same flow conditions presented differences as well as similarities to the experimental results. The investigation consisted of two parts, a prescribed motion and an aeroelastic solution. When a prescribed motion was applied to the wing lift enhancement and flow reorganisation were predicted in the stall region due to the structural vibration. These results were insensitive to the vibrating frequency, provided that it was above some minimum value. However, it appeared that these phenomena were also independent of the mode of vibration (symmetric or antisymmetric) contradicting experimental measurements which considered necessary an antisymmetric form of vibration for the lift enhancement (Taylor *et al.*-2005). Additionally, an increase in the amplitude of the prescribed motion produced an increase in the time average lift. Unlike the experiment, when the aeroelastic solver was implemented, no lift enhancement was observed, attributed to the low excitation frequencies implemented and the exclusion of viscous effects.

1.3 Objectives

The above literature survey has proven that the majority of the knowledge on unsteady aerodynamics and vortex flows is based on studies on slender delta wings. However, in recent years, great interest has arisen in flows over nonslender delta wings. Many UAVs and MAVs have employed nonslender delta wings and many of these configurations contain flexible planforms. A better understanding of such flows is necessary in order to establish their efficient use. Moreover, a better understanding of highly manoeuvrable aerodynamics is required, given that these vehicles are required to have the ability to perform difficult manoeuvres at high angles of attack $(> 20°)$. Evidence of this emerging need was provided by a symposium on vortex flows and high incidence aerodynamics (Luckring-2002), in which the complexity of these highly unsteady flows was highlighted. Both experimental and computational data were presented, and the final outcome was that more experimental data for vortical flowfields at high Reynolds numbers are required, and that novel

Computational Fluid Dynamics (CFD) techniques need to be extended to cover more complex applications.

The present study focuses on understanding and explaining vortical flows over nonslender, rigid and flexible, manoeuvring delta wings at moderate and high angles of attack. This project was inspired by, and followed the initiative taken by, Taylor *et al.*'s (2003) wind tunnel experiments on flexible nonslender delta wings with the aim of studying the physical mechanisms of the aerodynamics of flexible wings. Hence, an original assessment was performed to illustrate the effect of flexibility on the flowfield of a nonslender wing. In order to test possible hypotheses, oscillatory motions were compared to a stationary flexible wing, with the aim of understanding the role of vibrations in the enhanced lift and delayed stall observed on flexible wings. The effect of parameters such as sweep angles and various planform geometries, on the flowfield, was also investigated. The reason behind this parametric investigation was to identify if the response of the flowfield remains the same. The structure of the flowfield under forced large amplitude rolling manoeuvres was also analysed, with the aim of identifying the characteristics of the unsteady aerodynamics that prevail on that specific manoeuvre. Finally, a thorough study of the phenomenon of vortex breakdown, and some of its adverse effects on the aerodynamic characteristics of delta wings, was also included.

As mentioned earlier, high manoeuvrability and agility is required by modern UAVs and MAVs, and this has increased the interest in the use of nonslender planforms and in some cases the use of flexible wings. To this effect, understanding on the unsteady mechanisms governing the aerodynamics over these planforms is of paramount importance. The present study aims to identify the potential mechanisms for the regeneration of vortices in the stall region. Maintaining lift at high angles of attack is seen as advantageous in the context of the agility of an aircraft. Secondly, the aerodynamics of unsteady, dynamic motions, such as rolling of nonslender wings, is investigated, in order to understand how real-life manoeuvres can potentially affect the flowfield and generation of lift.

1.4 Figures Chapter 1

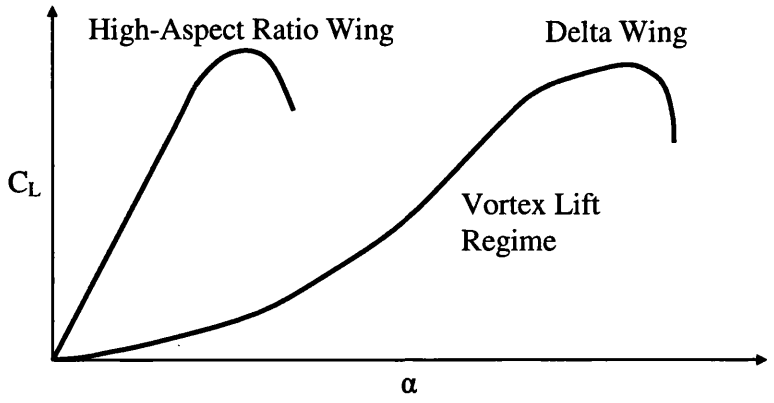

Figure 1.1: Qualitative diagram of the lift coefficient C_L versus the angle of attack, α.

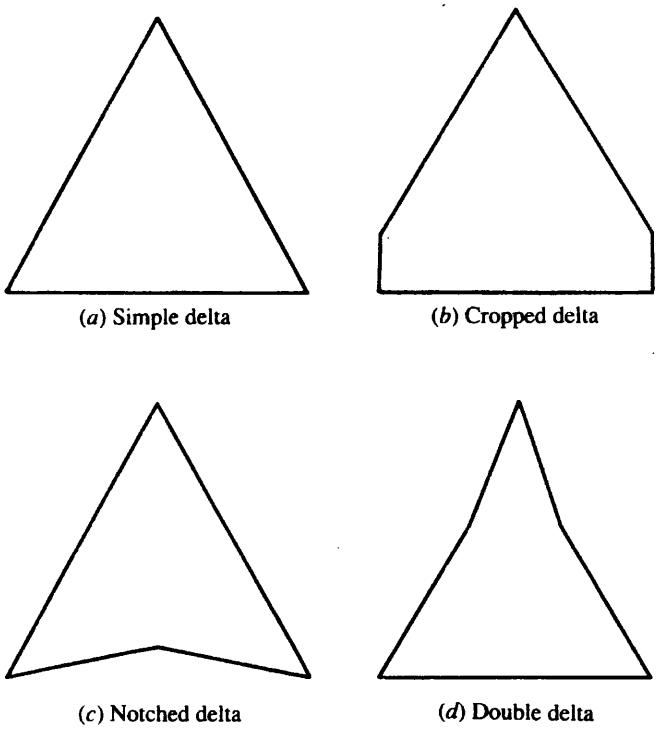

Figure 1.2: Variations of delta wing planforms (Anderson, Jr. J. D.-2001).

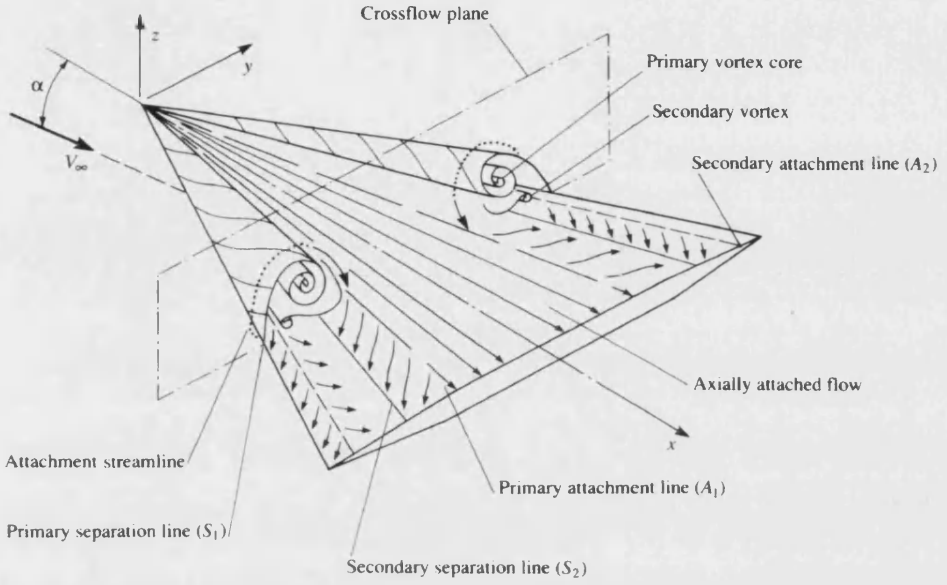

Figure 1.3: Schematic of the subsonic flowfield over a delta wing (Anderson, Jr. J. D.-2001).

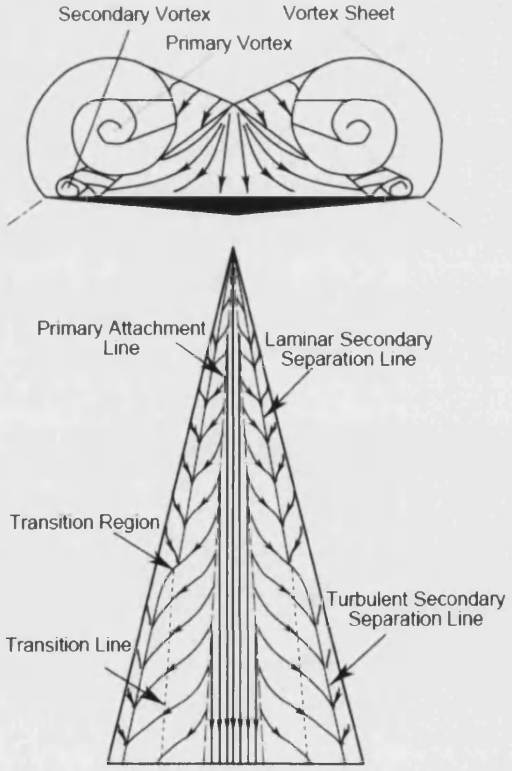

Figure 1.4: Schematic of the vortical flow of a delta wing (top); Streamline pattern on the surface of the wing (bottom) (Visser and Washburn-1994).

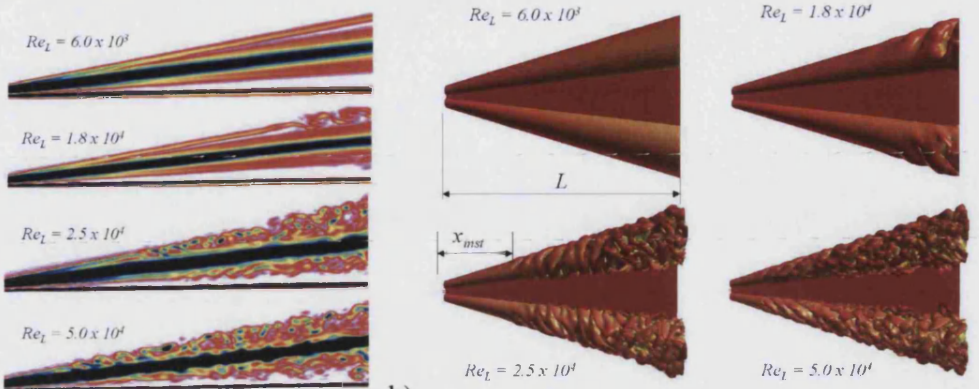

Figure 1.5: a) Contours of instantaneous vorticity magnitude through the vortex core on the evolution of vortical structures with increasing Re; b) Evolution of the shear layer structure with increasing Re as an isosurface of axial vorticity (Visbal and Gordnier-2003).

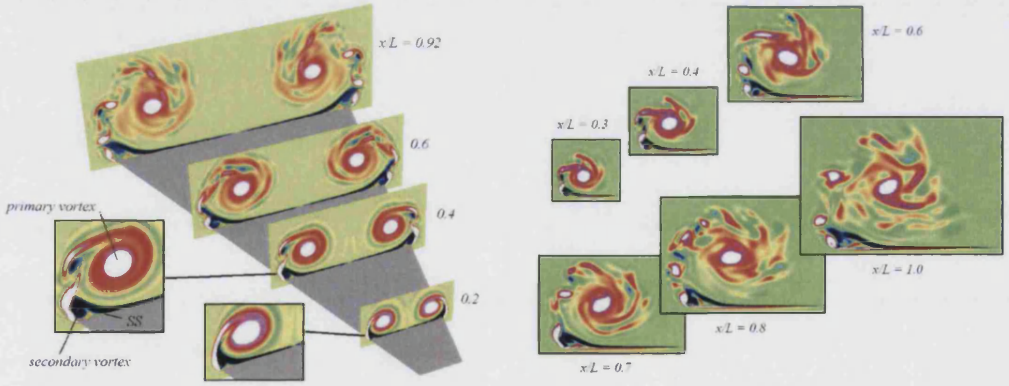

Figure 1.6: a) Contours of instantaneous axial vorticity at several crossflow plane along the wing at Re = 25,000 ; b) Re = 50,000 (Visbal and Gordnier-2003).

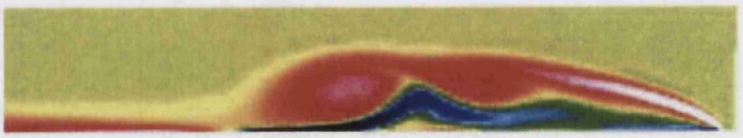

Figure 1.7: Computational simulations showing double vortex structures (Gordnier and Visbal-2003).

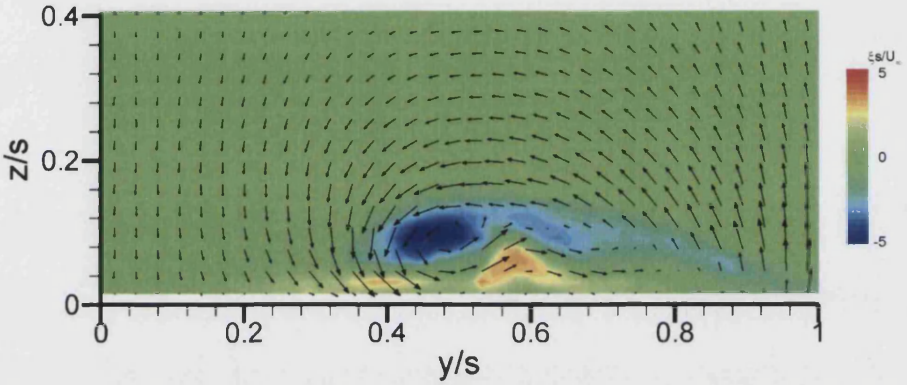

Figure 1.8: Experimental crossflow vorticity measurements showing double vortex structures (Taylor *et al.*-2003).

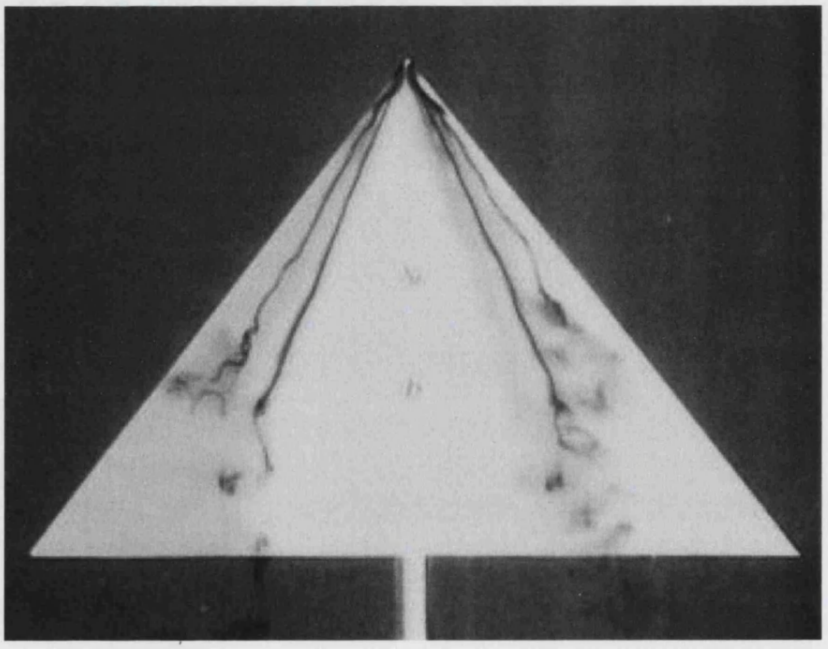

Figure 1.9: Flow visualisation of leading edge vortices over a $\Lambda = 50°$, at $\alpha = 5°$ (Taylor *et al.*-2003).

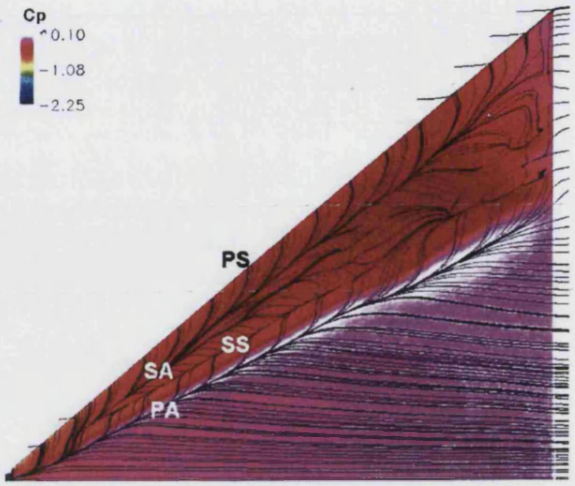

Figure 1.10: Surface streamline pattern and pressure coefficient at $\alpha = 5°$, PS: Primary Separation; PA: Primary Attachment; SS: Secondary Separation; SA: Secondary Attachment (Gordnier and Visbal-2003).

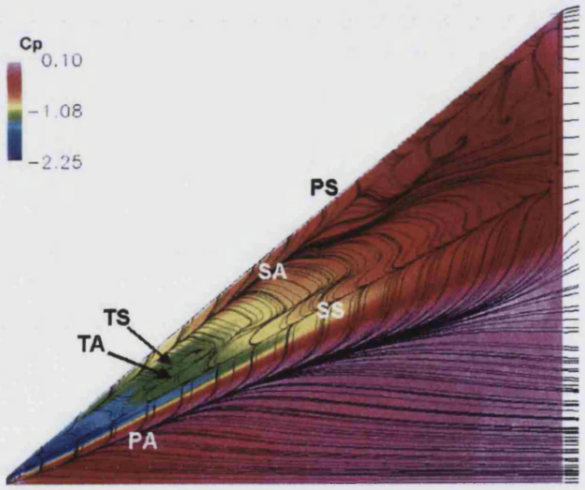

Figure 1.11: Surface streamline pattern and pressure coefficient at $\alpha = 10°$, PS: Primary Separation; PA: Primary Attachment; SS: Secondary Separation; SA: Secondary Attachment TS: Tertiary Separation; TA: Tertiary Attachment (Gordnier and Visbal-2003).

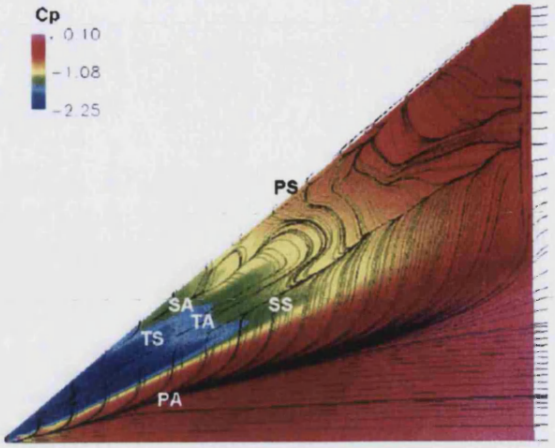

Figure 1.12: Surface streamline pattern and pressure coefficient at $\alpha = 15°$, PS: Primary Separation; PA: Primary Attachment; SS: Secondary Separation; SA: Secondary Attachment TS: Tertiary Separation; TA: Tertiary Attachment (Gordnier and Visbal-2003).

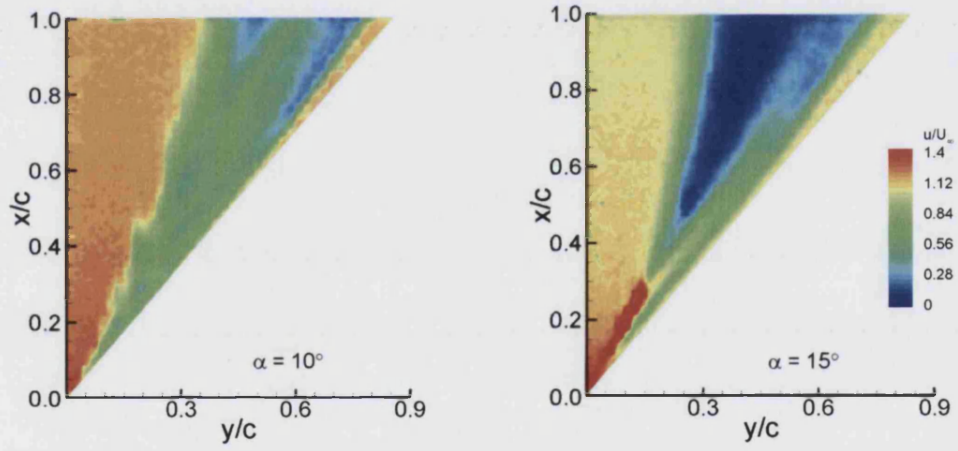

Figure 1.13: Velocity magnitude in the vortex core plane (Taylor & Gursul-2004b).

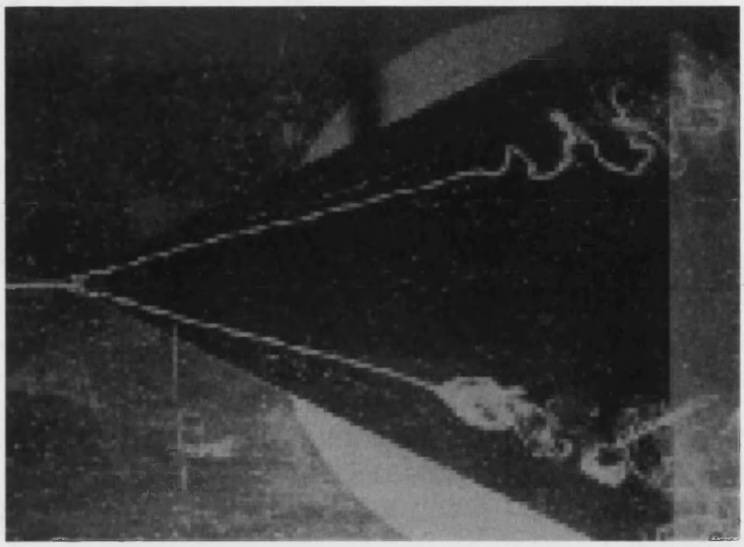

Figure 1.14: Vortex breakdown over a delta wing. Both spiral and bubble type are present (Lambourne and Bryer-1961).

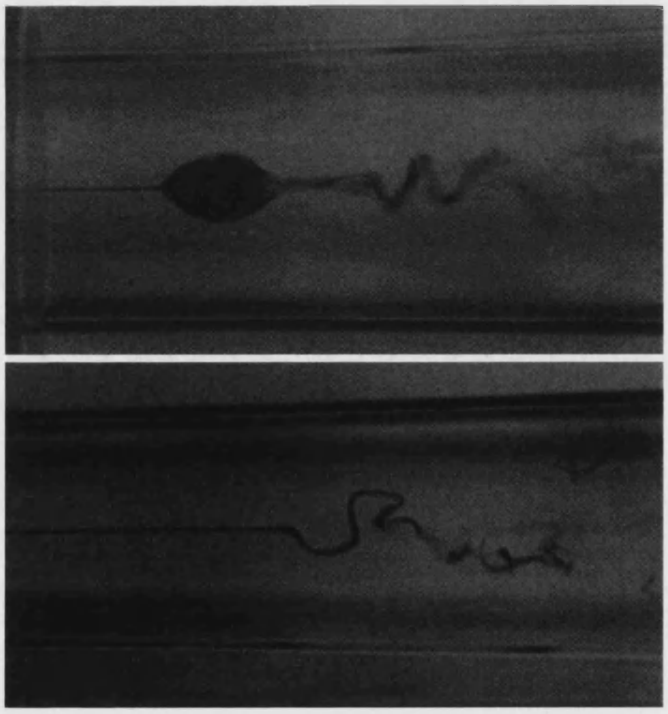

Figure 1.15: Bubble and spiral forms of vortex breakdown (Leibovich-1978).

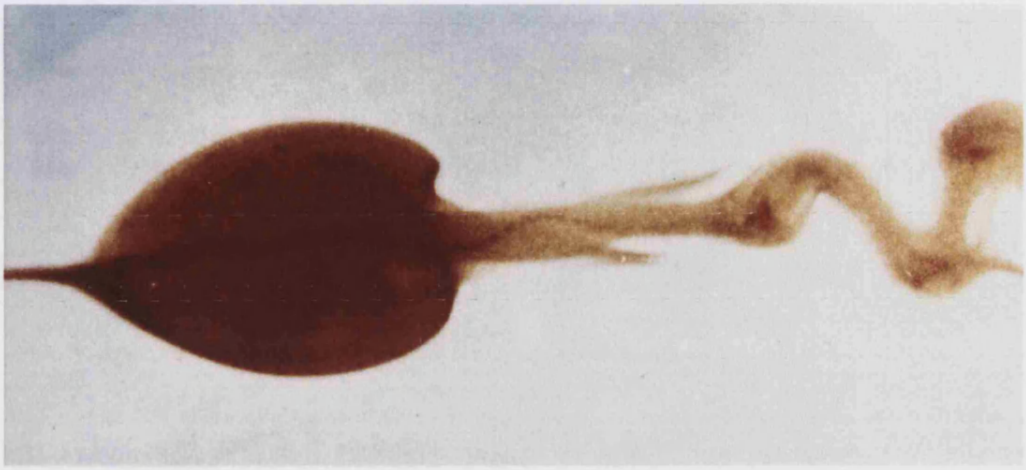

Figure 1.16: Bubble type vortex breakdown (Sarpkaya-1971a).

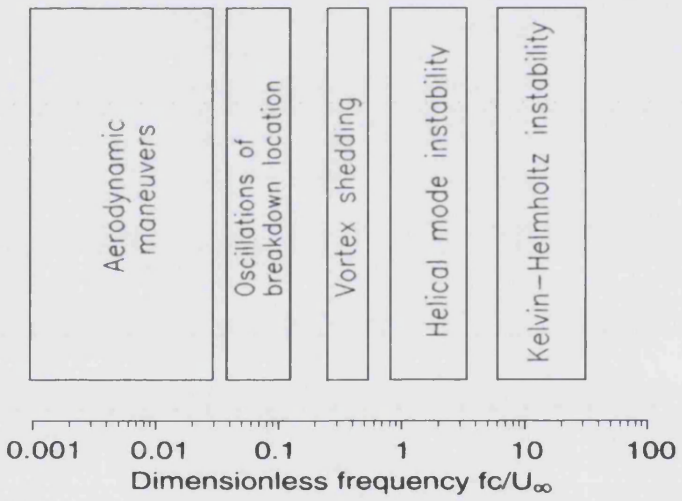

Figure 1.17: Spectrum of unsteady flow phenomena over rigid slender delta wings (Menke *et al.*-1999).

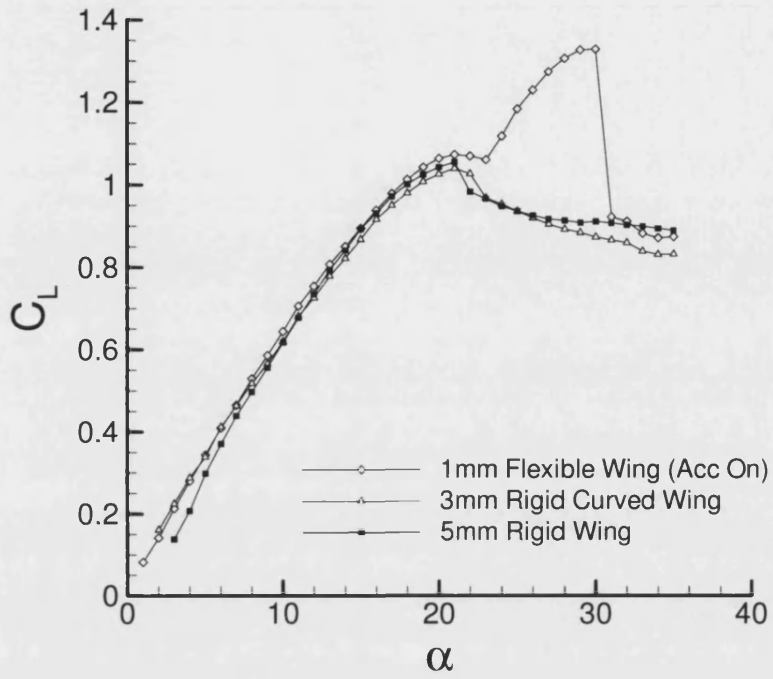

Figure 1.18: Comparison of lift generated by different delta wings (Taylor and Gursul-2004a).

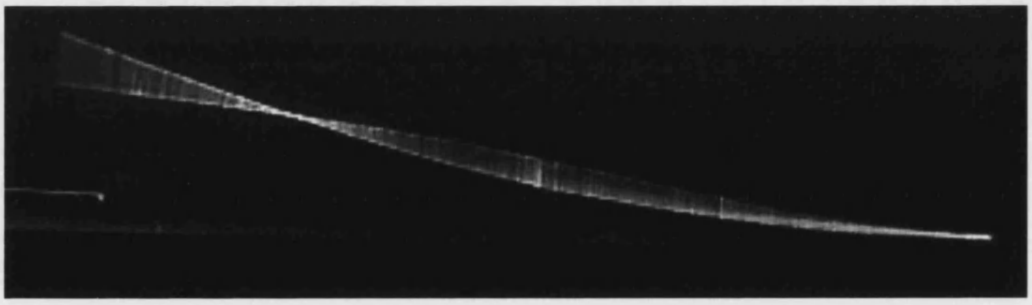

Figure 1.19: Visualisation of leading edge deformation for 1mm flexible wing at $\alpha = 25°$ Taylor and Gursul-2004a).

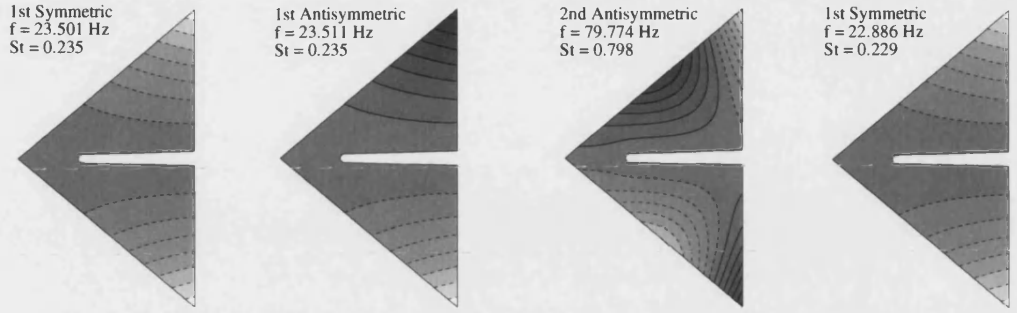

Figure 1.20: Finite element modal solution for 1mm wing Taylor and Gursul-2004a).

	C_{Lmax}		ΔC_{Lmax}	
Λ	**Rigid**	**Flexible**	**(a)**	$\Delta\alpha_{STALL}$
40	0.80	1.14	42.%	7°
45	0.86	1.19	38%	6°
50	0.96	1.17	23%	5°
55	1.12	1.13	1%	3°
60	1.30	1.23	-5%	0°

Table1.1: Statistics of lift enhancement and stall delay over flexible delta wings with varying sweep angles. Column (a): C_{Lmax} of flexible when compared with C_{Lmax} of rigid (Taylor *et al.*-2005).

CHAPTER 2: EXPERIMENTAL APPARATUS

2.1 Introduction

This chapter deals with the experimental apparatus employed for the completion of a three year research project on the aerodynamics of nonslender delta wings. A brief account of the test facility is given, followed by a description of the models used and the instrumentation employed to obtain the measurements. The experimental data procedures are then explained in Chapter 3.

2.2 Water Tunnel Facility

All experiments were conducted in the water tunnel facility, located in the Department of Mechanical Engineering, at the University of Bath. The tunnel is an Eidetics Model 1520 free surface water tunnel, which allows very easy access to the model from the top, as illustrated in Figures 2.1 and 2.2. The tunnel has a 0.381m×0.508m×1.524m test section, and speeds in the range 0 to 0.45m/s, which can be achieved through a closed circuit continuous flow system. The turbulence intensity of the tunnel is less than 1% rms. Some more detailed specifications for the water tunnel are provided in Table 2.1. The tunnel has four viewing windows, three surrounding the work section and one downstream to allow axial viewing. The height of the test section above the floor is sufficient to allow flow visualisation viewing from below as well as from the sides. The tunnel centreline is also located approximately at eye level to facilitate testing. The area behind the test section, where the axial viewing window is, provides room for photographic or video recording equipment, including light fixtures. The tunnel also incorporates a pressurised dye system with six available dye tubes, to enable flow visualization with different colours. Control of the dye velocity is achieved by gate valves and is equalised to that of the freestream. This was achieved by observation, whereby dye shed in a straight line is representative of a velocity equal to that of the freestream. The dyes used were food colouring and fluorescent laser reflecting dye. For the conditions tested, red food colouring dye was found to offer a satisfactory contrast,

and very good quality flow visualisation photos were captured. The fluorescent laser dyes used were Rhodamine B500% and Rhodamine 6G, since these two provided the best laser reflected colours.

The most important features of the water tunnel are the high quality flow, the horizontal orientation, which enables models to be changed without having to empty the tunnel, and the excellent quality of flow visualisation images. In addition to that, the glass allows maximum viewing of the model from the side, from underneath as well as from the back. In summary, a water tunnel is a very useful tool, as very accurate and qualitative flow visualisation results can be obtained.

2.3 Models

Twelve low sweep angle delta wings were tested in total, with varying sweep angles, thicknesses and chord lengths. The essential dimensions for each one of them are provided in Table 2.2. The last two cropped models, with $\Lambda = 10°$ and $\Lambda = 0°$, were not tested. The reason for that is explained in Chapter 6, where the results for the cropped models are presented.

Three out of the twelve wings tested were simple rigid delta wings, with sweep angles of $\Lambda = 50°$, 40° and 30°. The chord lengths were $c = 89\text{mm}$, 62.9mm and 43.3mm, and the thickness and span were $t = 2\text{mm}$ and $b = 150\text{mm}$ respectively, for all three wings. Towards the end of the project, a fourth rigid delta wing, with a 50° sweep angle (and the same chord and span as the aforementioned 50° wing) was built and used with fluorescent laser dye, providing very detailed flow visualisation images. However, the thickness had to be increased to 4mm, as the design of a cavity was necessary for the injection of the dye. A continuous dye supply was required, hence the minimum dye supply tubes that could be used to provide adequate flow were tubes with internal diameter of $d = 2\text{mm}$, giving a minimum thickness to the delta wing of 4mm. The thin slot (0.5mm), which was designed closer to the suction surface, provided the exit for the dye.

All the models, shown in Figures 2.3, 2.4, 2.5 and 2.6 were bevelled on the pressure surface by $\gamma = 45°$ on the leading and trailing edges. The windward bevelling of the models was done in order to produce a sharp leading edge, which ensured the proper formation of the leading edge vortices, as reported by Miau *et al.* (1995). All four models were made out of aluminium, and were mounted upside down on the tunnel using a sting projecting from the rear of the model, as shown in Figure 2.7. The sting was attached to the model with screws, which were countersunk into the model's suction surface. Any irregularities or rough surfaces near the screws were filled up with filler, so that an extremely smooth suction surface was produced. The model and the sting were both mounted on a flat plate resting on the upper surface of the water tunnel test section, as shown in Figure 2.7. Two supports, connected via bearings, held the flat plate and the rolling mechanism above the water thus enabling the setting of the required incidence, which was accomplished with ease, considering the free surface water tunnel. The blockage ratio was approximately 3.45% in the worst case, which was for the $\Lambda = 50°$ wing at $\alpha = 30°$.

Flexible delta wings were also made in order to undertake further investigations. A set of four flexible, 50° sweep angle delta wings were tested with thicknesses of 0.1905mm, 0.254mm, 0.381mm and 0.508mm. To avoid any permanent deformation, plastic delta wings were used instead of thin metal ones. The former two wings were made out of polyester and the latter two out of polypropylene.

In an effort to investigate the effect of both the sweep angle and the planform shape, a number of aluminium cropped delta wings were manufactured and tested with sweep angles of 50°, 40°, 30° and 20°. Another two cropped delta wings were built with sweep angles of 10° and 0° (square plate) but they were finally not tested. The principal dimensions are shown in Figures 2.8, 2.9, 2.10, 2.11, 2.12 and 2.13. The rest of the setup remained the same for all the flexible and cropped delta wings that were tested.

2.4 Instrumentation

2.4.1 Introduction

Experiments were conducted under both static and dynamic conditions, and for a number of different roll angles, incidences and frequencies. A rolling mechanism was used, controlled by a desktop computer. Flow visualisation techniques, Digital Particle Image Velocimetry (DPIV), Laser Doppler Velocimetry (LDV) and continuous emission laser (Argon-Ion) flow visualisation techniques were utilised for the completion of this research project. A detailed analysis for each of these follows.

2.4.2 Rolling Mechanism

The whole project was based on the study and analysis of an oscillating and manoeuvring nonslender delta wing, including rolling and pitching motions. In order to ensure the rolling motion of the delta wing, a mechanism was provided and was mounted with screws on the top of the mounting plate. The rolling mechanism comprised an electric motor and a drive mechanism, which was used to transmit the motion smoothly. The mechanism was controlled using a desktop computer. Data acquisition software Agilent (HP) VEE, v 6.2 was employed to control the amplitude and frequency of the periodic sinusoidal rolling motion. Measurements were taken for different values of the roll angle by adjusting the amplitude, and for different values of the dimensionless frequency of the rolling motion, by adjusting the period of the sine wave.

Additionally, a pitching motion was utilised. This was achieved by turning the rolling mechanism 90° in the horizontal direction and making minor adjustments to the support of the wing, which transformed the motion from roll to pitch.

2.4.3 Flow Visualisation

Flow visualisation is the oldest technique used to get information from a flowfield, and as Professor F N M Brown of the University of Notre-Dame (World Scientific Publishing Co., Bookshop, Engineering-2005) commented "... *A man is not a dog to smell out each individual track, he is a man to see, and seeing, to analyse...*", elegantly depicting its importance for the understanding of flows. Fittingly, the first experiments conducted for this project were dye flow visualisation.

Visualisation of the vortex trajectories was achieved using food colouring dye, diluted 1:4 with water. In the first flow visualisation experiments, two very thin metal hollow tubes, with internal diameter of 0.5mm, glued parallel to each other on the upper surface (pressure surface) of the delta wing, injected the dye as close to the apex of the model as possible, via a simple pressurised delivery system utilised by the water tunnel. A gate valve system was used in the exit to control the velocity of the fluid, in order to avoid any interference of the dye with the flow and the vortex formation. Later on, another method was implemented, inspired by the very famous flow visualisation photo (Figure 1.11) by Lambourne and Bryer (1961). A single metal hollow tube with a 1mm internal diameter was placed just in front of the apex of the delta wing, and a pair of vortices was therefore produced. Thus, better quality of flow visualisation images was obtained, as the dye was injected directly into the vortex core. The dye tubes in both cases were connected to the pressurised canisters of the water tunnel, through plastic tubing of the same diameter.

Excessive use of the dye coloured the water, greatly deteriorating the contrast between the visualised flow and the free stream. In order to restore the clarity of the water, diluted swimming pool chlorine was used. Chlorine was observed to deteriorate the metallic surfaces and accelerate corrosion. The tunnel was emptied and refilled with fresh water frequently, to prevent the excessive built up of chlorine. For all the food dye flow visualisation experiments conducted, the models were spray-painted matt white for corrosion protection and, additionally, to provide sufficient contrast between the model surface and the red dye. A flood light, placed either at the back of the water tunnel or at one of the side windows, and sometimes diffused by a large sheet of plain white paper, was used to enhance the clarity of the captured images. For the same reasons, the top of the tunnel was covered with large sheets of cardboard.

Towards the end of the project, another flow visualisation technique was employed, this time using laser induced fluorescent dye. The dye was diluted with water and a new wing was built to enable the effective use of it (Figure 2.6). The dye was injected into a cavity, which was built inside the wing, through two small metallic tubes with internal diameter of $d = 2mm$. A very thin slot 0.5mm was designed along the whole area of the leading edge providing the exit of the dye, hence giving information about the shear layer emanating from the leading edge. An Argon-Ion laser, which is described in Section 2.4.6, was utilised for the flow visualisation. Measurements in a crossflow plane were taken, providing useful qualitative data about the shear layer and small scale vortical structures. The model was

spray-painted matt black for corrosion protection, as well as to reduce unwanted reflections from the wing surface.

A JVC GR-DV4000EK digital video camera, with a capture rate of 25 frames per second (fps) and a resolution of 1600x1200 pixels (1,920,000 pixels), was used to capture images from the dye flow visualisation, and was interfaced to a desktop computer via the commercial software package PINNACLE STUDIO DV, v7.15.1, (Pinnacle Systems Inc.), enabling real time viewing of the wing, capture of camera images and video recordings. The camera was placed underneath the water tunnel and a flood light was located at the axial viewing window to enhance the clarity of the images. Additionally, white cardboard panels were placed at the top of the water tunnel, providing further contrast effects and clarity to the captured videos and images. Post processing of the data was performed using MATLAB Release 13 (The Mathworks Inc.), which is described in Chapter 3.

For the laser dye visualisations a Panasonic NV-DS99B digital video camera, with a capture rate of 50fps and a resolution of 570,000 pixels was used. The camera was placed at the axial viewing window of the water tunnel, and all the recording was done using Mini DV tapes. The videos were downloaded using PINNACLE STUDIO DV, v7.15.1 onto a desktop computer. Post processing of the data was done using CorelDRAW v12.0 and PINNACLE STUDIO DV v7.15.1 software.

2.4.4 Particle Image Velocimetry (PIV)

The use of DPIV was later implemented in order to get more quantitative data on both the crossflow plane, as well as parallel to the wing surface. The digital version of the PIV is user-friendly, hence the amount of labour required is reduced, as conventional film cameras or manual analysis of the data are not needed. A description of the DPIV used, its theory and the equipment used follows. Post-processing of the PIV data is provided in Chapter 3.

The PIV is a non-intrusive technique used to measure velocity by selected micro-sized particles that trace the flow. It is an instantaneous multi-point technique. The target area in the flow is illuminated using a light sheet (laser). The camera lens captures the illuminated area onto the CCD array of a digital camera. Two images are captured, and knowing the separation in time, Δt, and the distance that each particle has travelled, Δx and Δy, during that time the velocities of the particles can be calculated (Instruction Manual Particle Image Velocimetry Software-2001):

$$u = \frac{\Delta x}{\Delta t} \text{ and } v = \frac{\Delta y}{\Delta t}$$

Assuming that the particles are small enough to follow the flow, its velocity can be calculated. The spatial resolution of the method relies heavily upon the careful choice of seeding particles, and the optimisation of the laser and camera optics. The drawback of PIV is that the time resolution is limited and determined by the camera's capture rate, which in this investigation was 7.5 measurements per second.

However, the ability of the PIV to calculate thousands of velocity vectors instantaneously needs to be emphasised.

DPIV measurements were taken using a TSI (Inc. USA) PIV system, incorporating a pair of pulsed mini Nd: YAG lasers (neodymium-yttrium aluminium garnet, in the infrared range) with a maximum energy input of 120mJ per pulse. PIV applications require a high energy (large field of view) and/or a short exposure (high velocity), which makes the YAG lasers the best choice presently available (Stanislas and Monnier-1997). To illuminate the desired planes, the laser system was placed underneath the test section of the water tunnel, as shown in Figure 2.7, for crossflow measurements. Measurements in the plane parallel to the wing surface required the laser to be placed at the side of the water tunnel, inclined at the same incidence as the model. A combination of cylindrical and spherical lenses was used to adjust both the thickness and the width of the light sheet. Images were captured using an 8-bit TSI PowerView 4M CCD camera with a resolution of 2048 x 2048 pixels (4,194,304 pixels) and a maximum capture rate of 7.5fps, producing 3.75 frames in cross-correlation. Synchronisation of the camera captures and the laser pulses was accomplished through a synchroniser unit.

After capturing the images, these were analysed using one of the suggested methods, cross-correlation, auto-correlation or particle tracking. More information on the theory and application of DPIV is given by Willert and Gharib (1991), Westerweel (1997) and Adrian (1997).

The commercial software package Insight v6.0, (TSI Inc.) and a Hart cross-correlation algorithm (Hart-1998) were used to analyse the images, with an interrogation window size of 32 by 32 pixels, and to produce velocity vectors for further processing. The PIV camera was placed near the downstream viewing window, as shown in Figure 2.7 for crossflow measurements, whereas for measurements parallel to the models' surface, it was placed underneath the water tunnel at the same incidence as the model. Sequences of 30 instantaneous frames were taken for each case and the time-averaged (or phase-averaged, for dynamic motions) velocity fields were calculated. The number of instantaneous images taken was found to be sufficient for a smooth average flowfield. Time-averaged and phase-averaged images, which are shown in chapters 4, 5, 6 and 7, present a very reliable field and reduce the need to interpolate and validate the actual raw data.

The flow was seeded with hollow glass spherical particles of mean diameter of 8-12μm, provided by TSI. Clogging of the particles was prevented by mixing them with water and adding a small portion of detergent, before actually pouring them into the water tunnel. To ensure uniform seeding in the flow, particles were allowed to mix properly in the flow, so the tunnel was left running without the model for a few minutes before inserting the model in the water and starting the experiment. As mentioned earlier in this chapter, dynamic measurements were also taken. The PIV system was externally triggered, using a desktop computer and the data acquisition software Agilent (HP) VEE, v 6.2, in order to capture the flowfield at a specific roll angle during the dynamic oscillation. The models tested using the PIV were painted matt black to avoid reflections created from the laser.

2.4.5 Laser Doppler Velocimetry (LDV)

The use of a Laser Doppler Velocimetry (LDV) was considered necessary to enhance the amount of information provided for the flowfield. The LDV system incorporates a number of features which make its use very popular and attractive for measuring the direction and the speed of fluids. A wide range of velocities and distances can be covered, one, two or three velocity components can be measured at the same time, both instantaneous and time-averaged information can be provided. Finally, LDV is a non-intrusive measurement device.

The principle used to measure velocity is the scattering of light by the particles, which are assumed to travel with the velocity of the fluid given that they are small enough. Two laser beams (for each velocity component) which are focussed and intersected at an angle (half angle κ) at the focal length of the lens, create a fringe pattern or a series of light and dark fringes. As the particle moves through the measuring volume it scatters light when it crosses the bright fringe and scatters no light as it passes from the dark fringe. This results in a fluctuating pattern of scattered light intensity with a specific frequency, which corresponds to the velocity of the particle. The distance between the fringes and the time for the particle to travel between the fringes are known, hence the measured frequency can be transformed into velocity. The scattered light is optically collected and focussed onto the photomultiplier tube, which produces an electrical current proportional to the light flux. Variations of this electrical current are analysed to determine the velocity of the particle. The frequency of the signal, also known as Doppler frequency, is proportional to a component of the particles' velocity which is perpendicular to the planar fringe pattern produced by the beam crossing. As a result the Doppler frequency, f_D is measured and the velocity is calculated by multiplying it by the fringe spacing δ_f, which depends only on the wavelength of the light λ_f and half angle κ.

$$u = \delta_f \cdot f_D$$

and

$$\delta_f = \frac{\lambda_f}{2 \sin \kappa}$$

where:
- u: flow velocity
- λ_f: wavelength of light
- δ_f: fringe spacing

The three components of velocity can be measured by crossing four or six laser beams of different wavelengths or polarization in the same measuring volume, and separating out the scattered light using filters (Operations Manual for the Phase Doppler Particle Analyzer (PDPA)/Laser Doppler Velocimetry (LDV)-2001).

The key aspects of the LDV can be summarised by the following: measurements are generally independent of the properties of the medium; the desired velocity

component can be measured by properly orientating the laser beams; the signal exists only when a detectable particle is in the measurement volume.

The same seeding particles as the PIV were used for the LDV measurements. The choice of particles was made through the experience acquired using the PIV since it is more demanding as far as the size of the field to be seeded and the uniformity of the seeding is concerned.

The laser used was supplied by TSI and is a 300mW air-cooled Argon-Ion laser, which outputs different wavelengths. The three wavelengths used for LDV applications are: 514.5nm (green), 488nm (blue) and 476.5nm (violet) (Operations Manual for the Phase Doppler Particle Analyzer (PDPA)/Laser Doppler Velocimetry (LDV)-2001). The readings were passed through a data processing unit to a dual processor computer with controlling software. The probe could be fixed to a three axis computer controlled traverse for automated measurements. A TSI FlowSizer, v1.04 software was supplied with the LDV system and all the data was exported to ASCII type CSV files for post processing. FlowSizer software offers two sampling methods: "eventime" or "realtime" sampling. For the measurements taken during this project "eventime" sampling was chosen. The big advantage of "eventime" sampling is that the velocity bias associated with uneven collection of data, is removed. However, a higher data rate is required so that in each sampling point in time there is likely to be a measurement. Realtime measurements were preferred when an accurate reproduction of the velocity profile was required.

2.4.6 Argon-Ion laser

Crossflow visualisation tests were performed using a continuous emission laser to illuminate the desired plane with the aid of fluorescent dye. The laser used was a water-cooled Coherent Innova70, 12W Argon-Ion continuous emission unit. It is designed for applications that require continuous wave laser light in the blue and green visible spectrum. It operates in a wavelength of 514.5nm with an output of 12W (Operator's Manual for the Coherent Innova 70 Series Ion Laser-1989). The system comprises three major units: the laser head, the plasma tube within the laser head and the power supply. Light is transmitted via a fibre-optic cable to the optical head. A combination of spherical and cylindrical lenses is used to spread the beam into a sheet, adjust its thickness and divergence. The optical head was placed underneath the water tunnel and directed upwards to illuminate a crossflow plane.

2.5 Figures Chapter 2

Figure 2.1: Photo of Eidetics Model 1520 water tunnel (Courtesy Rolling Hills Research Corporation).

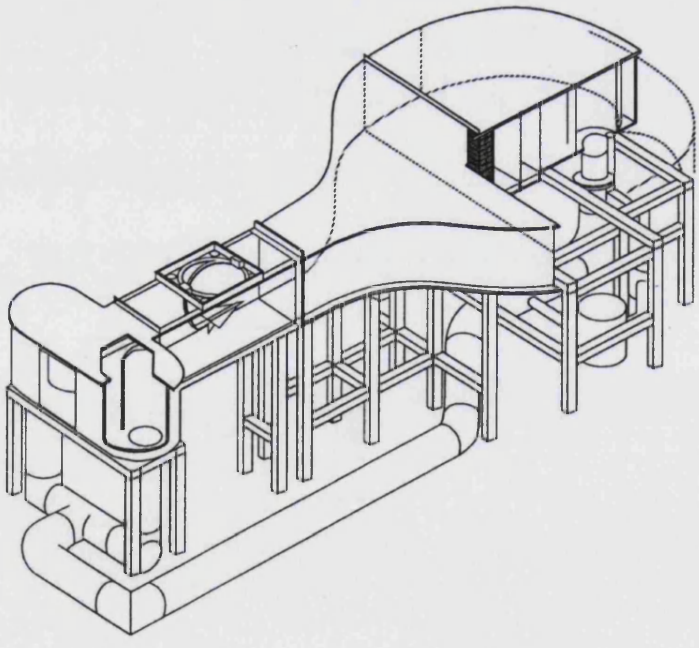

Figure 2.2: Schematic picture of Eidetics Model 1520 water tunnel (Courtesy Rolling Hills Research Corporation).

Size	30' x 15' x 6.5' (LxWxH)
Weight	7,500lbs. w/water
Capacity	1,000 gallons
Test Section	15" x 20" x 60" (WxHxL)
Down Stream Window	15" x 15" (WxH)
Flow Velocity	0 to 1ft/s nominal
Turbulence Intensity	<1.0% RMS
Centrifugal pump	2.0hp 230VAC 3Phase 60Hz 20A
Dye System	Pressurized 6 colour
Mounting Structure	Steel Frame

Table 2.1: Specifications of the Eidetics Model 1520 water tunnel (Courtesy Rolling Hills Research Corporation).

Rigid Delta Wings			
Λ[°]	**c [mm]**	**t [mm]**	**b [mm]**
50	89	2	150
40	62.9	2	150
30	43.3	2	150
50	89	4	150
Flexible Delta Wings			
Λ[°]	**c [mm]**	**t [mm]**	**b [mm]**
50	89	0.508	150
50	89	0.381	150
50	89	0.254	150
50	89	0.1905	150
Cropped Delta Wings			
Λ[°]	**c [mm]**	**t [mm]**	**b [mm]**
50	40.4	2	100
40	58	2	100
30	71.1	2	100
20	81.8	2	100
10	91.2	2	100
0	100	2	100

Table 2.2: Dimensions for the low sweep models.

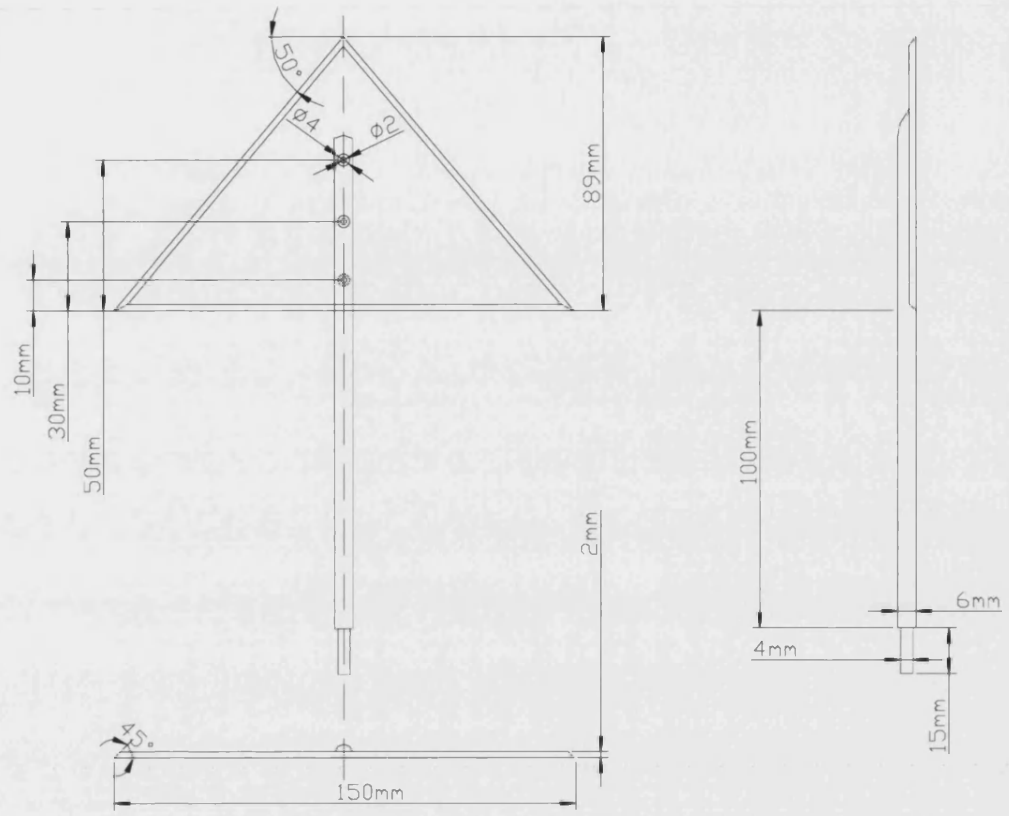

Figure 2.3: Rigid, 50° sweep angle model.

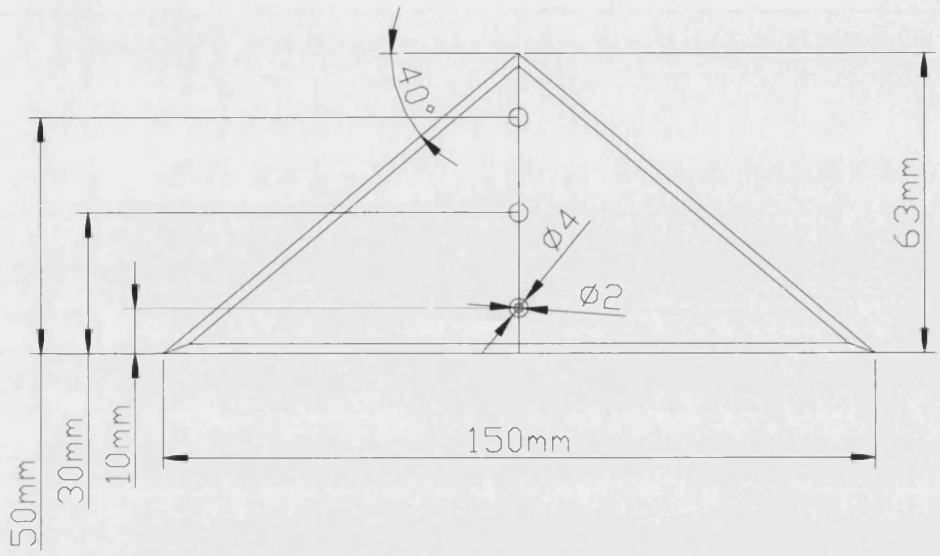

Figure 2.4: Rigid, 40° sweep angle model.

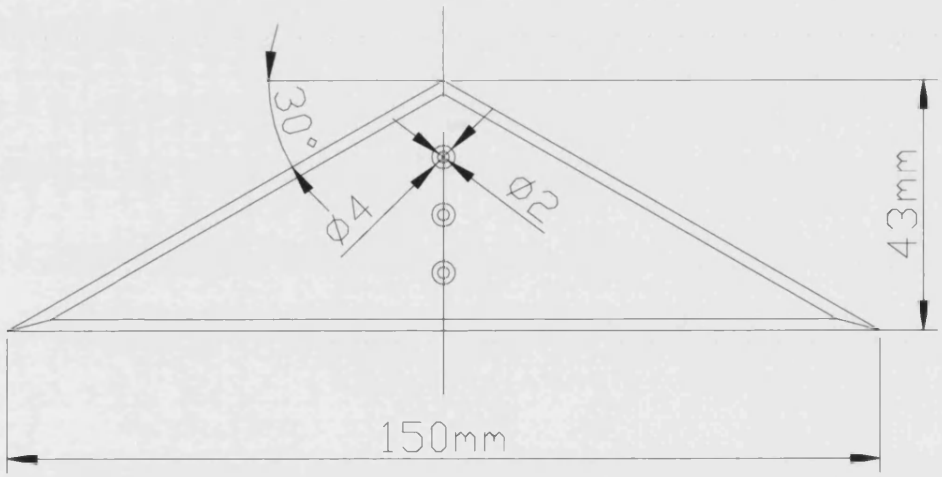

Figure 2.5: Rigid, 30° sweep angle model.

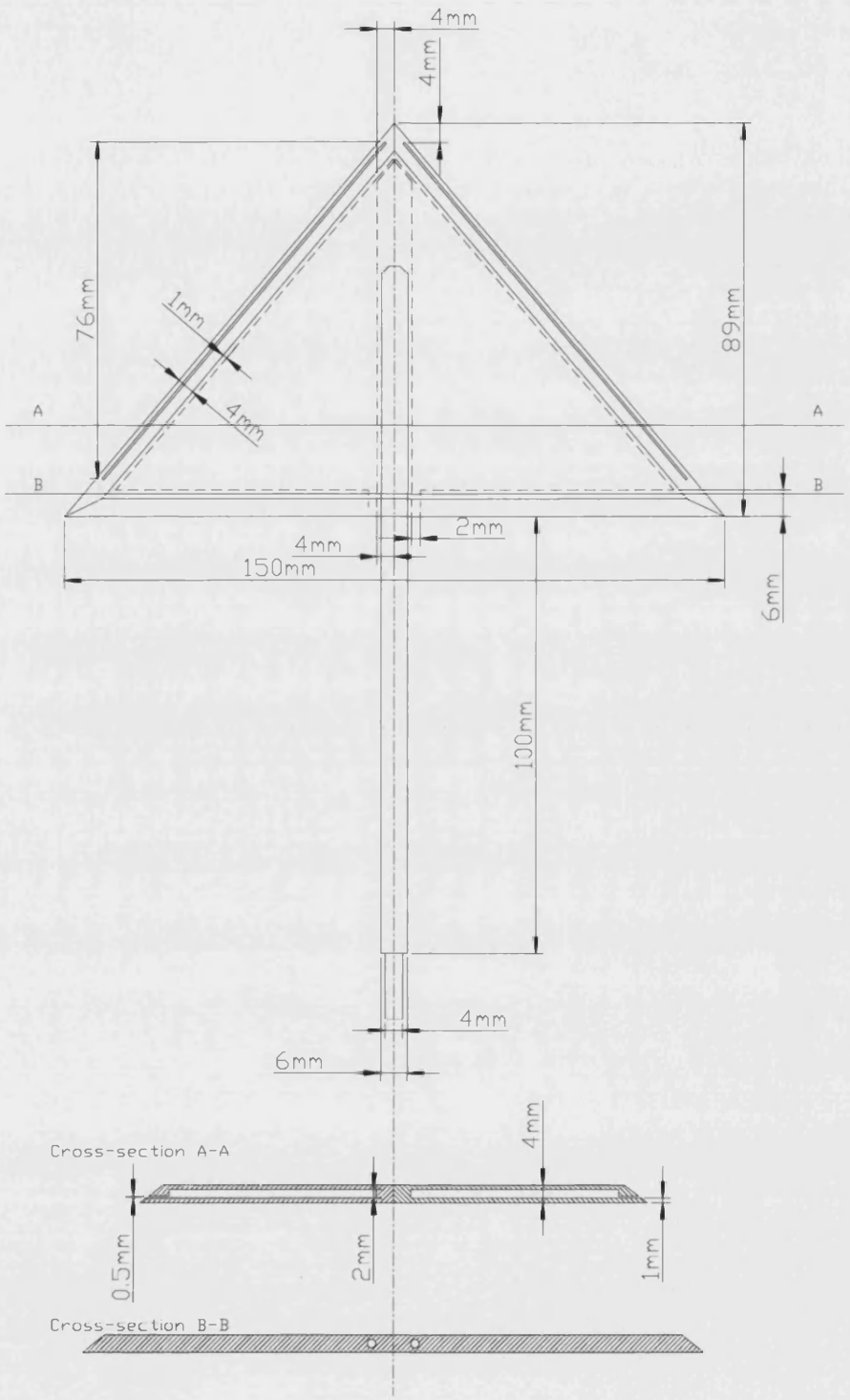

Figure 2.6: Rigid, 50° sweep angle model with cavity.

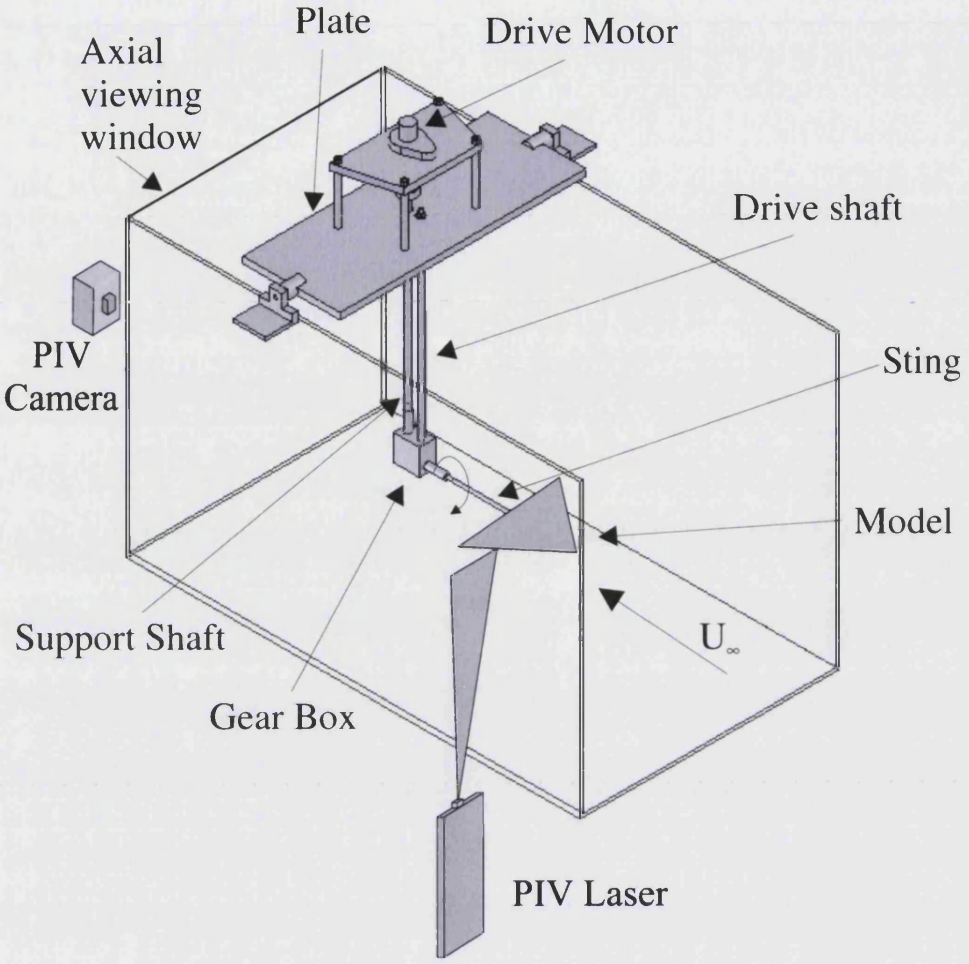

Figure 2.7: Overview of experimental setup.

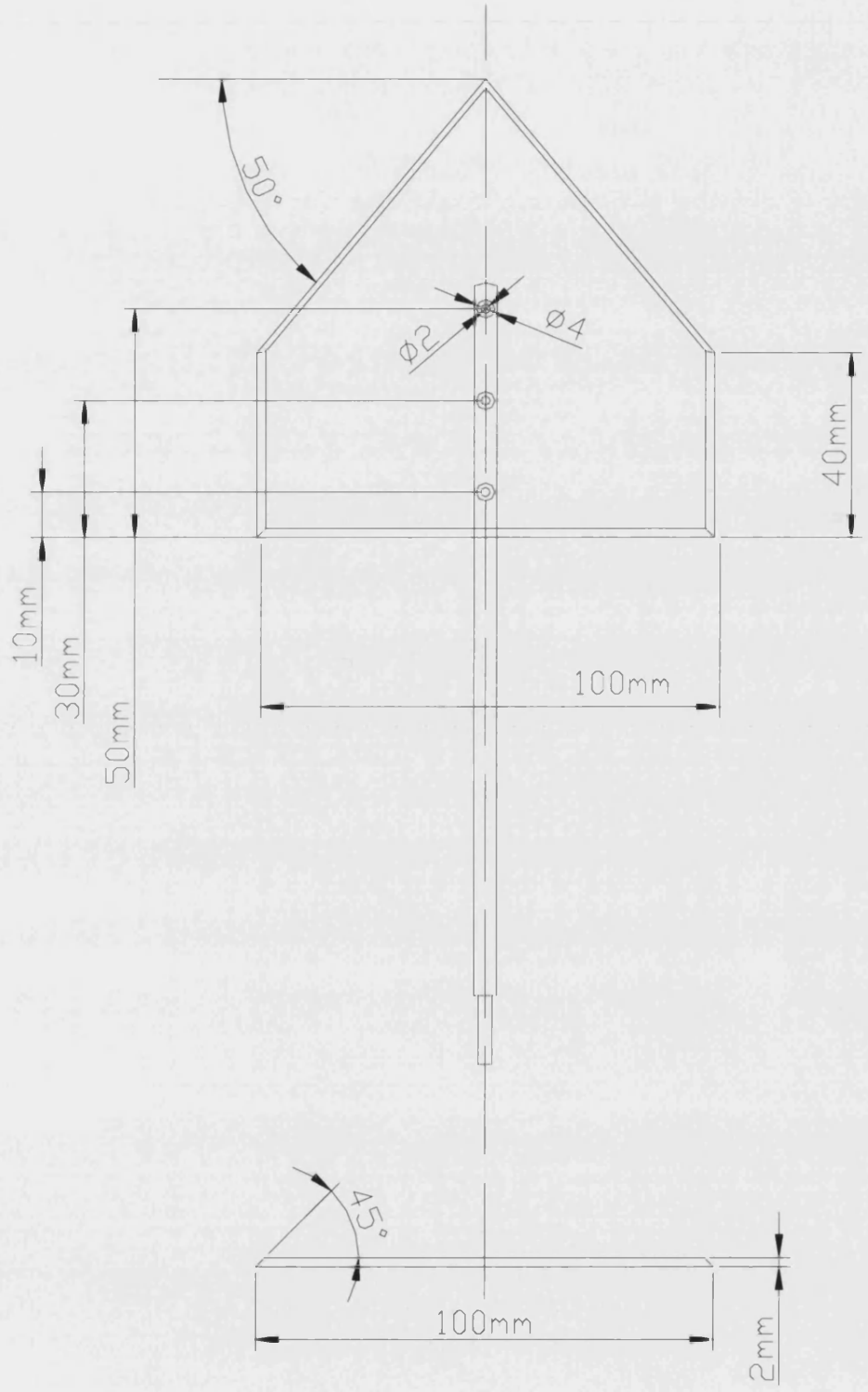

Figure 2.8: Principal dimensions of cropped model with $\Lambda = 50°$.

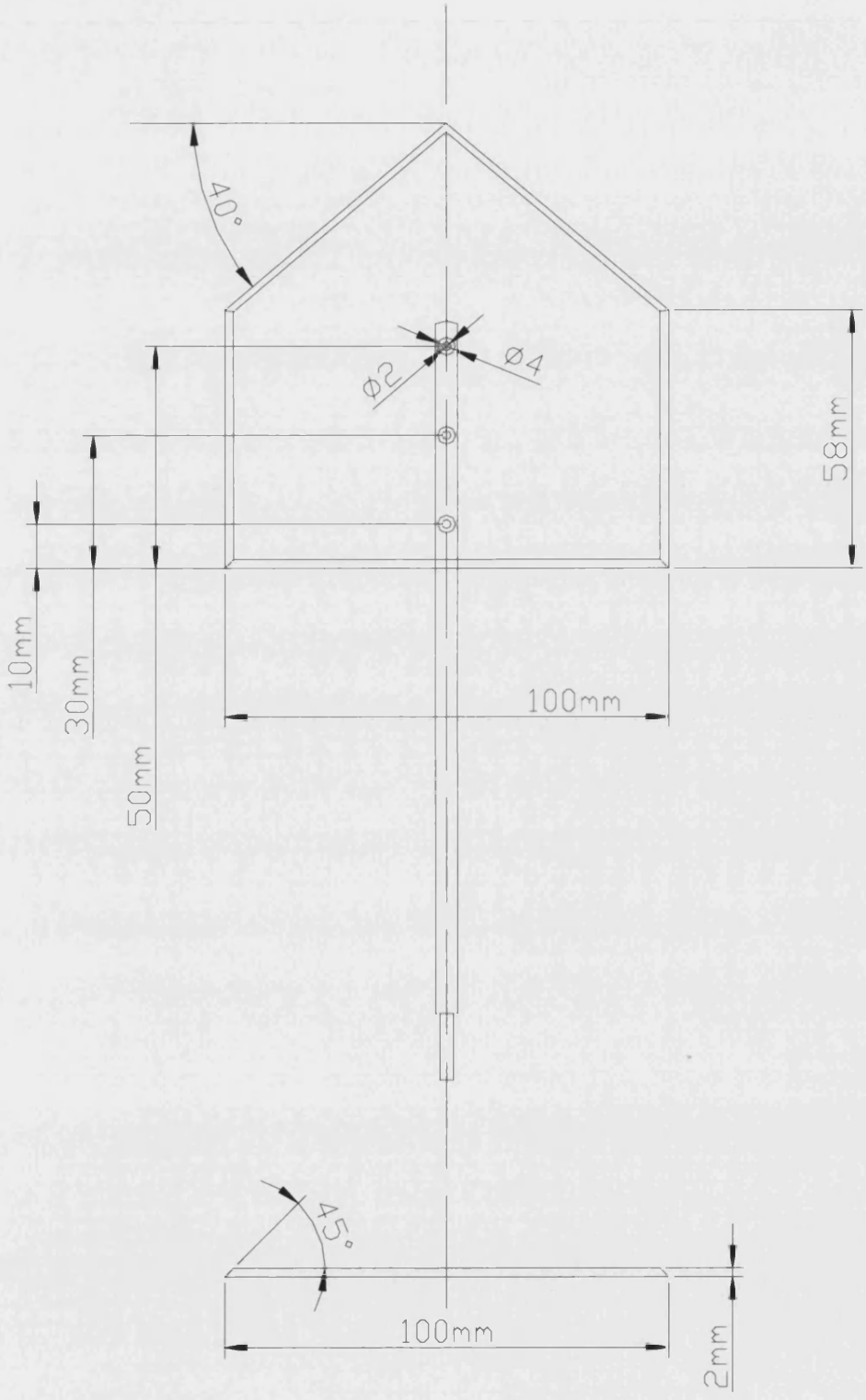

Figure 2.9: Principal dimensions of cropped model with $\Lambda = 40°$.

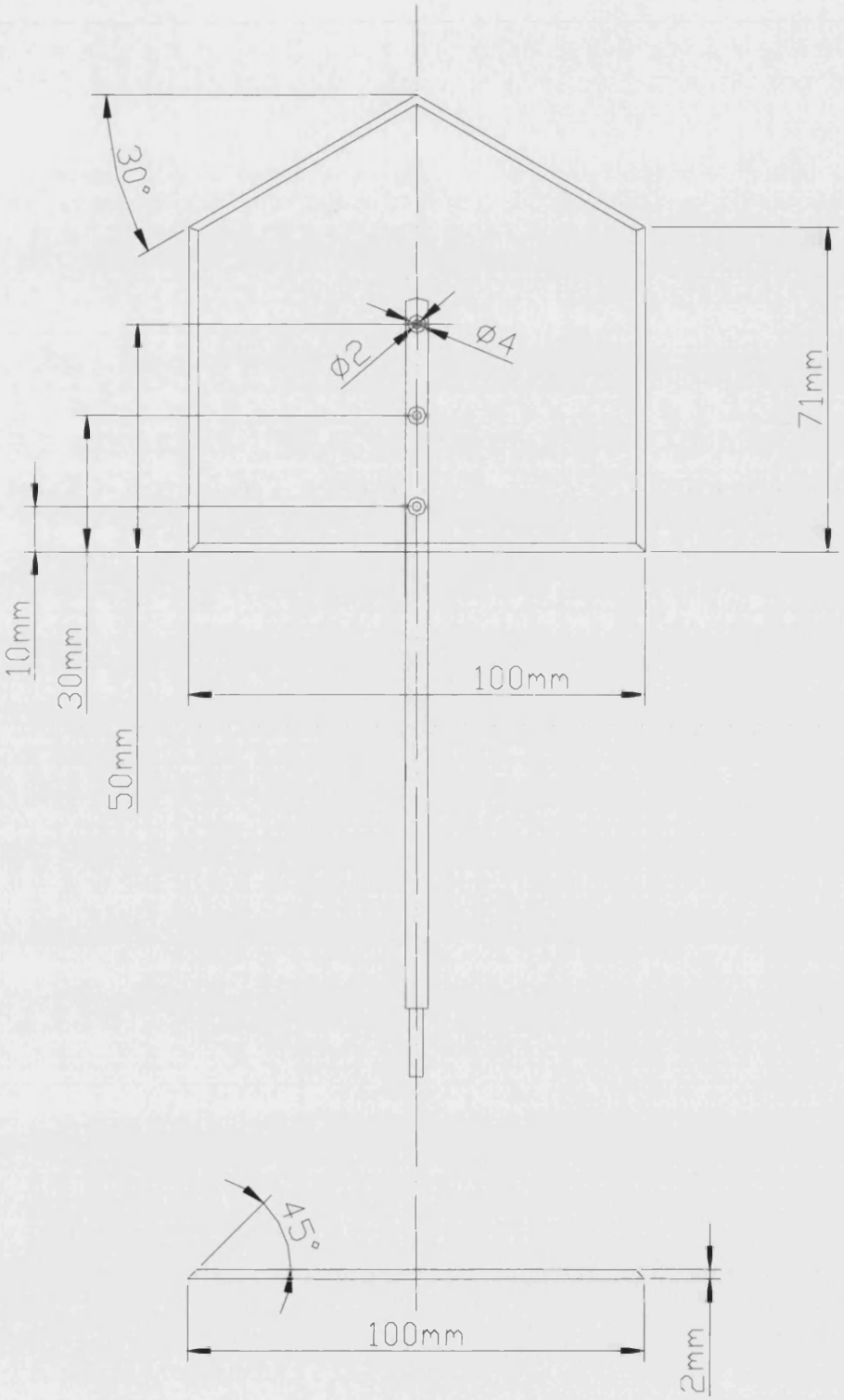

Figure 2.10: Principal dimensions of cropped model with $\Lambda = 30°$.

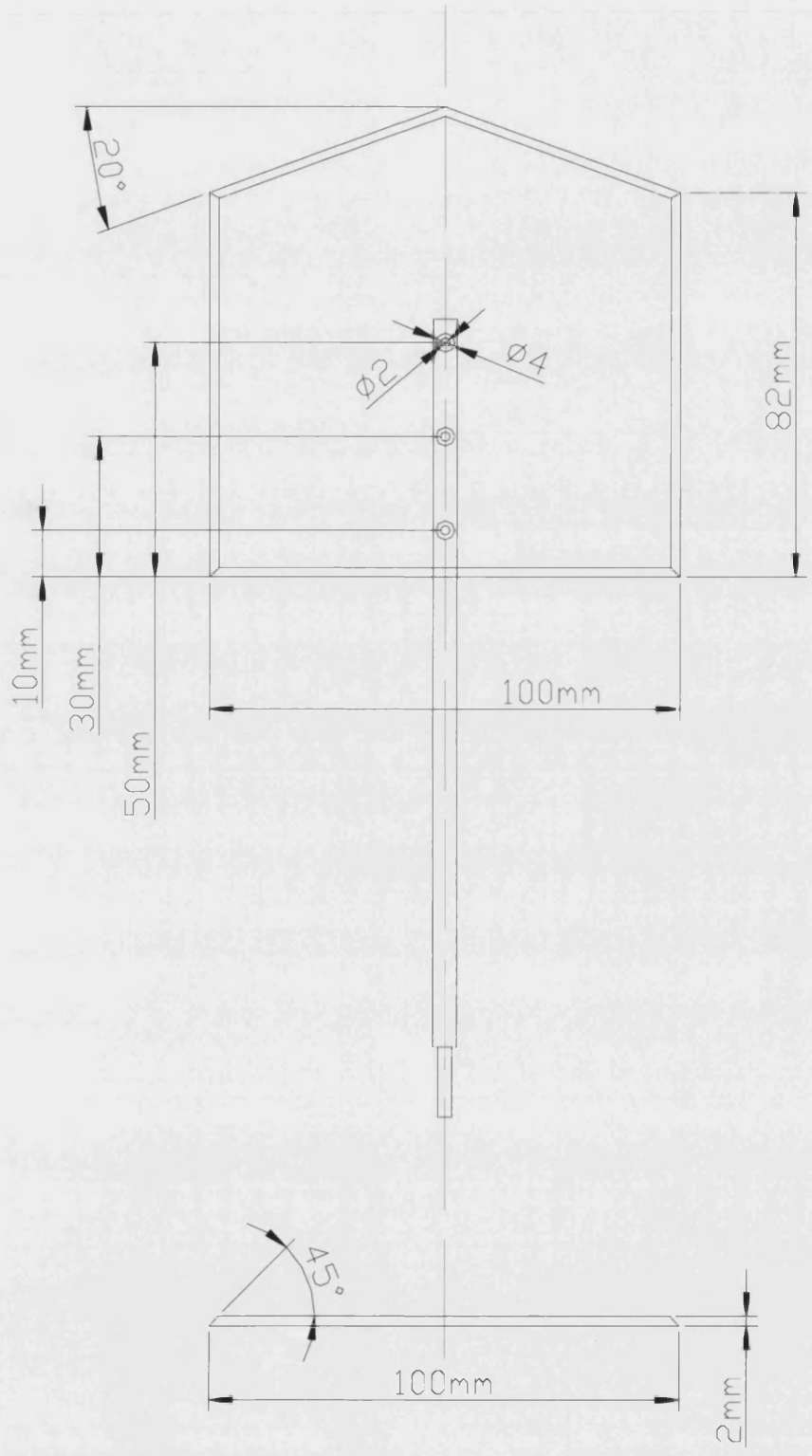

Figure 2.11: Principal dimensions of cropped model with $\Lambda = 20°$.

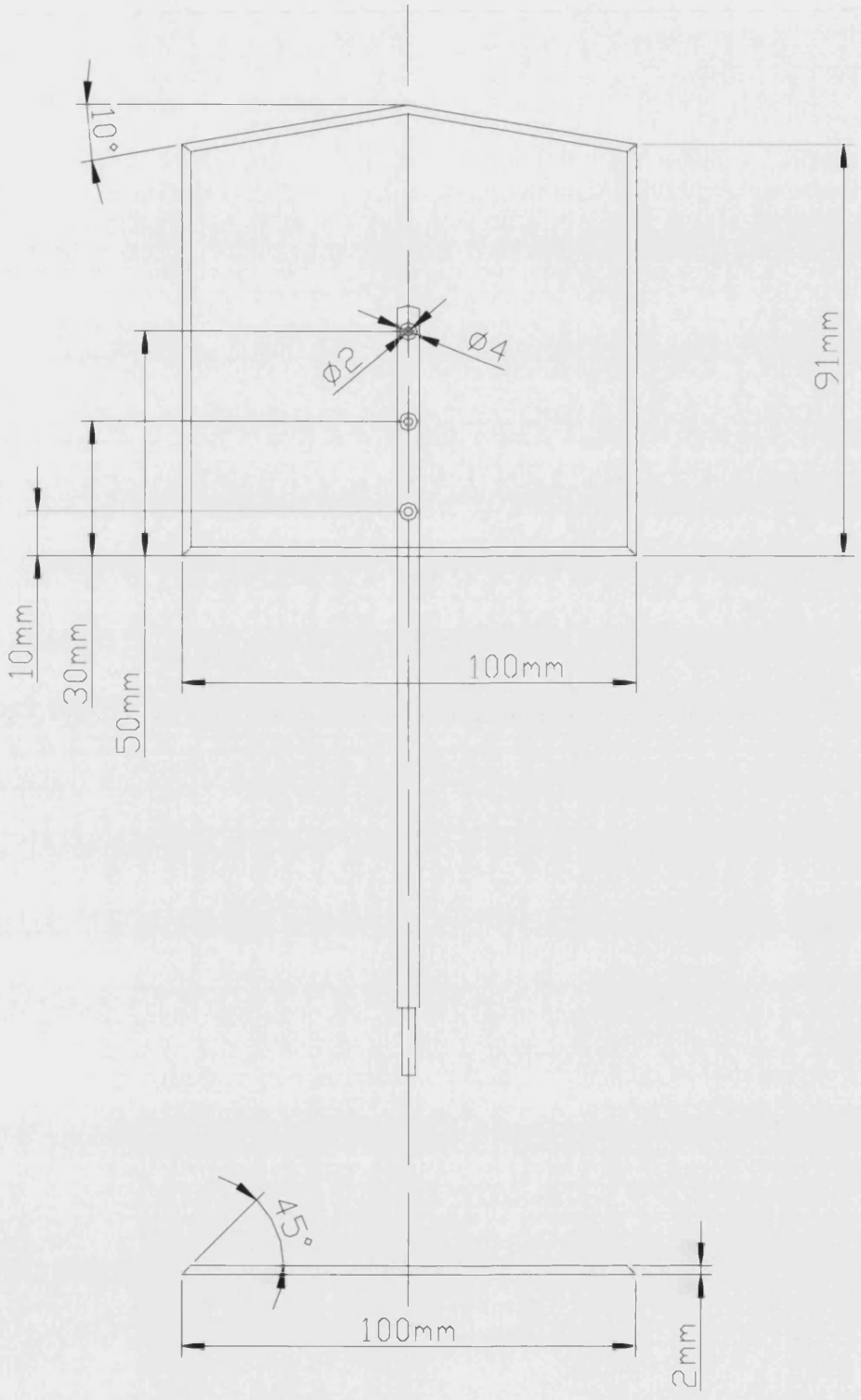

Figure 2.12: Principal dimensions of cropped model with $\Lambda = 10°$.

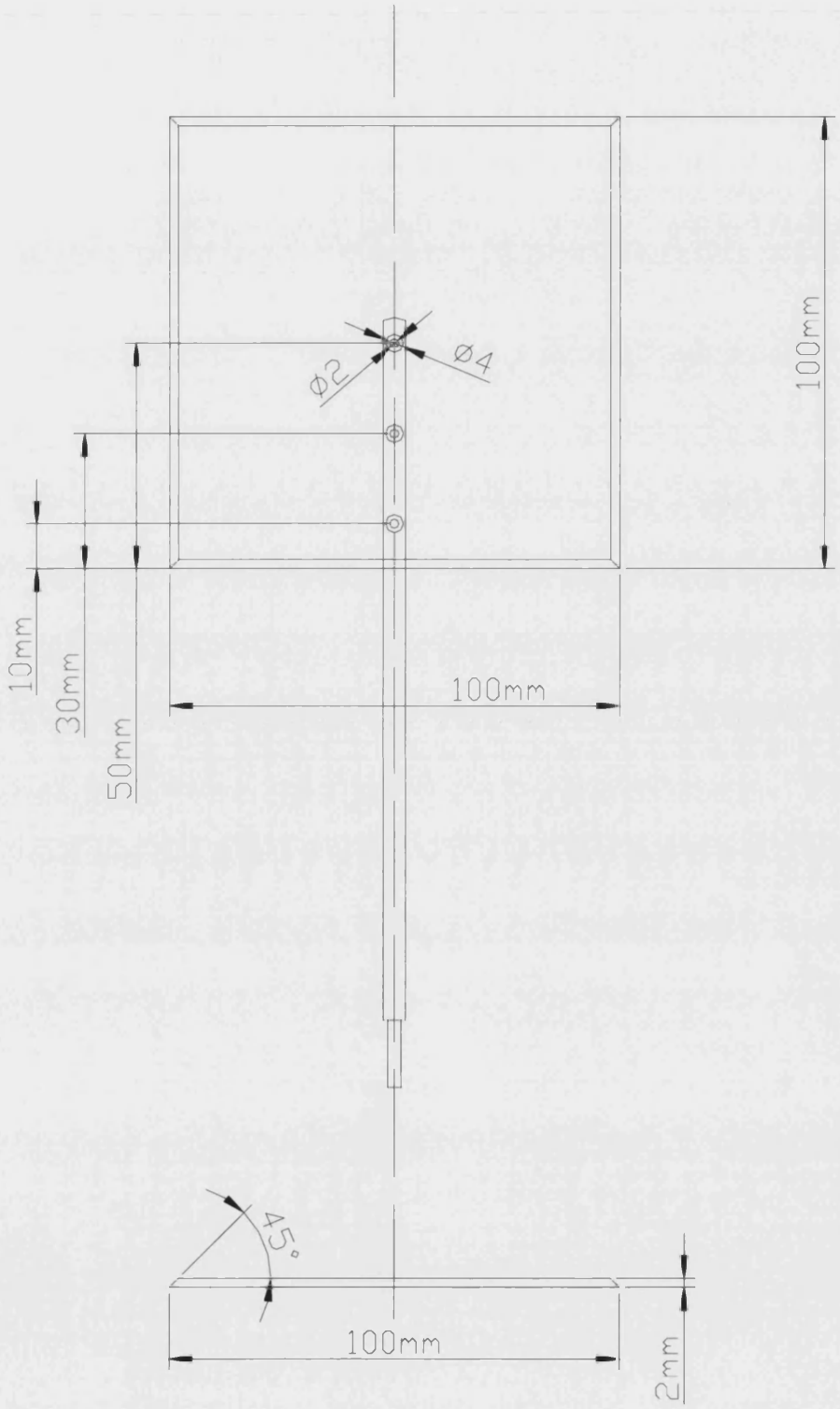

Figure 2.13: Principal dimensions of cropped model (square plate) with $\Lambda = 0°$.

CHAPTER 3: EXPERIMENTAL PROCEDURES

3.1 Introduction

This chapter discusses the methodology employed for the analysis of the results attained during this investigation. A brief overview of the experimental procedures undertaken is necessary, in order to explain the analysis of the results obtained from manoeuvrable nonslender delta wings.

3.2 Overview of Experimental Procedures

The methodology employed in both the stationary and the dynamic testing involved the use of a range of nonslender delta wings, both simple and cropped, with different sweep angles (for more details refer to Chapter 2). The effect of different parameters on the vortex breakdown location of the leading edge vortices was measured, along with the effect that different manoeuvres (roll and pitch) and small-amplitude oscillations had on the vortical flowfield. Additionally four flexible low sweep delta wings were also tested. The flexible wings had different material properties; hence the effect of flexibility was studied under both static and dynamic conditions.

3.3 Data acquisition and analysis

Flow visualisation of nonslender delta wings, followed by analysis of the flowfield using PIV and LDV equipment, were undertaken for this project. Additional calculations were performed using the recorded data. The method followed to obtain the results, and the processes used for their analysis, follows.

3.3.1 Flow Visualisation Images and Vortex Breakdown Location

All the flow visualisation experiments were conducted at a freestream velocity $U_\infty = 0.3\,m/s$. The Re was calculated, based on the chord length of the wing tested each time, using:

$$Re = \frac{U_\infty \cdot c}{\nu_\infty}$$

where: $\nu_\infty = 1.004 \times 10^{-6}\ m^2/s$ at $T = 20°C$ (The Engineering Toolbox-2002).

The information extracted from the dye flow visualisation images, apart from the actual image itself, was the location of the vortex breakdown, which is defined as the point at which the core rapidly expands. The dimension X_{bd} was defined as the distance measured from the apex of the wing, to the location of the breakdown, considering the chord length as seen on the image. For each of the graphs provided in this report, the location of the vortex breakdown was nondimensionalised with the chord length of the delta wing.

The images were recorded for a period of time which was usually dependent on the experiment itself, given that both static and dynamic tests were performed. For the dynamic case, an average of 50 cycles was captured each time, with the purpose of discarding approximately the first 10, in order to make sure that the flow was established. Phase-averaged variation of the vortex breakdown was obtained by averaging 30 cycles in the dynamic experiments. The static case was simpler, as a few seconds (in this case usually 30) were quite adequate to provide sufficient data to describe the flowfield. The recorded videos were either stored on the camera or simultaneously downloaded to a desktop PC. Further examination of the videos allowed individual frames to be captured as still images using PINNACLE STUDIO DV, v7.15.1 software. For the dynamic tests, a series of captures where required at constant time intervals. All of the vortex visualisation images (in both static and dynamic cases) were recorded with the camera placed underneath the water tunnel, inclined at 90°. In some of the measurements obtained, reference will be made to "clockwise" and "counter-clockwise" vortices, these being the left and right vortices respectively as viewed from the bottom of the inverted model.

The vortex breakdown location was calculated using MATLAB, in order to make the process quicker. The distance between the apex and the vortex breakdown location, divided by the chord length seen in the still captured image, provided the dimensionless vortex breakdown location (see Figure 3.1). Thirty images were time-averaged in the static case, and phased-averaged in the dynamic case. Finally, the mean average breakdown location was plotted against various parameters, such as the roll angle or the nondimensional frequency.

In some cases (for example for some of the low sweep and cropped delta wings), the calculation of breakdown location was very difficult, so another parameter had to be

calculated. Hence, the distance between the wakes of the two broken down vortices (Δy_w) was measured instead, at 50% of the chord length, and was divided accordingly by the local span $(2s)$, so as to give a dimensionless value. An example is given in Figure 3.2. With the aid of MATLAB, the wake distance was calculated using:

$$\frac{x_3 - x_4}{x_2 - x_1} = \frac{\Delta y_w}{2s}$$

For reference to the relevant lengths see Figure 3.3.

Both the instantaneous and averaged images of laser induced flow visualisation, in the static and dynamic cases, were captured at 80% of the chord length. The instantaneous images were captured using PINNACLE STUDIO DV v7.15.1 software. Corel PHOTO-PAINT v12.0 software was used to create the averaged images. Ten instantaneous images were time or phase averaged (for the static and dynamic cases respectively) by adjusting the opacity in each one of them and in the end superimposing them.

3.3.2 PIV Data

All the PIV data were collected, saved and processed on a dual processor computer using Insight (TSI), v6.0 software, which allowed the capturing of PIV images, performed the analysis, and at the same time was used to control the setup of the system. The software provided full control of the laser and the synchroniser settings. Insight divides an image into small regions (interrogation regions), and a cross-correlation algorithm is carried out on the particle images within each region, to determine particle displacement, which, in conjunction with time between laser pulses, provides particle velocity. The process is repeated to obtain particle velocities for the entire image, or for the selected area of interest. Whilst the wings were always painted in non-reflective matt black, some spurious vectors were always generated close to the surface due to reflections. These vectors were usually removed from the flowfield using a validation macro, in which they were replaced by vectors interpolated from the surrounding area. Another source of spurious vectors was the limits of the interrogation window. Although these areas are not important for the vortical flowfield, these vectors were also removed.

Analysis of the images captured was performed using the Hart cross-correlation technique, which was provided with the software. Fast Fourier Transform (FFT) cross-correlation algorithms have also been tried prior to the establishment of the use of Hart. The location of the particles in the image pairs were obtained after a single pass, giving a correlation map which was related to the dominant peak of the mean displacement of the particles in the interrogation window. Due to the level of background noise, this algorithm was discarded in favour of Hart, which reduces the interrogation spot size to improve spatial resolution by two. An overview of the technique follows, but a detailed account is given by Hart (1998). In the current

investigation, the algorithm was used with a 32 by 32 pixel grid. For both the time-averaged (static case) and phase-averaged (dynamic case) experiments, a sequence of 30 images was captured and found to be sufficient to yield a smooth averaged flowfield. Vector files were then loaded into the Tecplot v9.0 (Amtec Engineering Inc.) data-plotting package, where they were nondimensionalised. Finally, velocity and vorticity fields were calculated and in some cases the streamlines were also plotted.

3.3.2.1 Hart Correlation

The basic principle of Hart correlation is that each interrogation spot image is first compressed, based on a threshold defined by the user as compression ratio. The intensity information on the compressed images is then put into an encoded form and a correlation function is performed on it. Hart correlation can also be applied in a progressive fashion to allow the reduction of the interrogation spot size for high spatial resolution. A double correlation technique can possibly be used to increase the signal-to-noise ratio so that the correct velocity measurements can be made more robustly.

3.3.3 Calculation of Flow Quantities

3.3.3.1 Vorticity and Circulation

Circulation and vorticity are two flow quantities that are closely related and interconnected, and additionally have great significance in aerodynamics. They are commonly used in the analysis of rotating flows, such as vortices. Vorticity, denoted as ξ in most text books (see for example Anderson-2001, from where the symbol ξ for vorticity was taken), is a measure of angular velocity, and can be simply defined as:

$$\xi = 2\omega$$

where, in cartesian coordinates:

$$\omega = \frac{1}{2}\left[\left(\frac{\partial w}{\partial y} - \frac{\partial v}{\partial z}\right)i + \left(\frac{\partial u}{\partial z} - \frac{\partial w}{\partial x}\right)j + \left(\frac{\partial v}{\partial x} - \frac{\partial u}{\partial y}\right)k\right]$$

Since u, v and w denote the x, y, and z components of velocity respectively, an important conclusion is drawn: *"In a velocity field, the curl of the velocity is equal to the vorticity"* (Anderson-2001):

$$\xi = \nabla \times V$$

Vorticity is a useful measure of the amount of rotation undertaken by the fluid. The flow is called *"irrotational"* when vorticity is zero, the fluid elements have no

angular velocity and hence there is no rotation and their motion is purely translational. On the other hand, in a "*rotational*" flow, the fluid elements have a finite angular velocity, thus a rotation, and it is that rate of rotation that actually defines the vorticity.

PIV data provide the velocity vectors and from those, the vorticity is calculated. In the present report, nondimensionalised vorticity is denoted as:

$$\frac{\omega \cdot c}{U_\infty}$$

(Note that the symbol ω denotes vorticity and not angular velocity in the present document).

In some cases it is difficult to obtain "perfect" PIV velocity data, which makes the calculation of vorticity more complicated, due to the fact that the noise contained in the vector field is magnified by the differentiation. Therefore a better aerodynamic quantity needs to be defined: circulation. Circulation is the line integral of velocity around a closed curve in the flow, and it is a kinematic property depending only on the velocity field and the choice of the curve. The circulation, denoted by Γ in the present report, is defined as:

$$\Gamma \equiv -\oint_C V \cdot ds$$

The circulation is related to vorticity, and can also be defined as equal to vorticity integrated in an open surface:

$$\Gamma = -\iint_S (\nabla \times V) \cdot dS$$

However, the calculation of circulation through the integration of the velocity field removes the noise problem. Whenever the strength of a vortex is being discussed, circulation is the quantity to refer to. However, vorticity also provides information on the flowfield.

In the present investigation both circulation and vorticity are discussed. Vorticity was calculated using a Tecplot v9.0 macro provided by TSI. The crossflow vorticity flowfields presented in this report are taken at 80% of the chord length. Vorticity is nondimensionalised by multiplying by the chord length, and dividing by the freestream velocity. Note that the axes in these plots are nondimensionalised by the local semispan s, and the origin is the apex of the delta wing. Additionally, velocity crossflow fields are presented, which in turn are nondimensionalised with freestream velocity. The same rule employed for the axes and origin was applied in this case.

For the calculation of the circulation, the velocity definition is used in combination with a MATLAB macro. The integration area was rectangular in shape, and chosen manually by the author. The choice was based on the actual size of the vortex (how diffused the vortex was in each different case) with an additional area around the

vortex also included. By trial and error, the maximum value of circulation around each vortex was calculated, and it is this value that is presented in the results that follow. Inputs of the macro were the freestream velocity and the chord length of the wing. These were then used in order to nondimensionalise circulation as follows:

$$\frac{\Gamma}{U_\infty c}$$

The velocity field was loaded into MATLAB, and following the procedure described, the values of circulation were obtained.

3.3.4 Additional Parameters

3.3.4.1 Spanwise Bending Flexibility

The comparison between flexible and rigid delta wings required the use of a common quantity to identify all the material properties and dimensions of the wings tested. For this reason, a parameter defined as spanwise bending flexibility, denoted λ, was introduced and calculated for all the flexible and rigid wings tested. It is used to give an indication of the flexibility of the wing under given flow conditions, whereby a higher value of λ corresponds to a more flexible wing (so for a rigid wing the value is $\lambda = 0$).

The steps followed to calculate λ are as follows: the bending/flexural rigidity of a thin rectangular plate is defined as (Megson-1999):

$$D = \frac{E \cdot t^3}{12 \cdot (1 - \nu^2)}$$

in which: E Elastic modulus
ν Poisson's ratio of the plate material
t Thickness of the plate

The above equation is normalised by:

$$q = \rho_\infty \cdot U_\infty^2 \cdot s^3$$

where: ρ_∞ density of water
U_∞ freestream velocity
s semispan

Hence the equation for the spanwise bending flexibility, λ, is:

$$\lambda = \frac{12 \cdot (1 - \nu^2) \cdot \rho \cdot U_\infty^2 \cdot s^3}{E \cdot t^3}$$

For the wings tested, λ was calculated using the above equation. The rigid wing was made of aluminium, whereas two of the flexible wings were made out of polyester, and the other two out of polypropylene. The material properties of each wing are given in Table 3.1. Notice that the value of λ for the rigid wing (aluminium) is set to zero, which is an approximation of the actual value, 0.0007. For all the experiments, the freestream velocity was $U_\infty = 0.3 m/s$, the density of the water $\rho_\infty = 1000 kg/m^3$ and the semispan was at the trailing edge, and hence $s = 0.075 m$. In any other case, where a local semispan is considered for the calculation, it is clearly stated.

3.3.5 LDV Data

The LDV data were collected using FlowSizer TSI software, which was provided with the LDV system. At each station, the LDV was set to capture 10,000 data points, ensuring sufficient data rate to avoid velocity bias. However, for the power spectrum analysis that was performed, eventime sampling was required, so 6,000 data points were finally captured. The power spectrum analysis was performed using the MATLAB power spectrum function. The function is based on the interpolation of an even-time dT interval over the data time duration, and then performs a standard FFT to produce the spectrum.

Furthermore the mean and rms values of the velocities measured with the LDV, were calculated. The rms value of a variable is a useful parameter as it gives an indication of the magnitude of fluctuations of the variable about its mean. MATLAB functions were used for the calculation of these values.

3.4 Data Quality and Validation

3.4.1 Delta Wing Models

All models tested were mounted upside-down in the water tunnel using a strut attached to the pressure surface. This allowed undisturbed formation of the leading edge vortices on the suction surface. The process of designing and building the models was carefully undertaken to ensure the accuracy of the dimensions required. Due to the fact that the models were tested in the water, rust built up after long hours of testing, which was meticulously removed to avoid any interference with the flow. During the project, it was necessary to replace the models due to wear and tear. An attempt was made to use different models for flow visualisation and PIV/LDV experiments to avoid repainting them, and changing their thickness due to the many layers of paint.

The largest error present in this investigation was the measurement of the angle of attack of the model. Although every possible effort was made to ensure that the incidence was set accurately, the precision is estimated to be of the order of $\pm 0.5°$ at best.

3.4.2 Vortex Breakdown Location

It is important to know if measurements undertaken in a water tunnel can be extrapolated to air. In the present case, where all measurements were taken in the water tunnel, the Reynolds number was significantly low, and if similarity or comparison with air measurements is to take place, the flow must be insensitive to changes in Re. Providing that the leading edge is sharp, the formation of the leading edge vortices over a delta wing can be considered as independent of Re. For a nonslender delta wing with $\Lambda = 50°$, the flow reaches an asymptotic state at Re of around 25,000, and further increases result only in small variations in the location of the vortex core and the breakdown location (Taylor and Gursul-2004c). This is also evidenced by the comparison of wind and water tunnel PIV measurements, as shown in Figure 3.4 (Vardaki *et al.*-2005). Since good agreement is reached between wind and water tunnel experiments, it is reasonable to expect water tunnel investigations on a simple flat-plate delta wing configuration to be representative of air, provided the leading edges are sharp.

The measurement uncertainty in locating the vortex breakdown position was approximately 2% of the chord length. This is mainly attributed to the fact that the location of the vortex breakdown was determined based on the author's perception of the location in each case. Thirty images were time (static) or phase (dynamic) averaged and the mean value of the vortex breakdown location was plotted. The variation in the vortex breakdown location within a single case was between 1% and 2% of the chord length, mainly due to the oscillations observed in the breakdown location in the captured videos.

3.4.3 Rolling Mechanism Control

The rolling mechanism used was controlled by a desktop PC with a digital oscilloscope, implemented to provide feedback for the system. The rolling mechanism was calibrated at the beginning of this project, and an equation was generated combining the value of the voltage that had to be inserted in the software (Agilent HP VEE) and the corresponding roll angle. Since the initial calibration was made using a protractor, an error in the measurement of the roll angle was unavoidable and the accuracy is estimated to be in the order of $\pm 0.5°$. Further calibrations of the mechanism took place in the following years, ensuring that it was still functioning according to the initial calibration.

Experience with the rolling mechanism showed that the maximum tested operating frequency was $f_{max} \cong 34\text{Hz}$. Note that the amplitude was small for this frequency.

The frequency was nondimensionalised by multiplying by the chord length, c, and dividing by the freestream velocity, U_∞, hence:

$$f_r = \frac{f \cdot c}{U_\infty}$$

3.4.4 PIV

There are many potential sources of errors associated with the DPIV measurements. However, most of them can be reduced or even eliminated by optimisation of the experimental set up. These include the particle size, the amount of seeding particles in the flow, the size of the interrogation window compared to the magnitude of the local velocity values, the number of pairs of particles in the interrogation window and computational errors. The mean-bias and rms errors are another two major errors arising from the implementation of the cross-correlation technique. A large amount of literature has been devoted to quantifying and reducing these errors. The reader can find useful information and details of techniques applied for the elimination of these errors in publications from Willert and Gharib (1991), Huang *et al.* (1997), Nogueira *et al.* (1997) and Hart (1998).

Insufficient seeding was found to be one of the major sources of error, and was furthermore a difficult task to accomplish during the set up process. An optimum number of particles per interrogation window was required (three seeding pairs per window). The spatial resolution was considerably improved by the choice of the proper seeding density in the flow. Another source of error, which is enhanced by poor seeding density in the flow, derives from differences between the true displacement and the measured one. The average displacement vector obtained within the sampling region is only unbiased if there is no velocity gradient present. In all other cases the error will increase and only a higher seeding density will reduce it. This phenomenon is highly noticeable when derivative quantities, such as vorticity, are computed from the displacement data (Willert and Gharib-1991).

The size of the seeding particles could be another potential source of problems and error in the data collected from a PIV. Seeding particles have to ensure acceptable flow tracking, i.e. they need to be small enough to follow the flow. In liquid flows, perfect tracking is considered to be provided when the particle to fluid density ratio is one (Melling-1997). In the present study the flow was seeded with spherical hollow glass particles of mean diameter of 8-12 μm, provided by TSI Inc.

In vortical flows, it can be quite difficult to get velocity measurements near the vortex core or near the wing surface. High centrifugal velocities tend to displace the particles and eventually reduce the seeding density in the core. Reflections from the wing surface, particularly in crossflow measurements, where direct contact of the laser beam and the model is involved, can interfere and make the collection of reliable data a tenuous task. This results in areas with spurious velocity vectors, which are ultimately removed by a validation algorithm, leaving no velocities to be

calculated, and consequently using the surrounding velocity vectors in order to interpolate the field. An additional source of error is created in the vector field, as there will be a certain number of miscalculated vectors. This can be significantly reduced by careful preparation of the model (use of matt paint) and appropriate illumination of the desired field.

In the present investigation, laser light reflecting from the wing surface was a particular problem, as crossflow measurements were undertaken. The areas close to the wing surface have been masked and velocities have been interpolated, where necessary. Fortunately enough, there was no need to interpolate any velocity vectors near the vortices, and even the interpolated areas did not affect the overall quality of the results, given that emphasis was placed on the vortical flow and the immediately surrounding area. The region near the wing is of secondary interest, and masking of this area proved a good tool to avoid any spurious vectors.

An estimation of the uncertainty associated with PIV measurements may be expected to be of the order of 1-5%.

3.4.5 Flow Quantities

As mentioned earlier, there is an inherent error associated with the calculation of vorticity given that it relies on the differentiation of velocity. Any errors in the velocity field will propagate and get magnified in the vorticity calculation, resulting in a field with considerable amount of noise. The averaged vorticity fields presented in this document were the result of 30 instantaneous velocity fields. No further information was extracted from the vorticity fields. Circulation was used with more confidence as the velocity fields were directly used to calculate it.

The value of circulation increased with the increasing size of the rectangle used as an integration area, until it reached a plateau. Further increase in the size of the rectangle resulted in no significant change in the value of the circulation. However, by increasing the width of the rectangle the opposite vortex was included in the calculation which resulted in a decrease in the value of circulation. Therefore, the size of the integration rectangle proved to be critical in certifying the accurate calculation of the circulation.

3.4.6 LDV

The LDV is an extremely accurate measurement system, although the precision is limited by the type of seeding and background noise. It has been noted that measurements taken very close to the wing surface were extremely difficult due to the low data rate. Poor quality seeding was easily identified upon examination of real-time LDV signals, which appeared clipped and discontinuous. Increasing the density of the seeding particles was not always the ultimate solution, as errors in the PhotoMultiplier Tube (PMT) voltage saturation appeared. This indicated saturation due to the amount of light reflected from the particles. Consequently, high voltage

values are obtained, which had to be clamped to some value lower than the requested. Careful consideration of the seeding quantity in connection with the appropriate operating voltages and LDV settings, provided high quality data. Details on how the seeding properties, such as size or different material properties, can significantly affect LDV measurements, are provided by Algieri *et al.* (2005), and confirm the fact that seeding is a fundamental requisite for measurement accuracy. The size of the particles also affects precision, as they have to be small enough to follow the flow and at the same time have the ability to scatter light, and thus produce a good signal to noise ratio. This, however, poses a problem, as larger particles scatter more light, but do not necessarily follow the fluid flow, thus generating non-negligible errors. In the present investigation, both LDV and PIV experiments were undertaken using the same seeding particles, which provided satisfactory and accurate measurements.

The decision for the appropriate lens to be used in the LDV system was based on the measurement volume required for the experiments. A lens with a focal length of 500mm and beam separation of 50mm was found to be adequate to provide a suitable measurement volume with a length of 2.6mm and a diameter of 128μm.

The LDV setup was also used to measure the freestream velocity in the water tunnel, and an excellent agreement between the velocity measured and the calibration graph was found.

3.5 Figures Chapter 3

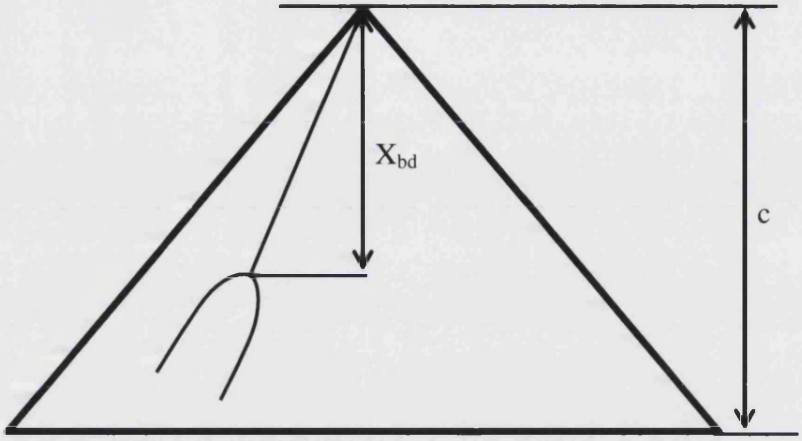

Figure 3.1: Schematic of calculation of the vortex breakdown location.

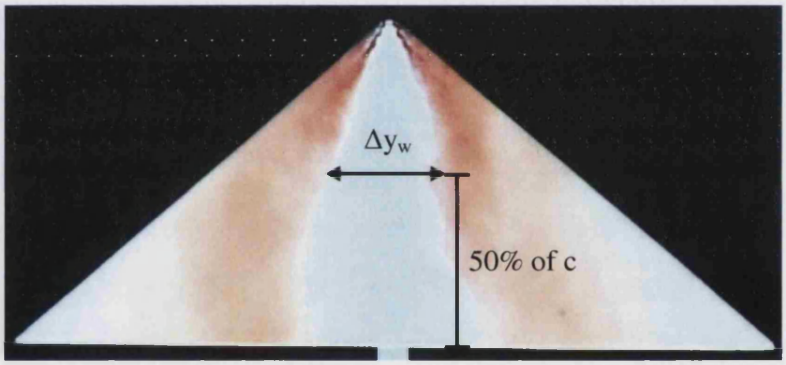

Figure 3.2: Explanation of the measurement of the wake distance, Δy_w, on a $\Lambda = 40°$ delta wing.

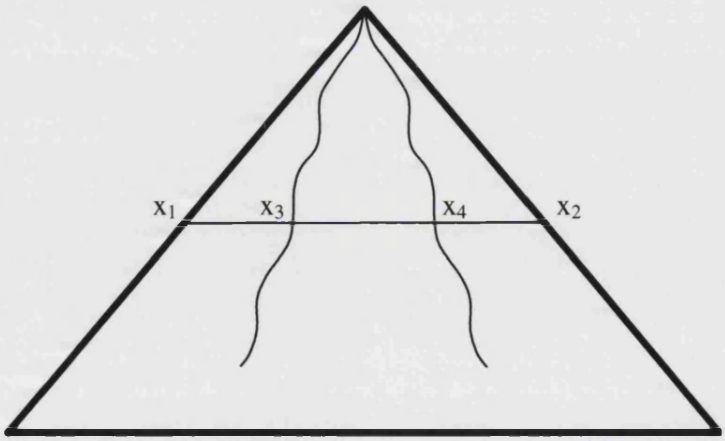

Figure 3.3: Schematic of calculation of the distance between wakes.

ν	ρ_∞ [kg/m^3]	U_∞ [m/s]	s [m]	E [N/m^2]	t [m]	λ
Polyester						
0.31	1000	0.3	0.075	$0.28\text{x}10^{10}$	$0.191\text{x}10^{-3}$	21.3
0.31	1000	0.3	0.075	$0.28\text{x}10^{10}$	$0.254\text{x}10^{-3}$	9.0
Polypropylene						
0.35	1000	0.3	0.075	$0.13\text{x}10^{10}$	$0.381\text{x}10^{-3}$	5.6
0.35	1000	0.3	0.075	$0.13\text{x}10^{10}$	$0.508\text{x}10^{-3}$	2.3
Aluminium						
0.33	1000	0.3	0.075	$7.31\text{x}10^{10}$	$2.000\text{x}10^{-3}$	0.0

Table 3.1: Material properties and spanwise bending flexibility for the flexible and rigid wings.

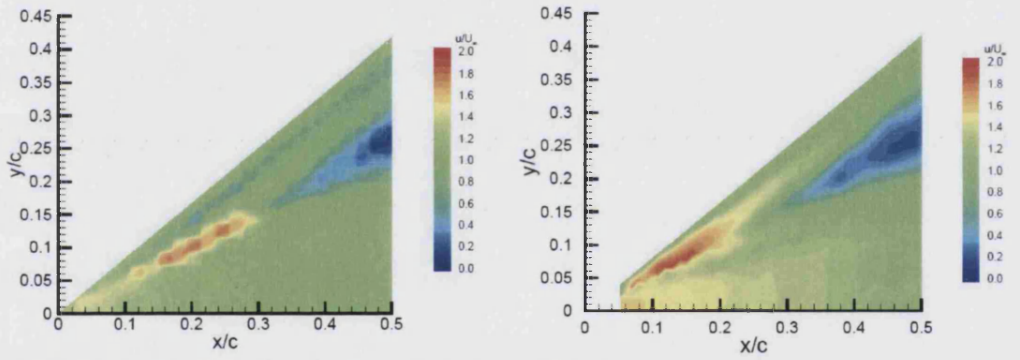

(a) Re_c = 26,000, water-tunnel experiments. (b) Re_c = 620,000, wind-tunnel experiments.

Figure 3.4: Contours of magnitude of time-averaged velocity in a plane through the vortex core in (a) water tunnel; and (b) wind tunnel experiments, $\alpha = 15°$ (Vardaki e*t al.*-2005).

CHAPTER 4: FLEXIBLE NONSLENDER DELTA WINGS

4.1 Introduction

The aim of this chapter is to describe the effect of flexibility on the flowfield over a delta wing in static testing, which was initially inspired by the encouraging results previously obtained by Taylor (Taylor and Gursul-2004a and Taylor *et al.*-2005). Force measurements in a wind tunnel over a range of nonslender delta wings demonstrated the ability of a flexible wing to enhance the lift and delay stall compared to a rigid wing with similar geometry (Taylor *et al.*-2005; also see Chapter 1). This brought about the possibility for experimentation in the water tunnel $(\mathrm{Re} = 26{,}600)$ using a $\Lambda = 50°$ wing. One rigid and four flexible nonslender wings, with different but sequentially increasing flexibilities and thicknesses were tested, using the PIV setup and dye flow visualisation techniques. The results obtained were analysed and compared, and are discussed in this chapter. Note that all the results presented in this chapter are stationary measurements taken at roll angle, $\phi = 0°$ and at a freestream velocity, $U_\infty = 0.3\,\mathrm{m/s}$, corresponding to Re based on the chord length of the $\Lambda = 50°$ delta wing, $\mathrm{Re} = 26{,}600$.

The effect of flexibility on a $\Lambda = 50°$ wing at low/moderate angles of attack $(\alpha = 15°$ and $\alpha = 20°)$ is initially described and then focus is moved to higher angles of attack $(\alpha = 25°)$, where the post-stall regime is encountered.

4.2 Effect of Flexibility at Low/Moderate Incidences

Figure 4.1 shows images captured from videos for the rigid wing and all the flexible wings tested, at $\alpha = 15°$. As seen from these images, the flow is still attached and the vortices have a distinctive appearance on the wing surface, for both the rigid and the flexible wings. Flexibility does not drastically change the flowfield, but rather

introduces some new characteristics. Clear vortical structures can be discerned in each flexible wing, starting from the least flexible $(\lambda = 2.3)$ moving to the most flexible one $(\lambda = 21.3)$. A small variation in the vortex breakdown location is noticeable, with a delay in its location followed by the increasing flexibility. A beneficial effect of flexibility is introduced in this incidence, but the effect is nonetheless minor.

The same information is enhanced and supported by Figures 4.2 and 4.3. Documentation of the crossflow vorticity and velocity fields was undertaken at $x/c = 0.8$. Figure 4.2 and 4.3 show the time-averaged crossflow vorticity and velocity field respectively. Although the streamwise vortices have already broken down at the station where the PIV measurements were taken, a small increase in the vorticity magnitude is observed in favour of the most flexible wing. Additionally, as flexibility increases, the velocity magnitude in the area close to the centreline of the wing is enhanced and a larger region of reattachment is visible (Figure 4.3).

In an effort to get a better understanding of the source of changes introduced to the flowfield it was proved necessary to consult findings of previous work and combine the results found with those from the present study. The large time-averaged structural deflections, which produce a spanwise camber, have been shown to be unlikely to enhance lift significantly. In a series of force measurement experiments on a rigid, a flexible, and a rigid wing with a spanwise camber resembling the time-averaged deflection of flexible wings, it was seen that the curved wing does not exhibit any lift enhancement (Taylor and Gursul-2004a). On the contrary, at $\alpha = 15°$, the rigid wing exhibited higher lift than the curved wing, $C_L = 0.89$ versus $C_L = 0.87$ respectively. The flexible wing exhibited a slight increase in lift compared to the rigid one, and consequently the highest of the three wings tested, $C_L = 0.90$. However, a study on the effect of dihedral applied to highly swept delta wings (Traub-2000a) showed an overall decrease in the lift coefficient. It is reasonable to say that based on Figure 4.1, 4.2 and 4.3 and on previous studies on nonslender delta wings (Taylor and Gursul-2004a, and Taylor *et al.*-2005) the effect of dihedral is negligible for nonslender delta wings at low incidences, when leading edge vortices still exist over the wing surface.

At $\alpha = 20°$ the vortices on the rigid wing have already broken down at the apex of the wing, so there are no visible vortices on the wing surface (Figure 4.4). Note that the flow has not stalled yet at 20°[1] for the rigid wing and a reattachment region is visible. However, on the flexible wings there are clear vortical structures and the increasing flexibility enhances the reformation of the vortices. The dye-free region near the wing centreline is much broader for the flexible wings, indicating earlier reattachment of the separated flow. In the least flexible wing $(\lambda = 2.3)$ there are no apparent vortical structures, but reattachment of the separated flow is obvious. For the following wings, clear vortices appear. For the most flexible wing $(\lambda = 21.3)$ it is

[1] According to force measurements (Taylor and Gursul-2004a) a $\Lambda = 50°$ rigid delta wing stalls at $\alpha_{stall} = 21°$.

interesting that the reformation of the leading edge vortex and rapid breakdown are visible in a region very close to the wing apex. The flow visualisation photos are good enough to provide qualitative evidence of the extremely beneficial effect that flexibility has over a rigid delta wing flowfield at $\alpha = 20°$, which is not completely stalled but for which there is no sign of vortical structure.

Additional PIV vorticity and velocity measurements in a crossflow plane (Figures 4.5 and 4.6, respectively) provide information on the flow and the changes encountered in the presence of flexibility. The low levels of diffused vorticity that are present in the rigid wing, are now being replaced by higher levels in the flexible wings. Note the significantly higher vorticity concentrations in the area close to the centreline of the wing (Figure 4.5) and the higher velocity magnitude in the area between the two broken down vortices (Figure 4.6) as the flexibility increases, indicating earlier reattachment of the flow. In conclusion, the flowfield over a rigid delta wing at an incidence of 20° bears no signs of clear vortices although there is evidence of reattached flow. On the other hand, flexibility is acting favourably towards the reformation of the vortices and promotes earlier reattachment at the same incidence.

4.3 Effect of Flexibility in the Post-stall Region

Figure 4.7 shows flow visualisation images at $\alpha = 25°$ for the rigid and two most flexible wings. On the rigid wing, the flow is completely stalled and there are clearly no signs of vortices. The presence of flexibility slightly changes the flowfield, and a very small, but quite distinct, dye-free region appears, indicating signs of potentially reattached flow. Figure 4.8 shows the time-averaged vorticity contour plots for rigid and flexible wings at an incidence of 25°. Figure 4.9 depicts the vectors and contours of magnitude of time-averaged velocity in a crossflow plane at $x/c = 0.8$ and at $\alpha = 25°$. For the rigid wing, there is no reattachment, however, for the flexible wings, there are larger velocities near the centreline and reattachment in the time-averaged sense.

Although the effect that flexibility had at $\alpha = 20°$ was greater compared to this case, it should be emphasized that changes in the $\alpha = 25°$ flowfield did occur due to the presence of flexibility. Furthermore from the measurements taken, it is obvious that there is a strong fluid structure interaction, but what is not clear is if it is the static spanwise deflection or the leading-edge vibrations that promote reattachment in the flowfield. It has been proved (Taylor and Gursul-2004a) that it is not the actual static deformation that promotes reattachment of the flowfield, but the self-excited wing vibrations. The same assumption can be drawn from the measurements in the post-stall region obtained in this chapter. A similar response to that observed at lower incidences in the presence of flexibility would be expected. Further experimental results, presented in the following chapters, will provide insight and additional information on this phenomenon.

It has been shown that the formation of vortices over a rigid nonslender delta wing strongly depends on the angle of attack and an additional study was made of the effect of flexibility in these incidences. There are three completely different flow regimes on a rigid wing: (i) vortex breakdown over the wing, (ii) vortex breakdown at the apex, but flow reattachment to the wing surface, and (iii) complete stall. Complete reformation of the vortices can possibly take place in the presence of flexibility. For the first regime, flexibility acts to delay the breakdown location, thus moving it closer to the trailing edge. When the breakdown is at the apex of the wing the presence of flexibility enables the vortex reformation, promotes earlier reattachment and breakdown takes place on the surface of the wing. Although vortex reformation does not take place on a completely stalled flow, evidence of reattachment was obtained in the presence of flexibility. In general, the beneficial effect of flexibility, appearing with different patterns on the flowfield depending on the angle of attack, was identified and needs to be underlined.

4.4 Circulation

From the PIV measurements obtained, circulation was calculated as an integral of the velocity measured, and the results over different spanwise bending flexibility, λ are presented in Figure 4.10. A conclusive graph, for all three incidences tested and both flexible and rigid wings, of the magnitude of circulation is the best way to give an overall view to the reader of the effect of flexibility on static measurements. Although velocity and vorticity contour plots provide a good insight into the flowfield, circulation is an integral quantity, providing a better way of quantifying the flow and additionally giving information on the strength of the vortices.

In general, the magnitude of circulation has been shown to increase with flexibility, providing evidence that the vortices increase their strength with increasing flexibility. Interestingly enough, the most flexible wing appears to have the highest values of circulation compared to the other wings in all three incidences. Furthermore, note that at $\alpha = 25°$, the most flexible wing appears to have the highest circulation, indicating the beneficial character of flexibility in the post-stall region and the promotion of an earlier reattachment of the flow. This can also provide supporting evidence for the lift enhancement phenomenon observed due to flexibility in the post-stall region documented by Taylor and Gursul (2004a). According to the present measurements, the gradual increase in the flexibility in the post-stall region, results in a corresponding increase in circulation.

Another observation worth mentioning, is that at the incidences where the vortices still exist over the wing, or where breakdown occurs at the apex ($\alpha = 15°$ and $\alpha = 20°$), the least flexible wing exhibits approximately the same circulation as the most flexible. This may be attributed to the fact that it is not the curvature of the wing that is responsible for lift enhancement (Taylor and Gursul-2004a), but another mechanism that lies behind it. More information is provided in the chapters that follow. A general decrease in the circulation is observed from $\alpha = 20°$ to $\alpha = 15°$, which can be attributed to the fact that although at $\alpha = 15°$ the vortices still exist

over the wing, at $\alpha = 20°$, where breakdown occurs at the apex, the flexibility introduces a more beneficial effect on the flowfield, hence increasing circulation. Circulation has the lowest average value in the graph at $\alpha = 25°$, compared to the other two incidences, which is expected since stalled flow is followed by lower velocity values. However, increasing the flexibility of the wing increases the circulation even in the post-stall region. Taking an overall look at the flow visualisation, the velocity and the vorticity images for all three incidences, it can be seen that the incidence where flexibility had the biggest effect is $\alpha = 20°$. This can also justify the highest average value in the circulation measurements at $\alpha = 20°$.

4.5 Figures Chapter 4

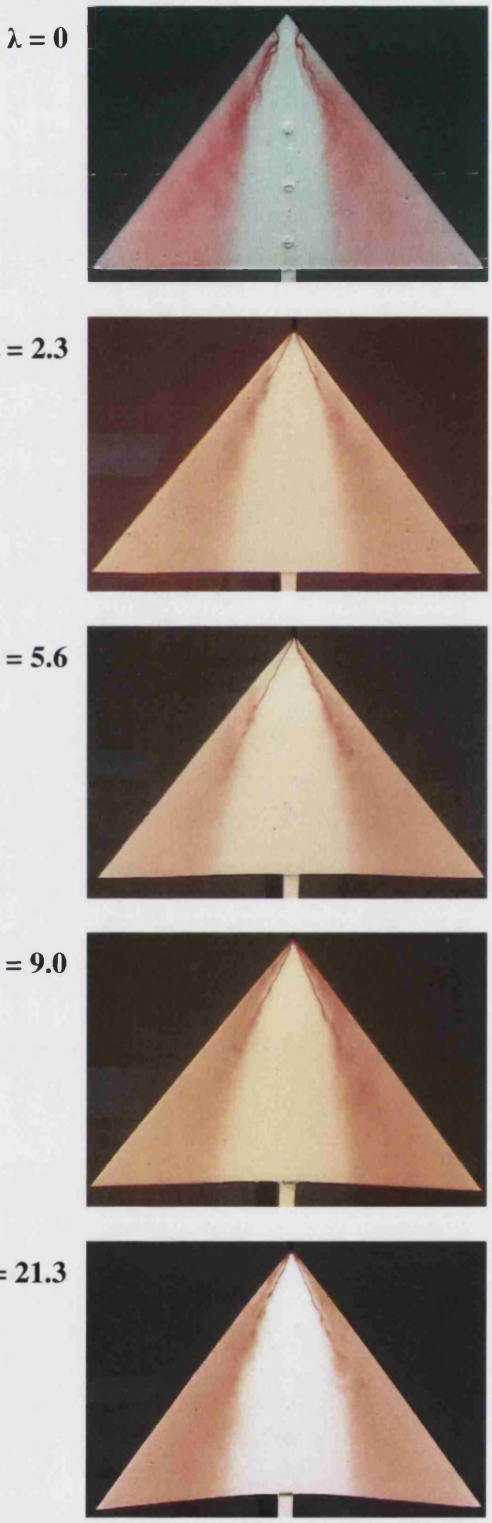

Figure 4.1: Effect of spanwise flexibility, λ, on $\Lambda = 50°$ delta wings at $\alpha = 15°$.

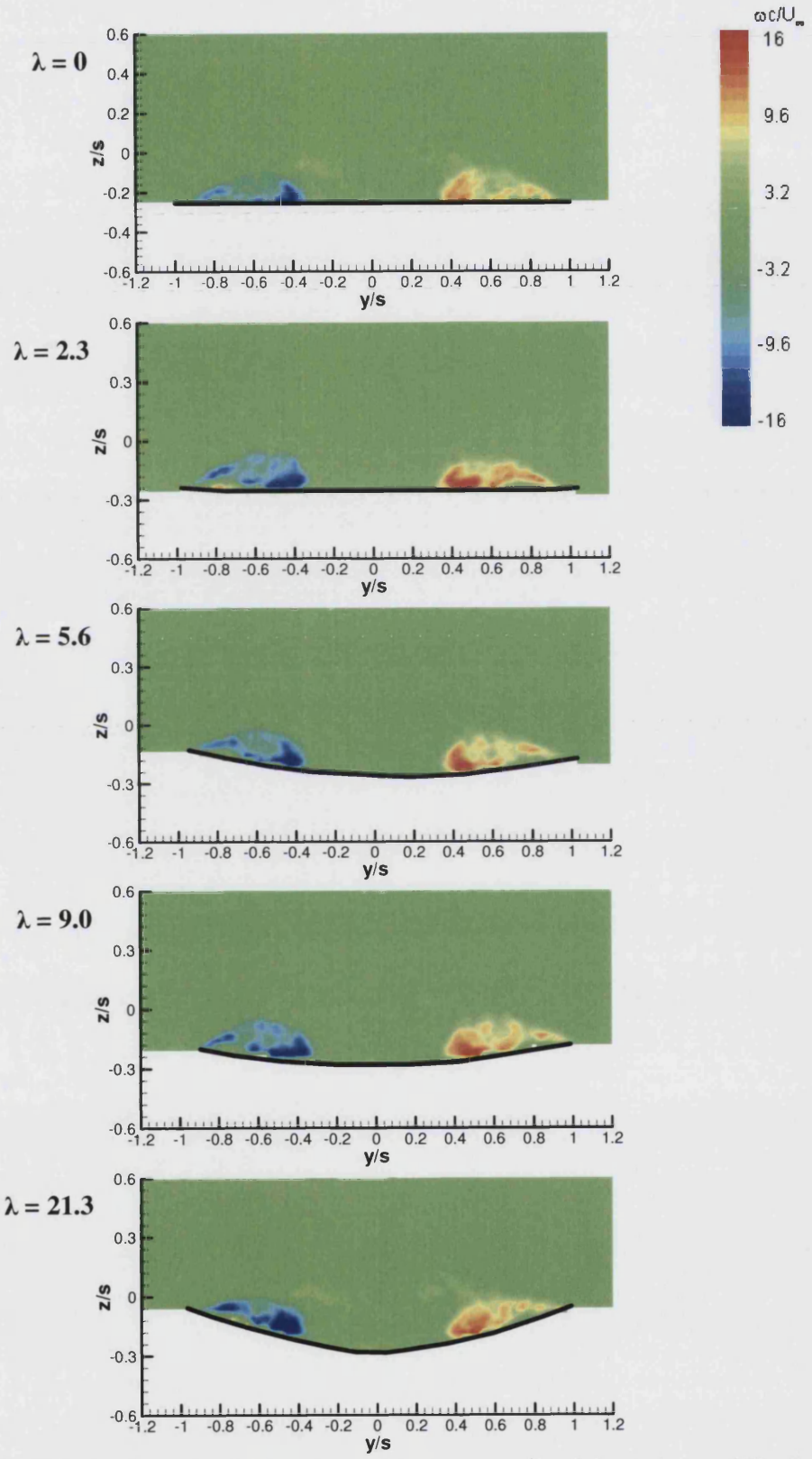

Figure 4.2: Cross flow vorticity measurements at $x/c = 0.8$ and $\alpha = 15°$ for different spanwise flexibility.

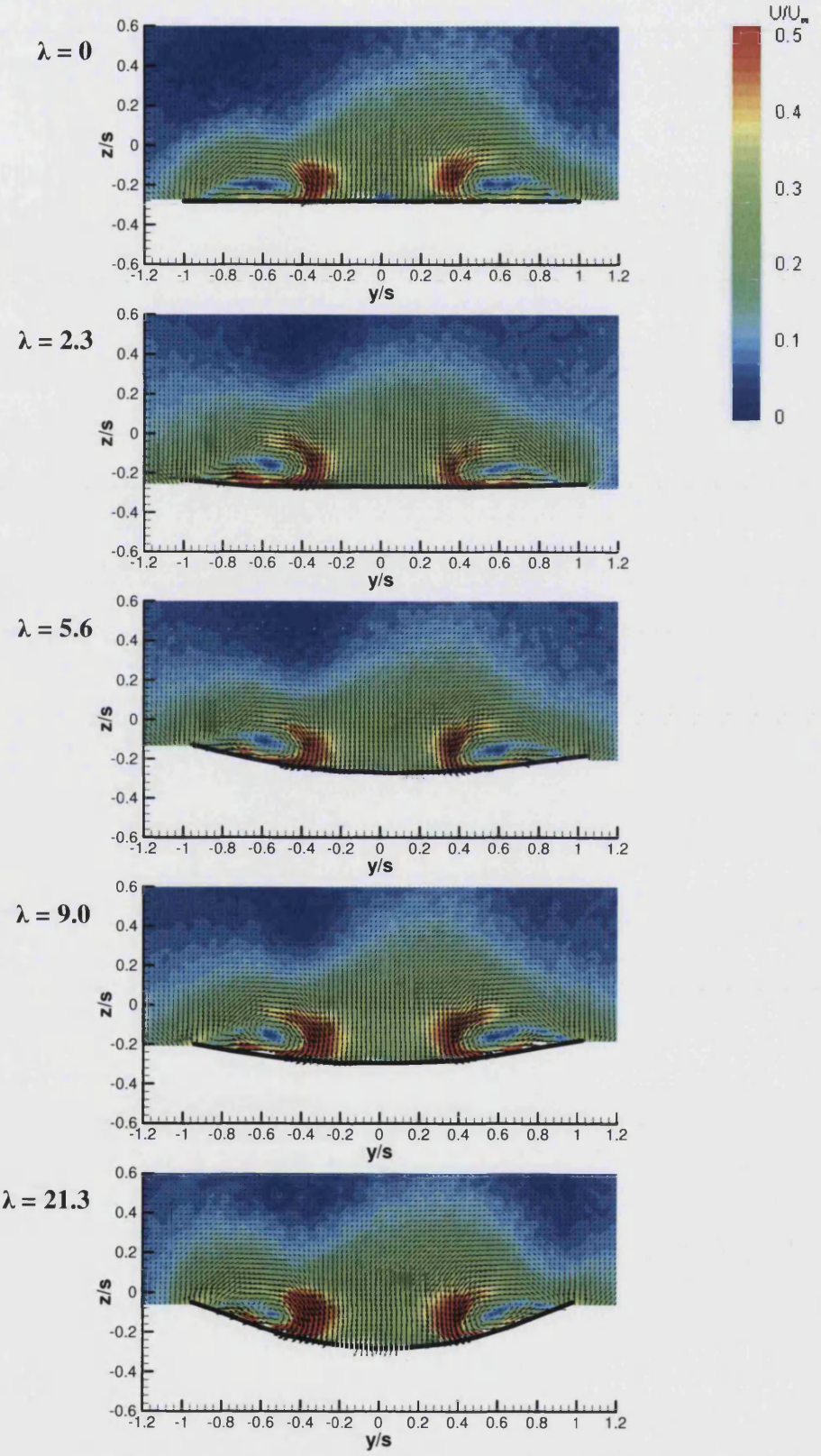

Figure 4.3: Cross flow velocity measurements at $x/c = 0.8$ and $\alpha = 15°$ for different spanwise flexibility.

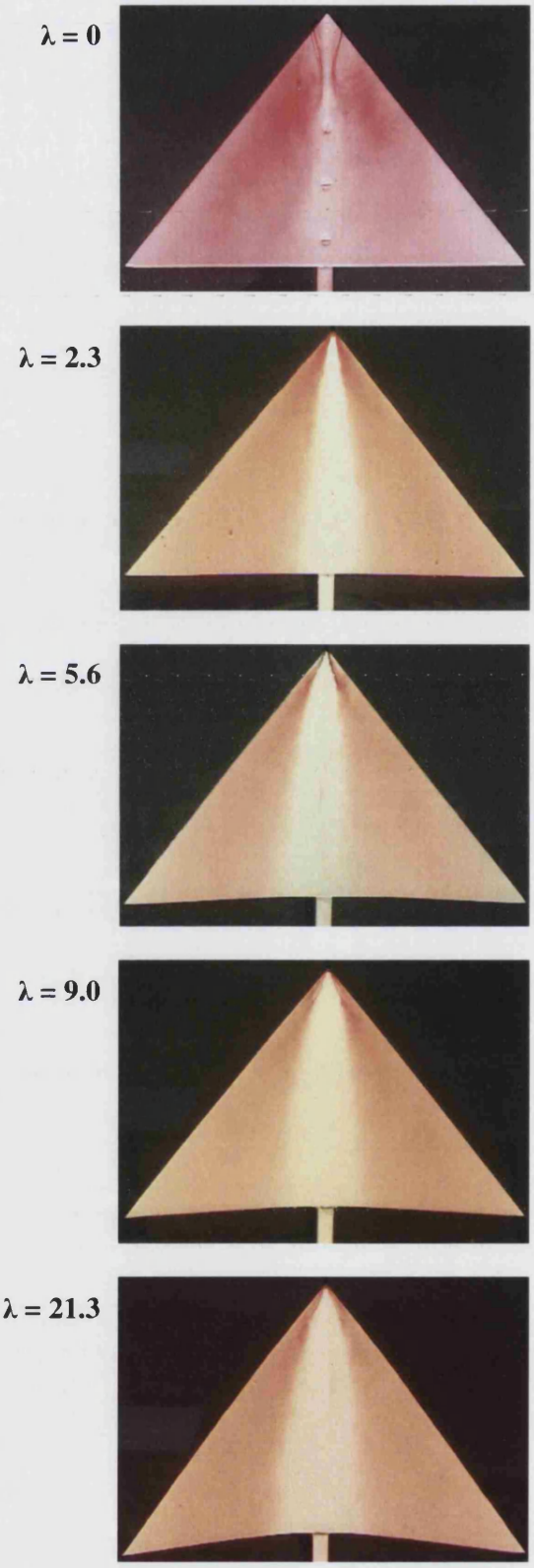

Figure 4.4: Effect of spanwise flexibility, λ, on $\Lambda = 50°$ delta wings at $\alpha = 20°$.

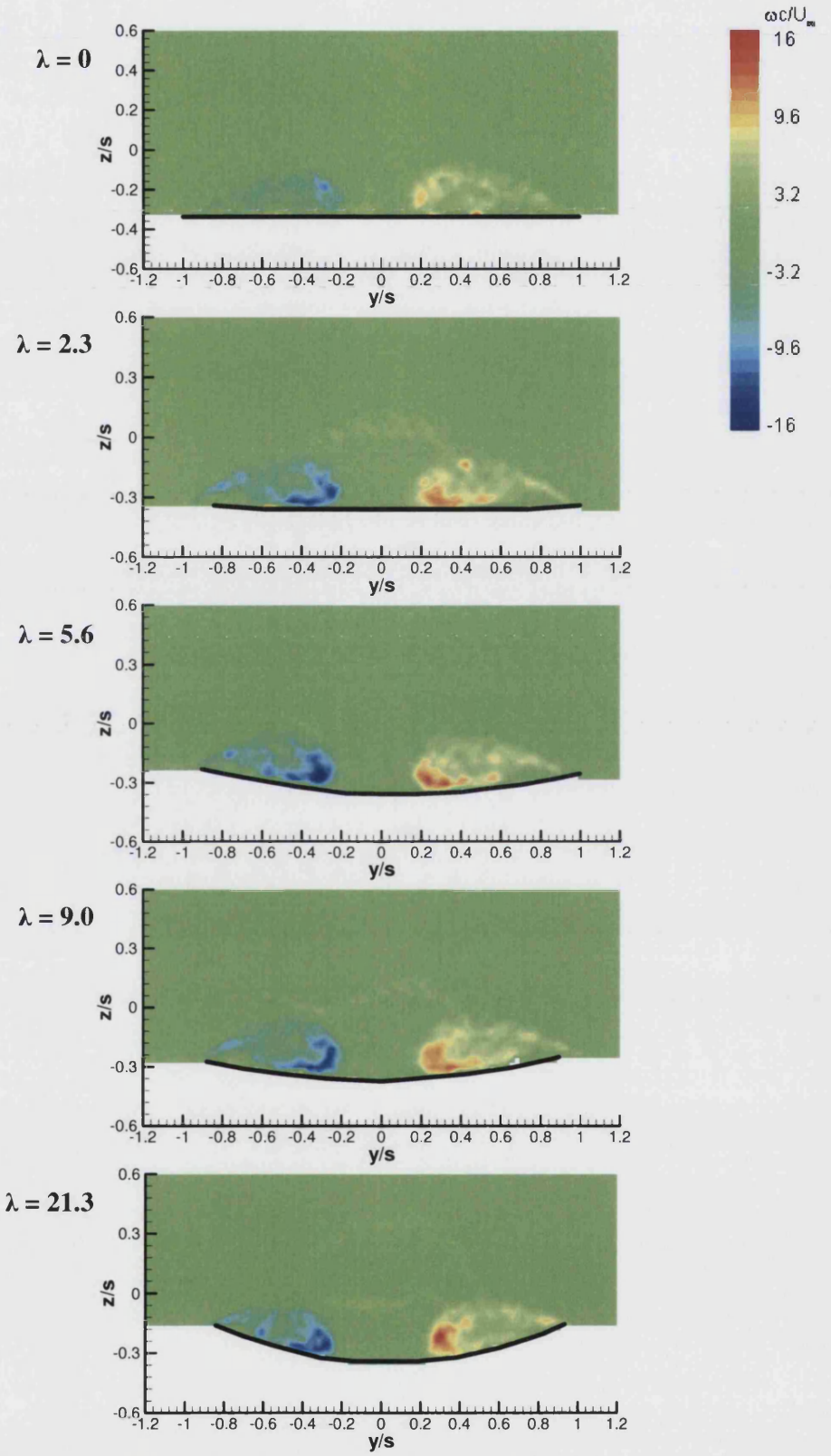

Figure 4.5: Cross flow vorticity measurements at $x/c = 0.8$ and $\alpha = 20°$ for different spanwise flexibility.

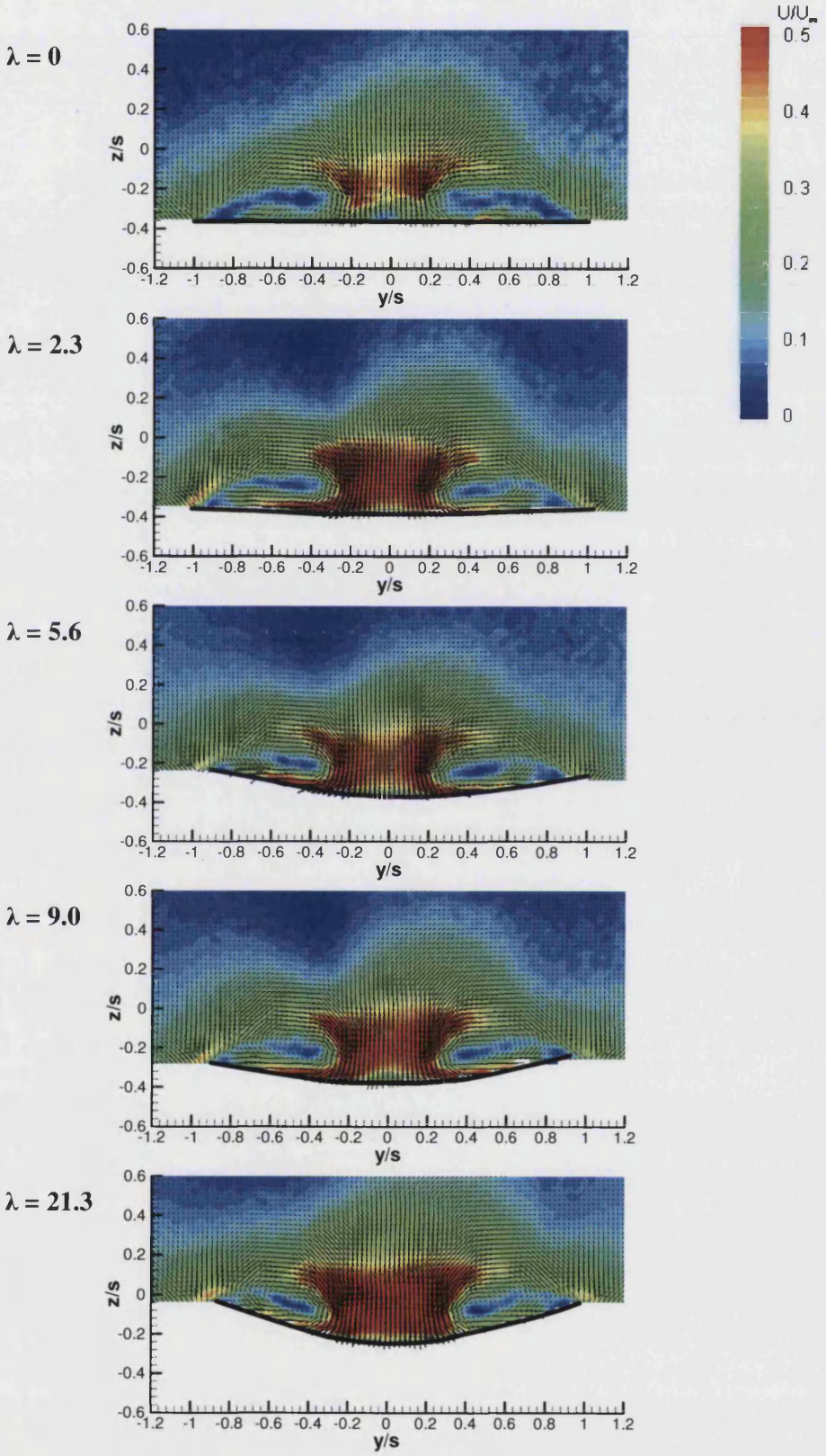

Figure 4.6: Cross flow velocity measurements at $x/c = 0.8$ and $\alpha = 20°$ for different spanwise flexibility.

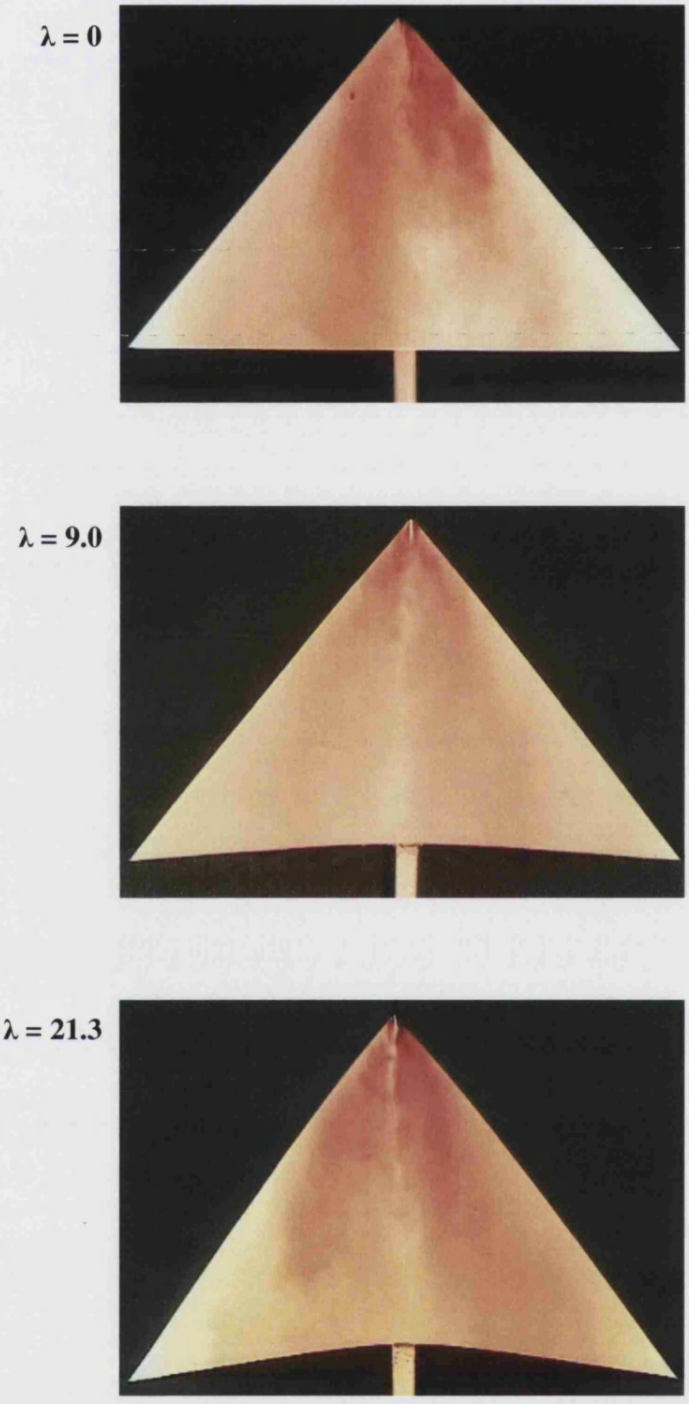

Figure 4.7: Effect of spanwise flexibility, λ, on $\Lambda = 50°$ delta wings at $\alpha = 25°$.

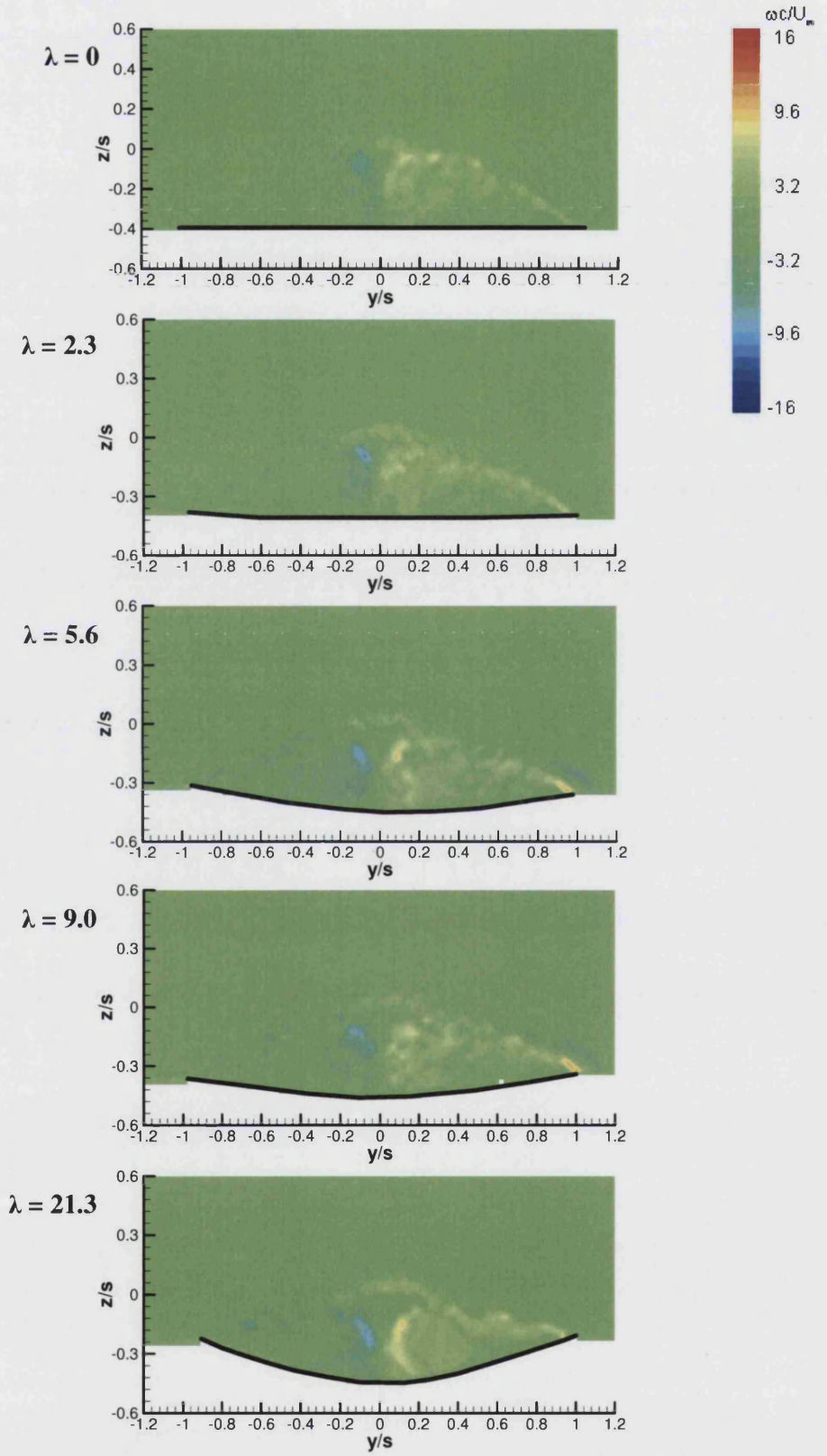

Figure 4.8: Cross flow vorticity measurements at $x/c = 0.8$ and $\alpha = 25°$ for different spanwise flexibility.

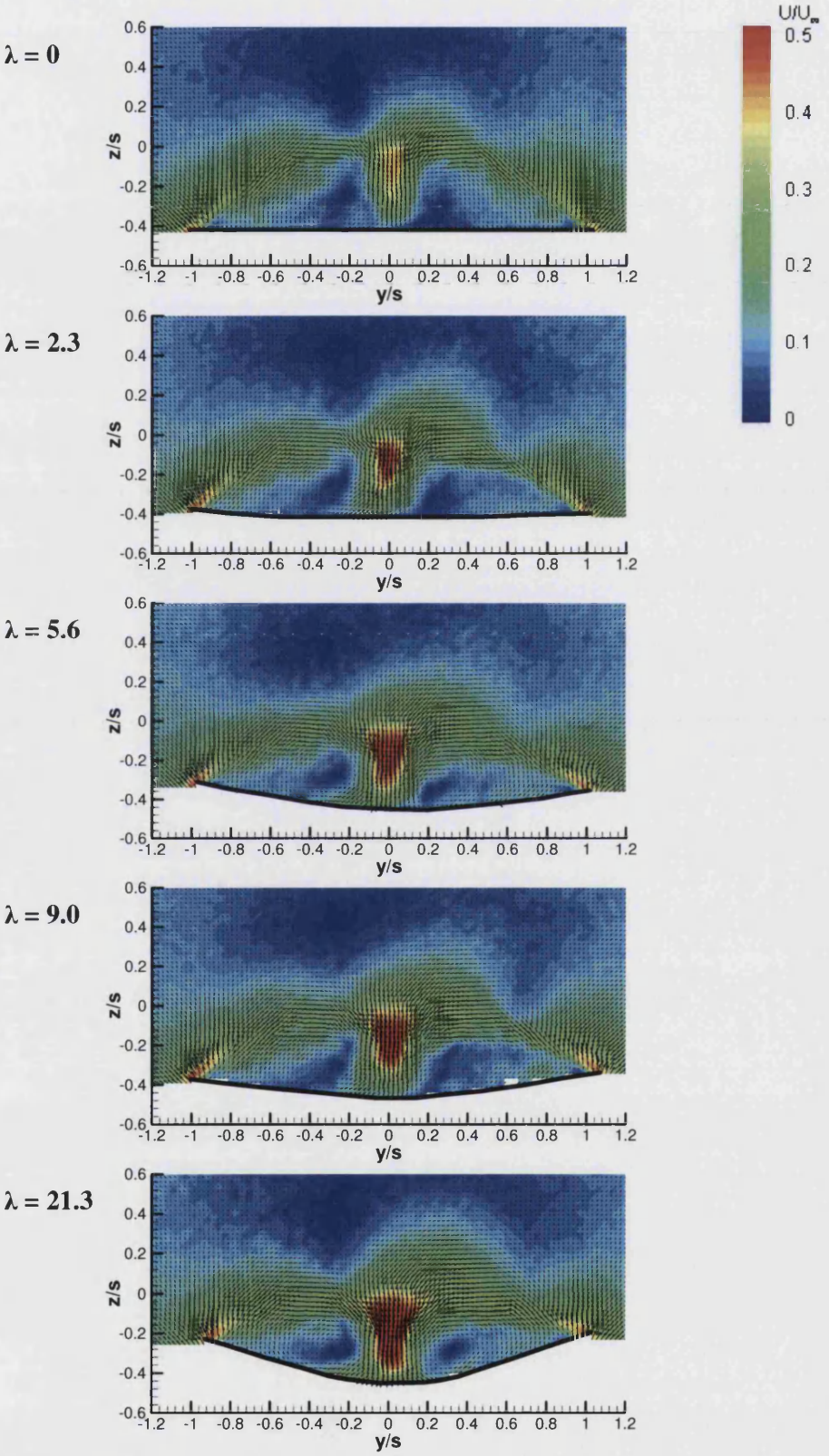

Figure 4.9: Cross flow velocity measurements at $x/c = 0.8$ and $\alpha = 25°$ for different spanwise flexibility.

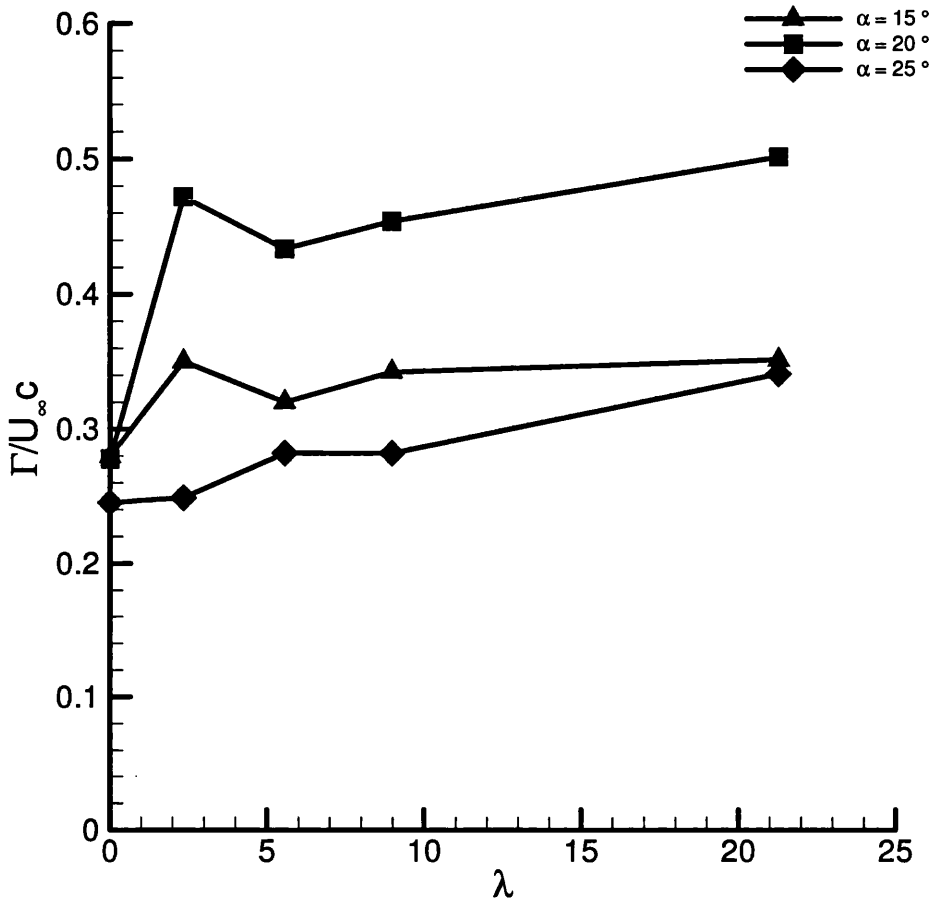

Figure 4.10: Variation of normalised circulation with wing spanwise flexibility, for different incidences.

CHAPTER 5: SMALL AMPLITUDE OSCILLATIONS OF NONSLENDER DELTA WINGS

5.1 Introduction

The findings obtained on the flexible delta wings, presented previously, served as a motivation for the experimental results presented in this chapter. These results, in combination with experiments undertaken by Taylor and Gursul (2004a) in the wind tunnel on a 50° flexible, rigid and curved delta wing, proved that the lift enhancement is produced by a form of self-induced vibration, as opposed to the static deflection of the wing. In order to simulate the effect of antisymmetric vibrations, and shed more light on previous findings, experiments with a rigid wing undergoing small amplitude rolling oscillations were conducted. These results will be presented and discussed in the following pages. This approach has the advantage of independent control of the frequency parameter, which cannot be varied for a flexible wing, without affecting the amplitude of vibrations. Moreover, this antisymmetric motion has also been seen as an active control method for lift enhancement in the post-stall region. Since all the flexible wings had a sweep angle of 50°, the same sweep angle was chosen for the rigid wing.

This chapter describes the results obtained from a 50° delta wing undergoing small amplitude oscillatory motions. The range of frequencies tested varied from $f_r = 0$ to 10 and the amplitudes ranged from 0° to 5°. Food dye and laser induced fluorescent dye flow visualisations, along with PIV and LDV measurements were used in order to describe the effect the oscillatory motion has on the flowfield. These results are discussed, and based on the experimental data, further calculations of flow quantities were performed. The comparison between stationary and oscillatory testing provided sufficient information on the flowfield and on the influence of the rolling motion. Interest was focussed on the post-stall region, where the biggest changes in the flowfield took place and since this was the area where the maximum lift

enhancement was previously observed (Taylor and Gursul-2004a). Moreover this is the region in which lift enhancement appears to play an important role.

All measurements were taken using a rigid 50° sweep angle delta wing, at a freestream velocity, $U_\infty = 30\text{cm/s}$, corresponding to Re based on the chord length of the wing of 26,600.

5.2 Effect of Small Amplitude Oscillations

5.2.1 Introduction

Focus has been given to the effect that small amplitude oscillations have on the flowfield over a nonslender delta wing. This investigation has been undertaken using laser induced and dye flow visualisation techniques, along with PIV and LDV measurements. Since the whole chapter is dedicated to the effect of small amplitude oscillations, the sections that follow are divided according to the equipment used to obtain the measurements.

5.2.2 Laser Induced Flow Visualisation

Figure 5.1 shows laser induced flow visualisation images of the 50° delta wing in stationary mode and undergoing a small amplitude oscillatory motion $(\Delta\phi = 1°)$, for two different incidences $(\alpha = 15°$ and $20°)$. The top half of the figure presents instantaneous cases, corresponding to both the stationary and the oscillatory case, at $x/c = 0.8$. As the dye was released from the leading edge, the vorticity shed through separation was "marked". The objective was to visualise the shear layer structures as clearly as possible. At this station the vortices have already broken down, as seen in Figure 4.1. However, small vortical substructures can be clearly seen on both sides of the wing. This has also been confirmed by previous studies (Gad-el-Hak and Blackwelder-1985). As the dye emanates from the leading edge, vortical substructures appear and rotate, as seen from the videos captured. Although at $\alpha = 15°$, in the stationary case, there is evidence of a reattachment region (a region that has no dye) and the flow is completely attached to the wing surface, there is still an effect attributed to the oscillatory motion. As seen in the image, in which a small amplitude forcing frequency is applied, the distance between the wakes of the two vortices increases, indicating earlier reattachment of the flow. Given that the flow is still attached and the vortices are still the main source of lift generation on the wing, the effect of the oscillatory motion in this case proves to be beneficial as it does not only maintain the vortices on the wing but it also promotes earlier reattachment of the flow.

On the other hand, considerable differences appear on the flowfield at an incidence of $\alpha = 20°$, as seen in the second set of images (Figure 5.1). In the static case, the reattachment line is barely discernible. Additionally, note that at this incidence, the

vortices break down at the apex. However, the vortical substructures appear consistent and very well organised. The implementation of a small amplitude oscillatory motion has a dramatic effect on the flowfield. Reattachment of the separated flow is evident and the almost stalled flow presented in the static case is now being replaced by fully attached flow, baring a close resemblance to that at $\alpha = 15°$. In this case the oscillatory motion has a strong effect on the flowfield by promoting earlier reattachment.

A time average of 10 instantaneous images (bottom half of Figure 5.1) is also presented, giving a more diffused effect to the flowfield. Although the small-scale structures cannot be seen in this case, and a lot of detail is lost due to the superimposition of the images, a time averaged character is given to the flowfield, providing a different perspective to it. It is clear from both the instantaneous and the time averaged measurements that the oscillatory motion is responsible for the significant and favourable effect on the flowfield of a 50° delta wing at $\alpha = 20°$.

A more detailed view of the flowfield is presented in Figure 5.2, where the camera was focused on half of the wing and dye was released only through that side. A magnification of the small-scale structures is provided through the use of these images. Additionally, since only half of the wing is visible in these images it is easier to see the increase in the diffusion of the vortex, compared to a lower incidence. For example at $\alpha = 20°$, the diffused vortex extends almost to the centreline of the wing. A closer look at those images can provide a number of interesting, and at the same time important conclusions. At $\alpha = 15°$ the application of an oscillating motion reduces both the height and the width of the vortex. At $\alpha = 20°$, similar reduction in the width of the vortex is observed, indicating earlier reattachment of the flow, but a small increase in height is also seen. Note that at both incidences, the small-scale structures along the entire length of the shear layer, can clearly be distinguished. The time averaged images present similar characteristics. Reduction in the dimensions of the vortices indicates earlier reattachment of the flow, as well as the creation of more coherent vortical structures. Although the small-scale vortical structures are not discernible in the superimposed images, they provide a time average sense to the flowfield.

So far, the vortices were either still visible on the wing surface $(\alpha = 15°)$, or had already broken down at the apex of the wing $(\alpha = 20°)$. In Figure 5.3, the images presented are recorded at $\alpha = 25°$, where the flow is completely stalled and there are no visible vortices on the wing. A range of different dimensionless frequencies is presented, using the stationary case as a reference point. The shear layer is clearly visible and there are signs of small-scale structures. The dye from the two sides seems to merge a feature previously identified using PIV (see Figures 4.6 and 4.9). The flowfield becomes distinctly different when even a very small forcing frequency $(f_r = 0.5)$ is applied. There are clear indications of separation between the wakes of the two vortices. The contour of the shear layer is clearly visible, and small-scale structures can be seen along it.

With an increase in dimensionless frequency $(f_r = 1)$, there is a clear reattachment of the shear layer, indicated by the dye-free region. The wakes of the two vortices can be identified on the wing surface, although in the stationary case the flow was completely stalled. This form of wing oscillations reenergises the flow and promotes reattachment. Note that wind tunnel measurements showed lift enhancement characteristics in the post stall region of a 50° flexible delta wing, in which self-excited oscillations were observed (Taylor and Gursul-2004a) and were responsible for the lift enhancement. In the present case, the introduction of a small amplitude oscillatory motion in the post stall region is sufficient to significantly alter the flowfield by introducing completely new characteristics to it, such as fully attached flow.

Although increasing the forcing frequency from $f_r = 0.5$ to 1 proved to be extremely beneficial to the flowfield, a further increase in the frequency was shown not to be favourable. In the last set of images, where $f_r = 2$, the dye-free region is reduced and the implementation of the frequency seems to have an adverse effect on the flowfield. Although the reattachment is still evident, there is an indication of potential merging. However, very clear small-scale vortices can be observed, especially in the clockwise vortex. The right side of Figure 5.3 presents the time averaged version of the images obtained by superimposing ten instantaneous images.

It is apparent that the implementation of an oscillatory motion introduces new characteristics to the stalled flowfield, which resemble that of an attached flow. Increasing the reduced frequency enhances those features, although there seems to be an optimum value. In the present case, the frequency at which the earliest reattachment is observed is $f_r = 1$. However, it is not yet safe to assume that this is the optimum value. This frequency is nevertheless in good agreement with wind tunnel experiments (Taylor and Gursul-2004a), where the dominant frequency found was $f_r = 0.75$ for a range of incidences between $\alpha = 24°$ and 28°.

A detailed version of these images follows in Figure 5.4, where only half of the wing is presented, providing a clearer view of the flowfield. The size of the vortex decreases with increasing frequency, and the completely stalled flow is replaced by an attached flow, with coherent vortical structures in it. Note in the last image of this figure, at $f_r = 2$, the well defined vortical structure close to the leading edge.

5.2.3 Laser Doppler Velocimetry (LDV) Measurements

The results presented so far were very encouraging, so further experimentation was deemed necessary in order to verify and complement the existing findings regarding the reattachment of the flow.

LDV measurements were conducted for the 50° delta wing under different conditions. Figure 5.5 shows LDV measurements of the mean and the rms chordwise velocity, U_{mean} and U_{rms}, for a range of dimensionless frequencies starting from the

stationary case and moving up to a reduced frequency 5. The measurements were taken at $\alpha = 25°$ and $x/c = 0.7$, moving away from the wing in the z direction with the first measurement being very close to the wing surface $(z/s = 0.02)$ and the last one at $z/s = 0.5$. The measurement location was placed at the wing centreline $(y/s = 0)$.

In the first graph, where the nondimensionalised mean velocity along the various locations is presented, very low values are observed near the wing surface for the stationary case, which then increase when moving away from the wing. In the last station in which measurements were taken, the mean velocity almost has the same value as the freestream velocity. These results are expected, since the flow is completely stalled at this incidence, $\alpha = 25°$. At a distance $z/s = 0.5$ away from the wing surface, the effect of the wing on the flowfield is minimal, so the velocity values measured are expected to be in the same order of magnitude as the freestream velocity.

The imposition of a small amplitude $(\Delta\phi = 1°)$ oscillatory motion, at $f_r = 0.3$, changes the values in the velocities recorded. The mean velocity measured even close to the wing is approximately three times larger than that recorded for the stationary wing. Additionally, a general increase is seen in the mean velocity values for all the measurement stations, with the last ones slightly exceeding that of the freestream. The same conclusions can be derived from the results for the $f_r = 1$ case, as large mean velocity values are observed compared to the stationary case. An increase in frequency is followed by correspondingly higher mean velocity values. The measurements further away from the wing show values close that of the freestream velocity. Such a profile in the mean velocity measurements is expected since the motion of the leading edge increases the velocity magnitude and promotes reattachment.

Further increase in the dimensionless frequency results in dramatic changes in the mean velocity values. The velocity near the wing surface at $f_r = 2$ is approximately that of the freestream, and very little variation is observed in the other measuring stations. Given the fact that measurements are taken at the wing centreline, and the significantly higher velocity values that follow the implementation of an oscillating motion, it can be concluded that this is due to earlier reattachment. However, there is barely no difference in the velocity values for $f_r = 5$, compared to the $f_r = 2$ case. This provides an interesting insight on the reattachment phenomenon, inasmuch as an optimum frequency can be achieved, after which no significant changes take place. It would be a mistake to make a judgement and propose a value for this frequency from a single graph only. Hence, a discussion will follow in which further results will be analysed. It is nevertheless correct to assert the existence of an optimum frequency value, also identified in the laser induced flow visualisation measurements discussed earlier.

In conclusion, the application of a small amplitude oscillating motion increases the mean velocity values, particularly in the area around the wing surface. Since the

measurements were taken at the wing centreline and at $x/c = 0.7$, the increased values provide a clear indication of earlier flow reattachment. Additionally, an upper limit in the dimensionless frequency after which few changes are observed in the flowfield, is detected. This provides an indication of an optimum f_r. Further discussion on this follows with the presentation of additional results.

The second plot in Figure 5.5 shows the nondimensionalised value of the rms velocity under the same conditions $(\alpha = 25°, x/c = 0.7, y/s = 0$ and $\Delta\phi = 1°)$, for the same reduced frequencies. As mentioned earlier, the rms value gives an indication of the magnitude of fluctuations of the variable around its mean, in this case, of velocity.

In the static case, a considerable variation is noticed. The values increase as the measurements move away from the wing surface, with a peak value at $z/c = 0.33$. After that, a decrease is observed. This is expected, and can be explained by the fact that velocity values away from the wing surface will tend to fluctuate less. Taking into consideration that the flow is completely stalled at this incidence, the increasing values can possibly be attributed to the large instabilities in the shear layer. Furthermore, the peak can be considered as the boundary of the shear layer.

A similar trend in the rms values is observed when using an excitation with a low dimensionless frequency $(f_r = 0.3)$. Although higher values appear, as expected due to the velocities imparted to the flow because of the forcing frequency, there is still a peak, which this time is closer to the wing. This is reasonable, as the oscillatory motion reduces the size of the wake in both the x and z direction, as seen for example in Figure 5.4, and more momentum is added to the flow hence creating higher velocity values. However, increasing the reduced frequency to 1 alters the trend of the graph completely, with the highest value in the rms velocity observed just 1mm away from the wing surface $(z/s = 0.02)$. This can be attributed to potential reattachment of the flow, taking effect at that specific f_r. As seen in Figure 5.4 the flowfield is very well organised at that f_r, with a distinct reattachment region and the appearance of a more coherent vortical structure.

A further increase in the dimensionless frequency $(f_r = 2$ and $5)$ significantly reduces the rms velocity, although the highest values still appear in the area close to the wing surface. There is almost no difference in the values between $f_r = 2$ and $f_r = 5$, again suggesting the possible hypothesis that there might be an optimum frequency, and that there is definitely an upper limit for the forcing frequency, after which no dramatic alteration of the flowfield is observed.

Further LDV experiments were performed at different locations on the flowfield around the wing. In Figure 5.6, the nondimensional mean and the rms value of velocity is presented at $\alpha = 25°$, $x/c = 0.7$ and at $y/s = 0.5$, which is the middle of the local semispan. The oscillating amplitude was set at $\Delta\phi = 1°$, so as to minimise the changes in the flowfield, but at the same time to efficiently simulate

antisymmetric vibrations observed on flexible wings and make comparison with previous LDV results discussed feasible.

Negative velocities can be observed close to the wing, in both the $f_r = 0$ and 0.3 cases, seen in the first plot (Figure 5.6), which shows the mean value of velocity versus the forcing frequency. Since the flow is completely stalled, turbulent and reversed flow is expected inside the wake, along with an approximately constant value of mean velocity until the periphery of the shear layer is reached. Thus, low and even negative velocity values are to be expected inside the actual wake. Interestingly, positive values of mean velocity are only observed after $z/s = 0.33$, which is approximately the boundary of the separated shear layer. Beyond that point, the mean velocity values recorded increase until they approach that of the freestream velocity. At a dimensionless frequency of $f_r = 0.3$, the mean velocity values remain unchanged.

The increase in frequency ($f_r = 1$, 2 and 5), creates considerable changes in the pattern followed by the mean velocity values. The velocities close to the wing surface are not negative. Moving further away from the wing up to $z/s = 0.29$, which approximately corresponds to the boundary of the shear layer, the mean velocity values decrease and become negative. After this point, the mean velocity values become positive and gradually increase to reach that of the freestream velocity. This trend in the mean velocity values is expected. Since the vortices on nonslender wings are created considerably closer to the wing surface compared to slender wings, higher velocities appear closer to the wing surface. However, it can be seen that frequency has little effect on the flowfield when frequencies above $f_r = 1$ are imposed. This confirms the conclusion that an increase in the frequency does not necessarily lead to earlier reattachment. On the contrary, an optimum frequency after which further increase only results in minimal variations in the flowfield is proven.

The second graph in Figure 5.6 shows the rms velocity values for the same location ($x/c = 0.7$ and $y/s = 0.5$) and the same frequencies ($f_r = 0$, 0.3, 1, 2 and 5). For the same reasons explained earlier, $f_r = 0$ and 0.3 do not show any differences in the pattern they follow. Very little variation is observed close to the wing, as expected from the mean velocity measurements, and some changes are only observed outside the shear layer. The implementation of a forcing frequency creates a small increase in the rms values.

Substantial changes are observed when higher frequencies are introduced into the flowfield. Larger variations in the rms values are observed between these curves, but the effect of frequency remains nonetheless unchanged. The above results agree well with the hotwire measurements performed in a wind tunnel for $\Lambda = 50°$ wing, providing information on the spectral features of the flow and their relation to the optimum observed frequencies (Gursul *et al.*-2005, 2006).

Given the indication that there is an optimum frequency, further experimentation was undertaken utilising different amplitudes of oscillation, $\Delta\phi = 1°$, 2.5, and 5, and

maintaining a constant dimensionless frequency, $f_r = 1$. The choice of frequency was based on the results from previous measurements. As discussed earlier, $f_r = 0.3$, proved to have little effect on the flow and results on $f_r = 2$ and 5 were essentially similar to those obtained from $f_r = 1$. Additionally, flow visualisation images at $\alpha = 25°$ (Figure 5.3) proved that the "optimum" frequency is around $f_r = 1$. The objective of these experiments was to see if the effect of the frequency on the flowfield is maintained under different oscillating amplitudes. The results obtained are presented in Figure 5.7, where mean and rms values of velocity are plotted as a function of distance from the wing. Again the reference case is the stationary wing, where $f_r = 0$ and $\Delta\phi = 0°$.

In the first graph, the nondimensional mean velocity values are presented for different amplitudes. As previously seen, the values in the stationary case are negative and relatively low within the wake, whereas positive and high values appear further away from the wing surface. The implementation of a forcing frequency improves the general image of the flowfield by increasing the mean velocity values in the area close to the wing. The effect of the amplitude is noteworthy. Although for a small amplitude, $\Delta\phi = 1°$, there are considerable changes in the mean velocity values compared to the stationary case, it is only at 2.5° and 5° that positive and high values appear. This is to be expected, since a larger amplitude in the oscillatory motion will add more momentum to the flow compared to a smaller one. It is nonetheless remarkable that even small amplitudes are capable of recreating the dramatic effects produced by flexible wings. It is interesting that after $z/s = 0.34$, there is almost no change in the mean velocity values, even for the highest amplitude motion, $\Delta\phi = 5°$. These measurements provide a good insight into the mean velocity profile for a relatively wide area above the wing surface, the shear layer, and the areas surrounding both of these.

In the second graph in Figure 5.7, the rms velocities follow a similar trend, with the largest amplitude case presenting the highest values. The effect of the amplitude is evident. The limited variation seen in the stationary case is now replaced by significant changes, which adjust accordingly with the increasing amplitude. Note that in the $\Delta\phi = 5°$ and 2.5° cases it is not feasible to record measurements close to the wing surface, since the roll oscillations block the laser. This explains why there are no measurements for the first two stations, as opposed to the stationary and $\Delta\phi = 1°$ case.

Since the $\Delta\phi = 5°$ proved to have the greatest effect on both the mean and the rms velocity values, further LDV experiments were conducted. In Figure 5.8, the mean and rms velocity contours were plotted from $y/s = 0$, which corresponds to the wing centreline, to $y/s = 0.5$, which is the middle of the local semispan, and for a range of z/s stations, from as close to the wing surface as possible, at $z/s = 0.08$, to 0.5. All the measurements were recorded at an incidence of 25°.

In the first contour plot, where the nondimensional mean velocity values are presented, low values dominate close to the wing surface, and increase moving away from it, (for measurements in the middle of the semispan area). As expected, moving towards the centreline increases the velocity values, which in some cases reach that of the freestream velocity. This provides a sign of earlier reattachment. The same pattern is followed in the rms contour plot, with very little variation occurring in the area close to the centreline, and the opposite inside the wake of the vortex.

5.2.4 Dye Flow Visualisation Results

Dye flow visualisation images have proved to be a very powerful tool for the understanding of the flowfield, and the changes that occur in it under small amplitude oscillations. Given that it was feasible to capture the whole area of the wing under both stationary and oscillatory conditions, a large number of videos was recorded, and segmented into instantaneous images. Again the main objective was to simulate the vibrations observed in flexible delta wings, and identify any possible evidence of lift enhancement and earlier reattachment in the flow.

Figure 5.9 shows the effect of a range of different frequencies on a $\Lambda = 50°$ rigid delta wing, set at $\alpha = 25°$, and undergoing a $\Delta\phi = 5°$ rolling motion. The first image corresponds to the stationary case, where the flow is completely stalled without any signs of reattachment or vortices. This kind of image is expected since on a $\Lambda = 50°$ stall occurs at $\alpha_{stall} = 21°$ (Taylor and Gursul-2004a). Applying an oscillatory motion with a low nondimensional frequency $(f_r = 0.15)$, does not seem to have any effect on the flowfield, and stalled flow persists over the wing surface. Doubling this frequency $(f_r = 0.3)$ though, results in significant changes to the flowfield. A very clear reattachment region can be seen, defined by the dye-free area along the centreline of the wing, and signs of vortices appear at the apex of the wing. It is interesting that even a very small frequency and amplitude rolling motion is capable of promoting reattachment in a previously completely stalled flow. Increasing the nondimensional frequency to $f_r = 0.5$ enlarges the dye-free region, thus promoting earlier reattachment of the shear layer. Furthermore, coherent leading edge vortices can now be seen on the wing surface. Further increase in the nondimensional frequency widens the reattachment region, and improves the vortex reformation. In all images presented here, the vortex breakdown location can be clearly seen, and is considerably delayed with increasing frequency. However, notice that at $f_r = 10$, earlier breakdown occurs compared to the previous nondimensional frequencies even though the vortices can be clearly discerned on the wing surface. Hence, the breakdown location is delayed with increasing frequency up to a certain point, after which a further increase only becomes detrimental.

In conclusion, the totally separated flow for the stationary wing becomes very well organised with an increasing frequency. The most interesting observation is the reformation of the leading edge vortices. Distinct vortices with a core and a breakdown location first appeared on the wing surface at $f_r = 0.5$, indicating that a

minimum forcing frequency is required in order for the reformation of the flowfield to take place. A significant delay in the breakdown location has been observed as the frequency increases up until $f_r = 1.8$, where premature breakdown occurred. Given that vortex breakdown is delayed with increasing frequency it can be suggested that the streamwise pressure gradient might be modified favourably due to the wing motion, since it encourages the flow to remain attached for a longer time. However, further experimentation is required in order to amplify the findings regarding the favourable modification of the streamwise pressure gradient.

Flow visualisation videos, and thus images, were also captured for incidences between 10° and 30°. In this way, a more diverse area, with different flow structures, was covered. That included incidences where the vortices are still present on the wing surface and vortex breakdown takes place on it, incidences where vortex breakdown occurs at the apex, and finally incidences where the flow is completely stalled with no signs of vortices. Thirty images were selected, and the vortex breakdown location was calculated for each and every case. The thirty values obtained were then averaged. The mean vortex breakdown location as a function of dimensionless frequency is presented in Figure 5.10 for all the incidences tested.

For a stationary wing at incidences in the range of 10° to 19°, where the vortices still exist on the wing surface, the breakdown occurs on the wing, and moves closer to the wing apex as the incidence increases. Delay in the vortex breakdown location is observed with an increase in the nondimensional frequency. For $\alpha = 10°$, 12.5°, 15° and 17.5°, the maximum delay appears at $f_r = 0.15$, whereas for $\alpha = 18°$ and 19°, it appears at $f_r = 1.5$ and 1.8 respectively. In either case, this proves that there is always an optimum frequency after which the implementation of a small amplitude rolling motion can have significantly adverse effects, such as promoting earlier breakdown (see for example $\alpha = 10°$, 12.5°, 15° and 17.5°, where the vortex breakdown at high frequencies takes place earlier than the static case). However, although the higher frequencies have an unfavourable effect by promoting earlier breakdown at $\alpha = 18°$ and 19°, its value is never lower than the stationary or lower frequency cases. This can possibly be an indication that the beneficial effect of a small amplitude motion as a form of flow control might be more valuable at higher incidences.

When higher incidences were tested ($\alpha = 20°$, 22.5°, 25°, 27.5° and 30°) the results obtained showed that for each incidence in the post-stall region, the breakdown location is zero for the stationary wing ($f_r = 0$), indicating that the vortices break down at the wing apex or completely stalled flow exists over the wing. (see Figure 5.10: continued). Maximum delay of the vortex breakdown location is achieved in the range of $f_r = 1$ to 2. This range compares well with the dominant frequencies of the shear layer instabilities for a nonslender wing of $\Lambda = 50°$ (Taylor and Gursul-2004a and Gordnier and Visbal-2003). In this range of incidences, the oscillatory motion is extremely beneficial, since the completely separated flow is being replaced by attached flow with clear vortical structures and breakdown.

A smaller amplitude $(\Delta\phi = 1°)$ oscillatory motion was also investigated in the post-stall region, under the same frequencies as the $\Delta\phi = 5°$ case at $\alpha = 25°$, in order to verify whether the same benefits could be obtained. Flow visualisation images were captured and are presented and discussed later in this chapter. The vortex breakdown location was calculated, and the variation of mean breakdown location as a function of dimensionless frequency is compared for two amplitudes of rolling motion, for $\alpha = 25°$ (Figure 5.11). It is clear that even for the small amplitude of 1°, leading edge vortices can be reestablished. The optimum dimensionless frequency is also in the same range. However, the magnitude in the value of the breakdown location is lower in the $\Delta\phi = 1°$ case.

Given the effect of frequency on the flowfield of a delta wing undergoing small amplitude rolling motions, further experimentation was considered necessary in order to investigate if the effect remains unchanged under various flow conditions (namely different Reynolds numbers). For this reason, the same experiments were conducted using a much lower Re (4,400). The results are compared in Figure 5.12, where the vortex breakdown location is plotted against the dimensionless frequency for two different values of Re. Previous work (Taylor *et al.*-2003) on the sensitivity of the vortices to Re, showed that the breakdown location moved towards the trailing edge in the presence of a lower Re. This fact is indeed confirmed by Figure 5.12. Interestingly enough, the effect of the frequency is the same; the optimum dimensionless frequency falls into the same range, and a similar pattern in the variation of the breakdown location is observed.

Additional flow visualisation experiments were conducted at $\alpha = 25°$ for an amplitude of $\Delta\phi = 1°$, and the same range of frequencies was tested as in the $\Delta\phi = 5°$ case (Figure 5.13). The low frequencies, $f_r = 0.15$ and 0.3, in combination with the small amplitude, cannot add enough momentum to the system in order to create any differences in the flowfield when compared to the static case. It is only at $f_r = 0.5$ that a clear reattachment region is seen, indicated by the dye-free region. Further increase in the nondimensional frequency promotes vortex reformation, and clear vortical structures can be seen up to the maximum dimensionless frequency, $f_r = 10$. Although the small amplitude rolling motion has a beneficial effect on the flowfield by promoting reattachment of the previously stalled flow and energising the vortex reformation, the delay in vortex breakdown does not reach the same value as in the $\Delta\phi = 5°$ case. This also becomes apparent in Figure 5.11.

In conclusion, the implementation of a small amplitude rolling motion on a stalled flow can significantly improve the flow by promoting reattachment and vortex reformation, and hence delaying vortex breakdown. However, a minimum value of frequency has to be implemented for the transformation of the flowfield to occur, depending on the amplitude of the motion, under the same flow conditions (Re). Moreover, there is an optimum frequency after which deterioration in the flowfield is observed. The results obtained highlight the beneficial effect of the rolling motion, and, at the same time, the concept that antisymmetric vibrations are responsible for lift enhancement. There are no direct and explicit data to prove the lift enhancement.

However, vortices are the main source of lift in delta wings, and therefore their regeneration can be considered as the cause for the lift enhancement. Flow visualisation images are not enough on their own to support this statement, hence further experimentation is required.

5.2.5 PIV Results

In the case of a rigid wing undergoing small amplitude rolling motions, the dimensionless frequency fc/U_∞ is not only a ratio of time scales of convective time and rolling motion, but also the ratio of the leading edge velocity and freestream velocity for a given wing. Figures 5.10 and 5.11 suggest that an increasing velocity of the leading edge does not necessarily delay breakdown location, at least not for the entire range of the frequencies tested. However, time-averaged vorticity flux is expected to increase with velocity of the leading edge as this term is proportional to $\overline{U_s^2}$, where U_s denotes the velocity outside the boundary layer at the separation point. This is confirmed by the vorticity distributions in a crossflow plane, at $x/c = 0.8$, as shown in Figure 5.15 for $\alpha = 25°$ and $\Delta\phi = 5°$. Note that the results shown in this figure are phase-averaged over 30 cycles, and correspond to a zero roll angle, as the roll angle changes from negative to positive values (See Figure 5.14 moving from position 2 to 3). This is the reason for the slight asymmetry, which is the result of the well-known hysteresis effect (Hanff and Huang-1991, Verhaagen and Jobe- 2003 and Nelson and Pelletier-2003).

In the stationary case, the levels of vorticity are very low, and as expected, no signs of leading edge vortices are observed. Larger values of vorticity exist with increasing frequency. Notice the coherent vortical structures that appear in the flowfield in the presence of large frequencies, for example at $f_r = 1.2$, 1.5, 1.8 and 2.1, whereas before that, small concentrations of vorticity appear. Earlier reattachment of the separated flow (evident via the zero vorticity values in the centreline of the wing), and coherent vortical structures are the main characteristics of the flowfield, providing indications of potential lift enhancement.

The variation of circulation with the dimensionless frequency, for both the clockwise and counter-clockwise vortices, is shown in Figure 5.16 for a wing at $\alpha = 25°$ and $x/c = 0.8$, for $\Delta\phi = 5°$. The circulation of both vortices increases with frequency compared to that of the stationary wing. The counter-clockwise vortex appears to have higher circulation than the clockwise one, a feature clearly seen in the vorticity plots. Such a result is expected since the motion of the wing clearly improves the vorticity and acts in favour of the counter-clockwise vortex. Moreover given that the images are captured at a zero roll angle (see Figure 5.14 moving from position 2 to 3) the counter-clockwise vortex is stronger (position 2, Figure 5.14) due to the effect of the effective sweep angle, hence presenting a higher circulation. A small decrease in the circulation of both vortices is observed after $f_r = 0.9$ for the counter-clockwise vortex and to $f_r = 0.7$ for the clockwise vortex. This provides an indication for an optimum frequency, at which maximum circulation occurs. Interestingly enough, the

frequencies where maximum circulation was calculated fall again in the same range of optimum frequencies.

PIV measurements under the aforementioned conditions were also captured for the $\Delta\phi = 1°$ oscillation, and are presented in Figure 5.17. The effect of frequency in this case is not as remarkable as with $\Delta\phi = 5°$, but is strong enough to transform the flowfield by creating a fully attached flow, with coherent vortices. It is interesting to notice the differences in the evolutions of the two vortices with increasing frequency. The counter-clockwise vortex increases its strength with frequencies up to $f_r = 1.5$. At $f_r = 1.8$ the vorticity levels seem to drop off, only to be followed by an increase in the $f_r = 2.1$ case. On the other hand, the clockwise vortex follows a different pattern. Its strength is amplified, compared to the stationary case with increasing frequency up to $f_r = 0.7$.

The same observations can also be made in Figure 5.18, where the variation in normalised circulation of the flow is plotted against frequency for both vortices. The pattern the two vortices follow, described in the vorticity contour plots, appears to be emulated by the circulation. A comparison between Figures 5.16 and 5.18 shows that the magnitude of circulation is considerably higher for the $\Delta\phi = 5°$ oscillation, but both vortices appear to respond in the same way to the application of the same frequencies.

In order to enhance our understanding of the flowfield, some PIV measurements near the surface of the $\Lambda = 50°$ delta wing, were considered necessary in addition to the crossflow experiments already presented. For this reason, velocity measurements were recorded near the wing surface (the laser was set at 1mm away from the wing surface) at a $\phi = 0°$ and $\alpha = 25°$, for a range of frequencies. The streamline pattern of the time-averaged flow is shown. Furthermore, an additional perspective on the flowfield can be acquired. The results are presented in Figure 5.19, where the near-surface streamline patterns are plotted for the surface of the wing. Note that for these measurements, the laser was set parallel to the wing surface at an incidence of 25°.

In the stationary case, the streamline pattern appears to be highly unorganised, with no streamlines starting from the apex, indicating a stalled flow, thus confirming the flow visualisation images and vorticity plots discussed earlier. The implementation of a small frequency (0.15) rolling motion significantly changes the streamline pattern, by introducing a certain degree of structure. The flow seems to move in the outward direction, with clear attempts of reattachment towards the midchord location. A further increase in dimensionless frequency results in a consistent streamline pattern where reattachment of the separated flow is clear, shown by the straight streamlines across the centreline of the wing, and a very well organised flow towards the sides of the wing, indicating vortex reformation. The slight asymmetry observed is due to the dynamic rolling motion, whereas the stationary case is almost perfectly symmetrical. The near-surface streamline pattern further confirms the fact that the application of a small amplitude rolling motion to a fully separated flow is capable of promoting earlier reattachment of the flow, enables vortex reformation thus delaying the vortex breakdown, and consequently enhances lift. However, a

minimum dimensionless frequency needs to be applied for the reformation of the flowfield to occur.

Further calculations were performed from the near-surface measurements. The fact that the vortices have strengthened (PIV-circulation results) while breakdown is delayed, suggests that the streamwise pressure gradient can be modified by an oscillatory motion to act in favour of the flowfield. For this reason, a form of normalised pressure gradient was calculated from the wing surface PIV measurements, by using:

$$\frac{U \cdot c \cdot \frac{dU}{dx}}{U_\infty^2}$$

with the purpose of verifying if this is the case. In Figure 5.20, the variation of the normalised pressure gradient as a function of the chord length, starting from the leading edge (denoted as $x/c = 0$), and ending at the trailing edge $(x/c = 1)$, is plotted at $\alpha = 25°$ for different dimensionless frequencies, at $y/s = 0$.

As expected in the stationary case, where the flow is stalled, the normalised pressure gradient is almost zero, with very small variations. These variations seem to change slightly in the presence of an oscillating motion, where a tendency of the pressure gradient to move to positive values is observed with increasing frequency. However, it is only at $f_r = 0.6$ that positive values start to appear across almost the entire chord length, apart from a small portion close to the trailing edge. This is in very good agreement with the streamline pattern in Figure 5.19, where clear reattachment is first observed at $f_r = 0.6$. A further increase in frequency resulted in positive values along the entire chord length. This provides a clear indication that the streamwise pressure gradient becomes favourable in the presence of a small amplitude rolling motion. These results in combination with the flow visualisation images obtained and discussed earlier in section 5.2.4, provide evidence and a conclusive result on the constructive effect that the streamwise pressure gradient has on the flowfield, by promoting earlier reattachment and retaining the flow attached for a longer period of time. It is worth mentioning that in all the cases where positive pressure gradient values are observed, there is always a peak in the range of $x/c = 0.15$ to 0.18, which is very close to the wing apex, where reattachment starts.

The final conclusion of the experimental work performed in this chapter is that small amplitude oscillations can significantly alter a completely stalled flow by actually transforming it to a fully attached one, accompanied by vortex reformation and consequently breakdown. Evidence of the streamwise pressure gradient becoming favourable and consequently the reason that the flow remains attached for longer time, is provided. There is a minimum frequency required for the modification of the flowfield along with an optimum one after which deterioration is observed. Additionally, the possibility of lift enhancement in the post-stall region, which can be regarded as an active flow control method, can also be confirmed.

5.3 Figures Chapter 5

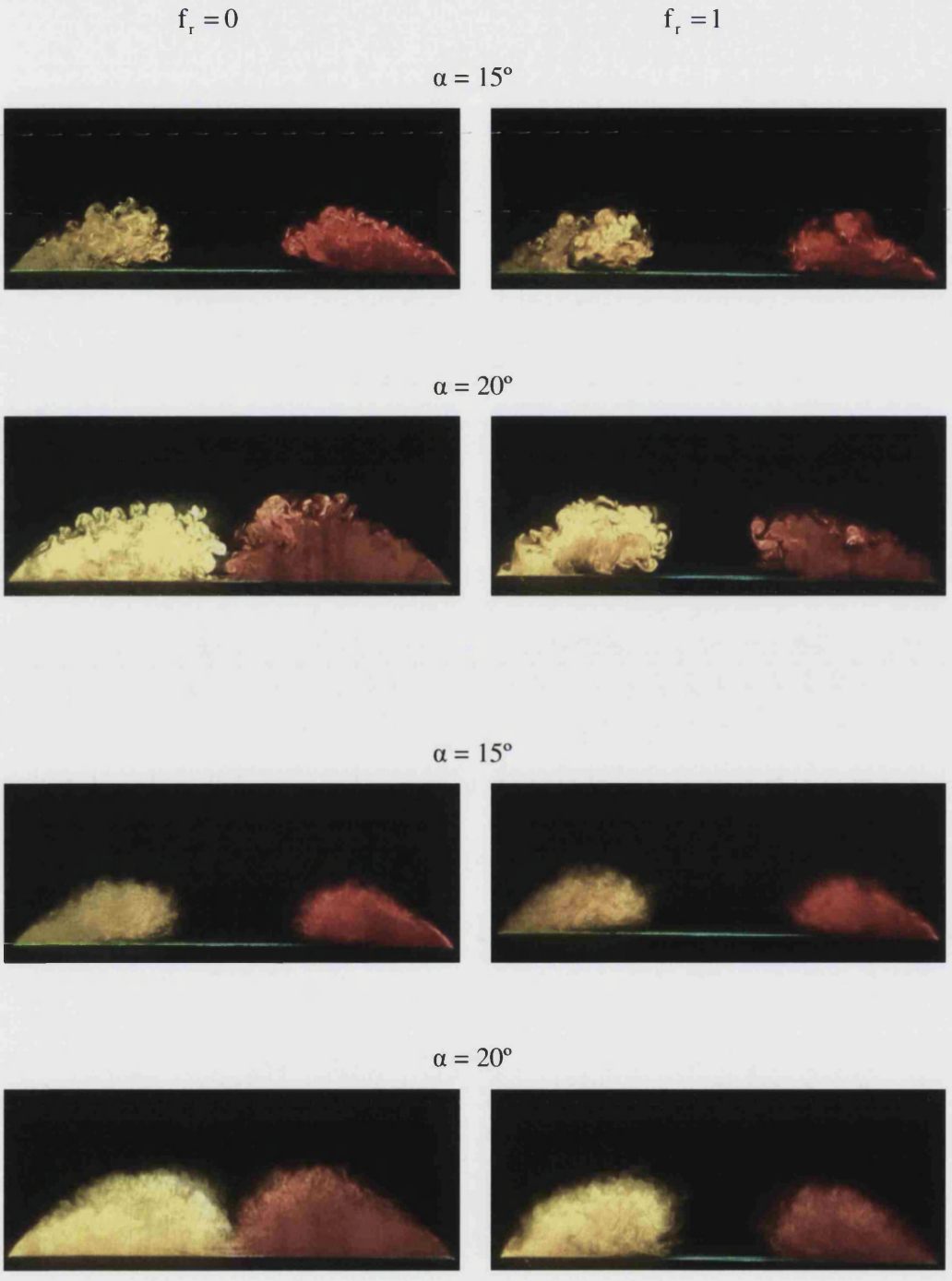

Figure 5.1: Comparison between static and dynamic instantaneous (*top half*) and time average (*bottom half*) laser induced flow visualisation images in crossflow plane at $x/c = 0.8$, for $\Delta\phi = 1°$ and at $\alpha = 15°$ and $\alpha = 20°$.

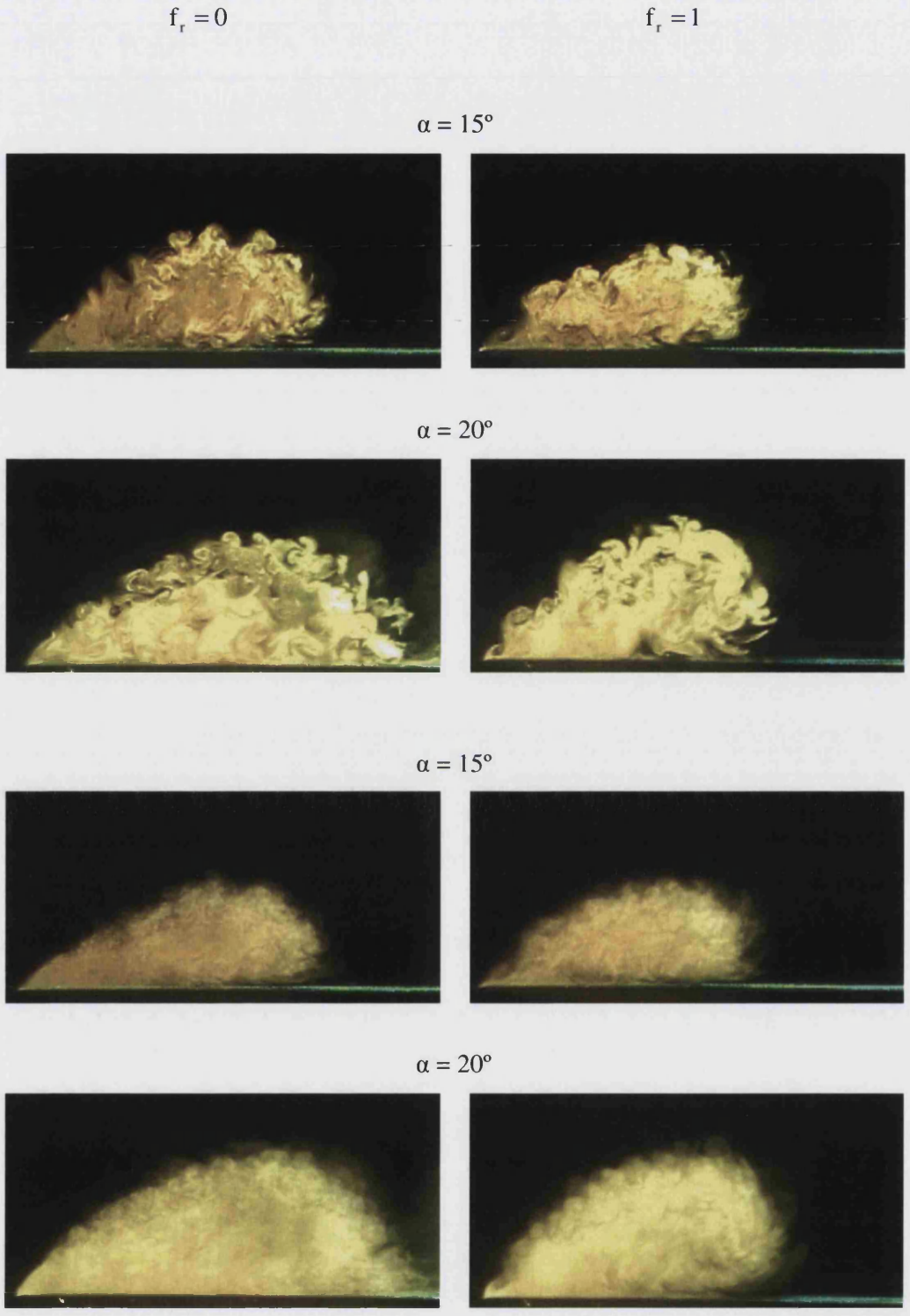

Figure 5.2: Detailed comparison between static and dynamic instantaneous (*top half*) and time average (*bottom half*) laser induced flow visualisation images in crossflow plane at $x/c = 0.8$, for $\Delta\phi = 1°$ and at $\alpha = 15°$ and $\alpha = 20°$.

$f_r = 0$

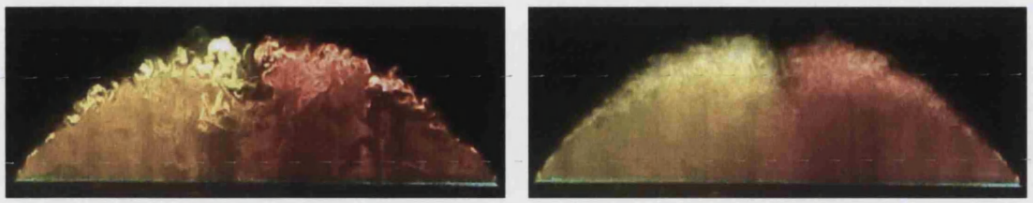

$f_r = 0.5$

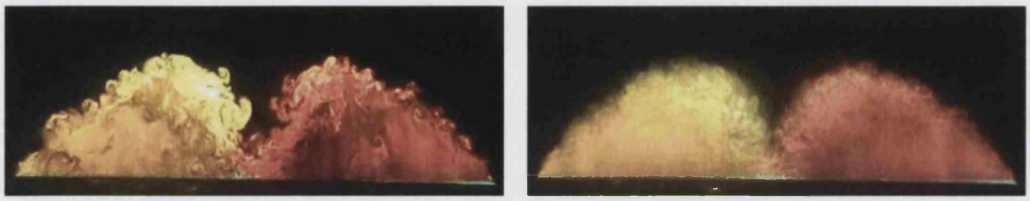

$f_r = 1$

$f_r = 2$

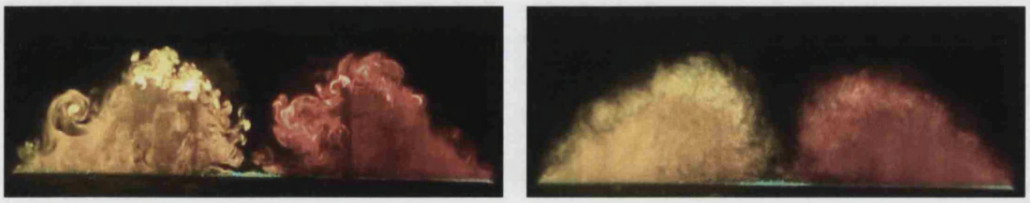

Figure 5.3: Instantaneous (*left side*) and time average *(right side)* laser induced flow visualisation images in crossflow plane at $x/c = 0.8$, $\alpha = 25°$, for different dimensionless frequencies and $\Delta\phi = 1°$.

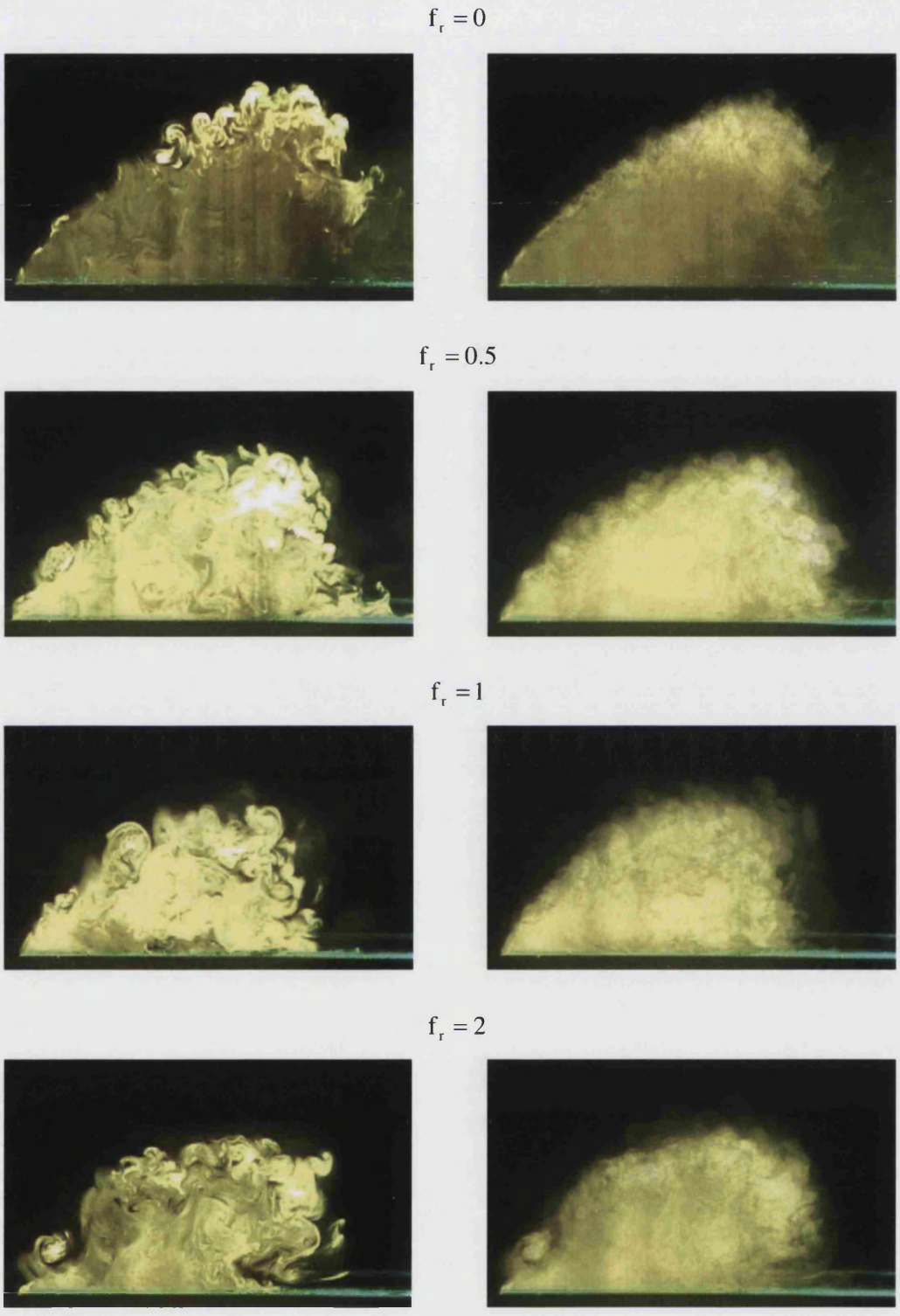

Figure 5.4: Detailed instantaneous (*left side*) and time average (*right side*) laser induced flow visualisation images in crossflow plane at $x/c = 0.8$, $\alpha = 25°$, for different dimensionless frequencies and $\Delta\phi = 1°$.

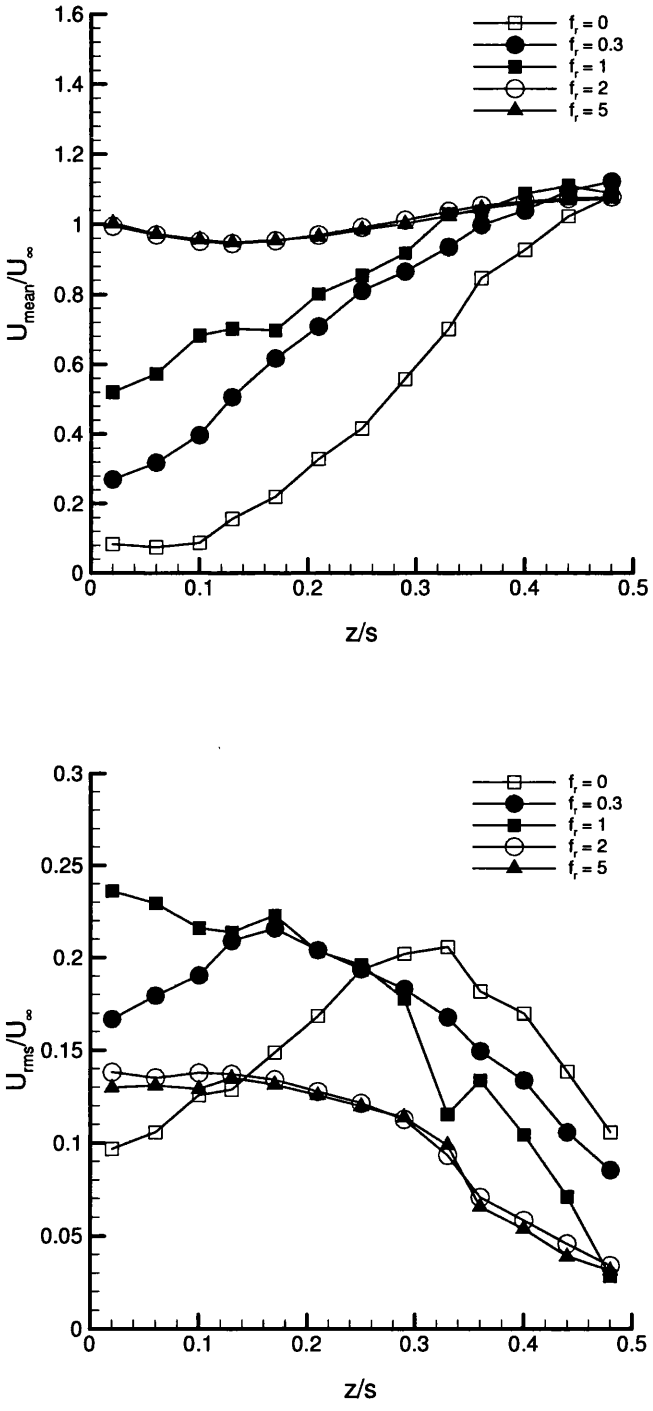

Figure 5.5: Mean and rms velocity measurements at $x/c = 0.7$ and at $y/s = 0$, for $\alpha = 25°$, for different dimensionless frequencies and $\Delta\phi = 1°$.

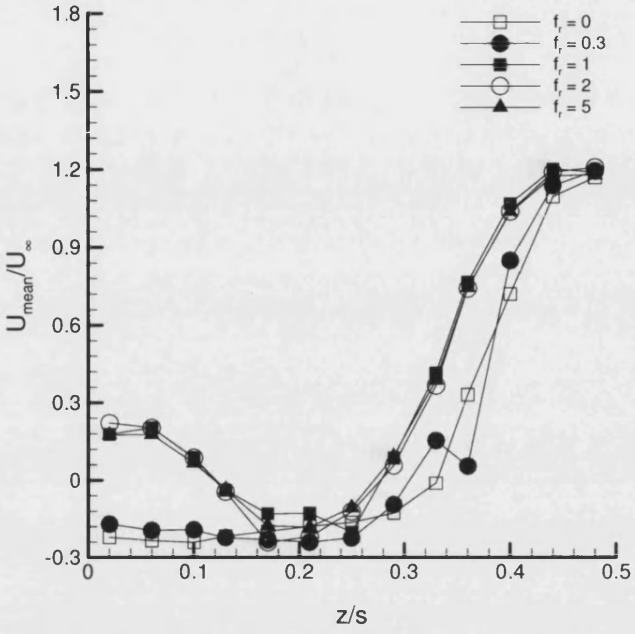

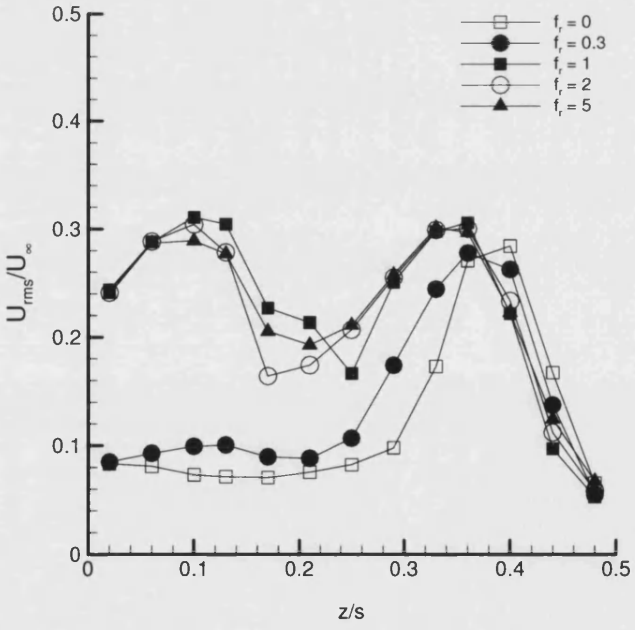

Figure 5.6: Mean and rms velocity measurements at $x/c = 0.7$ and at $y/s = 0.5$, for $\alpha = 25°$, for different dimensionless frequencies and $\Delta\phi = 1°$.

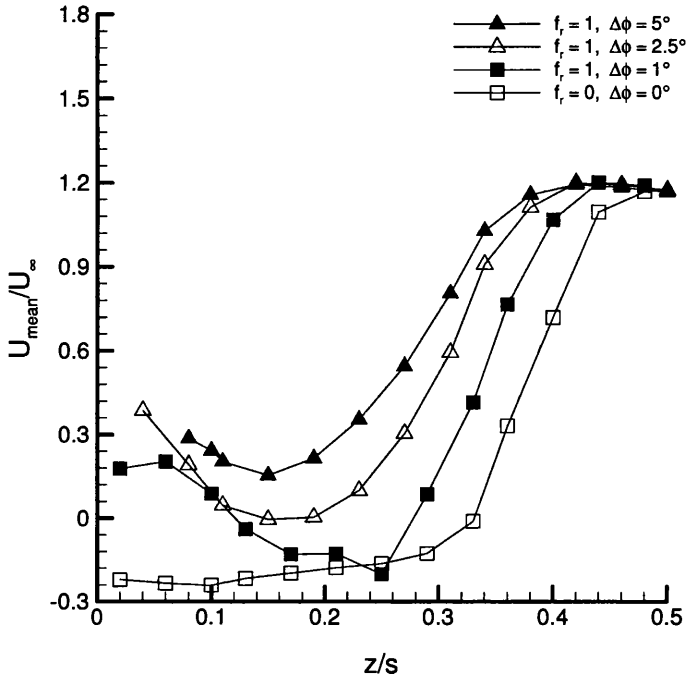

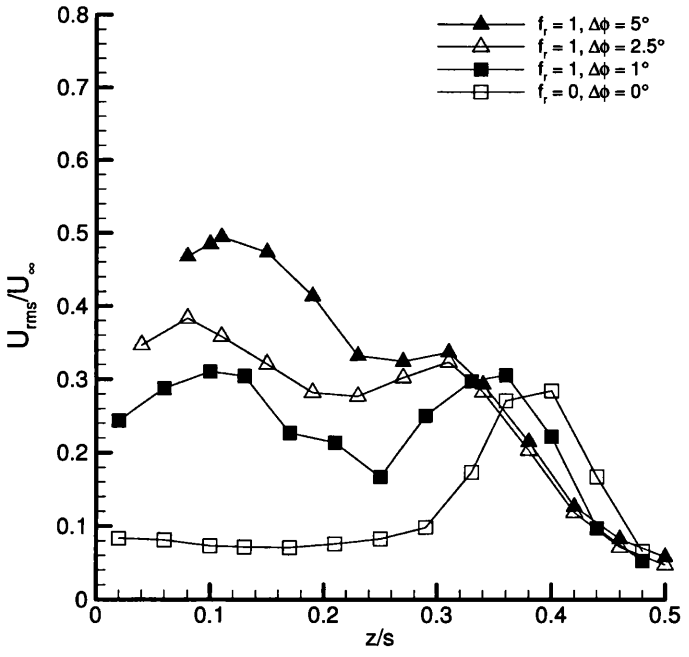

Figure 5.7: Mean and rms velocity measurements at $x/c = 0.7$ and at $y/s = 0.5$, for $\alpha = 25°$, for different amplitudes and $f_r = 1$.

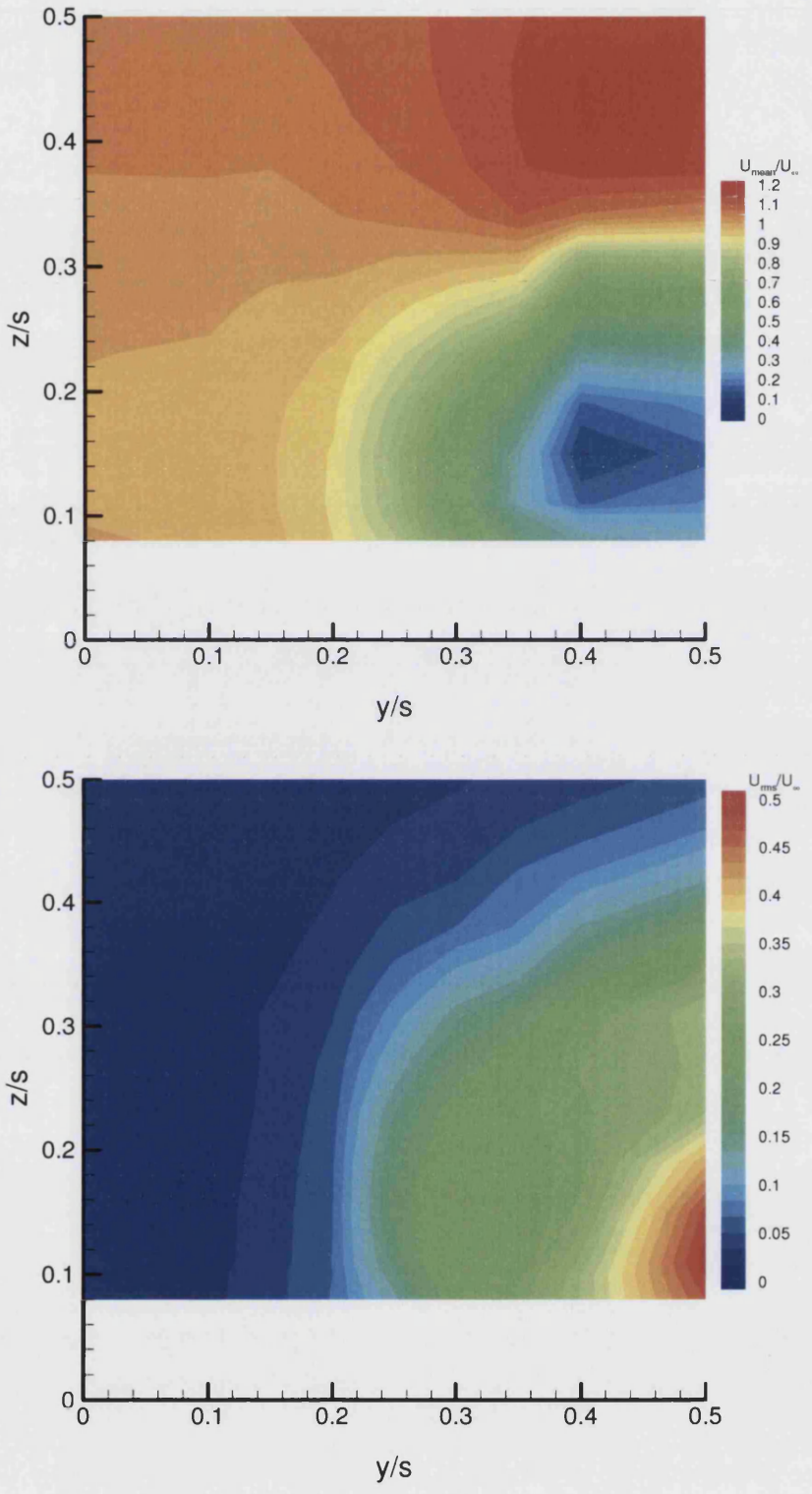

Figure 5.8: Mean and rms velocity contours at $x/c = 0.7$, $\alpha = 25°$, $\Delta\phi = 5°$ and $f_r = 1$.

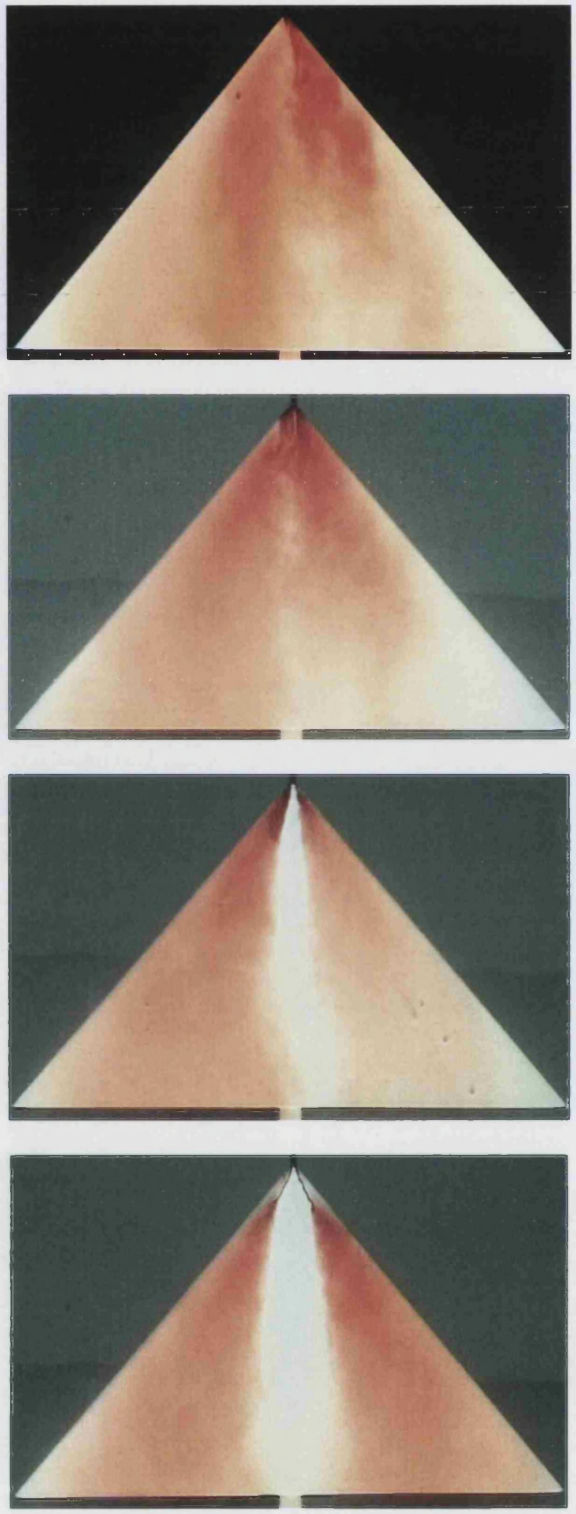

Figure 5.9: Effect of dimensionless frequency, f_r, on Λ = 50° delta wing at $\alpha = 25°$ under small amplitude $(\Delta\phi = 5°)$ rolling motion.

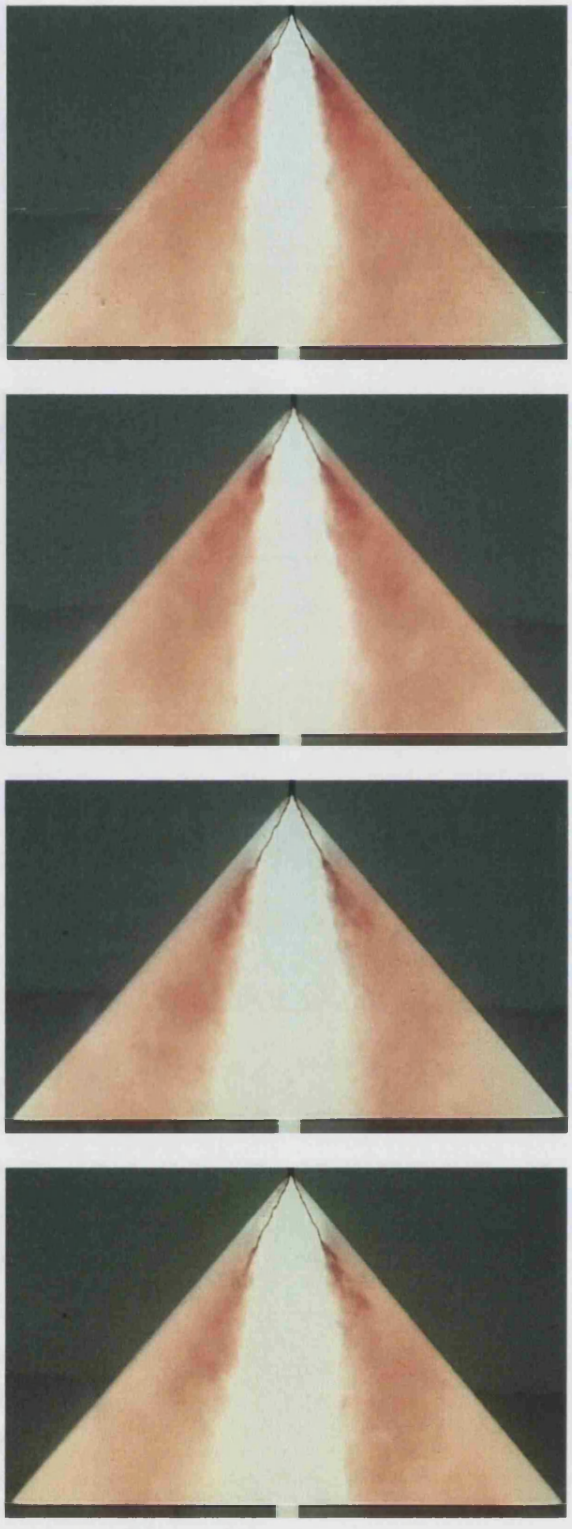

Figure 5.9: continued

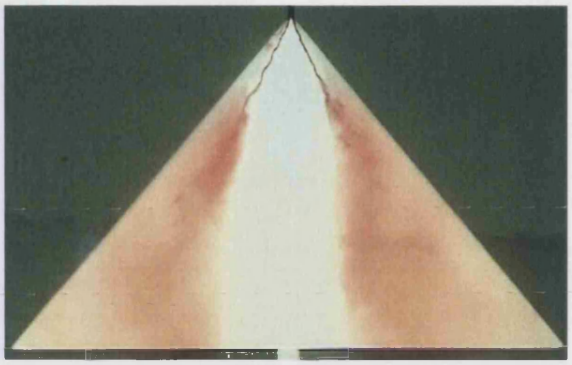

$f_r = 1.8$

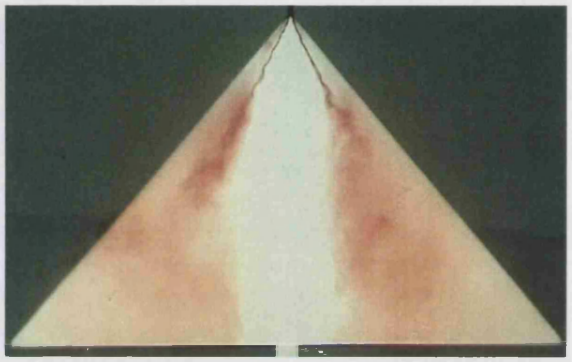

$f_r = 2.1$

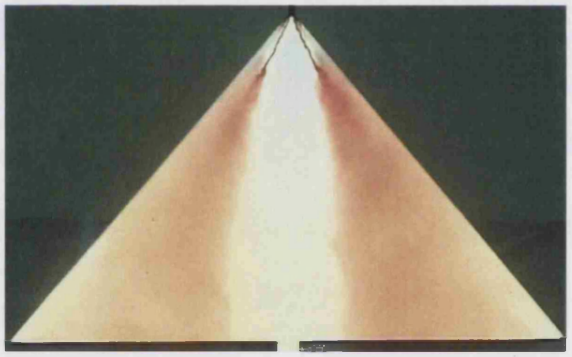

$f_r = 10$

Figure 5.9: continued

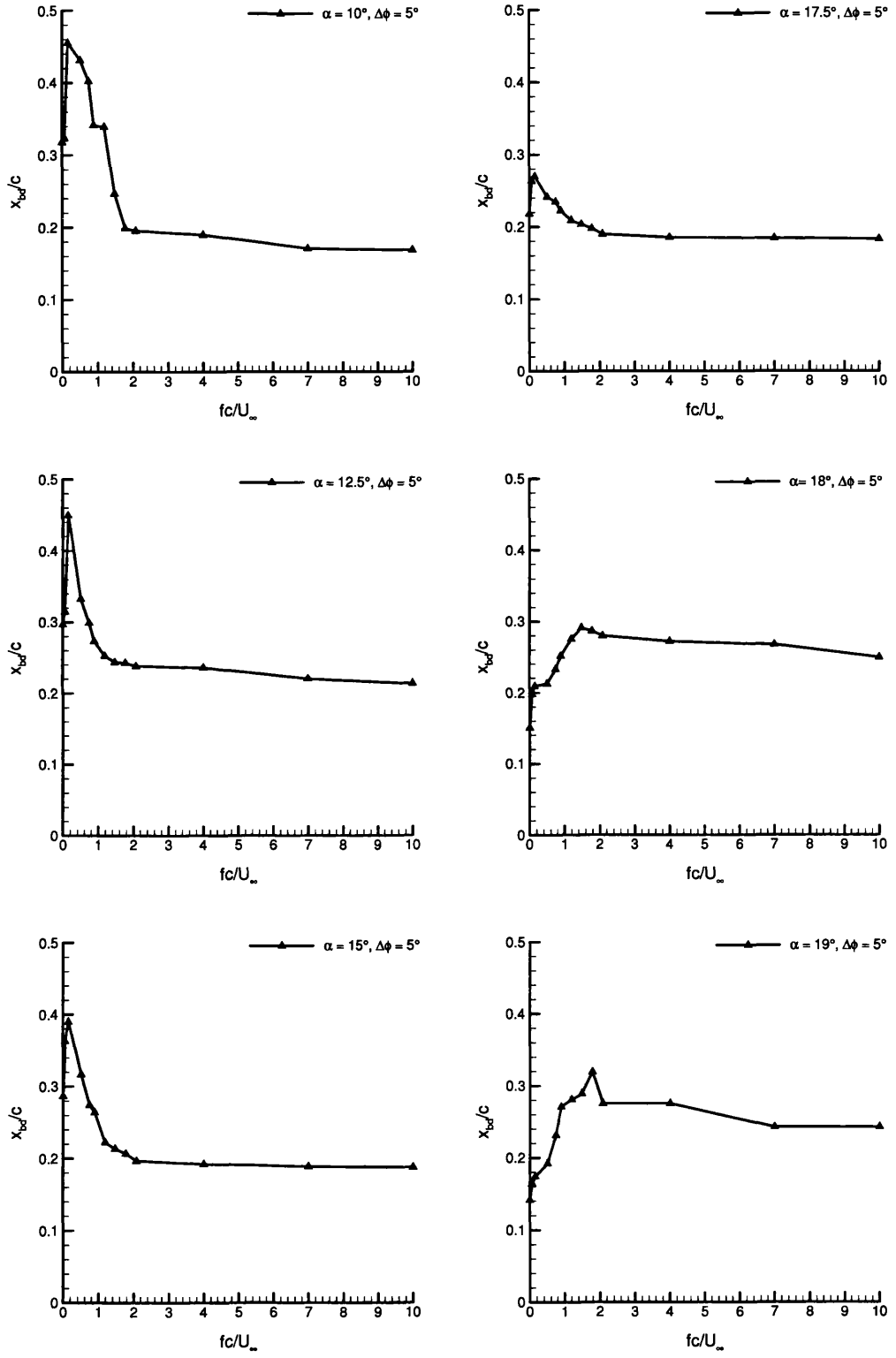

Figure 5.10: Variation of the mean breakdown location as a function of the dimensionless frequency, f_r, for different incidences.

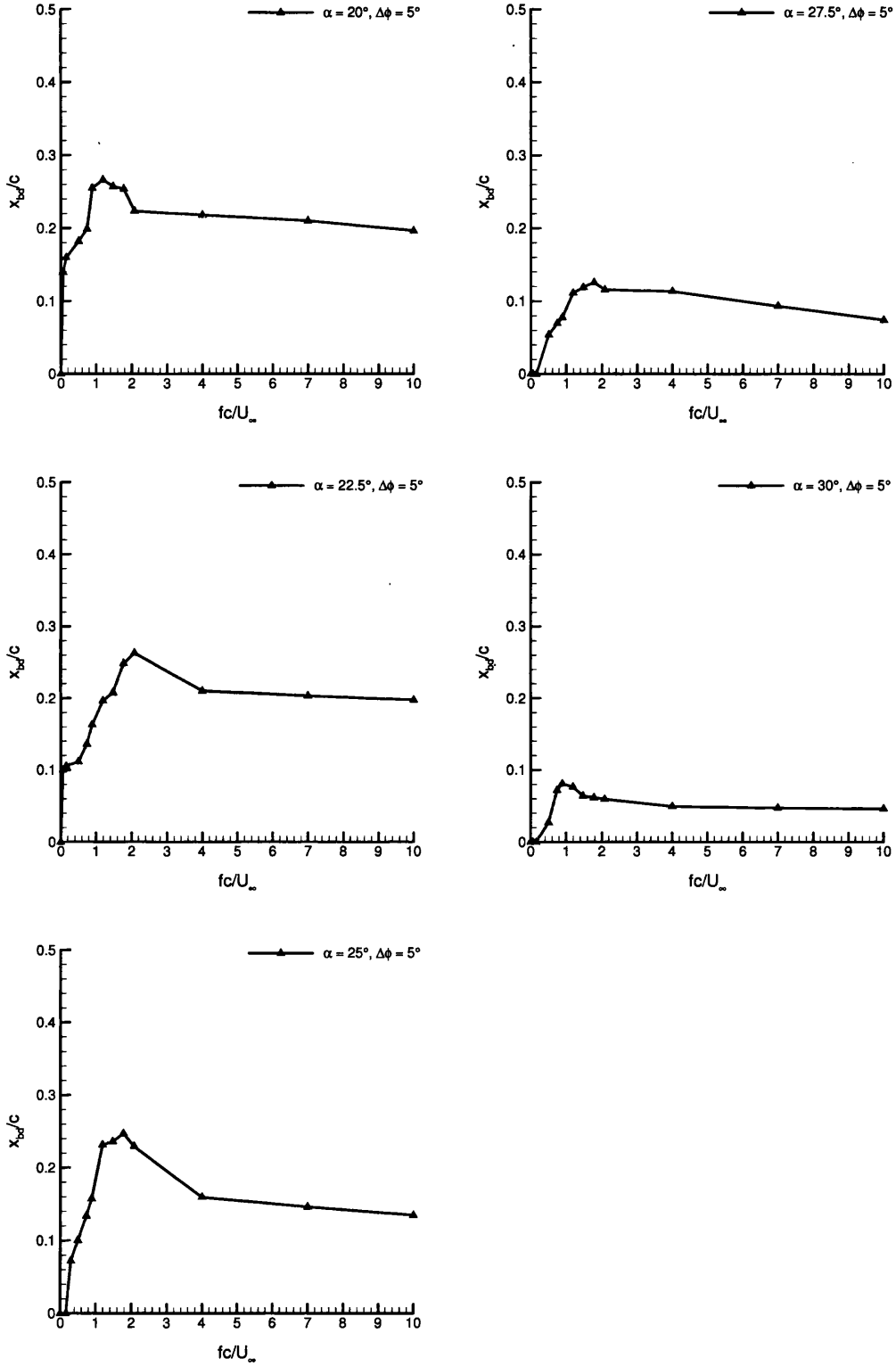

Figure 5.10: continued

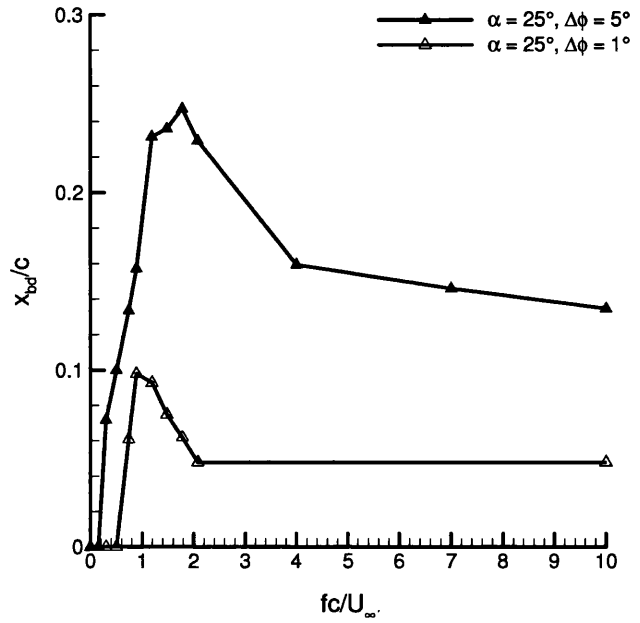

Figure 5.11: Variation of the mean breakdown location as a function of the dimensionless frequency, f_r, at $\alpha = 25°$, under different amplitude rolling motion.

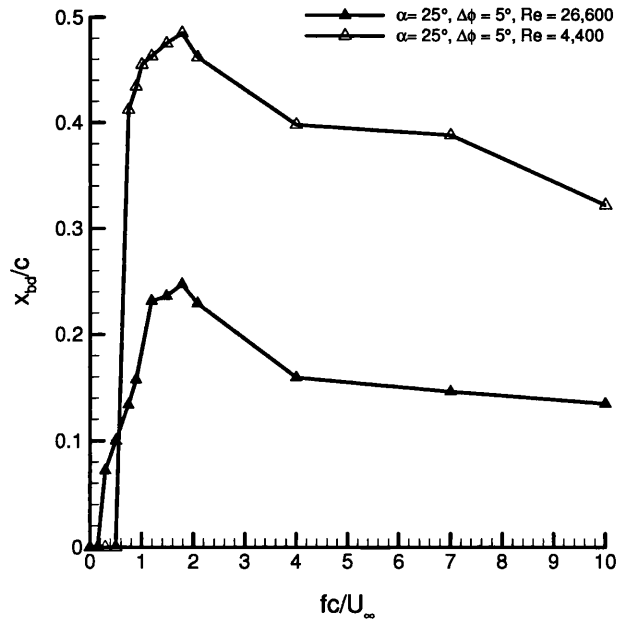

Figure 5.12: Variation of the mean breakdown location as a function of the dimensionless frequency, f_r, at $\alpha = 25°$, for different Re.

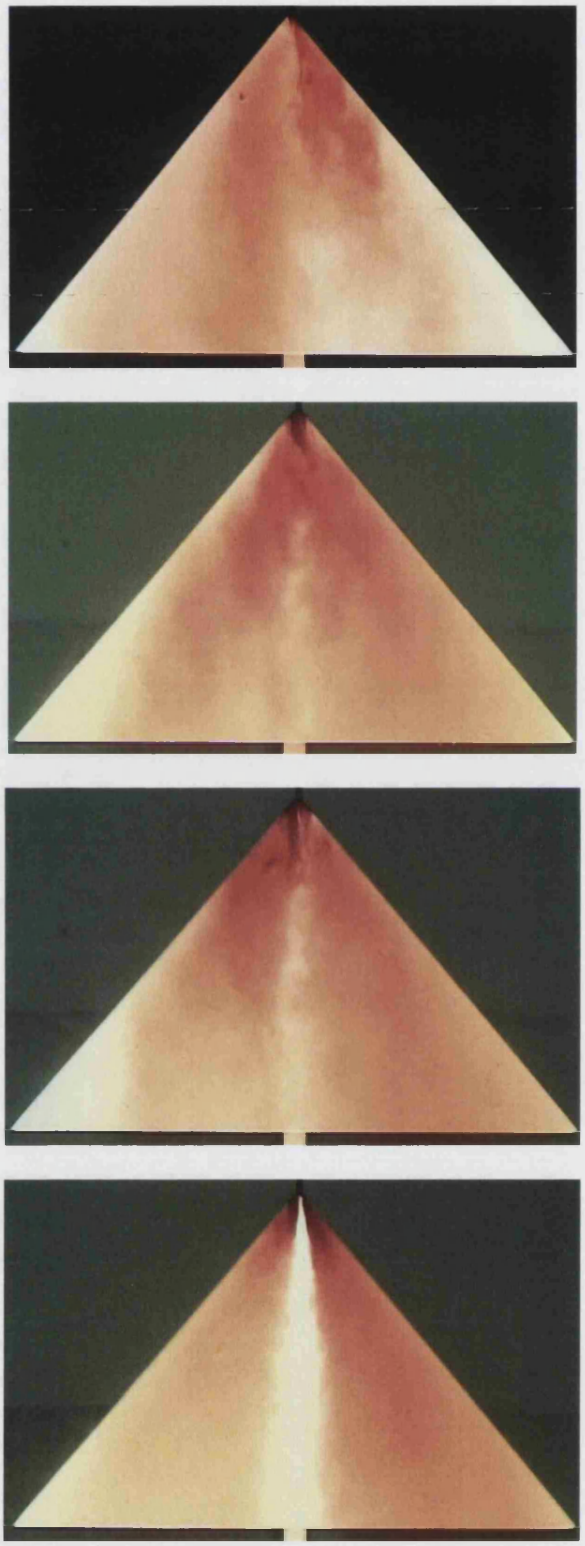

Figure 5.13: Effect of dimensionless frequency, f_r, on $\Lambda = 50°$ delta wing at $\alpha = 25°$ under small amplitude $(\Delta\phi = 1°)$ rolling motion.

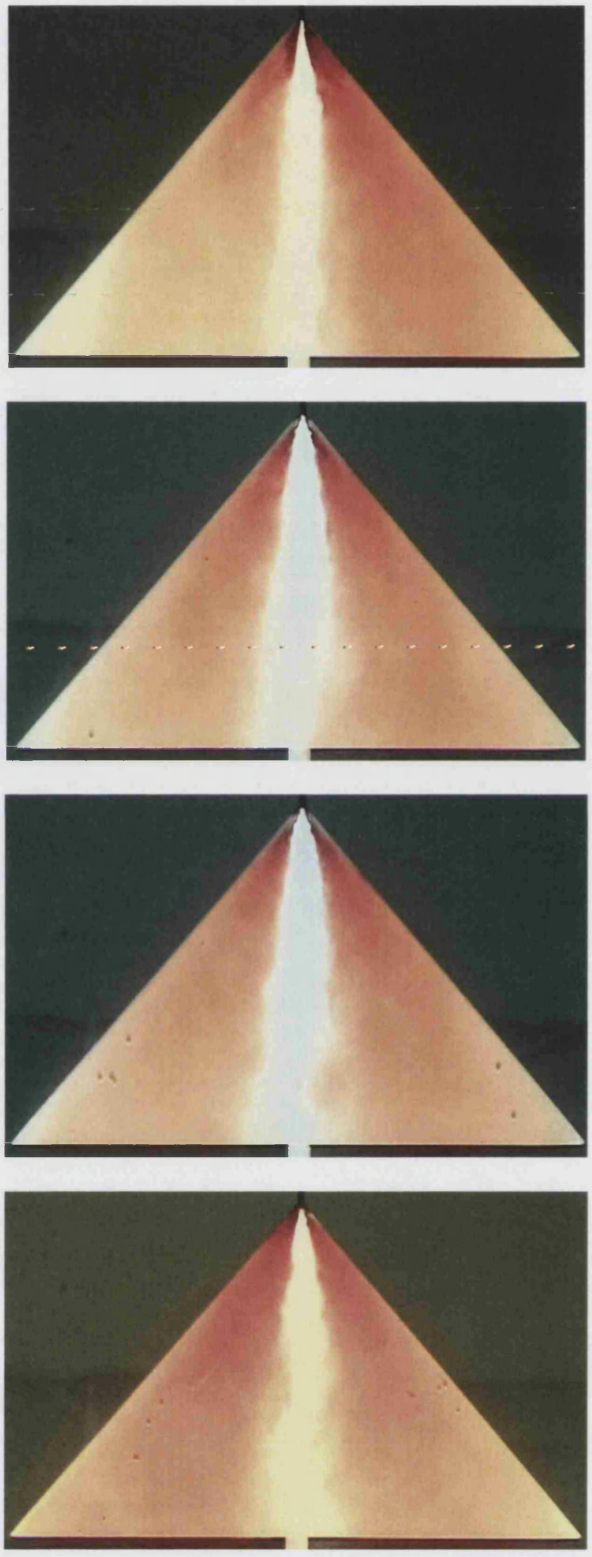

Figure 5.13 (continued):

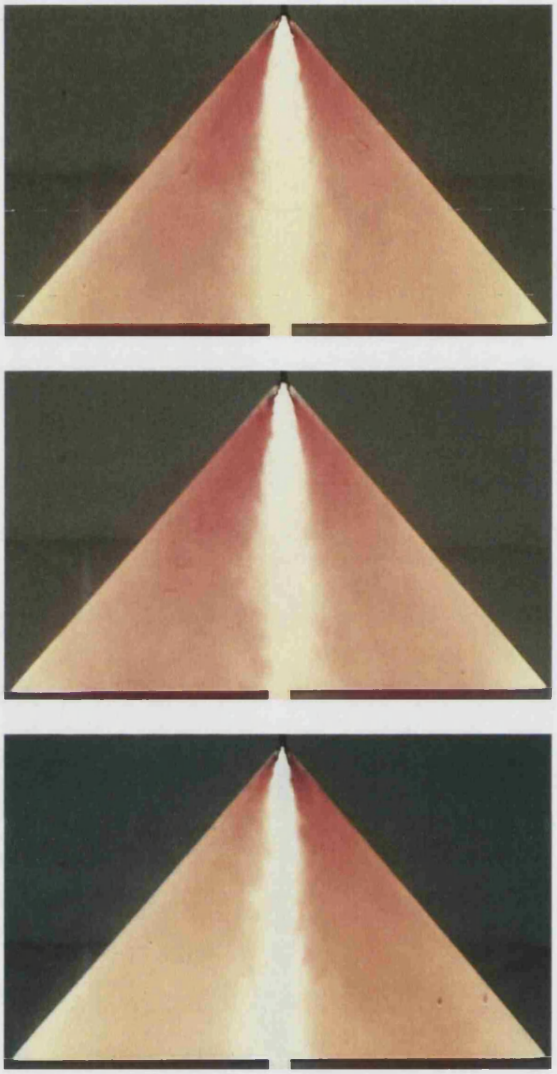

Figure 5.13 (continued)

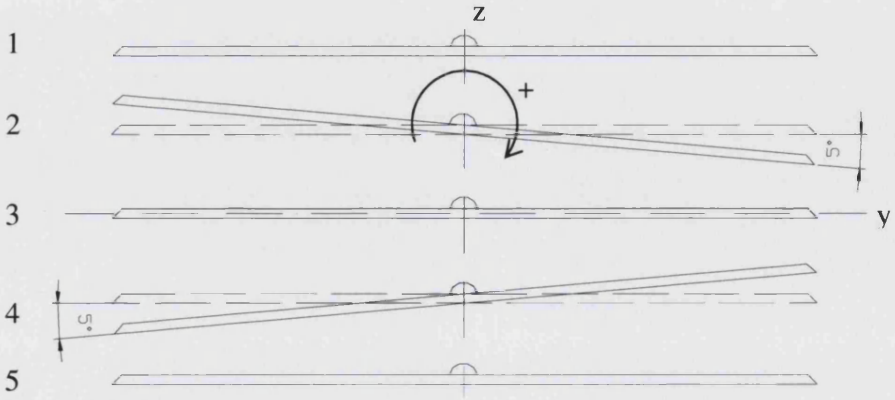

Figure 5.14: Positions of the wing, as seen from the back during the oscillatory motion, at 0.25 time intervals of the cycle at different times.

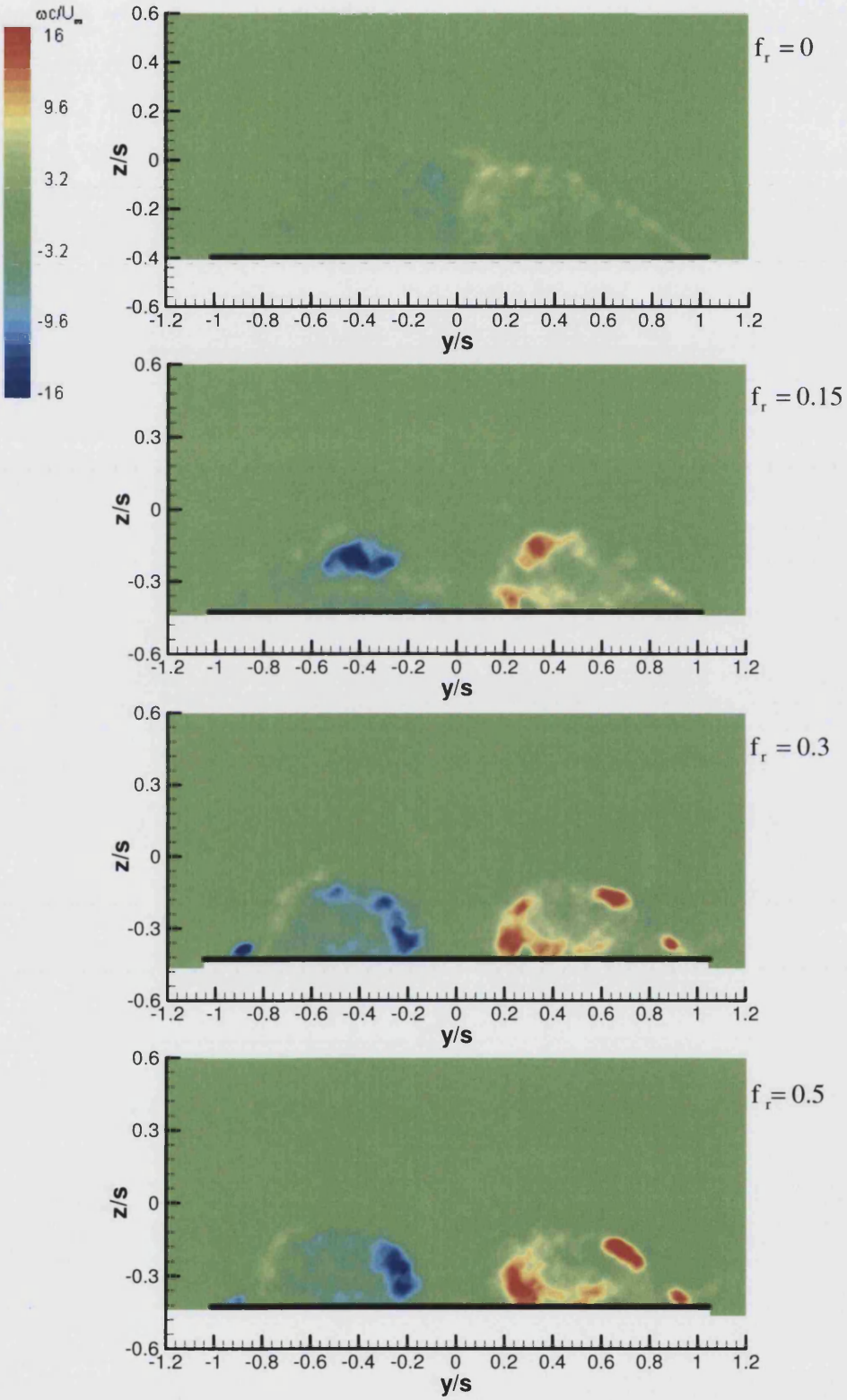

Figure 5.15: Magnitude of vorticity in a crossflow place $(x/c = 0.8)$ for stationary and small amplitude $(\Delta\phi = 5°)$ rolling motion, at $\alpha = 25°$.

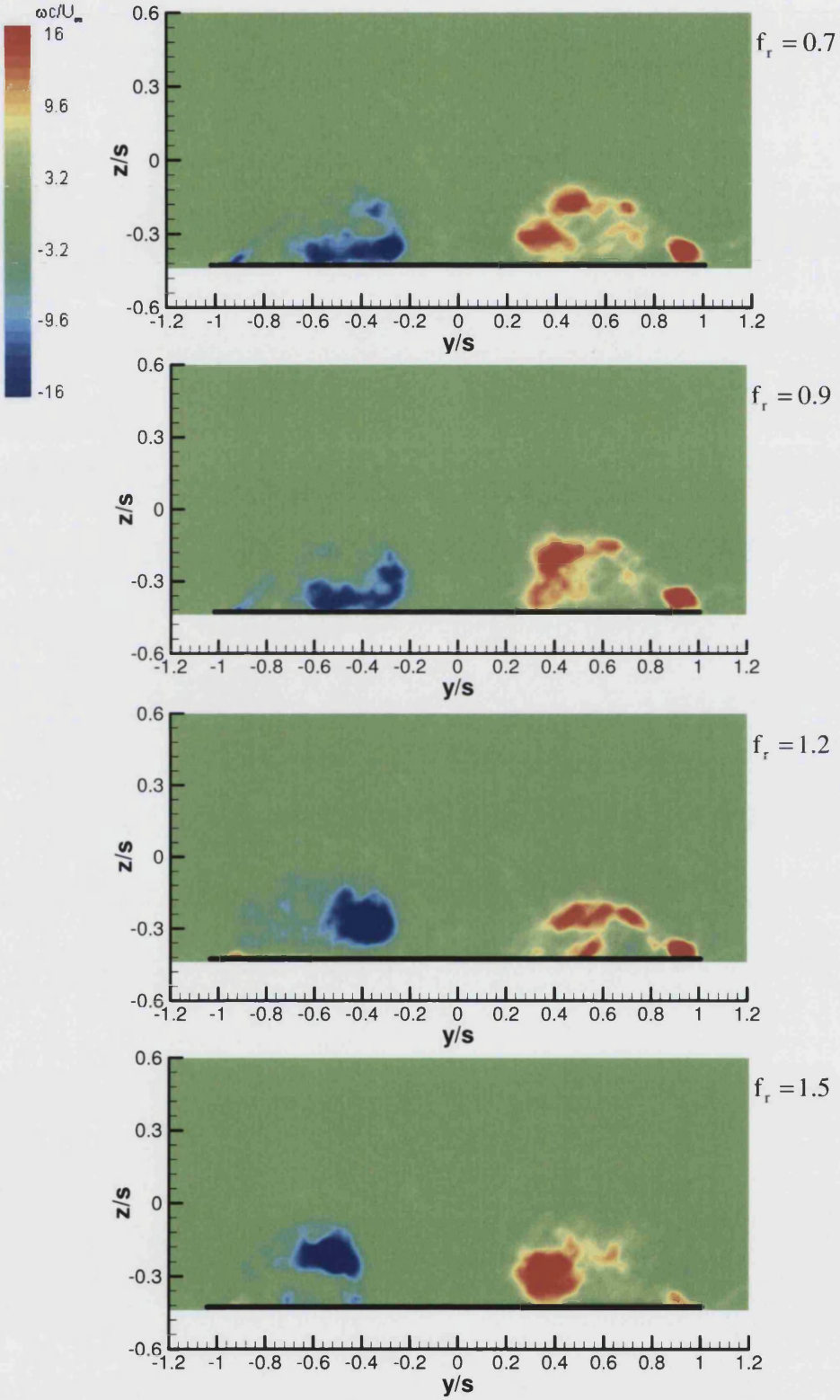

Figure 5.15: continued

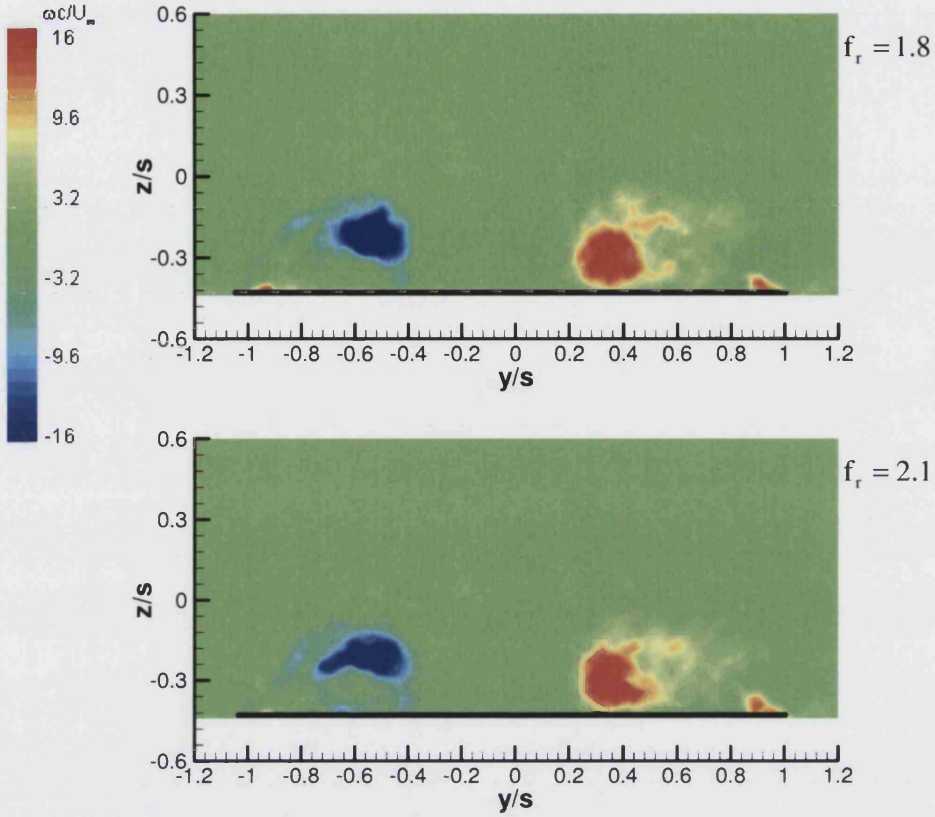

Figure 5.15:continued

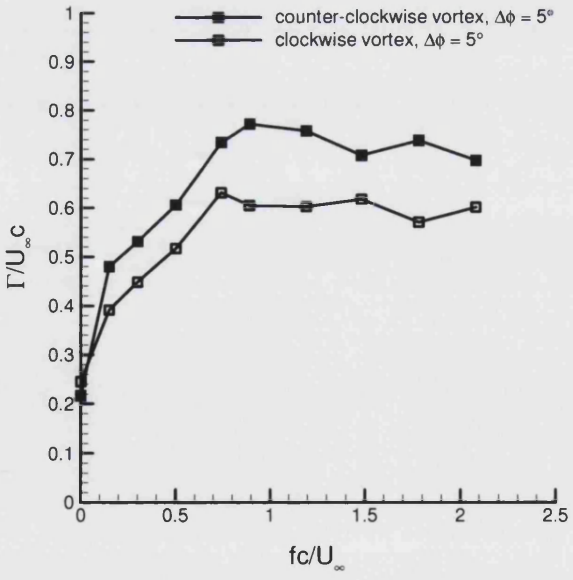

Figure 5.16: Variation of normalised circulation of vortical flow in a crossflow plane at $x/c = 0.8$ as a function of a dimensionless frequency, at $\alpha = 25°$.

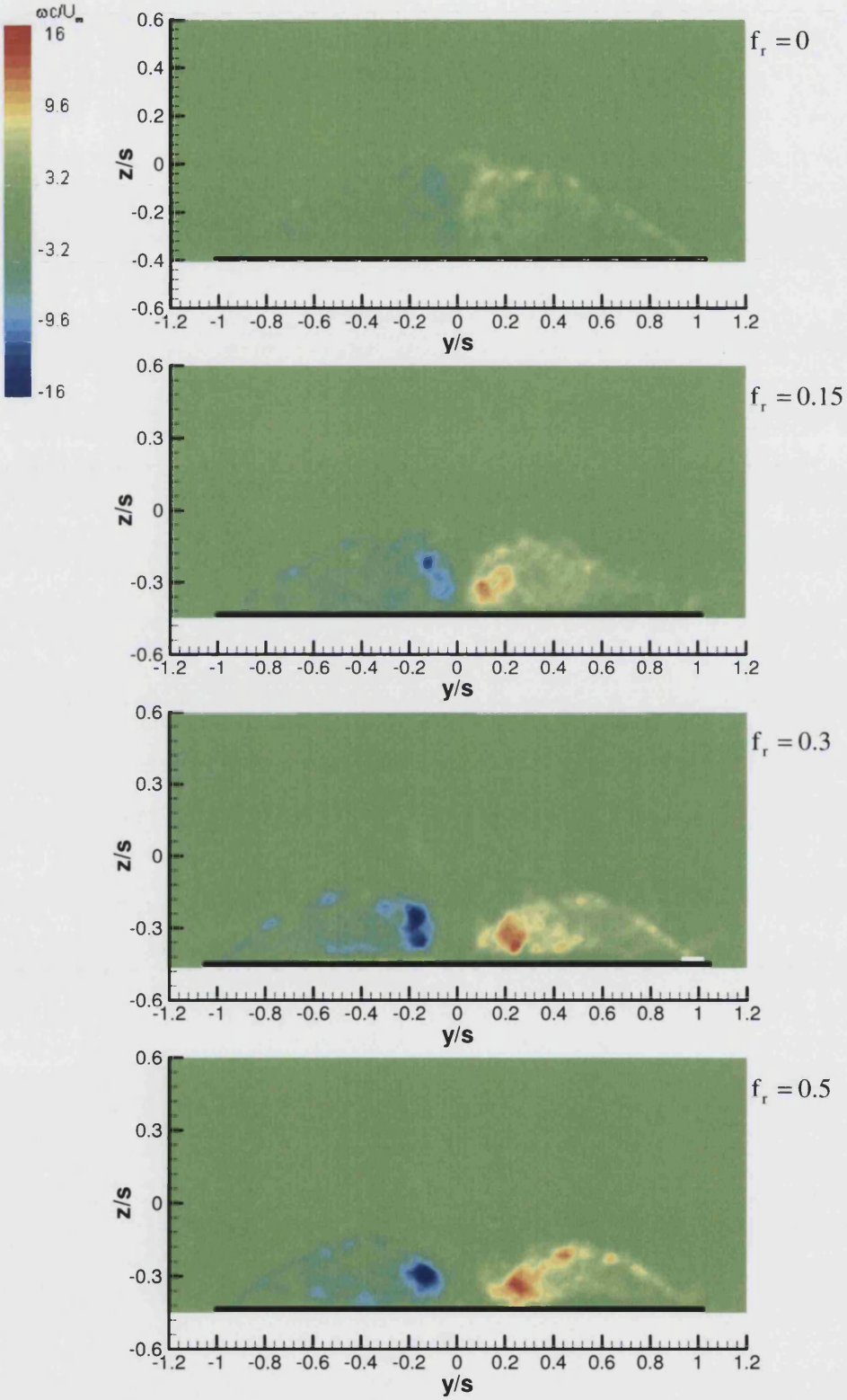

Figure 5.17: Magnitude of vorticity in a crossflow place $(x/c = 0.8)$ for stationary and small amplitude $(\Delta\phi = 1°)$ rolling motion, at $\alpha = 25°$.

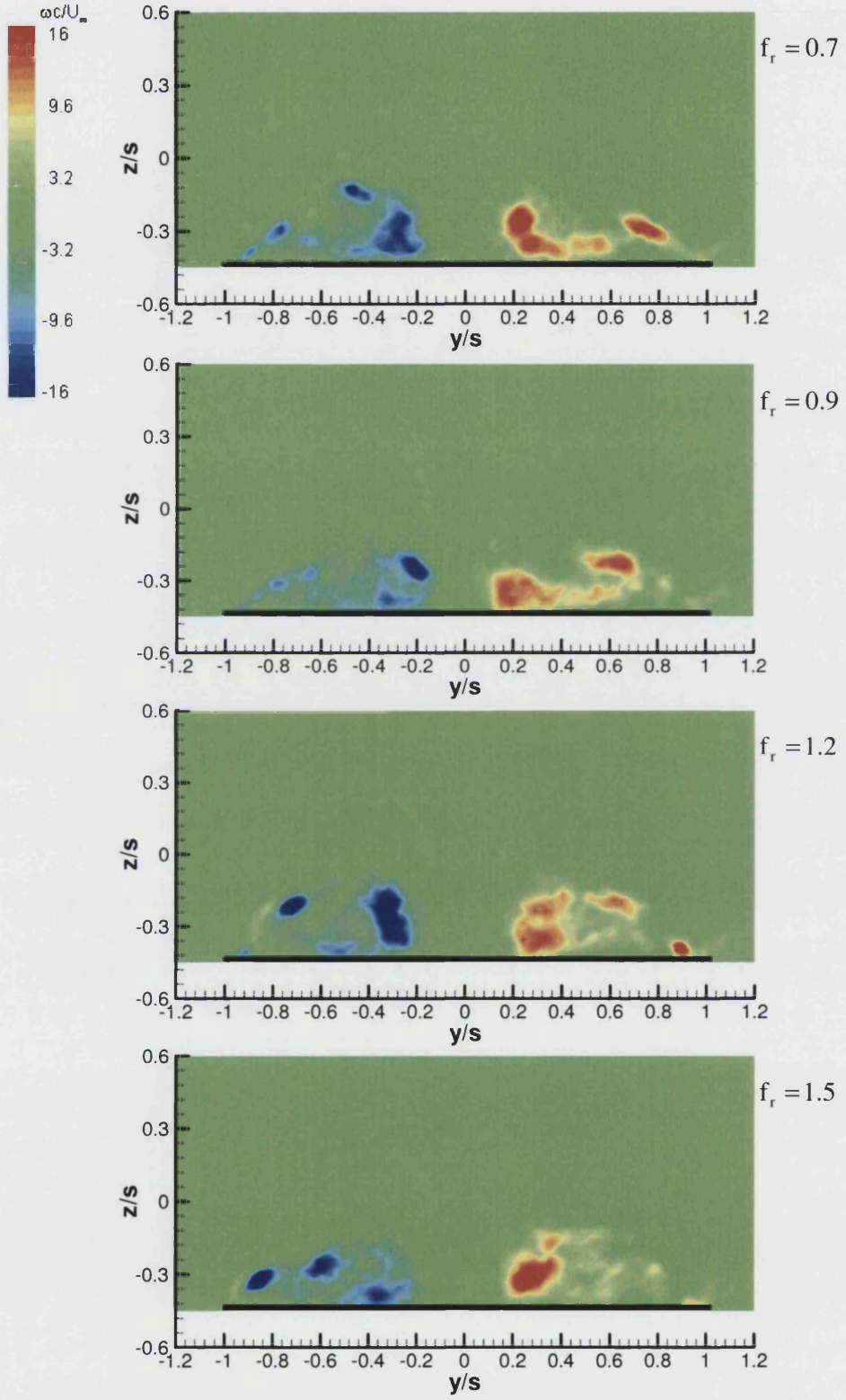

Figure 5.17: continued

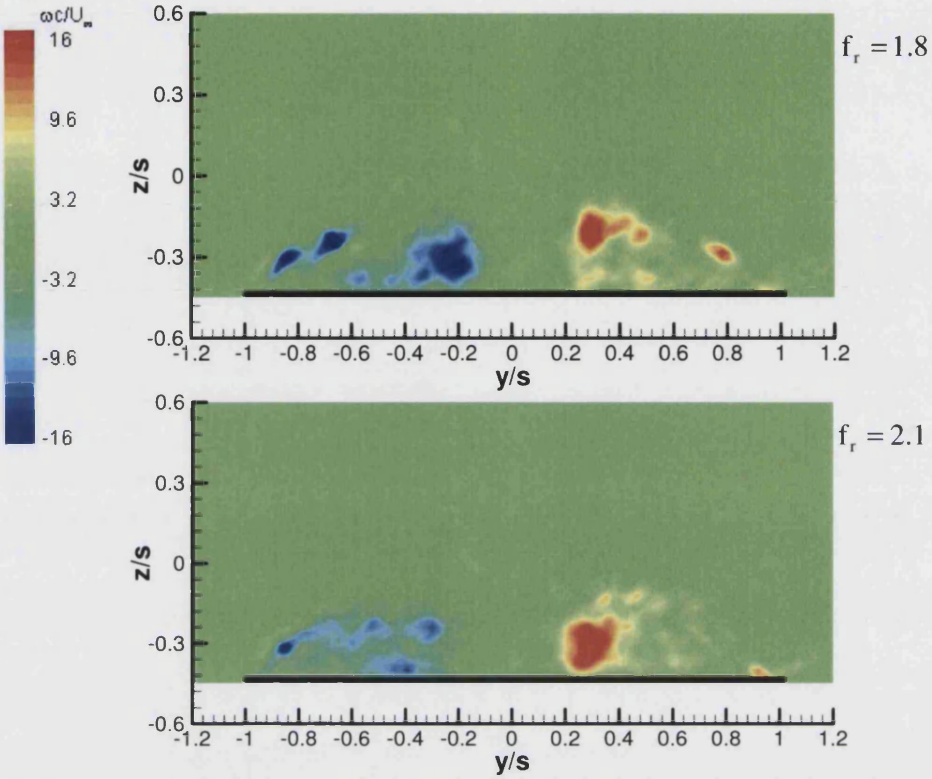

Figure 5.17: continued

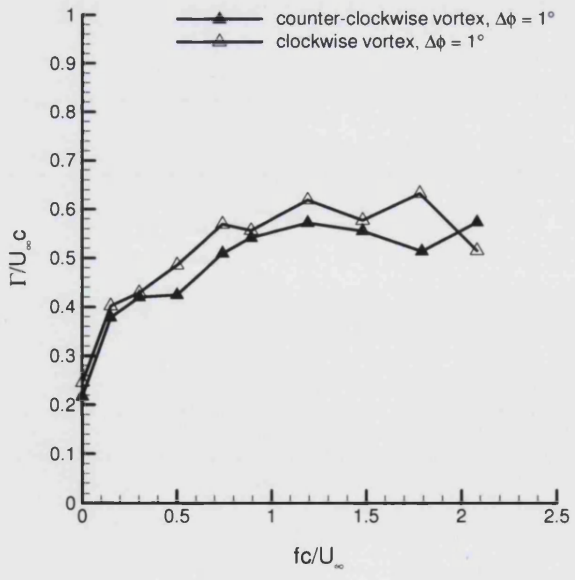

Figure 5.18: Variation of normalised circulation of vortical flow in a crossflow plane at $x/c = 0.8$ as a function of a dimensionless frequency, at $\alpha = 25°$.

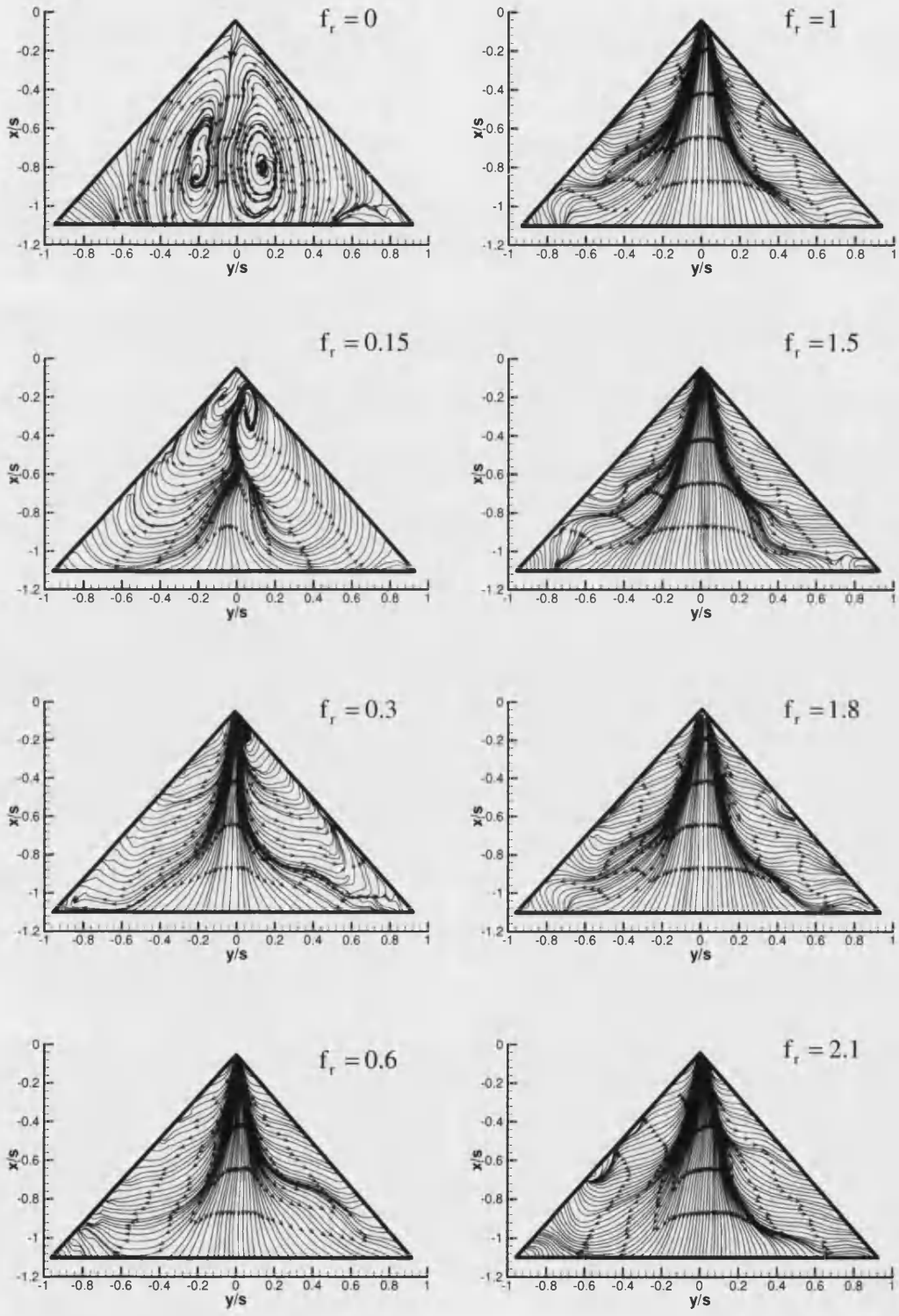

Figure 5.19: Near-surface streamline patterns for different dimensionless frequencies, at $\alpha = 25°$, for $\Delta\phi = 5°$.

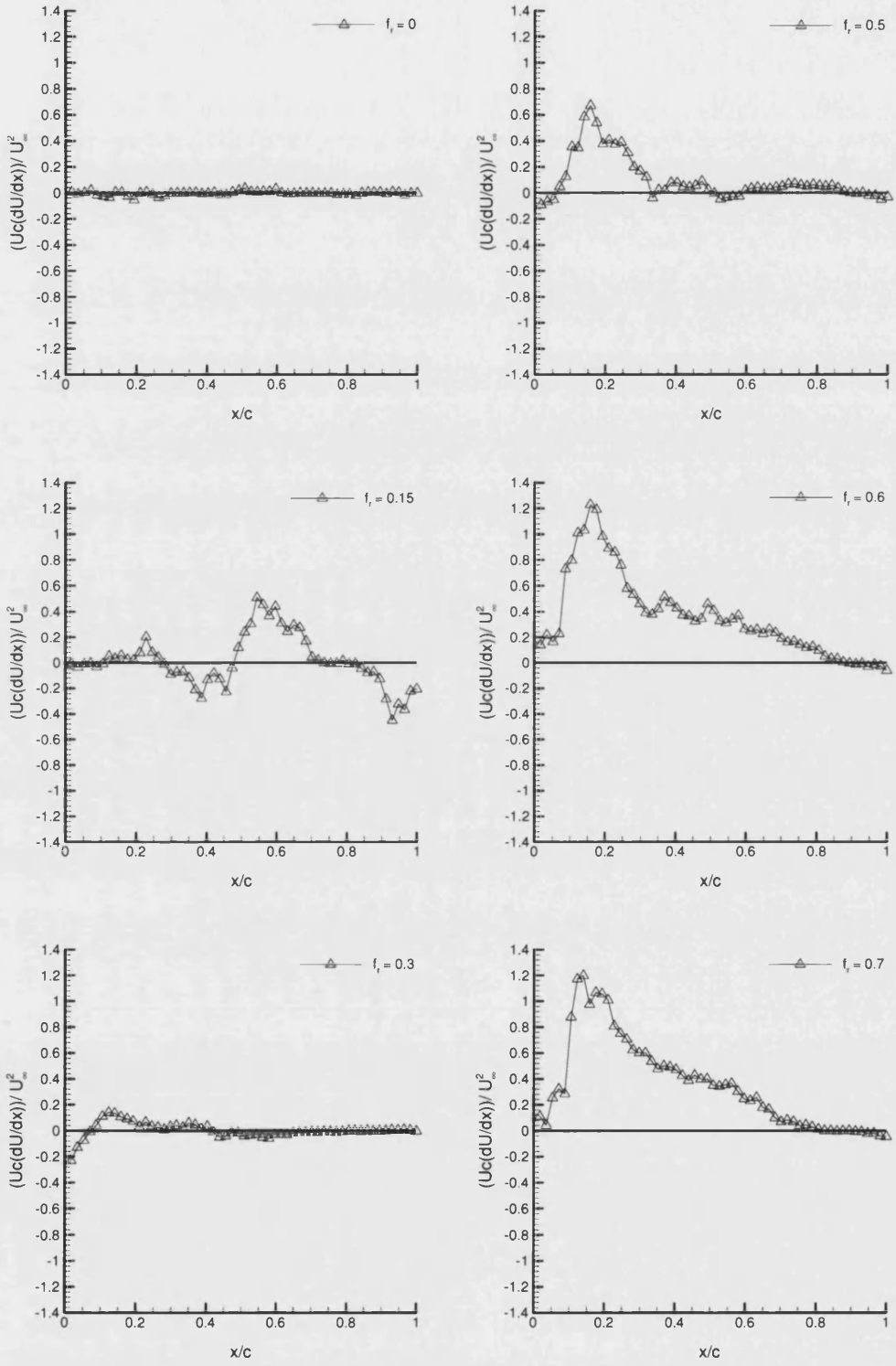

Figure 5.20: Variation of normalised pressure gradient as a function of the chord length, $\alpha = 25°$ for different dimensionless frequencies and for $\Delta\phi = 5°$.

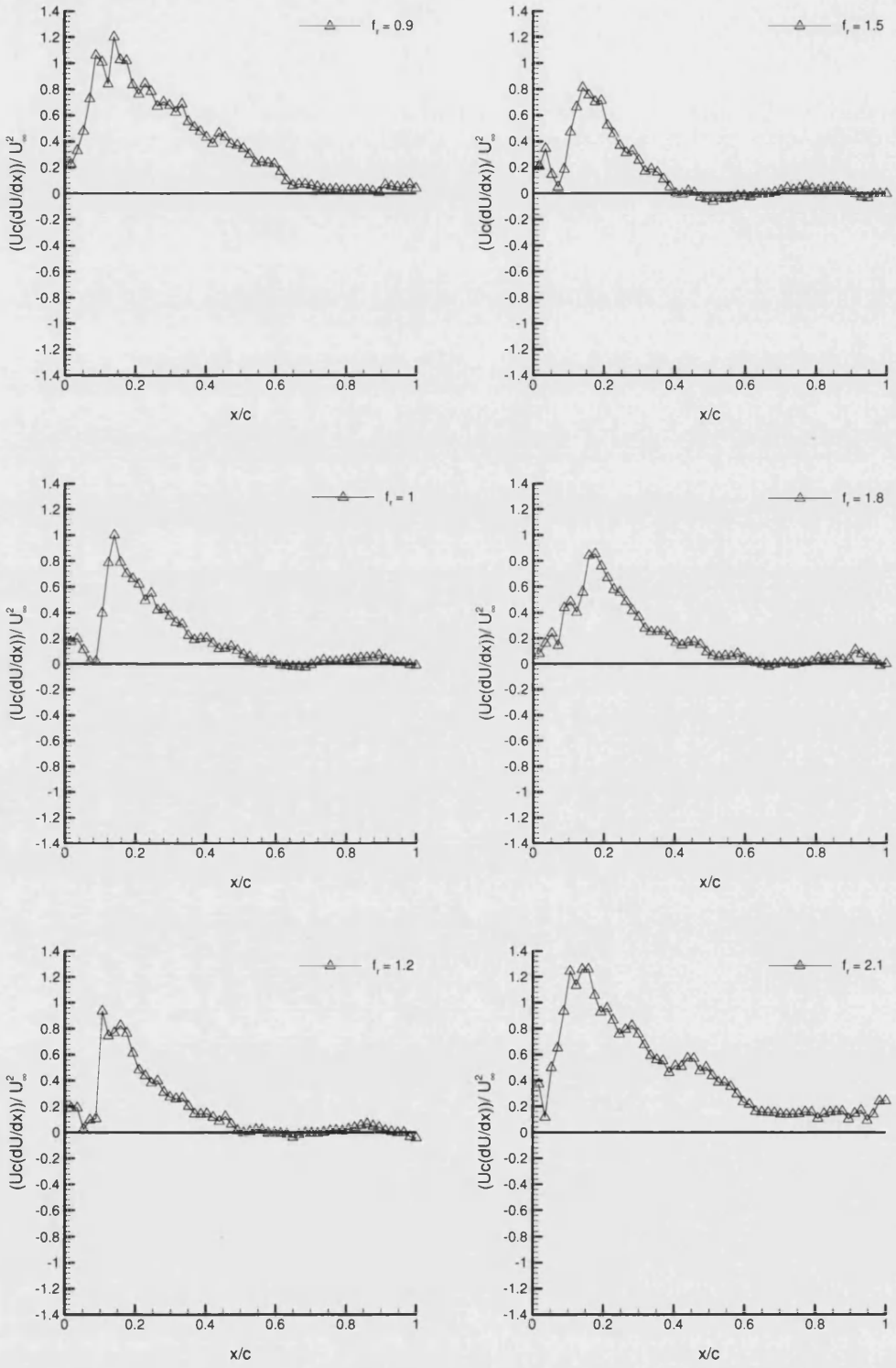

Figure 5.20: continued

CHAPTER 6: PARAMETRIC EFFECTS

6.1 Introduction

In the previous two chapters, only flexible and rigid $\Lambda = 50°$ simple delta wings were tested, with the purpose of studying their flowfield. This chapter incorporates a different approach, and describes the parametric effects on the flowfield of various low sweep angle delta wings. The parametric effects include delta wings with different sweep angles, different planform shapes such as cropped delta wings undergoing small amplitude rolling motion, and different forcing modes. In Chapter 5, the flowfield over a simple delta wing undergoing small amplitude rolling motion was studied, whereas in this chapter small amplitude pitching motion is also investigated. The objective of this chapter is to identify if the different sweep angles and planforms have the same response to the oscillatory motion, and additionally compare the effect of small amplitude pitching and rolling motions on the flowfield of a simple wing.

Different models had to be built in order for this part of the project to be completed. Two simple delta wing models were built, with $\Lambda = 40°$ and 30° with the purpose of studying the effect of the sweep angle. The span was the same as the $\Lambda = 50°$ wing, hence, due to the change in chord length, the Reynolds number also changed, $(U_\infty = 30\,\text{cm/s})$. Hence, for $\Lambda = 40°$ wing, $\text{Re} = 18{,}800$ and for $\Lambda = 30°$, $\text{Re} = 12{,}900$. The effects of the different planform shapes were studied using $\Lambda = 50°$, 40°, 30° and 20° cropped delta wings. Two more cropped wings were built $(\Lambda = 10°$ and 0° (a square plate)) but were never actually tested. The reasons are explained in Section 6.3, where the planform shape effect is discussed. For the pitching motion, a $\Lambda = 50°$ simple delta wing was used.

6.2 Sweep Angle Effect

The effect of the sweep angle on a delta wing undergoing small amplitude oscillations was studied using a $\Lambda = 40°$ and a 30° model. From the previous chapter the optimum frequency was found to be in the range of $f_r = 1$ to 2. Hence, for the study of the sweep angle effect, a stationary wing was compared to one oscillating with $f_r = 1.2$, with the objective of ascertaining whether the same results could be obtained with wings of differing sweep angles.

Flow visualisation images were captured for a wide range of frequencies to ensure a reasonable comparison with the previous results. However, only results from the stationary case and a selected frequency are presented. This provides quantitative data on the flow, and enhances our understanding of its features. The rest of the flow visualisation images were used for the calculation of the breakdown location, which is discussed later.

For the aforementioned reasons, flow visualisation was conducted on the $\Lambda = 40°$ delta wing for $f_r = 0$ and 1.2, and the results are shown in Figure 6.1. Three different incidences were tested, to ensure consistency with the previously obtained results, in a small amplitude $(\Delta\phi = 5°)$ rolling motion. For $\alpha = 15°$, in the stationary case, the vortices seem to break down at the apex of the wing. However, the flow reattaches. Considering the fact that the lower sweep angle promotes earlier vortex breakdown compared to a higher one, the results are expected. For $\alpha = 20°$, the flow appears to be stalled for the stationary wing. Reformation of the leading edge vortices and vortex breakdown are visible at both incidences for the oscillating wing. At the largest incidence, $\alpha = 25°$, the completely stalled flow on the stationary wing becomes reattached with wing oscillations.

These first results on a lower sweep angle delta wing show that the oscillatory motion can actually regenerate the attachment line and promote vortex reformation, confirming the results obtained for the $\Lambda = 50°$ delta wing. Hence, similar response to the small amplitude motion is observed.

For the oscillatory wing at higher incidences, vortex breakdown may occur at the apex, but flow reattachment is still possible. In order to quantify the effect of excitation on the stalled flow, the quantity Δy_w was defined as the distance between the broken down wakes at midchord, as shown in Figure 3.2. This was nondimensionalised with the local span $(2s)$. Although this is not directly related to the reattachment line, it gives a measure of the effect of excitation on the flow. Additionally, the calculation of the vortex breakdown location was proven to be difficult and inaccurate in this case, therefore the quantity Δy_w provided an effective tool for the definition of vortex reformation. Figure 6.2 shows the variation of this parameter as well as breakdown location as a function of dimensionless frequency at $\alpha = 15°$. The variation of this parameter is very similar to that of the breakdown location, and both curves show a peak at around the same optimum frequency. The parameter Δy_w can easily be measured, and is more reliable; hence it was calculated

for all the delta wings tested in this chapter. Figure 6.3 shows the variation of the parameter Δy_w as a function of dimensionless frequency, at three different incidences. Optimum frequencies for all three cases are around $f_r = 1$.

As mentioned earlier, a $\Lambda = 30°$ simple delta wing was also tested in order to evaluate the effect of the sweep angle on the flowfield of a wing undergoing a small amplitude motion. Figure 6.4 shows flow visualisation images for a $\Lambda = 30°$ delta wing at various angles of attack, for stationary and oscillating cases. Again, only one frequency is presented here, $f_r = 1.2$. In all cases, except for the largest angle of attack $(\alpha = 25°)$, flow reattachment occurs over the wing for roll oscillations at $f_r = 1.2$. Since stall occurs at a smaller incidence $(\alpha \approx 15°)$ for this wing, the implementation of an oscillation is beneficial around that range, but does not seem to have an effect at all at $\alpha = 25°$. Notice that at $\alpha = 10°$, the flow is still attached in the stationary case, although the vortices seem to have broken down at the apex, whereas by employing oscillatory motions, vortices are reformed, and reattachment is enhanced.

Figure 6.5 shows the variation of the parameter Δy_w as a function of dimensionless frequency for $\alpha = 10°$, 15°, and 20°. Again, the optimum frequency is around $f_r = 1$, which is similar to the results for $\Lambda = 50°$ and 40° delta wings. A distinct feature for the largest incidence, $\alpha = 20°$, is observed in Figure 6.5: for frequencies much higher than the optimum frequency, flow reattachment becomes impossible.

Reattachment is a generic process for all nonslender delta wings and there is an optimum frequency range between $f_r = 1$ and 2, which is observed with the implementation of a small amplitude rolling motion, giving the flowfield an antisymmetric character. The excitation of the shear layer, which is accomplished by this antisymmetric motion, results in earlier reattachment and vortex reformation for all the low sweep delta wings. However, the effect of the sweep angle on the vortex breakdown and, consequently, stall, is known and should not be ignored, since it has a substantial influence on the vortex reformation.

6.3 Planform Shape Effect

Cropped delta wings were also studied in order to investigate the effect of planform shape on the results, in particular on the optimum frequency. Six different cropped delta wings were designed, with sweep angles $\Lambda = 50°$, 40°, 30°, 20°, 10° and 0°. Only four of these, however, were finally tested, for reasons that will become apparent in the following analysis.

Figure 6.6 shows flow visualisation pictures that reveal the effect of dimensionless frequency for a $\Lambda = 50°$ cropped delta wing undergoing a small amplitude rolling motion, at $\alpha = 25°$. The results seem to be qualitatively very similar to those for a simple delta wing with the same sweep angle. The stalled flow that appears in the stationary case is being replaced by reattached flow and vortex reformation, in the

presence of the rolling motion. Interestingly enough, reattachment appears at $f_r = 0.3$, which coincides with the frequency at which reattachment appears on the $\Lambda = 50°$ simple delta wing. Additionally, notice the deterioration in the vortical flowfield at high frequencies $(f_r = 4)$. So far, the effect of the planform on the results seems to be unimportant, as they appear similar to that of the simple wing with the same sweep angle.

The wake distance was calculated from the flow visualisation images. Figure 6.7 shows the variation of the parameter Δy_w as a function of dimensionless frequency for $\alpha = 25°$. For comparison, the variation of breakdown location for the simple delta wing at the same angle of attack is shown (Figure 6.7). The results are quantitatively very similar, and indicate optimum frequencies in the range of $f_r = 1$ to 2.

The effect of wing oscillations at various incidences for selected frequencies, $f_r = 0$, 1 and 2 for cropped delta wings with $\Lambda = 40°$, 30°, and 20° is shown in Figure 6.8, 6.9 and 6.10, respectively. The frequencies tested and presented were selected based on the optimum frequency range. For $\Lambda = 40°$ and 30°, earlier reattachment at low incidences, and reattachment of completely stalled flow at higher incidences, are very similar to previous observations for other wings. Notice that for the $\Lambda = 40°$ cropped wing, immediate reformation of the vortices takes places in the presence of the oscillatory motion at $\alpha = 15°$, where the vortices break down at the apex for the stationary wing. Additionally, stall takes place at a lower incidence, and vortex reformation occurs only due to the effect of the higher frequencies.

The same behaviour is observed in the $\Lambda = 30°$ cropped wing in Figure 6.9. Lower incidences had to be tested in this case because breakdown and stall occurred earlier. In the stall area, at $\alpha = 15°$ and 20°, the oscillations promote reattachment, but not vortex reformation. Although the effect of dimensionless frequency was not studied as a parametric study for these cases, the oscillations at $f_r = 2$ appear to be more effective than those at $f_r = 1$. However, as can be seen in Figure 6.10 for the $\Lambda = 20°$ wing, it is clear that wing oscillations do not cause reattachment, and furthermore do not seem to have any effect at all on the flowfield. Hence, there appears to be a lower limit of sweep angle below which the beneficial effect of the oscillatory motion diminishes. This value is at around $\Lambda = 20°$. For this reason, the $\Lambda = 10°$ and the $\Lambda = 0°$ cropped delta wings were not tested.

While work in previous chapters was mainly focussed on a sweep angle of 50°, this chapter shows that shear layer reattachment and vortex reformation are also possible for lower sweep angles. For the $\Lambda = 50°$, 40°, and 30° simple and cropped delta wings studied, at various angles of attack, an optimum frequency of around $f_r = 1$ was identified. Either the breakdown location (measured from the apex), or the distance between the broken down wakes (a rough measure of the distance between the reattachment lines) was found to be a maximum at this frequency, indicating a similar response to the effect of small amplitude oscillations on the flowfield of a simple delta wing.

6.4 Effect of Symmetric Excitation

In order to investigate the effect of symmetric versus antisymmetric perturbations, it was necessary to employ symmetric wing oscillations. Additionally, the interest in studying the effect of different forcing modes, particularly the effect of the motion in the range of the optimum frequency, required the implementation of pitching motion.

Symmetric perturbations in the form of small amplitude pitching oscillations $(\Delta\alpha = 1°)$ were studied for a $\Lambda = 50°$ simple delta wing. The pitching axis was located at 1.12 chord lengths downstream of the wing. The results from the flow visualisation are shown in Figure 6.11 for $\alpha = 25°$. The same range of frequencies was tested to enable comparison with the small amplitude rolling motion. Again, the pitching wing shows signs of earlier reattachment, and even reformation, of the leading edge vortex for increasing dimensionless frequency. It is interesting that the earlier reattachment takes place at the same frequency as in the rolling case, $f_r = 0.5$ (see Figure 5.13). Although relatively high frequencies were not tested under the pitching oscillation due to limitations of the pitching mechanism, it is evident that the pitching motion becomes more beneficial with increasing frequency.

The vortex reformation was very clear under the pitching motion, hence the vortex breakdown location was calculated. Figure 6.12 shows a comparison of the variations in the breakdown location as a function of dimensionless frequency for pitching and rolling oscillations of equal amplitude $\Delta\alpha = 1°$ and $\Delta\phi = 1°$. Small amplitude symmetric oscillations appear to be more effective. However it is not possible to make a direct comparison of which forcing mechanism (symmetric versus antisymmetric) is more efficient, as the leading edge velocity perturbations are vastly different in their geometric form. Nevertheless, the results show that symmetric perturbations also promote reattachment and vortex reformation.

For active control purposes, both symmetric and antisymmetric excitations are effective. Evidence of the fact that excitations cause earlier reattachment can also be found on Yaniktepe and Rockwell (2004) and Yavuz *et al.* (2004). However, passive control for a flexible wing occurs only in the antisymmetric mode (Taylor and Gursul-2004a, Taylor *et al.*-2005 and Vardaki *et al.*-2005).

This chapter proves that flow reattachment and vortex reformation followed by the application of a small amplitude oscillatory motion is not limited on the $\Lambda = 50°$ simple delta wing but can observed on other simple nonslender wings $(\Lambda = 40°,$ $30°)$. Additionally, the same phenomena were observed in different nonslender planform shapes, such as cropped wings. However, there is a lower limit to the sweep angle, which in this case was found to be $\Lambda = 20°$. Finally, the implementation of a symmetric excitation (in the form of a pitching motion) was found to present similar characteristics to the flowfield of a $\Lambda = 50°$ simple delta wing undergoing antisymmetric oscillations.

6.5 Figures Chapter 6

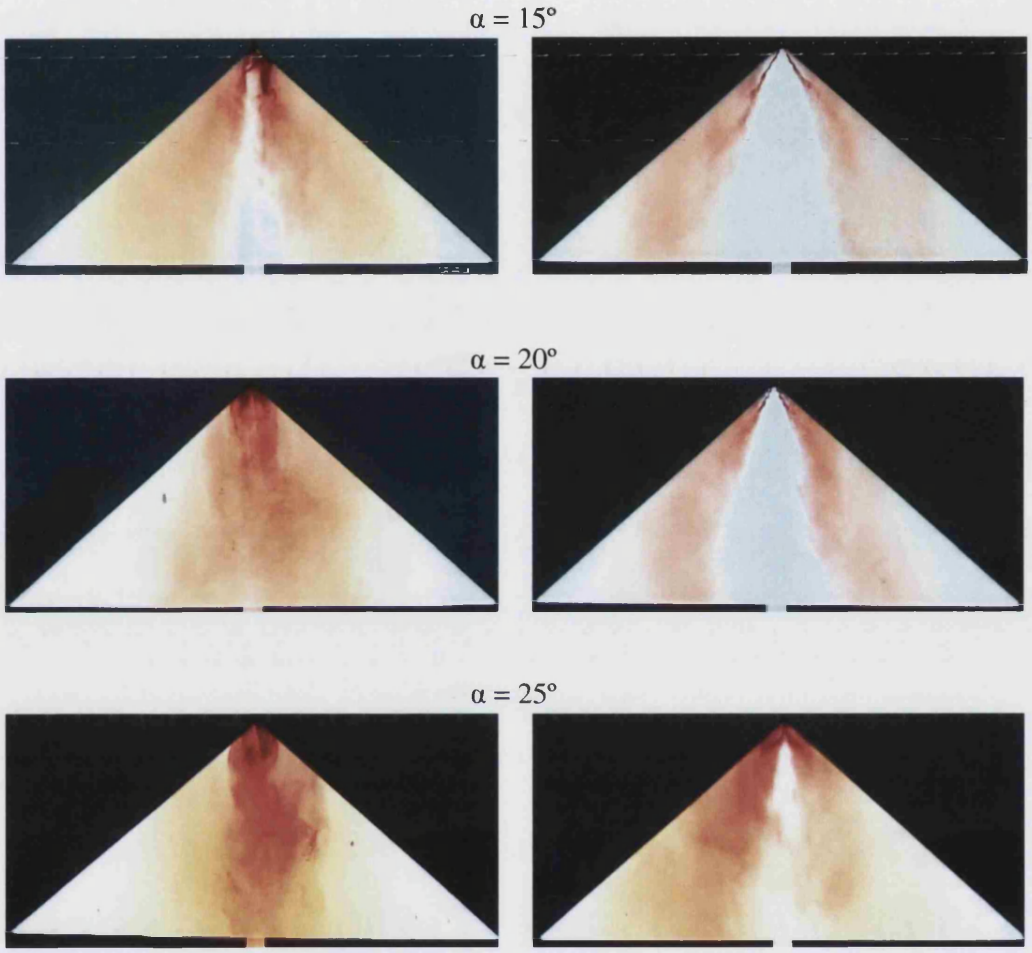

Figure 6.1: Effect of dimensionless frequency, $f_r = 0$ (*right side*), $f_r = 1.2$ (*left side*) on $\Lambda = 40°$ delta wing at different incidences under small amplitude $(\Delta\phi = 5°)$ rolling motion.

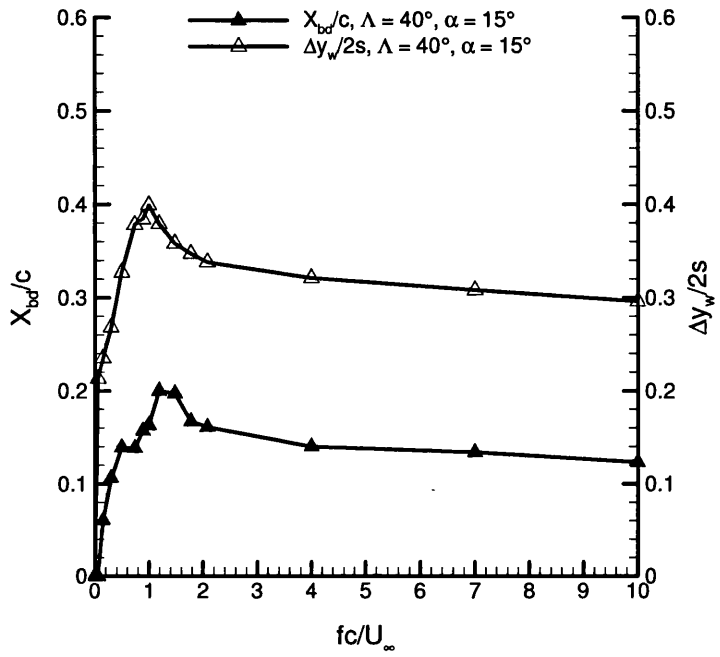

Figure 6.2: Variation of the breakdown location and the wake distance as a function of the dimensionless frequency at $\alpha = 15°$ on a $\Lambda = 40°$ delta wing.

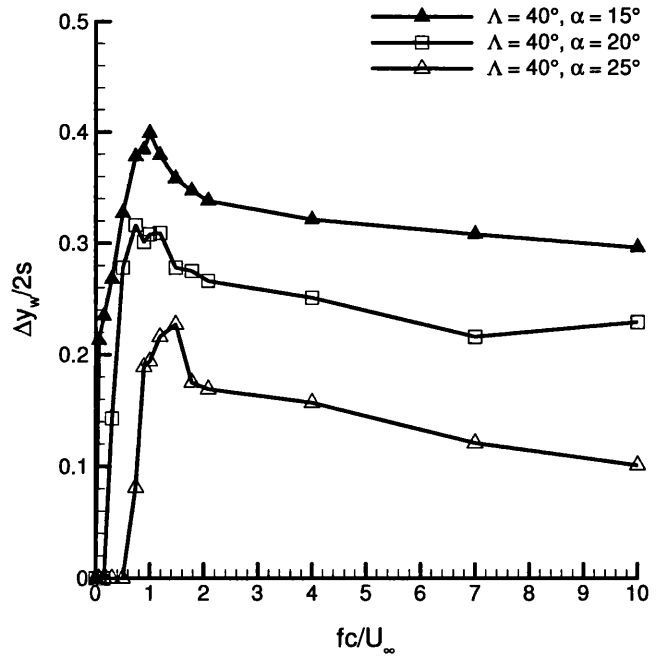

Figure 6.3: Variation of the mean wake distance as a function of the dimensionless frequency, at different incidences, for a $\Lambda = 40°$ delta wing.

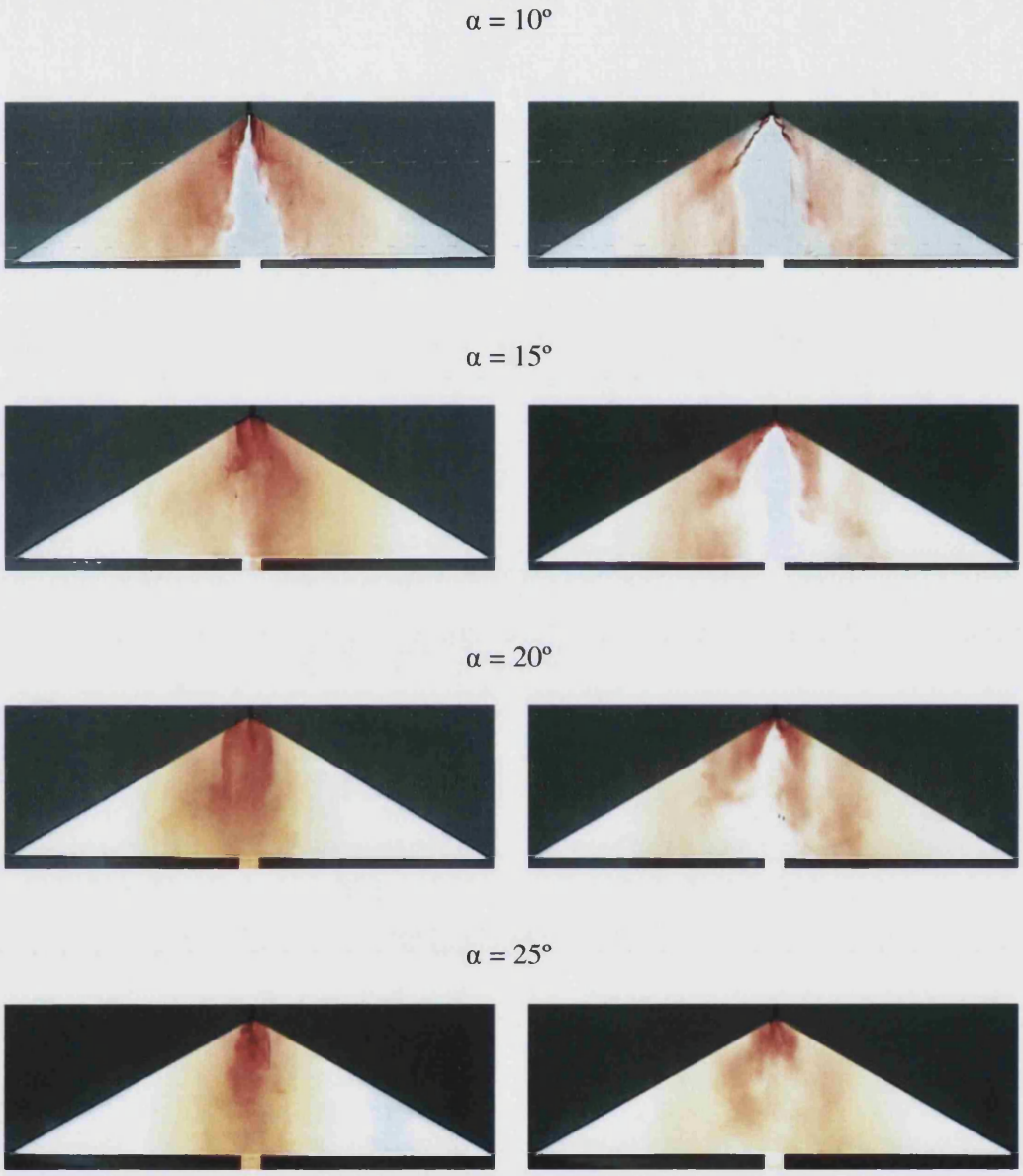

Figure 6.4: Effect of dimensionless frequency, $f_r = 0$ (*right side*), $f_r = 1.2$ (*left side*) on $\Lambda = 30°$ delta wing at different incidences under small amplitude $(\Delta\phi = 5°)$ rolling motion.

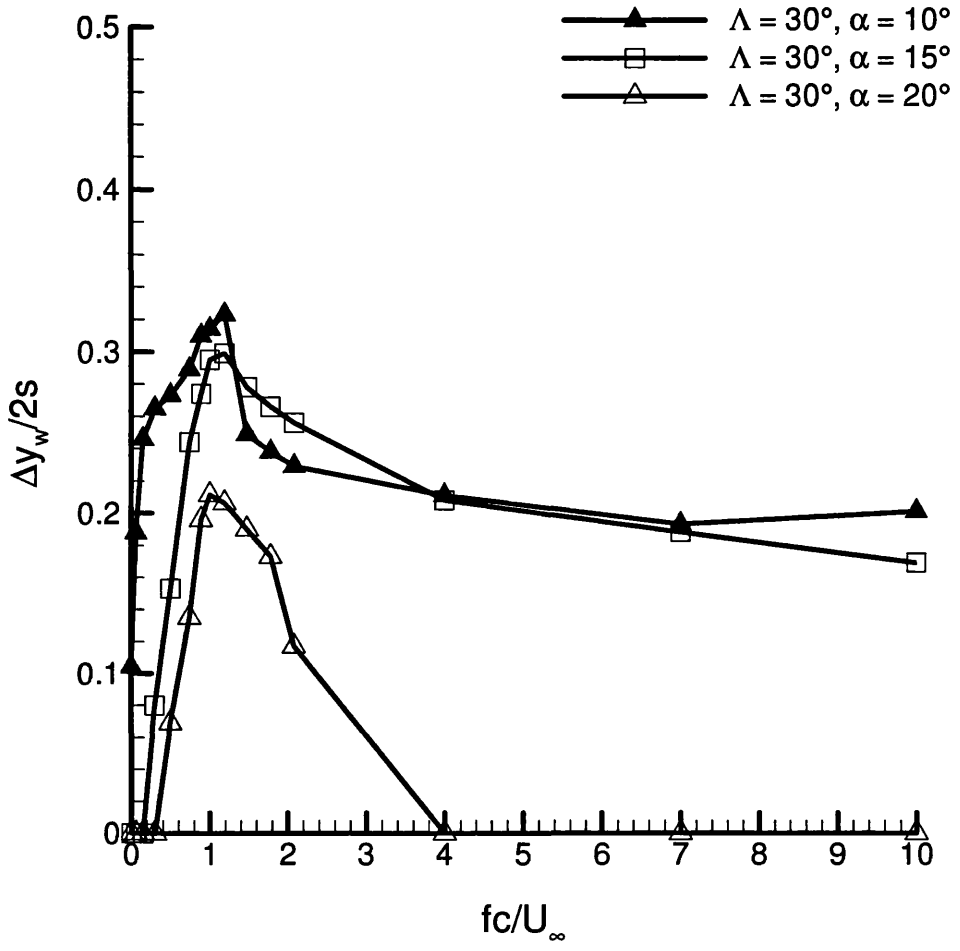

Figure 6.5: Variation of the mean wake distance as a function of the dimensionless frequency, at different incidences, for a $\Lambda = 30°$ delta wing.

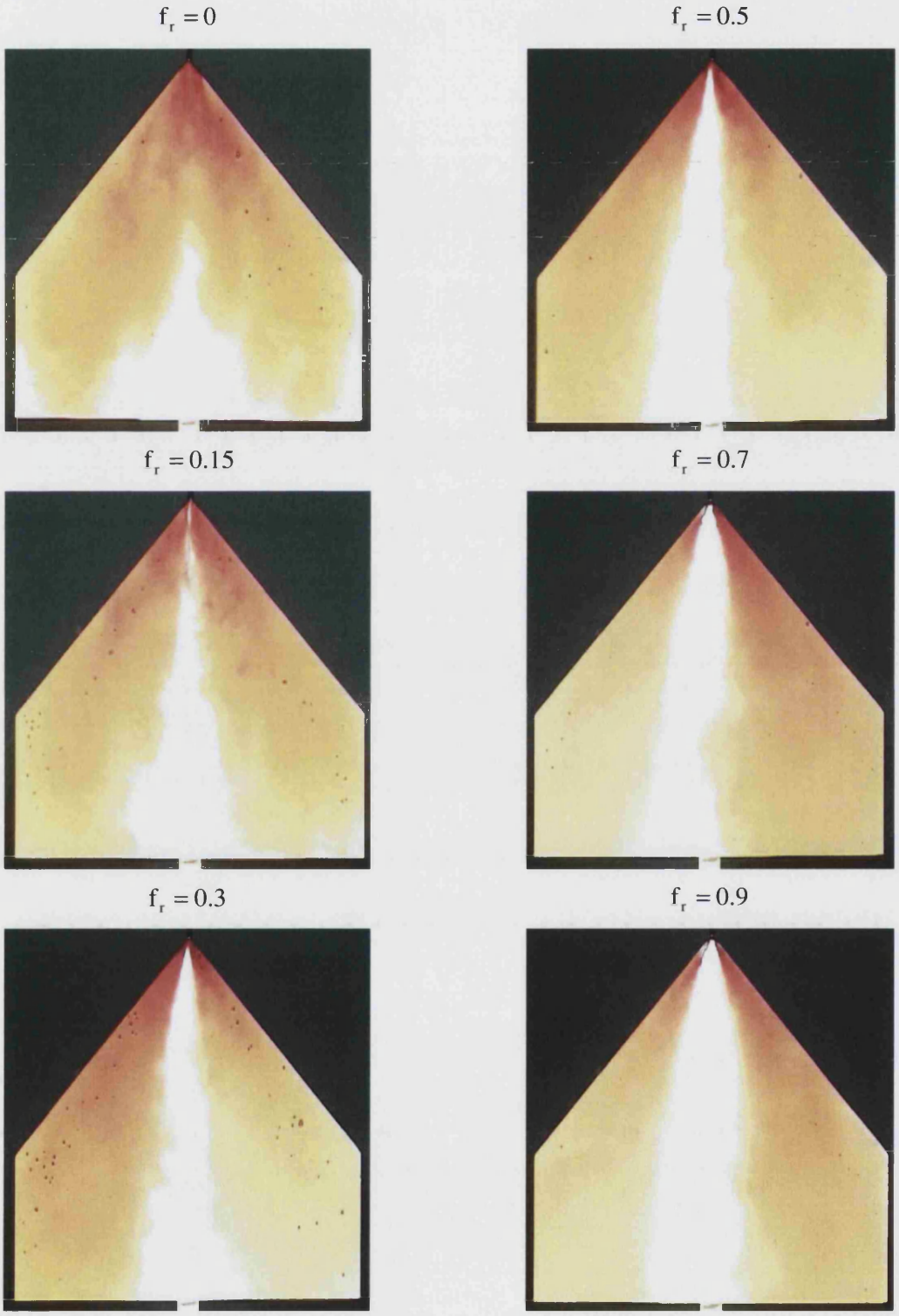

Figure 6.6: Effect of dimensionless frequency, on a $\Lambda = 50°$ cropped delta wing at $\alpha = 25°$ under small amplitude $(\Delta\phi = 5°)$ rolling motion.

$f_r = 1.2$

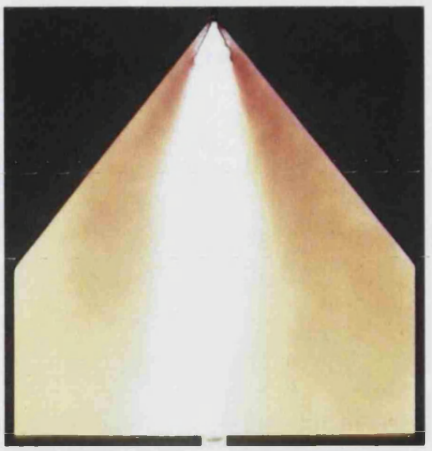

$f_r = 1.8$

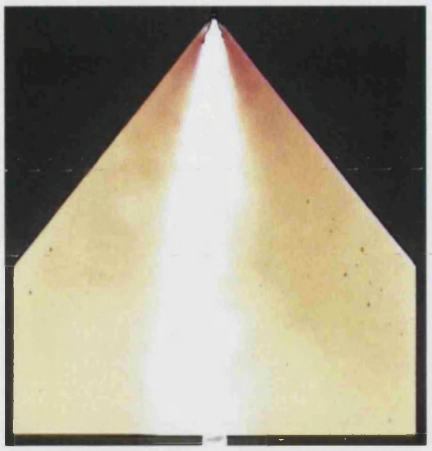

$f_r = 1.5$

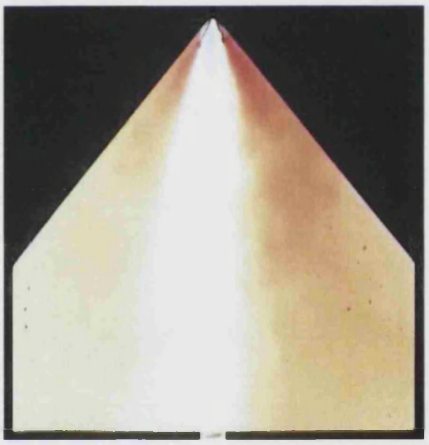

$f_r = 2.1$

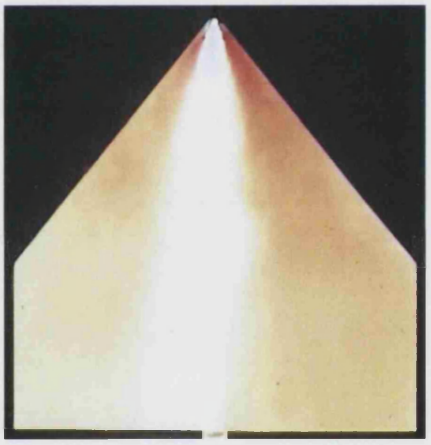

$f_r = 4$

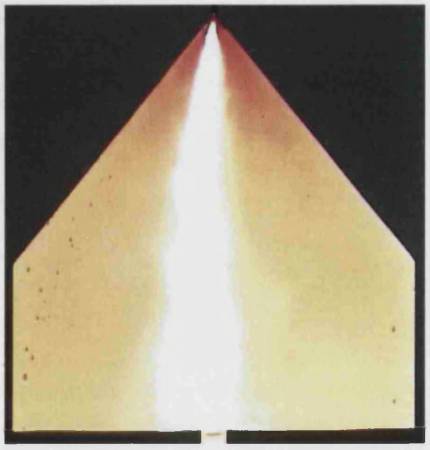

Figure 6.6: continued

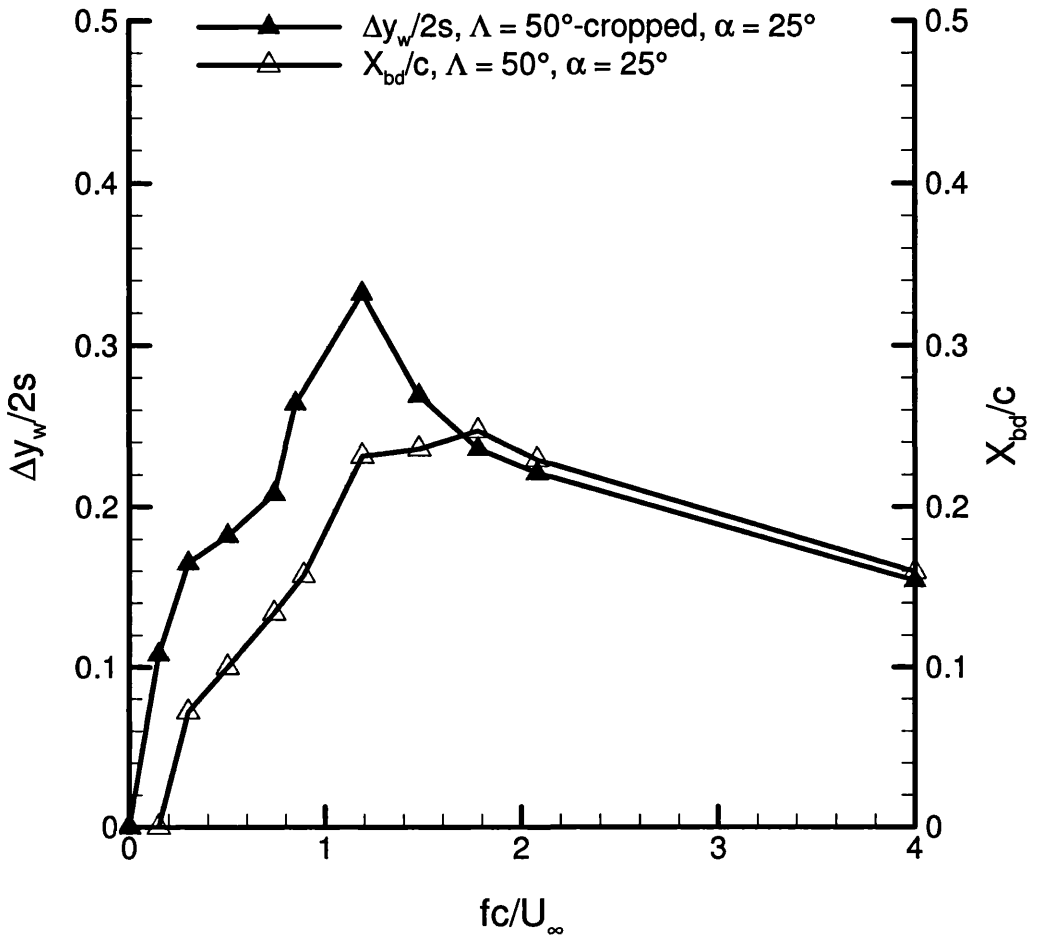

Figure 6.7: Variation of the mean wake distance and the breakdown location as a function of the dimensionless frequency, at $\alpha = 25°$, for a $\Lambda = 50°$ cropped and simple delta wing.

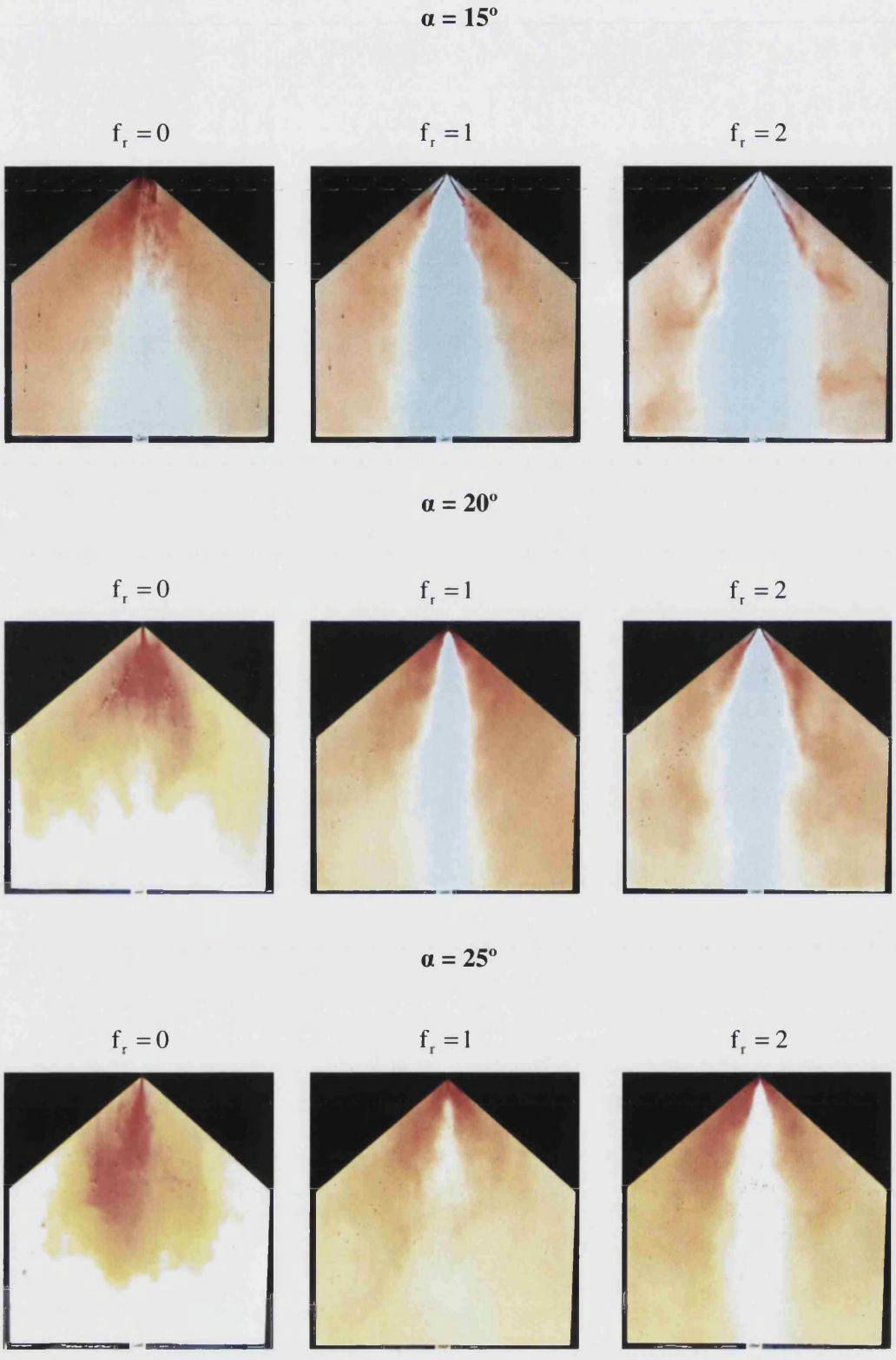

Figure 6.8: Effect of dimensionless frequency, on a $\Lambda = 40°$ cropped delta wing at different incidences under small amplitude $(\Delta\phi = 5°)$ rolling motion.

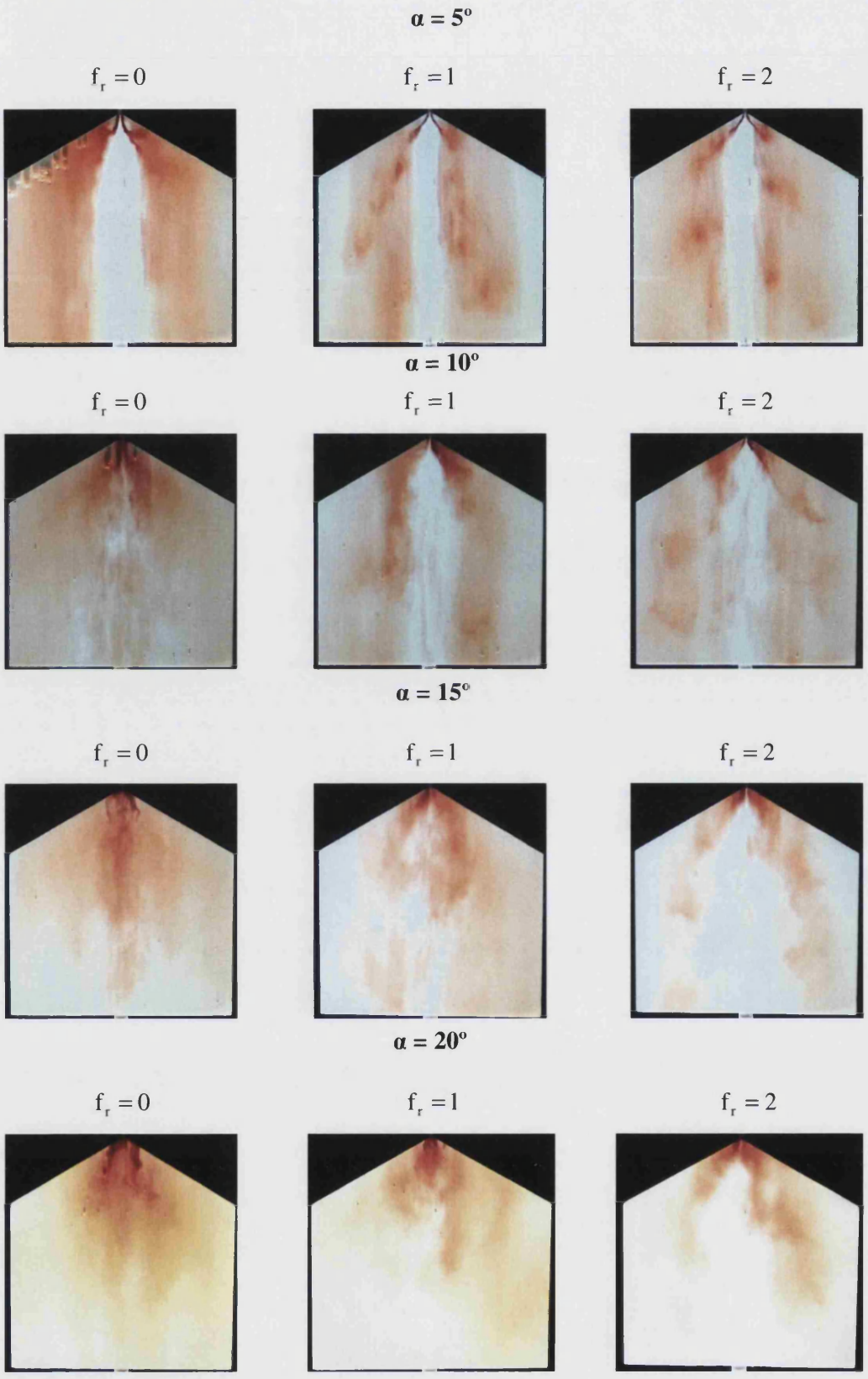

Figure 6.9: Effect of dimensionless frequency, on a $\Lambda = 30°$ cropped delta wing at different incidences under small amplitude $(\Delta\phi = 5°)$ rolling motion.

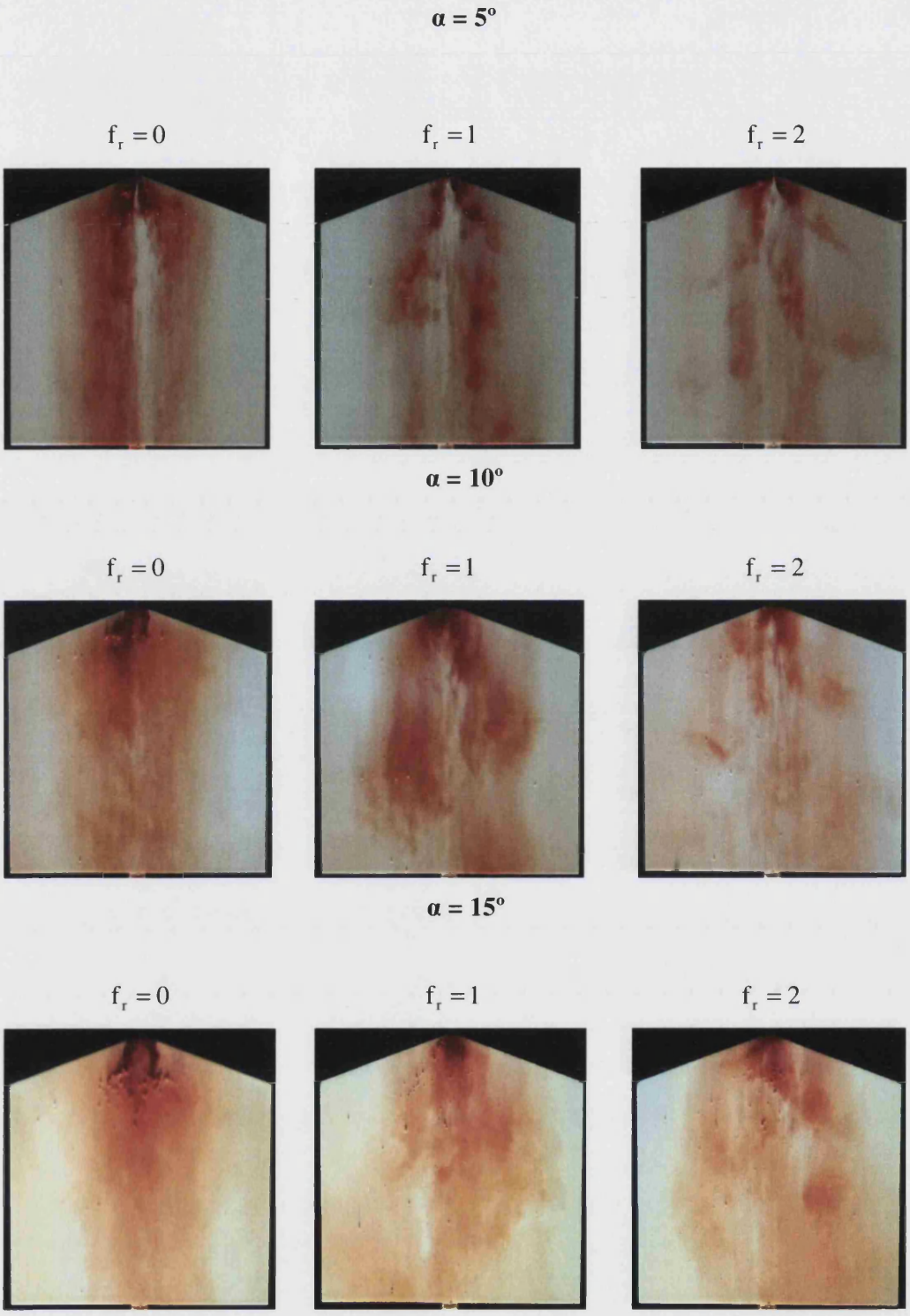

Figure 6.10: Effect of dimensionless frequency, on a $\Lambda = 20°$ cropped delta wing at different incidences under small amplitude $(\Delta\phi = 5°)$ rolling motion.

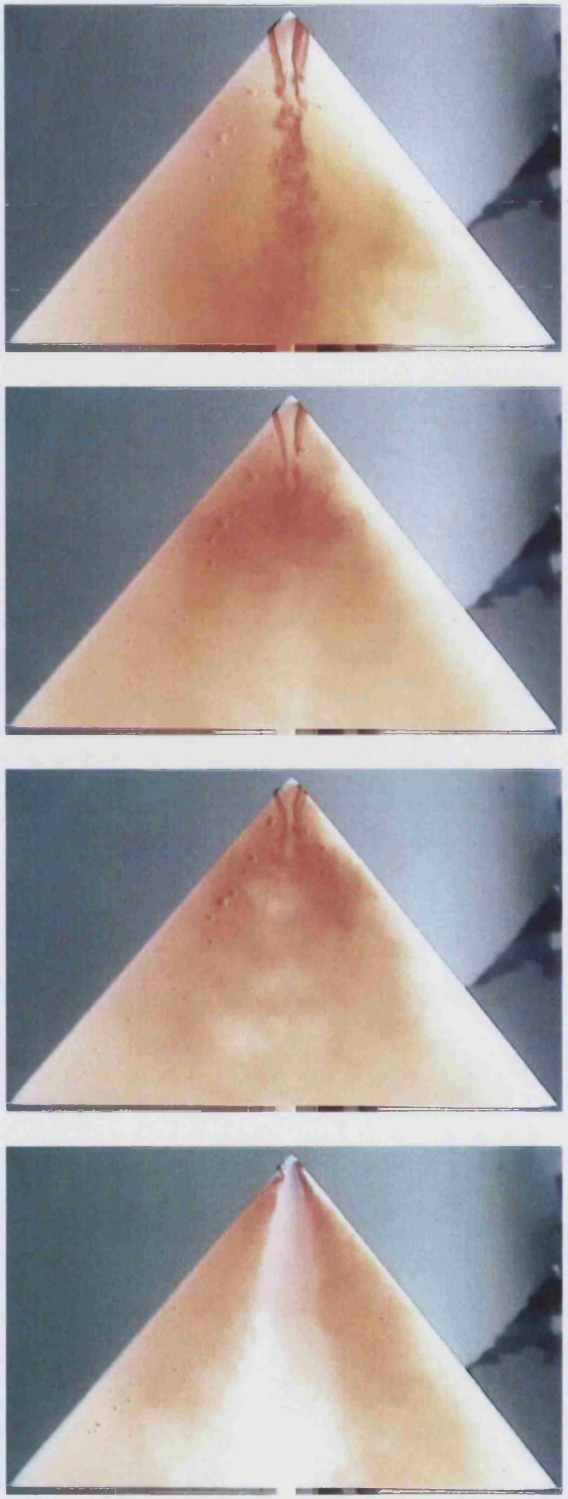

Figure 6.11: Effect of dimensionless frequency, f_r, on $\Lambda = 50°$ delta wing at $\alpha = 25°$ under small amplitude $(\Delta\alpha = 1°)$ pitching motion.

$f_r = 0.7$

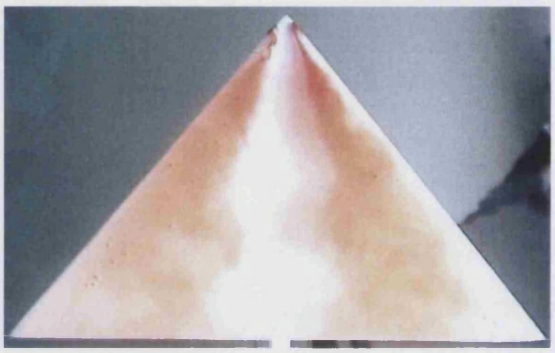

$f_r = 0.9$

$f_r = 1$

$f_r = 1.2$

Figure 6.11: continued

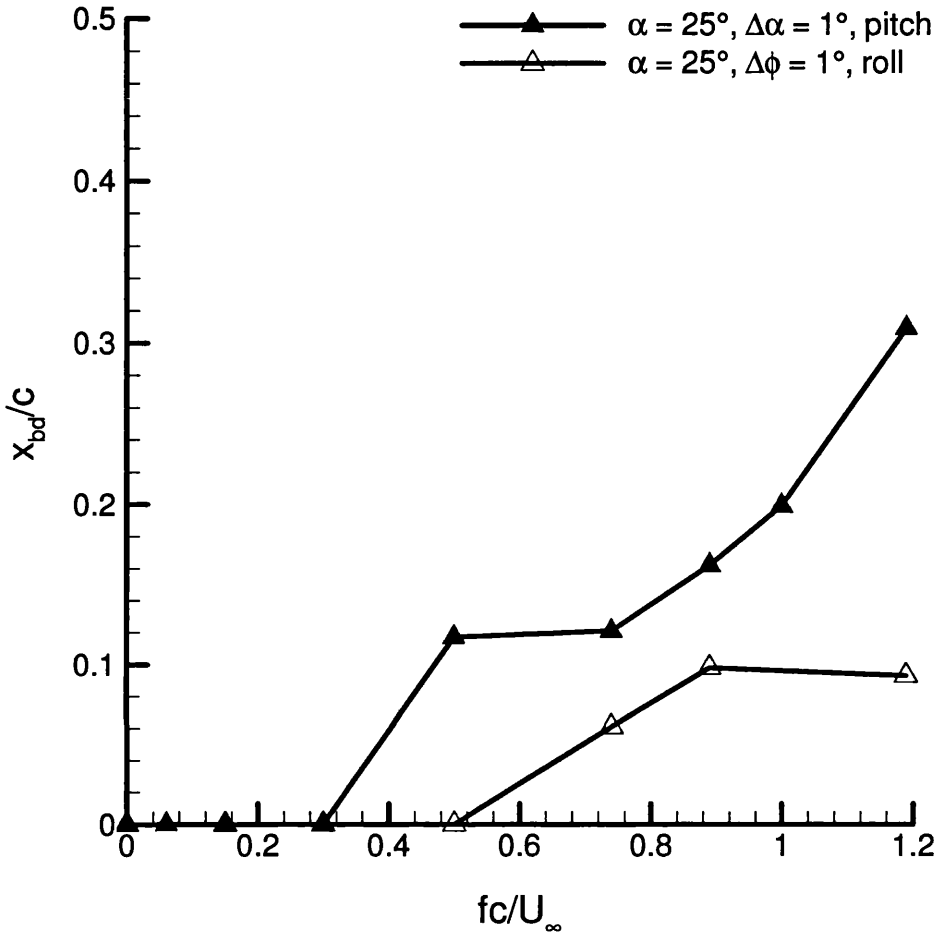

Figure 6.12: Variation of the mean breakdown location as a function of the dimensionless frequency, at $\alpha = 25°$, under small amplitude pitching and rolling motion.

CHAPTER 7: LARGE AMPLITUDE MANOEUVRES OF NONSLENDER DELTA WINGS

7.1 Introduction

The final chapter of results obtained from this project deals with large amplitude rolling manoeuvres of both rigid and flexible delta wings. Only the $\Lambda = 50°$ delta wing is examined. Two out of the four flexible delta wings were tested: the two most flexible ones, with $\lambda = 9$ and 21.3. The results for the flexible wings compare the dynamic with the static case, but an additional comparison is made with the rigid wing under the same conditions. Moreover, additional measurements on rolling manoeuvres, starting from a nonzero roll angle, are presented in the final pages of this chapter. The aforementioned experiments were conducted at $Re = 26{,}600$.

The aim of this chapter is to study and understand the unsteady structure of the vortical flow over a $\Lambda = 50°$ delta wing, at moderate and high angles of attack, undergoing a large amplitude and low frequency rolling manoeuvre, as well as to identify the differences compared to a stationary case.

7.2 Large Amplitude Manoeuvres of Rigid Delta Wings

Both the dimensionless frequency ($f_r = 0.01$, 0.03, 0.06 and 0.15) and the roll angle ϕ were varied, to test the rigid wing undergoing a large amplitude manoeuvre. Videos were recorded for the flow visualisation cases, and specific roll angles were selected for the images that were later on captured and processed. Two different manoeuvres were tested, with the difference being in the maximum roll angle. As such, the maximum roll angles were selected to be $\phi_{max} = 30°$ and 40°. The instantaneous images were captured at $\phi = 0°$, 15°, 30° and $\phi = 0°$, 20°, 40°, for the

two manoeuvres respectively. Additionally, three different incidences were tested, $\alpha = 15°$, 20° and 25°.

Although flow visualisation videos were recorded for all the different cases, it was considered best to present images from the lowest $(f_r = 0.01)$ and highest $(f_r = 0.15)$ frequency manoeuvres, along with a direct comparison with the static case. For the rest of the videos, information was extracted, and the results were plotted and presented. The arrows drawn in all flow visualisation images presented in this report indicate the direction of the rolling motion for both static and dynamic conditions.

In Figure 7.1, flow visualisation images are presented at $\alpha = 15°$ for the stationary case $(f_r = 0)$, and the $\phi_{max} = 30°$ manoeuvre, for the smallest dimensionless frequency $(f_r = 0.01)$. In these images, the positive roll angle is defined as the port wing tip (the left tip as viewed in Figure 7.1) upwards. This results in an increase in the effective sweep of that leading edge, and a decrease on that of the starboard tip (the right tip as viewed in Figure 7.1). In the stationary case, and for a zero roll angle, the vortices are very well defined and their breakdown takes place on the wing surface. However, the variations in the breakdown location for both sides of the wing are relatively small, as the roll angle is varied. A closer look at these photos reveals that the wake on the left side of the wing gradually decreases with increasing roll angle.

In the dynamic case, the vortex breakdown location moves closer to the trailing edge for the clockwise vortex (left vortex as viewed in the image), suggesting a small, but nonetheless beneficial feature following this slow manoeuvre. The increasing roll angle, in combination with the increase in the effective sweep angle, delays the vortex breakdown when compared to the static case. Notice that the vortex breakdown location is more pronounced and clear in the dynamic case, due to the well defined expansion and following wake, which again decreases in the presence of the roll angle on the left side.

The highest frequency manoeuvre that was recorded is presented in Figure 7.2, along with a direct comparison with the stationary case. For this case, promotion of the vortex breakdown seems to prevail, when compared to the stationary case for both the vortices on the wing. Notice that for the same roll angles, vortex breakdown takes place a lot closer to the apex than that in the static wing (see for example the image for $\phi = 30°$ and both the images for the $\phi = 15°$ case). The effect of the rolling manoeuvre under both frequencies was proved to create a considerable variation on the flowfield. The lower frequency case seemed to be beneficial by delaying breakdown when compared to the stationary case, whereas in the higher frequency case, the opposite effect was observed.

For the static case, PIV measurements of vorticity field in the crossflow plane at $x/c = 0.8$ and $\alpha = 15°$ were recorded for four different roll angles, and are presented in Figure 7.3. The observations from the flow visualisation images are consistent with these PIV measurements. The increase in vorticity magnitude due to the increasing roll angle is evident and significant, as the leading edge vortex on the left

side becomes more coherent, while the opposite is noticeable on the other side. There is a suggestion of a dual vortex structure with the same sign of vorticity for the clockwise vortex at $\phi = 30°$, a feature only observed in nonslender delta wings.

Instantaneous images, at specific roll angles, were captured from the flow visualisation videos and the vortex breakdown location was calculated. Thirty instantaneous images were averaged in each case, and the nondimensional mean breakdown location against the roll angle was plotted for each of the cases. A summary of the findings for all the different manoeuvres is shown in Figure 7.4. The static case and all four dynamic cases in ascending order are compared. The arrow shows the direction of the rolling motion for the dynamic condition. The breakdown position measured from the apex of the delta wing is normalised with the chord length.

There is little variation observed in the breakdown location with increasing roll angle in the static case (first graph in Figure 7.4). There is, however, a delay in the breakdown location in the clockwise vortex as the positive roll angle increases. This is countered by the corresponding promotion of the onset of breakdown in the counter-clockwise vortex. This trend may be explained if the effect associated with an increase or decrease in the effective sweep angle is taken into account. In the case of the clockwise vortex, the effective sweep angle is increased, and consequently the breakdown location is delayed, with the opposite taking place for the counter-clockwise vortex. Due to this effect, maximum delay would be expected at maximum roll angles (30° or -30°). This is shown not to be the case in the first graph in Figure 7.4. The maximum breakdown position is at approximately 58% of the chord length for the clockwise vortex and takes place at a roll angle of 10°. On the other hand, for the counter-clockwise vortex, that maximum breakdown position takes place at about 40% of the chord length, for all roll angles apart from one. At 20°, in fact, the breakdown position is at 35%. Measurements of the breakdown location for the static case were only taken for the positive roll angles, as the negative ones are expected to be the same, due to symmetry.

Interestingly, the highest frequency case correlates very well with the static case, in the sense that the maximum breakdown location does not differ much at high roll angles. However, at the lowest frequency $(f_r = 0.01)$, the maximum breakdown position, at 60% of the chord length, is achieved at the highest roll angle. A reasonable symmetry between the two sides of the wing is evident in the dynamic cases, together with an increasing hysteresis at higher frequencies, especially at $\phi = 0°$. There is little variation in the breakdown location between the static case and the two dynamic cases, agreeing with observations from flow visualisation images.

The rolling manoeuvre creates a different pattern in the breakdown location, with the maximum positive and negative roll angle presenting the maximum delay in breakdown of the clockwise and counter-clockwise vortices respectively. Notice the decrease in the variation of the breakdown location with increasing frequency. At $f_r = 0.01$ the maximum breakdown is at around 62% of the chord length, and reduces down to almost 48% in the $f_r = 0.15$ case. Also notice the increase in the

hysteresis in the highest frequency case, which is attributed to the higher forces applied on the wing. A very good symmetry is observed between the two vortices in the dynamic case. It is seen that the dynamic motion does not necessarily imply a beneficial character, in the sense that it does not always delay the vortex breakdown. In general, at an incidence where the vortices still exist over the delta wing, and breakdown takes place on the wing surface, a very low frequency manoeuvre seems to act in a more constructive way compared to a higher frequency or static cases, as a considerable delay in the breakdown location is observed.

Changing the manoeuvre slightly by increasing the maximum roll angle to 40° changes the flow significantly. Figures 7.5 and 7.6 show flow visualisation images for a $\phi_{max} = 40°$ manoeuvre at $\alpha = 15°$, and for $f_r = 0.01$ and 0.15. The selected instantaneous roll angles for these manoeuvres were $\phi = 0°$, 20°, 40°. In the static case, a considerable movement of the breakdown location towards the trailing edge is observed at the maximum roll angle, attributed to the beneficial effect of the effective sweep angle for the port side of the wing. Very clear and coherent streamwise vortices are observed along the whole range of static roll angles for both sides of the wing (Figure 7.5). Additionally, evidence of dual vorticity is apparent at $\phi = 20°$ and 40° on the port side of the wing.

The low frequency rolling motion adds to the favourable character that the static roll angles introduced to the wing flowfield, by delaying the breakdown even further. Even at zero roll angle, the manoeuvring wing delayed the vortex breakdown, moving it closer to the trailing edge. However, at the maximum roll angle $\phi = 40°$, the dynamic motion seems to promote earlier breakdown of the counter-clockwise vortex when compared to the stationary case. Note also the adverse effect on the clockwise vortex, which seems to break down earlier in the dynamic case. Consequently, the dynamic motion in this case seems to create a favourable effect in the breakdown location at zero roll angle, by moving it closer to the trailing edge. Such a result can lead to the conclusion that a high amplitude and very low frequency rolling motion is not particularly advantageous for the flowfield for which vortices still exist over its surface since the adverse effects of the manoeuvres start taking place at high roll angles (40°).

Great differences are observed when the frequency of the manoeuvre is increased (Figure 7.6). A large asymmetry is observed at zero roll angle between the two vortices, and a movement of the breakdown location towards the apex is detected. This is particularly the case at the maximum roll angle $(\phi = 40°)$. At $\phi = 40°$, in the static case, the clockwise vortex remains coherent throughout most of the wing, whereas in the dynamic case, on the other hand, breakdown occurs before reaching 50% of the chord length. Although the $\phi_{max} = 30°$ manoeuvre created little but beneficial effect on the breakdown location for small roll angles, it seems that the $\phi_{max} = 40°$ manoeuvre at $\alpha = 15°$ has a somewhat unfavourable effect on the flowfield.

A summary of the variation in breakdown location for all the cases is shown in Figure 7.7. In the stationary case, the breakdown location reaches almost 90% of the chord length at the maximum roll angle, which, conversely does not occur in any of the dynamic cases. It is interesting to observe the dramatic movement in the breakdown location towards the trailing edge after $\phi = 30°$. With increasing frequency, the average breakdown location appears to move closer to the apex, and hysteresis is also enhanced. In all dynamic cases, the zero roll angle presents the largest hysteresis effect. However, reasonable symmetry is observed between the two sides of the wing during the rolling motion.

Although the general trend in the low frequency cases ($f_r = 0.01$ and 0.03) is for the vortex breakdown on the side undergoing the beneficial sweep angle effect to move further from the apex with increasing roll angle, the same cannot be claimed for the higher frequency cases ($f_r = 0.06$ and 0.15). The breakdown location at the maximum roll angle in these cases either moves towards the apex, or remains unchanged compared to the zero roll angle case. The conclusion from this set of results can be summarised by the fact that the application of a high amplitude rolling motion into a fully developed flowfield with coherent vortices, might not necessarily lead to its improvement in terms of the breakdown location. Furthermore, it may in some cases have an adverse effect on it, especially when high roll angles are encountered.

The relative insensitivity of vortex breakdown to changes in the static roll angle found at $\alpha = 15°$ is completely reversed when considering a 20° incidence. Figures 7.8 and 7.9 show flow visualisation pictures for the $\phi_{max} = 30°$ manoeuvre, whereas Figures 7.11 and 7.12 show the $\phi_{max} = 40°$ case. In Figure 7.8, where the smallest frequency is presented, the vortices in the stationary case break down at the apex of the delta wing. However, the implementation of a static roll angle of 15° does not change the general image of the flowfield, and there are no coherent vortices. The roll angle has to be increased to 30° in order to see a coherent vortical structure on the port side of the wing. It is interesting that not only a coherent structure appears, but also the breakdown takes place very close to the trailing edge. However, the starboard side of the wing remains completely unaffected with no signs of vortices whatsoever.

Complete reformation of the vortices is observed in the dynamic case. Even a small frequency creates a major transformation of the flowfield with vortices appearing at zero roll angle. Increasing the roll angle enhances vortex reformation considerably, especially on the left side of the wing. There are vortices on the right side, but their breakdown takes place very close to the apex. Notice that the breakdown location of the clockwise vortex in the dynamic case takes place closer to the apex of the wing, when compared to the corresponding breakdown for the stationary roll angle.

The same manoeuvre, $\phi_{max} = 30°$, at the same incidence, $\alpha = 20°$, but for the highest frequency, presented a considerably different flowfield (Figure 7.9). The higher frequency manoeuvre, at zero roll angle, replaces the vortices that break down

at the apex of the wing with coherent vortices on both sides of the wing. The increasing roll angle is followed by two distinct vortical structures on each side with their breakdown taking place closer to the trailing edge. Comparing the images taken at the maximum roll angle $\phi_{max} = 30°$, for the static and dynamic cases, the counter-clockwise vortex is found to be well formed in the dynamic case, with its breakdown being further away from the apex. On the other hand, the breakdown of the static clockwise vortex takes place close to the trailing edge, a lot further downstream compared to that of the dynamic case.

At this stage, it is reasonable to say that the large amplitude manoeuvre is a lot more beneficial at $\alpha = 20°$. Contrary to the $\alpha = 15°$ case, the vortices here break down at the apex, and even a very low frequency manoeuvre is enough to recreate them. Hence, the beneficial character of the large amplitude rolling motion is proven and enhanced when the vortices breakdown at the apex of the wing. Furthermore, vortex reformation also takes place at high static roll angles.

The graphs for the vortex breakdown location versus the roll angle, for all frequencies considered, are presented in Figure 7.10. Considerable variations in breakdown position are perceived between the static and dynamic cases (Figure 7.10). For this angle of attack, increasing the roll angle results in the movement of the breakdown position downstream, closer to the trailing edge, to almost 80% of the chord length. In the stationary case, vortex reformation takes place at $\phi = 20°$ and breakdown occurs at 80% of the chord length, for $\phi_{max} = 30°$. In the dynamic cases, on the other hand, breakdown always occurs on the wing, even at small roll angles, proving the existence of vortices on both sides of the wing for the whole cycle of the motion. For the highest frequency $(f_r = 0.15)$, the breakdown position is at 45% of the chord length at the highest roll angle for the counter-clockwise vortex, which is almost half of that in the zero frequency case. Notice that the general pattern of the graph looks very similar for the two lowest frequencies ($f_r = 0.01$ and 0.03). The maximum roll angle delays breakdown, and very good symmetry is seen in both cases between the two sides. A larger hysteresis is observed, though, for the higher frequency $(f_r = 0.03)$. The same observations apply for the other two frequencies, $f_r = 0.06$ and 0.15, but this time the magnitude of the nondimensional breakdown location is higher for the higher frequency case $(f_r = 0.15)$. Hysteresis is found to be quite large at $f_r = 0.15$, whereas it is almost nonexistent for $f_r = 0.01$ case. These conclusive graphs underline one more time, the favourable character of the stationary roll angle, and that of the large amplitude rolling motion, for the reformation of the streamwise leading edge vortices at incidences where breakdown occurs at the apex.

The manoeuvres studied with $\phi_{max} = 40°$ at $\alpha = 20°$ are presented in Figures 7.11 and 7.12 for the $f_r = 0.01$ and 0.15 cases respectively, again compared to the stationary case. Figure 7.11 shows that for the stationary case there is no coherent streamwise vortex at this incidence and small roll angles, and that vortex breakdown takes place at the apex. However, with increasing roll angle (in particular for $\phi = 40°$), there is a coherent vortical structure. Figure 7.11 demonstrates that static

rolling of the low-sweep delta wing induces a similar response to that observed over slender wings, with the breakdown on the side with increased effective sweep (clockwise vortex) moving downstream, closer to the trailing edge.

The low frequency dynamic case in Figure 7.11 creates some interesting characteristics in the flowfield. Coherent vortices are present on either side of the wing, for the whole cycle of the rolling motion. The two zero roll angle images present remarkable symmetry. At the maximum roll angle, the clockwise vortex is very distinct, and its breakdown location moves closer to the trailing edge due to the increased effective sweep angle. It should be mentioned at this point, that the breakdown location of the clockwise vortex at the maximum roll angle, in both the static and dynamic cases, appears to be in approximately the same location. This underlines two important conclusions: the first one is that increasing the roll angle, even in a stationary case, moves the breakdown location towards the trailing edge; the second one applies to the dynamic motion: even a very low frequency rolling motion is capable of creating the desired effect on the flowfield by moving the vortex breakdown location further away from the apex and creating visible vortices on both sides of the wing. However, the fact that the dynamic motion is responsible for the regeneration of vortices in all cases, suggests its better performance compared to the stationary case.

Figure 7.12 compares flow visualisations of the leading edge vortices in the static and dynamic cases, for the largest dimensionless frequency ($f_r = 0.15$) and for a maximum roll angle of 40° and an incidence of 20°. In the dynamic case, gradual increase in the roll angle also moves the vortex breakdown downstream, but the existence of coherent vortices is apparent even at $\phi = 0°$. The vortex breakdown position at the highest roll angle reaches approximately 60% of the chord length. It is interesting that although the breakdown position for the clockwise vortex is significantly delayed by the high roll angle in the static case, the same does not seem to apply in the dynamic case. This is contrary to the results for the low frequency results (see Figure 7.11). However, the rolling motion of the delta wing promotes vortex formation at low roll angles, as there is a clear and coherent vortex structure rather than the stalled flow which appears in the static case.

Figure 7.13 summarises the variation of the phase-averaged location of the vortex breakdown for $\alpha = 20°$ and the $\phi_{max} = 40°$ rolling motion. A peculiar behaviour of the vortical flow is seen, whereby the streamwise vortex reforms at high static roll angles. In the static case, the increase in angle of attack significantly affects the breakdown position by moving it upstream, closer to the apex, although at low roll angles there is no vortex structure at all. Only after $\phi = 15°$, the flow presents signs of a vortex structure and consequently breakdown. Further increase in roll angle to $\phi_{max} = 40°$ moves the breakdown position even closer to the trailing edge, to approximately 96% of the chord length. Figures 7.10 and 7.13 show that the effect of the roll angle for the static wing can be substantial. The situation is not the same in the dynamic case. Clear leading edge vortices appear even at $\phi = 0°$. Even for small dimensionless frequencies such as 0.01, the dynamic roll motion promotes vortex formation. The maximum vortex breakdown location can reach roughly 60% of the

chord length. On the other hand, the breakdown location reaches 28% of the chord length on the other side. For the highest frequency ($f_r = 0.15$), the breakdown position of the counter-clockwise vortex is at 55% of the chord length at the highest roll angle, which is almost half of that in the zero frequency case. Considerable variations in breakdown position occur between the static and the dynamic cases in Figure 7.13. Again, the variation in the vortex breakdown locations for the highest and lowest dynamic cases ($f_r = 0.01$ and 0.15), is similar to those for the smaller maximum roll angle amplitude shown in Figure 7.10. Hysteresis increases with dimensionless frequency. There is also some asymmetry between the two sides. The counter-clockwise vortex has the tendency to move further away from the apex at every roll angle compared to the clockwise one. As such, there appears to be a natural tendency for asymmetry between the two vortices for large amplitude rolling motions.

In Figure 7.14, vorticity in a crossflow plane at 80% of the chord length and at $\alpha = 20°$ over a cycle, is presented for the static and dynamic cases ($f_r = 0.15$) for $\phi_{max} = 30°$. In the static case, the increase in roll angle creates a more coherent clockwise vortical structure, whereas the opposite is seen after the first half of the cycle. On the other hand, in the dynamic case, it is the counter-clockwise vortex that exhibits larger vorticity when the roll angle increases from zero. Also notice that higher vorticity levels appear towards the centreline of the wing for the static case, whereas in the dynamic case they can be seen both close to the wingtip as well as towards the centreline (see for example $\phi = 0°$, -10° and -20°). The highest vorticity in the static case is observed at the largest roll angle ($\phi_{max} = 30°$). This is also confirmed by flow visualisation images in the form of coherent vortical structures, with breakdown locations very close to the trailing edge. However, in the dynamic case, there is a large hysteresis, which is most evident at zero roll angle. There is also evidence of multiple vortices of the same sign of vorticity at high roll angles (see, $\phi = 0°$ and -20° as examples) in the dynamic case.

In Figure 7.15, the variation of circulation for the counter-clockwise vortex is shown over a cycle for the static and dynamic ($f_r = 0.15$) cases, for $\alpha = 20°$. Circulation has been nondimensionalised using the free stream velocity and chord length. There is a large hysteresis loop and, moreover, higher average circulation in the dynamic case. The largest differences compared to the static case are observed for increasing roll angles. Because of the increase in time-averaged vorticity flux created by motion of the leading edge, the time-averaged circulation is also expected to increase. Comparing Figures 7.10 and 7.15 shows that the variations in breakdown location are related to those in circulation. However, in the dynamic case the latter are larger. For increasing roll angles, the counter-clockwise vortex is stronger than for decreasing roll angles, which results in the vortex breakdown being closer to the apex.

To complete the first part of this study on large amplitude manoeuvres of rigid delta wings, further experimentation was conducted for incidences where the flow is completely stalled, that is at $\alpha = 25°$. Figure 7.16 shows flow visualisation images

for the stationary and dynamic $(f_r = 0.15)$ cases at $\alpha = 25°$ for $\phi_{max} = 30°$. In the stationary case and for zero roll angle, the flowfield is completely stalled with no apparent signs of vortices. The effect of increasing the static roll angle seems to be unimportant, since no drastic changes occur in the flowfield. There is evidence of vortex reformation on one side of the wing at high roll angles ($\phi = 20°$ and 30° and $\phi = -20°$ and -30° respectively for each half of the rolling cycle). For these static roll angles a vortex is seen, and sometimes the location of the breakdown location can be defined, (see for example at $\phi = -30°$). Although the effect of the static roll angle is not as major as that at the other incidences studied, a beneficial result is still observed when applied to a completely stalled flow.

Contrary to the effect of the static roll angle, it seems that the dynamic rolling motion creates significant changes to the flowfield (Figure 7.16). Coherent vortical structures with distinct breakdown locations are seen along the whole cycle of the rolling motion. At low roll angles ($\phi = 0°$, 10° and 20°), reattachment of the separated flow takes place, and one visible and distinct vortex on the right side of the wing can be seen. Notice that the wake on the left side of the wing is wider, indicating that the vortices have broken down at the apex of the wing. However, increasing the roll angle to 30° results in the formation of two streamwise leading edge vortices with very distinct breakdown locations. Evidently, the opposite takes place in the other half of the cycle. A more detailed look at the images reveals that the breakdown location of the reformed vortices created at negative roll angles is a lot more prominent compared to the one found at positive roll angles, and is sometimes found to have moved further away from the apex (see for example $\phi = -10°$). Hysteresis as well as great asymmetry between the two sides is observed, which appeared in all the previous investigations studied at high roll angle and high frequency manoeuvres.

Crossflow vorticity PIV measurements were conducted at 80% of the chord length for both the static and dynamic cases $(f_r = 0.15)$, at $\alpha = 25°$. The results over a cycle are presented in Figure 7.17. In the static case, the low levels of vorticity following the stalled flow persist over the cycle with the increasing roll angle, and it is only at $\phi = 30°$ that signs of higher vorticity levels are observed. Moving to the dynamic case, high levels of vorticity as the roll angle increases can be seen with clear reattachment taking place. Strangely enough, the high levels of vorticity are not seen at the highest roll angle, but at the lowest roll angles ($\phi = 0°$ and 10°), which is confirmation of hysteresis. Similar observations are made for the increasing negative roll angles (see for example the last image of the crossflow measurements in the dynamic case, $\phi = -10°$, which presents remarkably high vorticity levels with a strong coherent vortex towards the centreline of the wing, and smaller vortical structures along the wing tip). The same behaviour is observed throughout the cycle for low roll angles, providing additional proof of flow reattachment and vortex reformation in the presence of the dynamic rolling motion.

In conclusion, when vortex breakdown is present over the wing at zero roll angle $(\alpha = 15°)$, it is little affected by static or dynamic roll angles. However, in a

crossflow plane, there are relatively large variations in maximum vorticity and the size of the vortical flow region. When in the static case vortex breakdown is at the apex of the wing $(\alpha = 20°)$ at zero roll angle, a coherent vortex is formed and its breakdown can be observed over the wing for large roll angles. In fact, vortex breakdown may be delayed to the trailing edge region at high roll angles, such as $\phi = 30°$ and 40°. In the dynamic case, even for small dimensionless frequencies, there are coherent leading edge vortices on both sides of the wing throughout the whole cycle, rather than partially or completely stalled flow present in the static case. However, the variation of breakdown location over a cycle is much smaller. When the dimensionless frequency of the rolling motion is substantially increased, the amplitude of cyclic variations in breakdown location become smaller. Also, hysteresis increases with frequency, and is most noticeable at zero roll angle. The existence of multiple vortices with the same sign of vorticity as the primary ones is apparent in some roll angles. The variation in circulation, for the dynamic case, also shows hysteresis and has certain similarities to the variations of the breakdown location, although the magnitude of the latter is much larger. The time-averaged circulation in the dynamic case is larger than that in the static case, which is a result of the unsteady velocity of the leading edge.

In the last case, where the flow is completely stalled $(\alpha = 25°)$ the effect of the static roll angles seems to be insignificant since the changes taking place on the flowfield are minor. Evidence of vortex reformation appears only at relatively high roll angles. However, the enforcement of a dynamic rolling motion onto the completely stalled flow enables its earlier reattachment, and vortices appear on both sides of the wing at high roll angles. Consequently in the dynamic case, breakdown locations can easily be identified. These findings are extremely important for the $\alpha = 25°$ case. A fully separated flow with no signs of vortical structures is replaced by a fully attached flow with discrete vortices and breakdown location in the presence of a large amplitude dynamic rolling motion. Since the stalled flow is accompanied by a loss in lift, it is apparent how important and fundamental the reformation of the vortices is. It would not be wrong to assume that a considerably higher magnitude in circulation for the dynamic case could be followed by potential lift enhancement.

7.3 Large Amplitude Manoeuvre of Flexible Delta Wings

Apart from the rigid delta wing, the two most flexible delta wings, with $\lambda = 9$ and 21.3, were also tested under high frequency $(f_r = 0.15)$, large-amplitude manoeuvres. A comparison between the stationary and the dynamic case provides useful information on the flowfield characteristics of these wings. Additional information is offered by the comparison between flexible and rigid delta wings undergoing the same manoeuvre.

Figure 7.18 shows static and dynamic vorticity PIV measurements in the crossflow plane, taken at 80% of the chord length and $\alpha = 20°$ over a cycle with $\phi_{max} = 30°$ for the $\lambda = 9$ delta wing. In the stationary case, vortices can be seen on both sides of the wing at zero roll angle, underlining one of the many differences when compared

to the rigid wing. At this incidence, the vortices on the rigid wing break down at the apex. Furthermore, notice the high levels of concentrated vorticity towards the centreline of the wing for both vortices, and the clear reattachment region indicated by the zero levels of vorticity between the vortices. Due to the effective sweep angle an increase in the roll angle strengthens the clockwise vortex, as seen from the relatively high levels of vorticity, and weakens the counter-clockwise one. The opposite takes place in the other half of the cycle.

In the dynamic case, the opposite effect is observed compared to the stationary case. At zero roll angle, a strong counter-clockwise vortex exists, and evidence of a clockwise vortex appears in the form of very low levels of vorticity. Strangely enough, the increase in roll angle seems to weaken the counter-clockwise vortex, but does not seem to greatly strengthen the clockwise one. There is obviously an increase in the strength of the clockwise vortex, but it is definitely not comparable to the counter-clockwise vortex or the static case. Flexible wings have been shown in Chapter 4 to enhance vortex reformation and earlier reattachment, in a case where the vortices on a rigid wing had broken down at the apex. This was also proven by the zero roll angle static PIV image for the flexible wing. However, notice the change in the flowfield when the positive roll angle starts decreasing. The clockwise vortex becomes considerably stronger than the respective clockwise vortex with increasing roll angle, and is certainly stronger than in the stationary case. Notice at $\phi = 20°$ and $10°$ (decreasing positive roll angle) that both vortices appear to be stronger in the static case. However, further dynamic wing deformations due to the rolling motion can be appreciated in the dynamic case, which does not necessarily act in favour of the wing flowfield.

Circulation was calculated as a line integral of the velocity for the dynamic case $(f_r = 0.15)$, for the rigid, $(\lambda = 0)$ and flexible $(\lambda = 9)$ wings. The variation in the normalised circulation of the counter-clockwise vortex with roll angle and at $\alpha = 20°$, for the two afore-mentioned cases, is presented in Figure 7.19. The magnitudes of circulation tend to be similar for the rigid and flexible wing, when the positive roll angle increases and decreases. Hence, the biggest differences are observed in the negative roll angles. This indicates an asymmetry, which was considered in the case of the rigid wing as a characteristic of large amplitude manoeuvres. A large hysteresis loop is observed in both cases and, moreover, the average circulation is higher for the flexible wing. This is expected, and is possibly attributed to the increase in vorticity flux, as a result of the oscillations of the leading edge. Previous work (Taylor and Gursul-2004a) along with the results presented in Chapters 4 and 5 have proven that it is not the actual curvature of the wing, but the leading edge vibrations that reenergise the flow by adding momentum to it, and consequently promoting earlier reattachment and vortex reformation.

Crossflow vorticity measurements, were also conducted using a PIV system for the most flexible delta wing $\lambda = 21.3$, at $\alpha = 20°$, for both the static and dynamic $(f_r = 0.15)$ cases. The results are presented in Figure 7.20. At zero roll angle and at $\alpha = 20°$, in the stationary case, both vortices can be seen on the wing, with a very distinct reattachment region. The vortices are strong and coherent and can still be

seen at 80% of the chord length, where the measurements were taken, whereas on the rigid wing under the same conditions, only the wake of the vortices was visible. Again, increasing the roll angle strengthens the clockwise vortex and weakens the counter-clockwise with the opposite result taking effect over the cycle. It is interesting that in the static case that the maximum vorticity appears at the maximum roll angle (see the images at $\phi = 30°$ and -30°), whereas this does not take place in the dynamic case. Also notice that in some static roll angles, the strong vortex is so dominant that the other one is almost non-existent (see for example the crossflow vorticity plots at $\phi = -30°$ and -20°).

In the dynamic case only the counter-clockwise vortex is significantly stronger than the clockwise one, at zero roll angle, and its strength is reduced with increasing positive roll angle. This is expected, as the effective sweep angle acts in favour of the clockwise vortex to increase its strength. The same dynamic deformation exists in the decreasing roll angles, $\phi = 20°$ and 10°, with the vortices there being considerably more consistent than at the same roll angles at the beginning of the cycle. As opposed to the results obtained in the static case, in the dynamic case the maximum magnitude of vorticity prevails at the lower roll angles ($\phi = 20°$ and 10° or $\phi = -20°$ and -10°), and not the maximum one ($\phi = 30°$ or -30°). The combination of the dynamic deformation and the beneficial nature of the effective sideslip and sweep angle are responsible for the advantageous outcome of higher levels of vorticity in these roll angles.

7.4 Additional Measurements on Rolling Manoeuvres

In this section, large amplitude oscillations of a rigid nonslender delta wing are described, with the distinctive difference that the starting roll angle is nonzero. For the purpose of these experiments, a 50° rigid delta wing with a cavity was used, and fluorescent dye was injected through the leading edges of the wing, via thin slots extending along the whole length of the leading edge. Using this technique, a successful visualisation of the shear layer emanating from the leading edge was achieved, as details on the small vortical structures could be obtained.

The dynamic rolling motion described here is an attempt to simulate forced wing rock, since very low dimensionless frequencies are engaged, and the motion starts from a nonzero roll angle. The term 'forced wing rock' is used to describe a forced roll oscillation in the area close to stall angle, instead of the self-excited one which would be described as wing rock. Previous work on the wing rock phenomenon over nonslender delta wings (Hüschler-2003 and McClain-2004) indicated the importance of these oscillations thus providing a starting point for the present study. Although wing rock has usually been observed over slender wings it has also been seen over nonslender wings (with both sharp and rounded leading edges) and moreover the mean roll angle of these oscillation was found to be nonzero (Gursul *et al.*-2005). All these interesting findings initiated further experimentation, which was carried out in the form of forced low frequency rolling motions starting from a nonzero roll angle.

Hence, in the present study, the dynamic case, starts with a roll angle of $\phi_{start} = 40°$, and the amplitude of the rolling motion is $\Delta\phi = 5°$. For the static case, the three roll angles tested were $\phi = 35°$, 40° and 45°, to match those in the dynamic case.

Figures 7.21 and 7.22 show instantaneous and time-averaged flow visualisation images respectively of the stationary and the very low frequency $(f_r = 0.02)$ cases at $\alpha = 22.5°$. Three different roll angles were captured with a vertical laser beam placed at 80% of the chord length when the wing was at zero roll angle. This means that the effective chord length illuminated by the laser beam varies throughout its span, when positioned at a roll angle. The selection of the angle of attack is not arbitrary. A set of wind tunnel measurements on wing rock over a 50° delta wing undertaken by Hüschler (2003) gave the most interesting results at this incidence and was thus used in this research.

In the instantaneous images captured for the stationary case (Figure 7.21) at $\phi = 35°$, the separated shear layer rotates to create a coherent counter-clockwise vortical structure, and a more diffused one on the other side. There is evidence of a reattachment region. Furthermore, notice the numerous small-scale vortical structures that can be seen along the outline of the shear layer starting from the leading edge, on both sides of the wing. Increasing the roll angle to $\phi = 40°$ results in a more coherent counter-clockwise structure, as well as in a very distinctive reattachment region. Notice that the dye is visible on the pressure surface of the wing, on the side of the clockwise vortex. Even in this case, the periphery of the shear layer is outlined by small scale vortices. Moving onto the highest static roll angle case, $\phi = 45°$, the reattachment region remains clear and the counter-clockwise vortex becomes more consistent. Taking a close look at the counter-clockwise vortex, the outline of the dye clearly depicts the separated shear layer, followed by the formation of a leading edge vortex.

In the dynamic case (Figure 7.21-right side), the flowfield changes, and the potential evidence of reattachment at a static roll angle of 35° now becomes a clear reattachment region for the dynamic case $(\phi = 35°)$. Both vortices appear to be a lot more coherent, hence the dye-free region between them is considerably larger due to earlier reattachment. Small scale structures are still apparent. The dynamic motion promotes earlier reattachment of the flow. Increasing the roll angle to 40° induces a more consistent structure to the counter-clockwise vortex, where the shear layer emanates from the leading edge only to be followed by a vortex with an almost round core. However, the distance between the two vortices is smaller. Notice that with an increasing roll angle the counter-clockwise vortex moves further away from the wing surface. The opposite takes place on the other side, ultimately resulting in the reduction of the distance between the two. The reattachment line on the left side moves to the right very quickly as the left vortex expands in the spanwise direction. Meanwhile, the vortex on the right side becomes smaller and more coherent. Interestingly enough, a further increase in the roll angle results in a widening of the distance between the vortices, approaching that of the $\phi = 35°$ case. The counter-

clockwise vortex retains its coherent structure, whereas the clockwise one seems to have reduced its height and width.

Even a very low frequency rolling motion starting from a roll angle of 35° is enough to bring the same effective results in a flowfield, by promoting earlier reattachment and inducing more coherent vortical structures to appear. The existence of multiple small scale vortical structures along with a very distinctive outline of the shear layer, are the characteristics of this low frequency motion. Figure 7.22 shows a superimposition of ten instantaneous images, thus providing a more diffused and less detailed view of the flowfield in the time averaged sense.

7.5 Figures Chapter 7

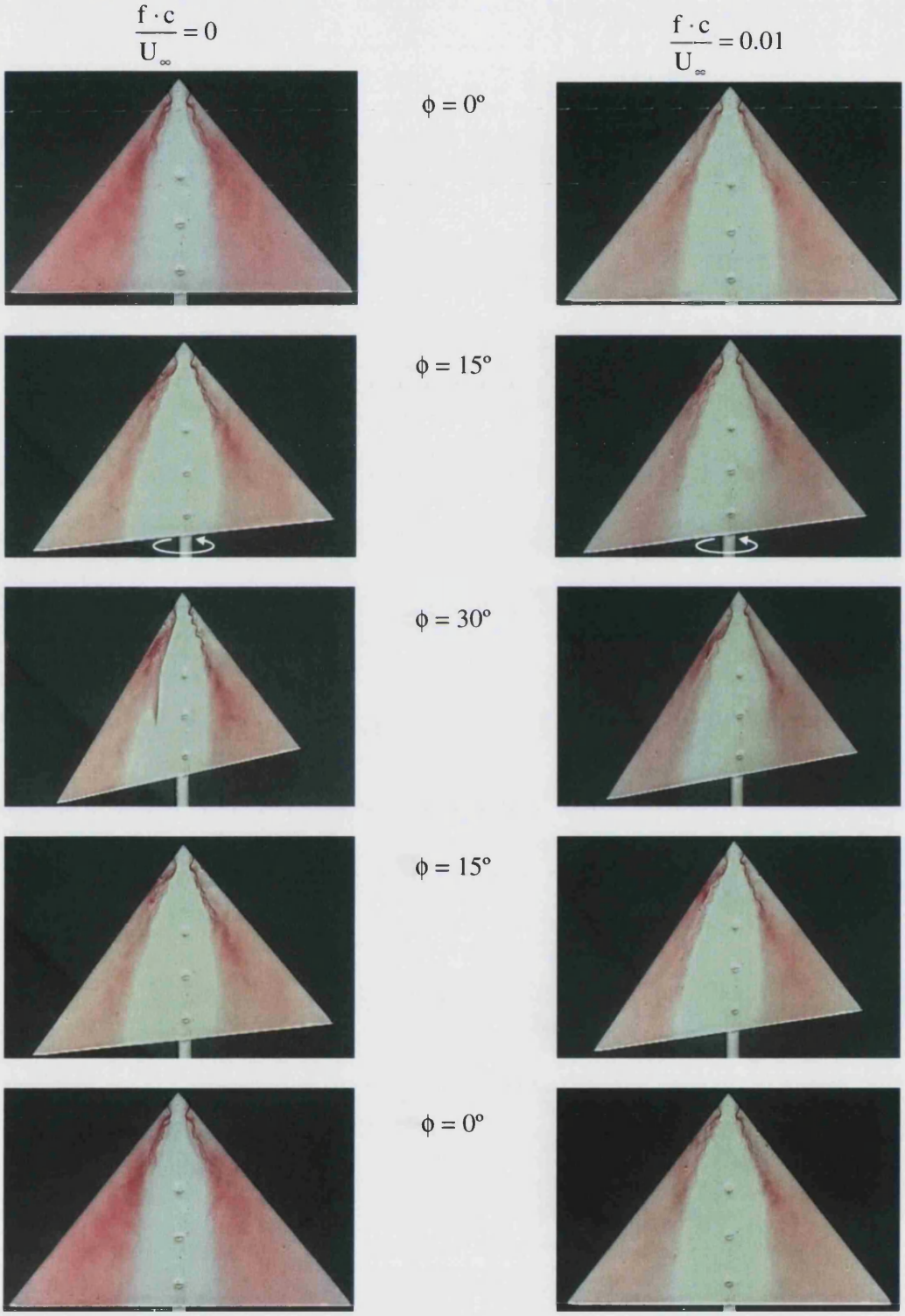

Figure 7.1: Comparison between static (*left side*) and dynamic case (right side, $f_r = 0.01$) flow visualisation images at $\alpha = 15°$ for $\phi_{max} = 30°$.

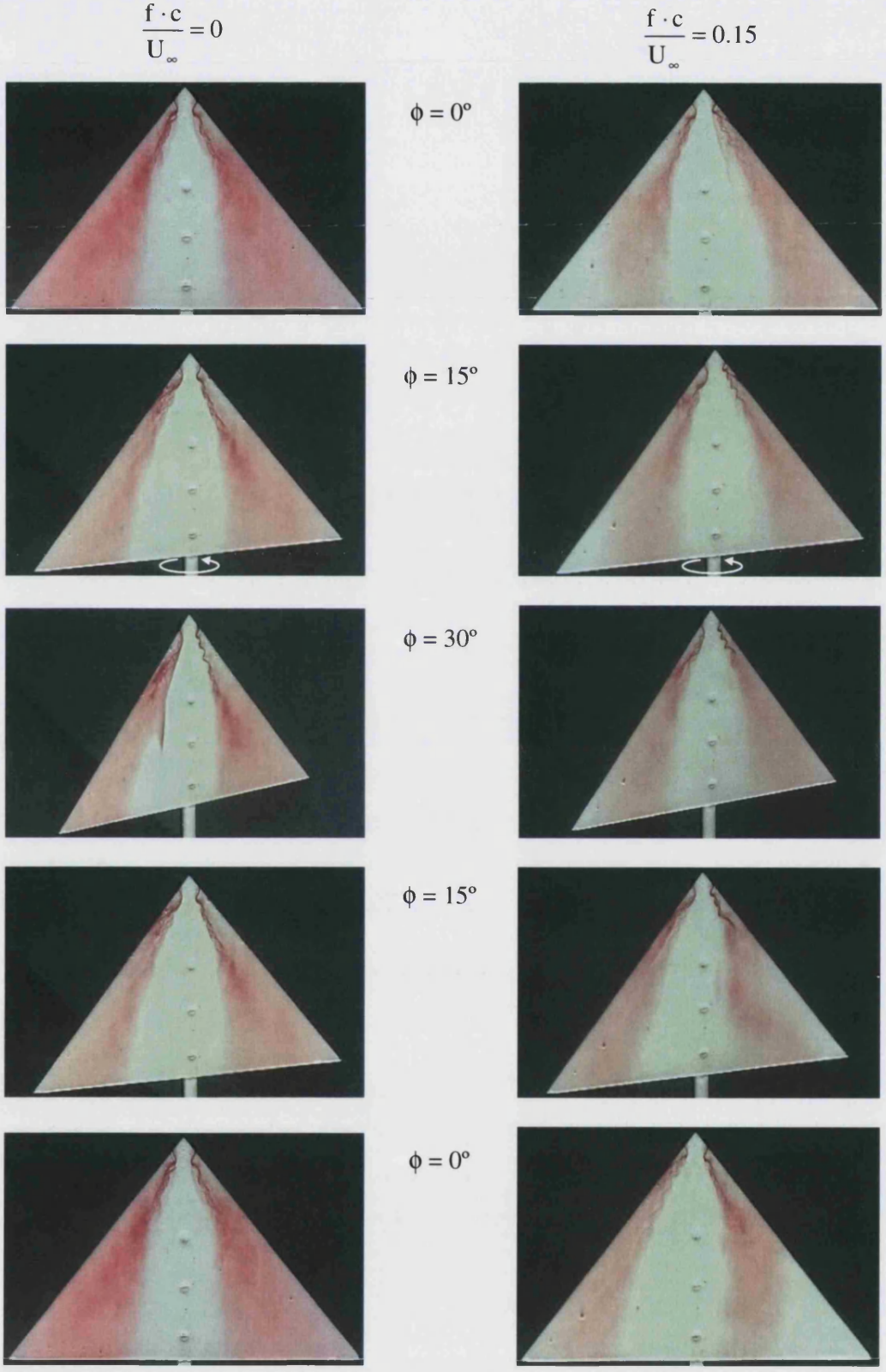

Figure 7.2: Comparison between static (*left side*) and dynamic case (right side $f_r = 0.15$) flow visualisation images at $\alpha = 15°$ for $\phi_{max} = 30°$.

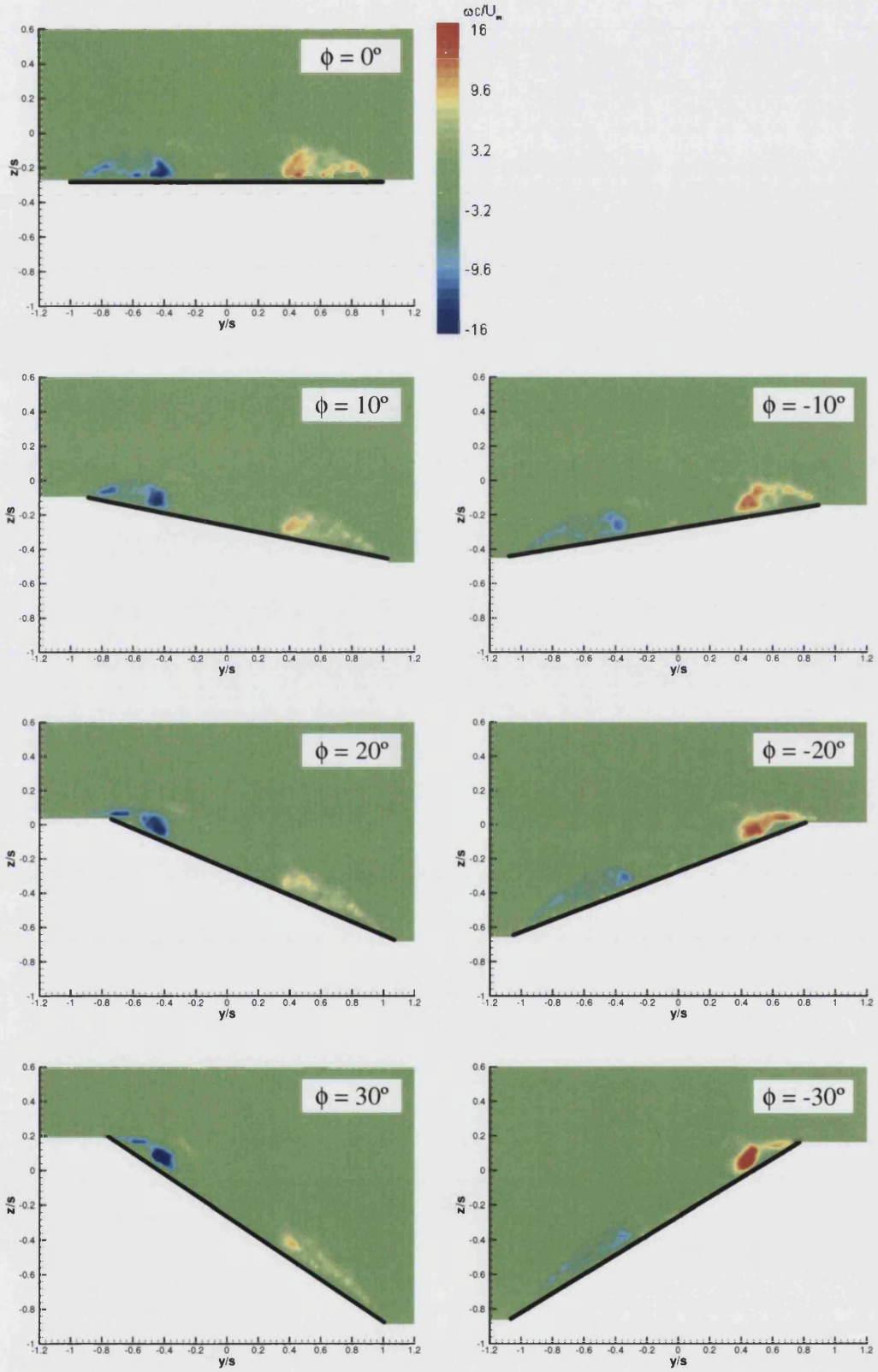

Figure 7.3: Cross flow static vorticity measurements at $x/c = 0.8$ and $\alpha = 15°$ for different roll angles.

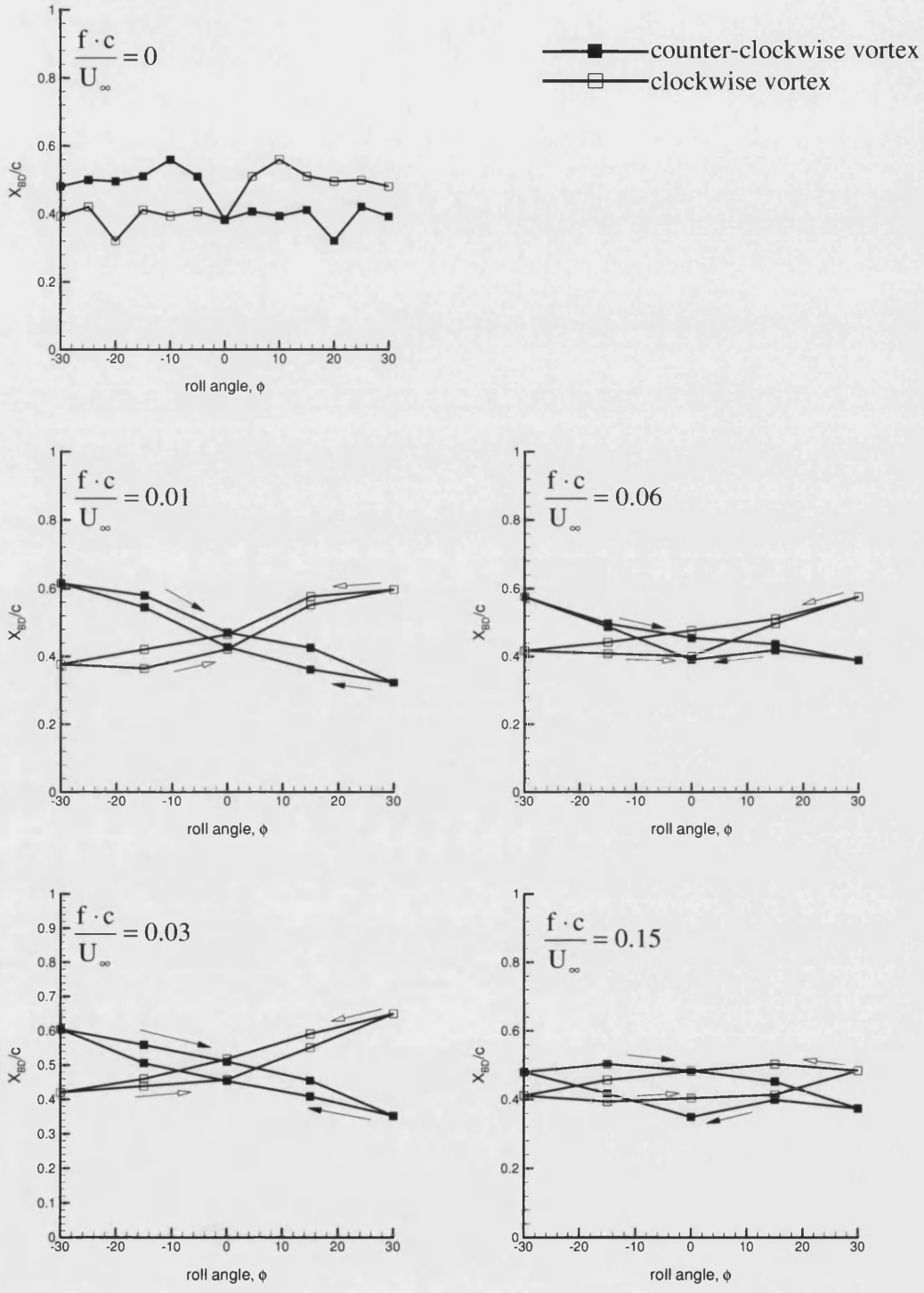

Figure 7.4: Variation of the vortex breakdown position, X_{BD}/c, with the roll angle, for different cases of the wing motion, at $\alpha = 15°$ and for $\phi_{max} = 30°$.

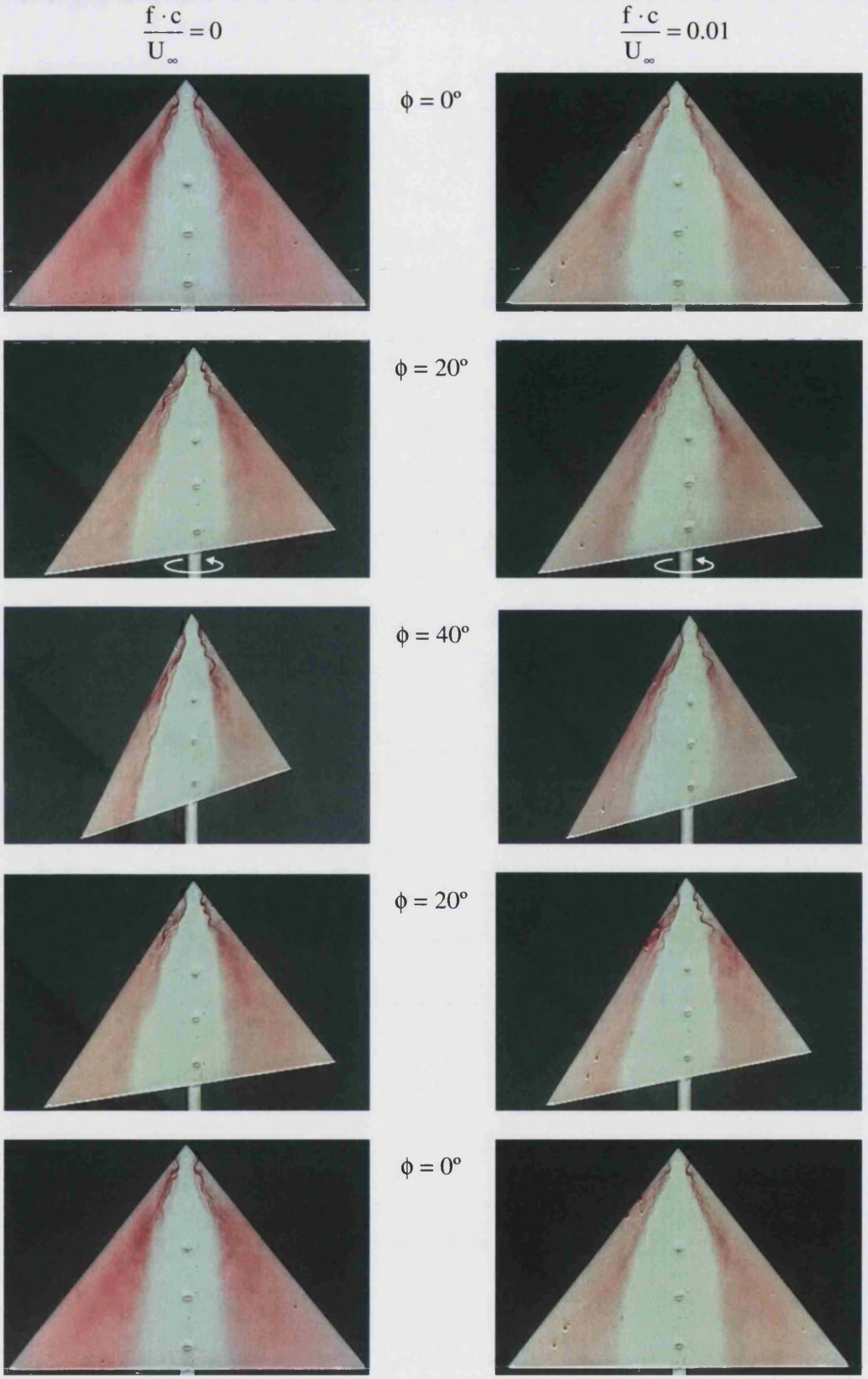

Figure 7.5: Comparison between static (*left side*) and dynamic case (right side, $f_r = 0.01$) flow visualisation images at $\alpha = 15°$ and for $\phi_{max} = 40°$.

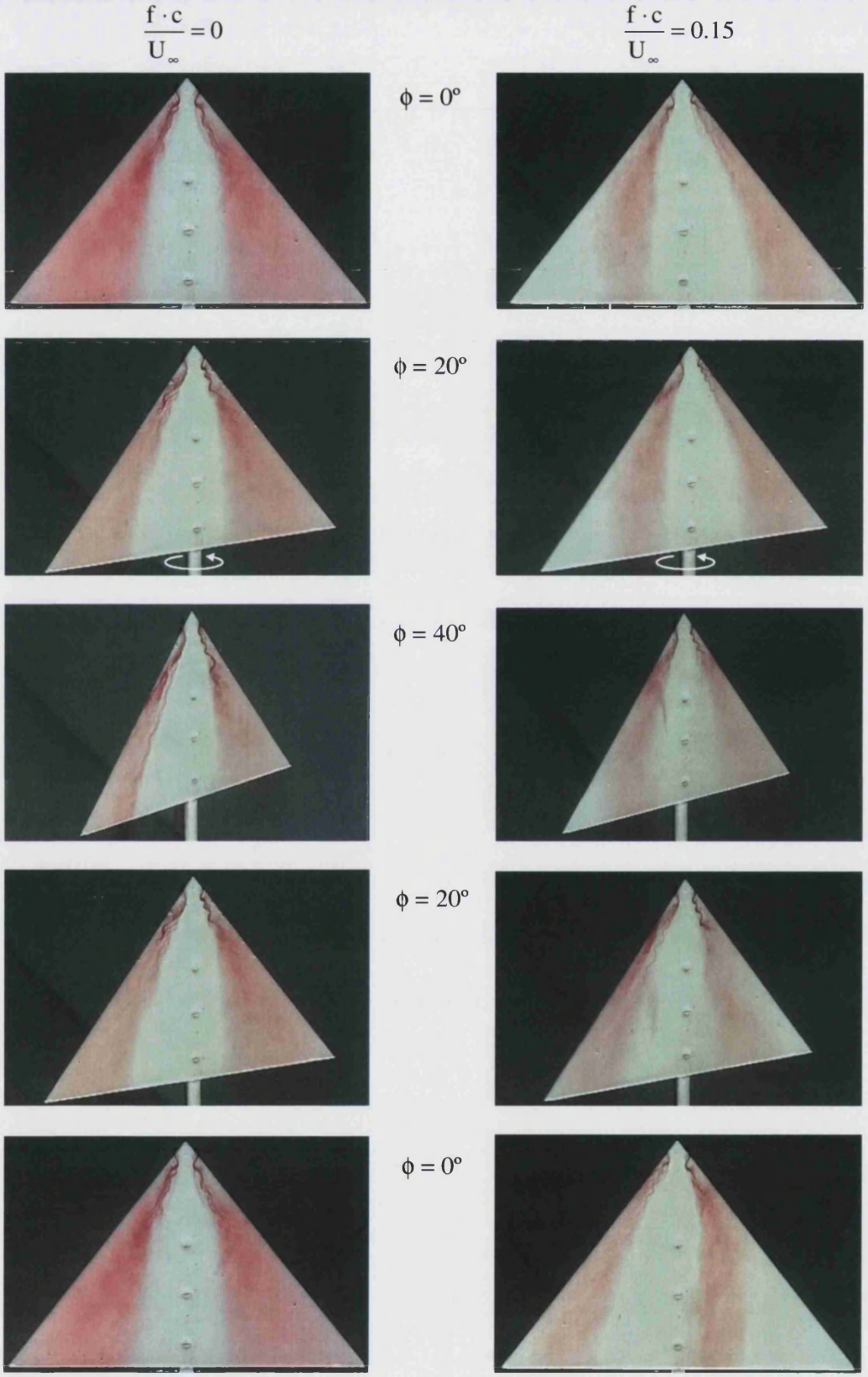

Figure 7.6: Comparison between static (*left side*) and dynamic case (right side $f_r = 0.15$) flow visualisation images at $\alpha = 15°$ and for $\phi_{max} = 40°$.

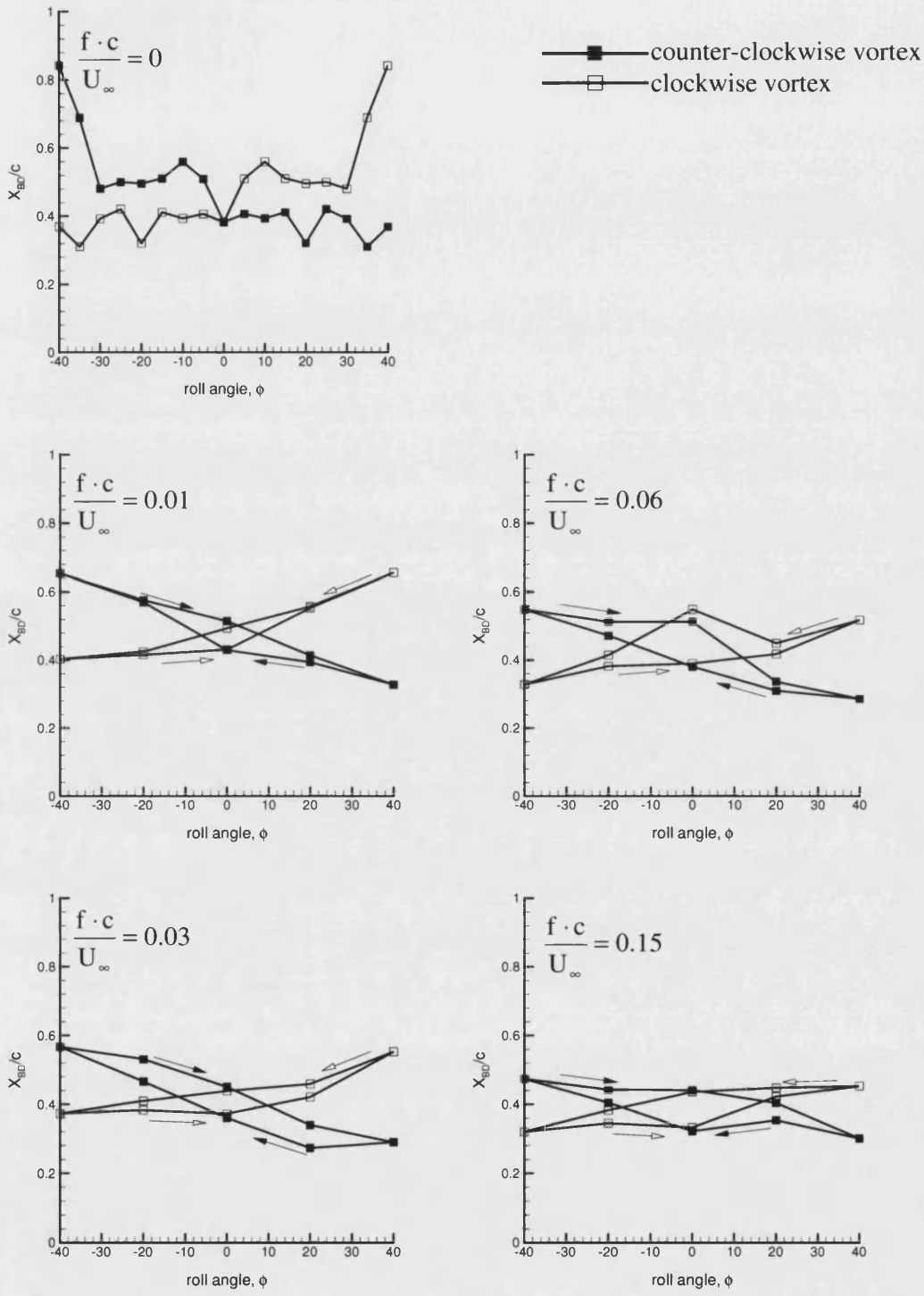

Figure 7.7: Variation of the vortex breakdown position, X_{BD}/c, with the roll angle, for different cases of the wing motion , at $\alpha = 15°$ and for $\phi_{max} = 40°$.

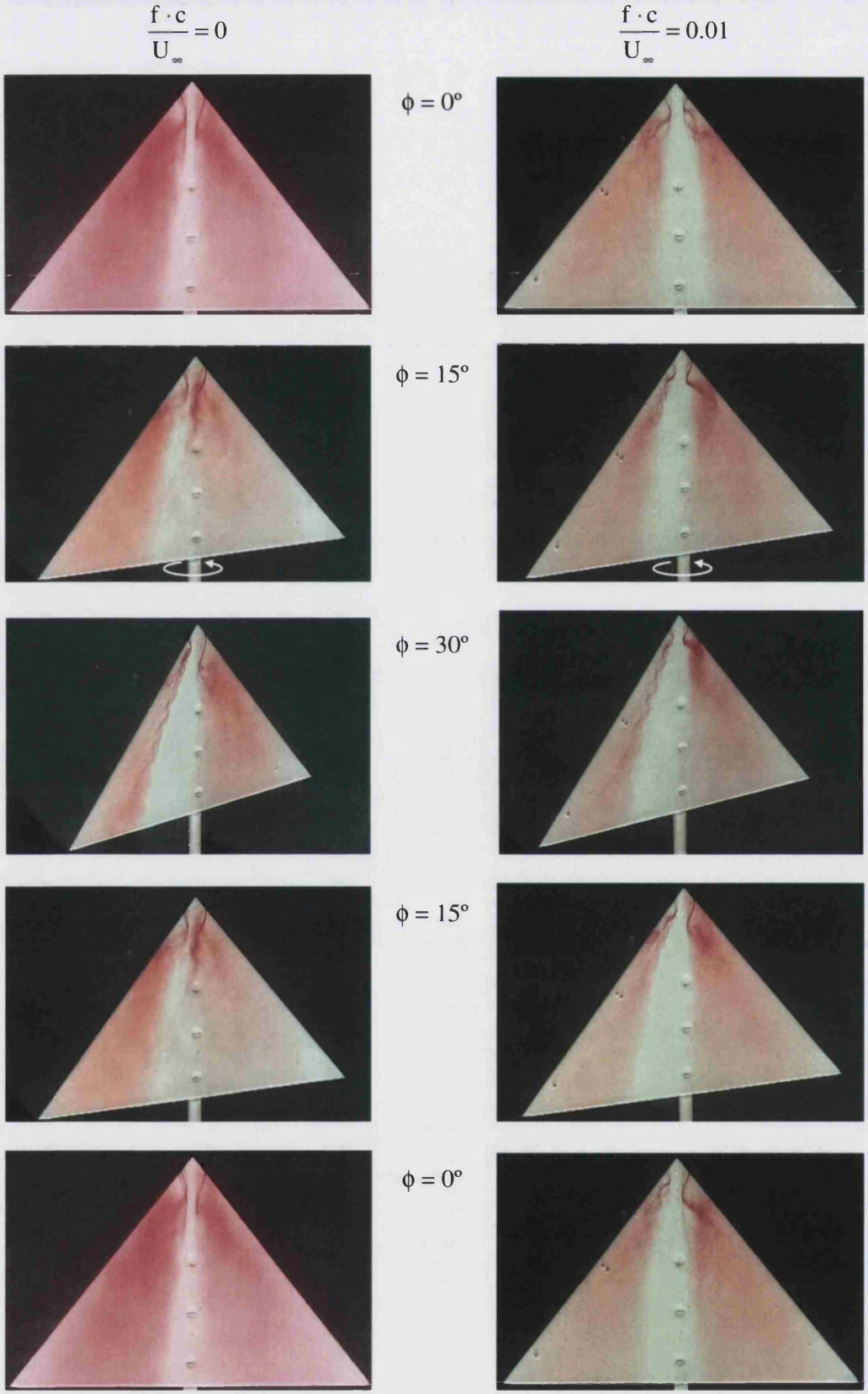

Figure 7.8: Comparison between static (*left side*) and dynamic case (right side, $f_r = 0.01$) flow visualisation images at $\alpha = 20°$ and for $\phi_{max} = 30°$.

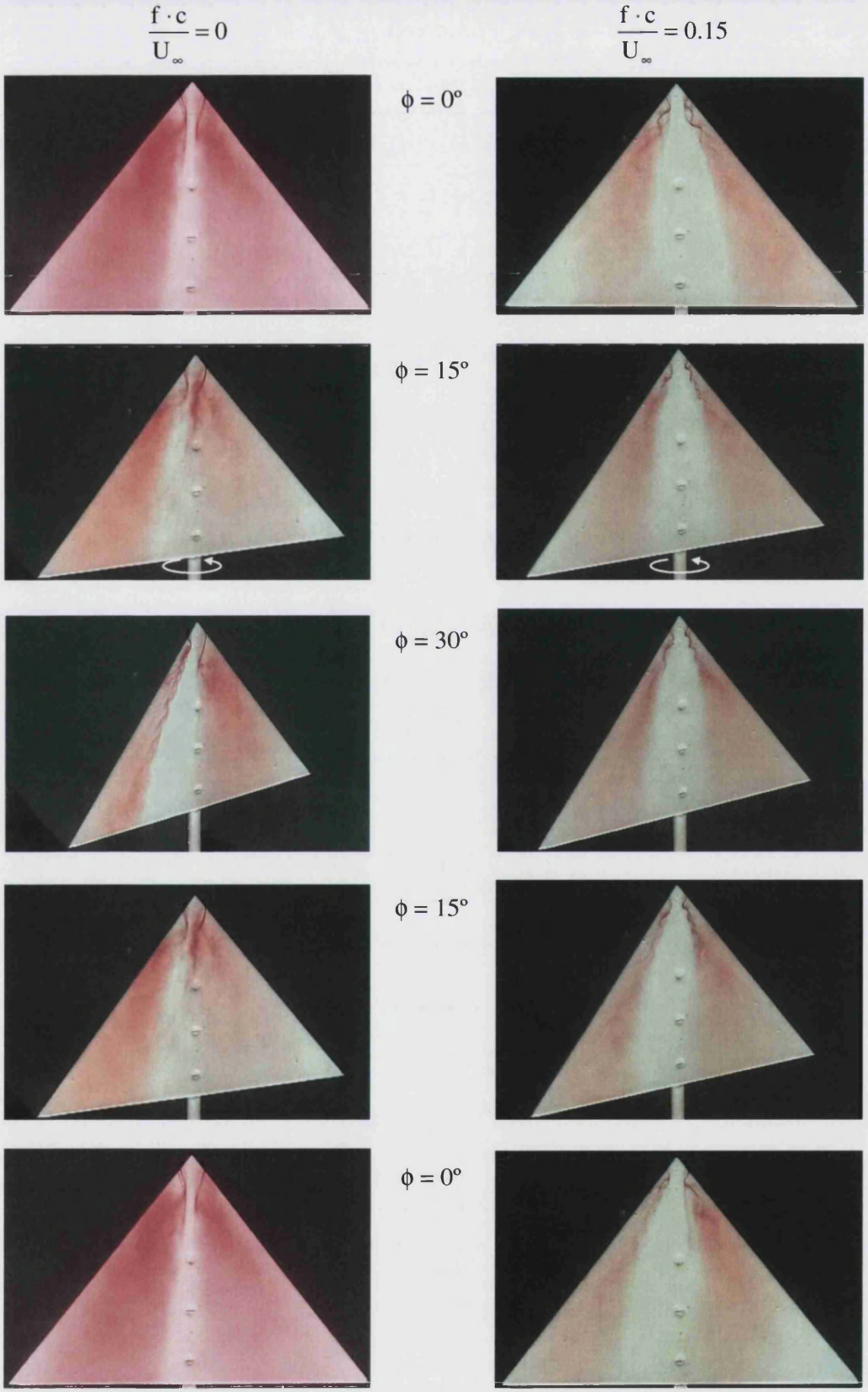

Figure 7.9: Comparison between static (*left side*) and dynamic case (right side $f_r = 0.15$) flow visualisation images at $\alpha = 20°$ and for $\phi_{max} = 30°$.

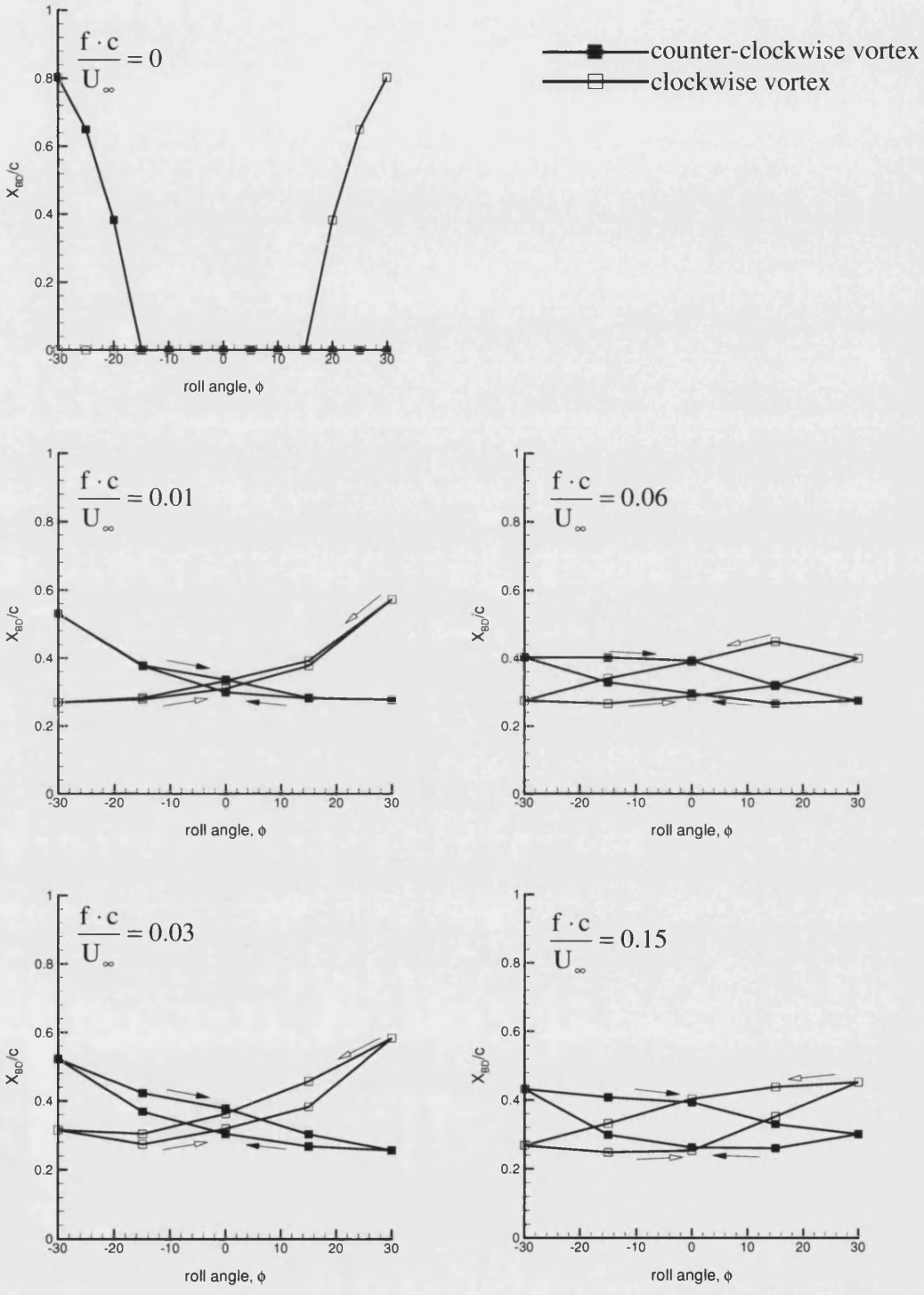

Figure 7.10: Variation of the vortex breakdown position, X_{BD}/c, with the roll angle, for different cases of the wing motion, $\alpha = 20°$ and for $\phi_{max} = 30°$.

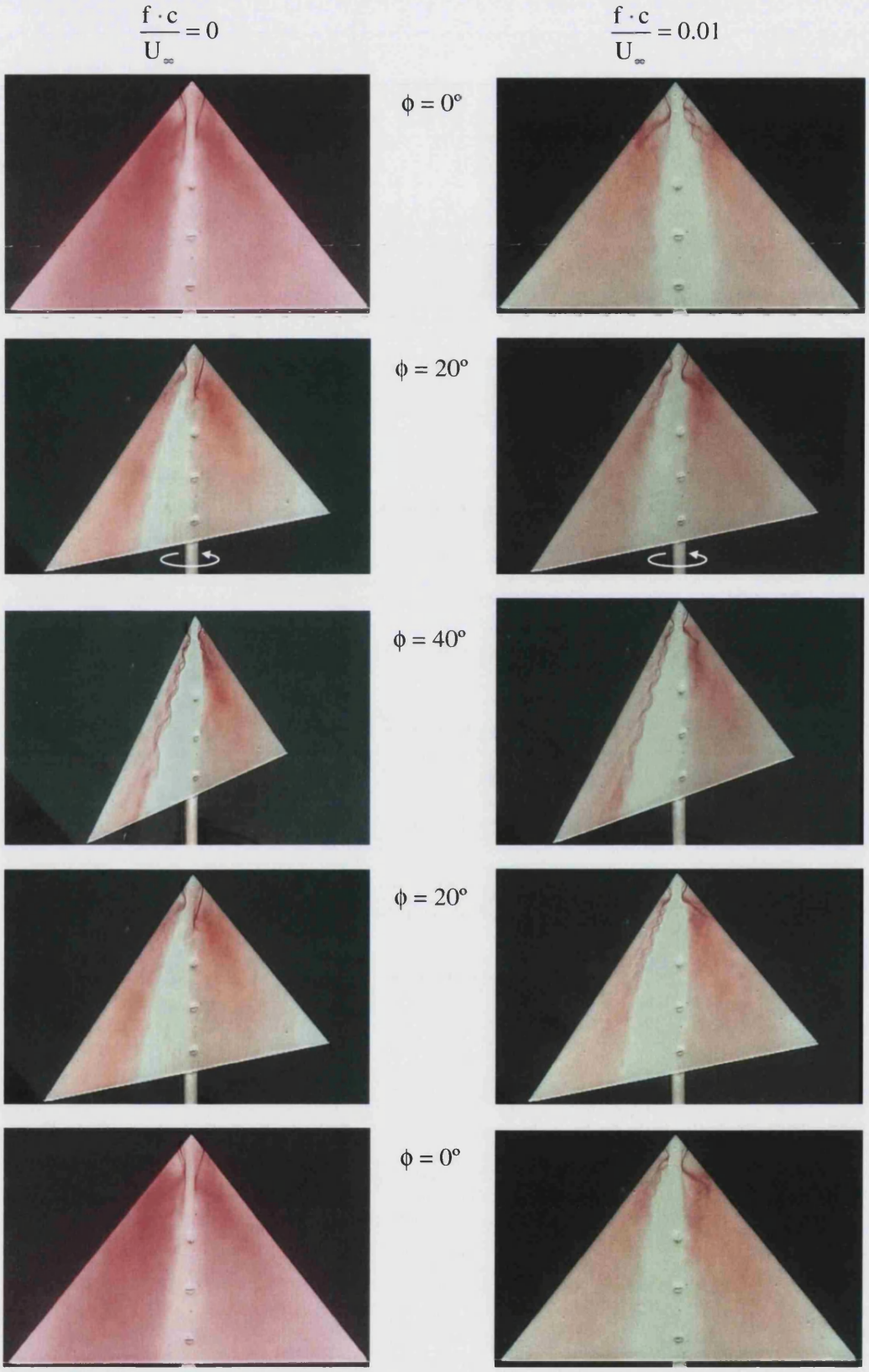

Figure 7.11: Comparison between static (*left side*) and dynamic case (right side $f_r = 0.01$) flow visualisation images at $\alpha = 20°$ and for $\phi_{max} = 40°$.

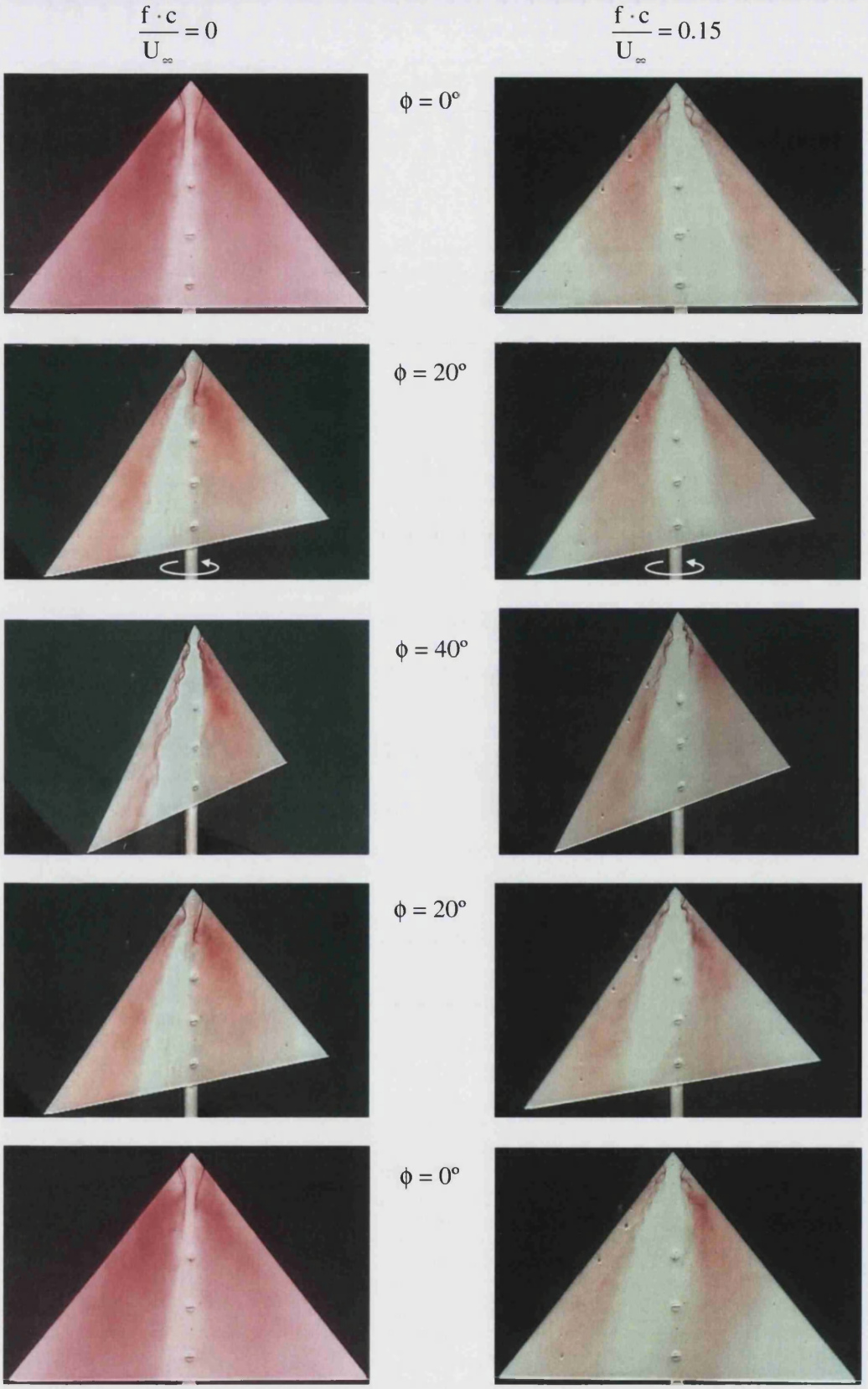

Figure 7.12: Comparison between static (*left side*) and dynamic case (right side $f_r = 0.15$) flow visualisation images at $\alpha = 20°$ and for $\phi_{max} = 40°$.

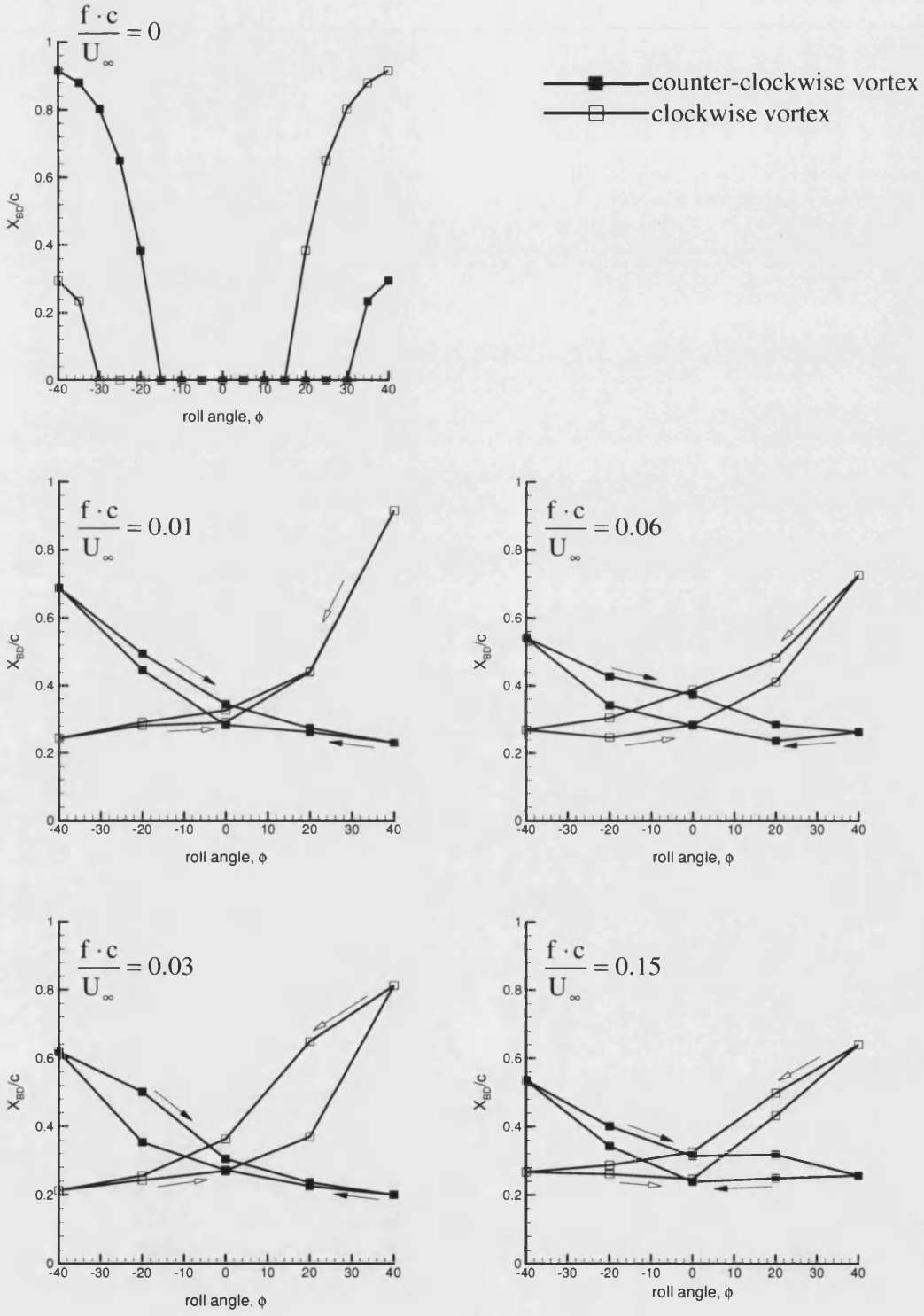

Figure 7.13: Variation of the vortex breakdown position, X_{BD}/c, with the roll angle, for different cases of the wing motion , at $\alpha = 20°$ and for $\phi_{max} = 40°$.

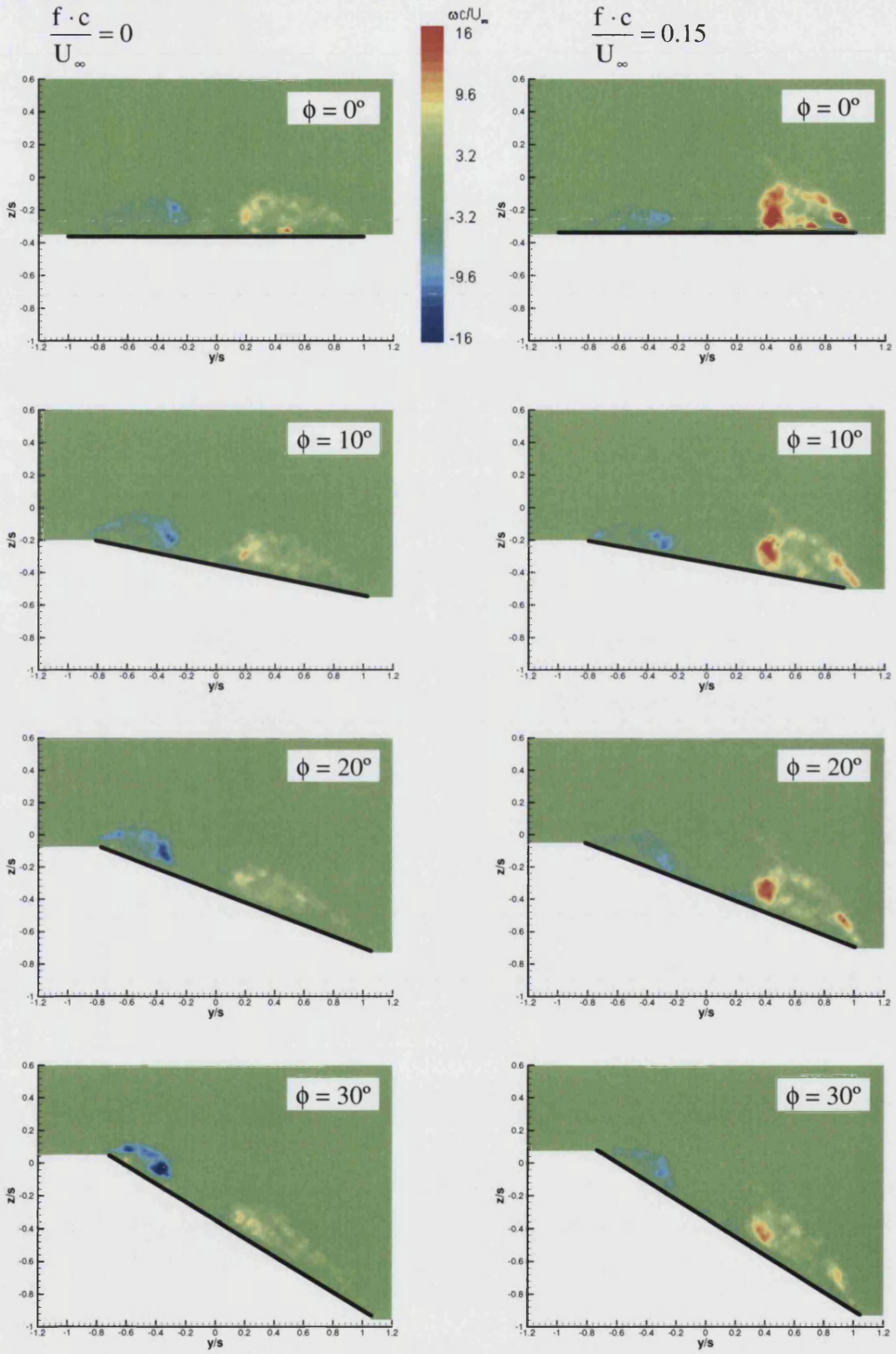

Figure 7.14: Comparison between static and dynamic vorticity in a crossflow plane at $x/c = 0.8$ and $\alpha = 20°$ over a cycle.

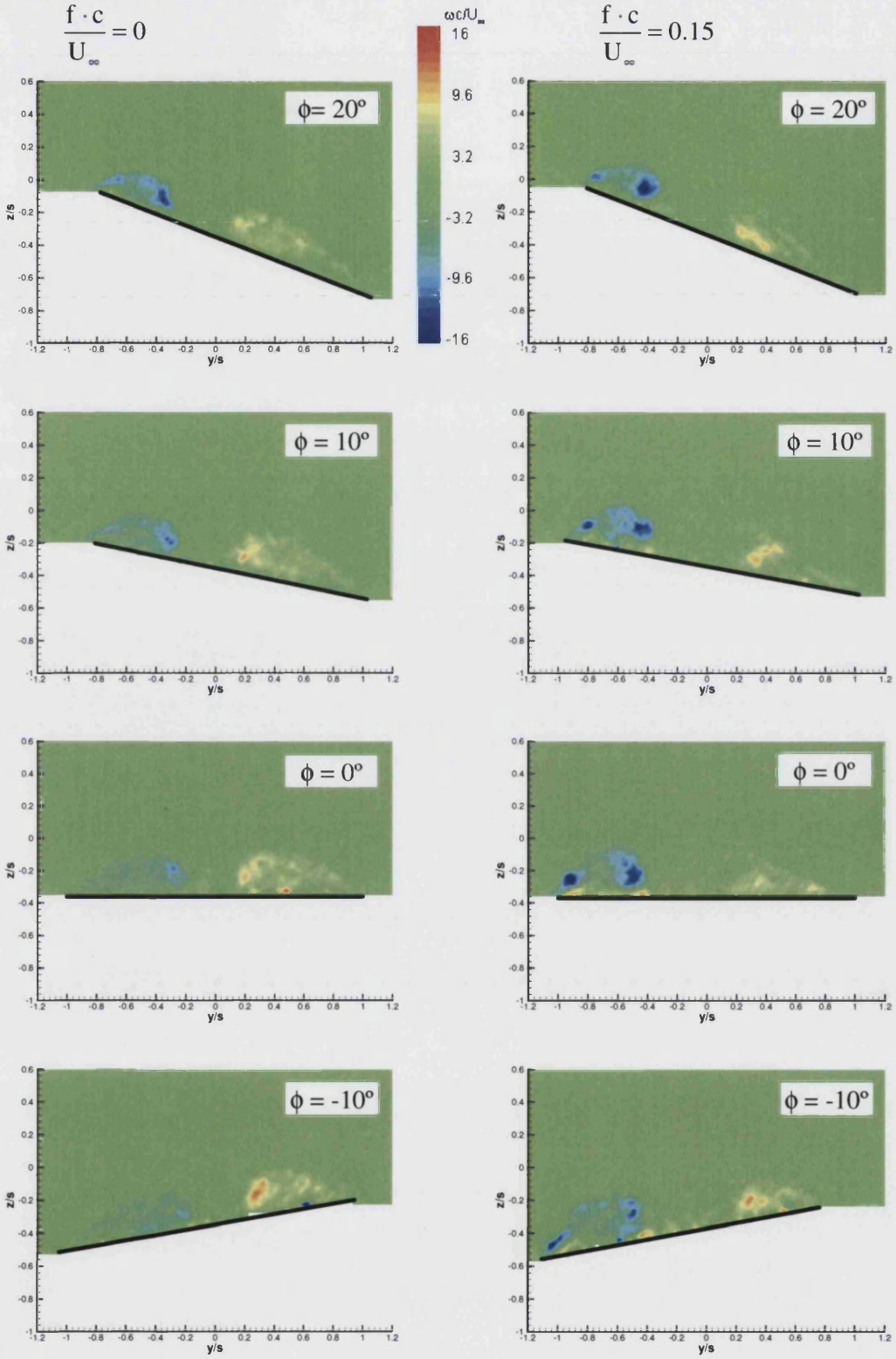

Figure 7.14: continued

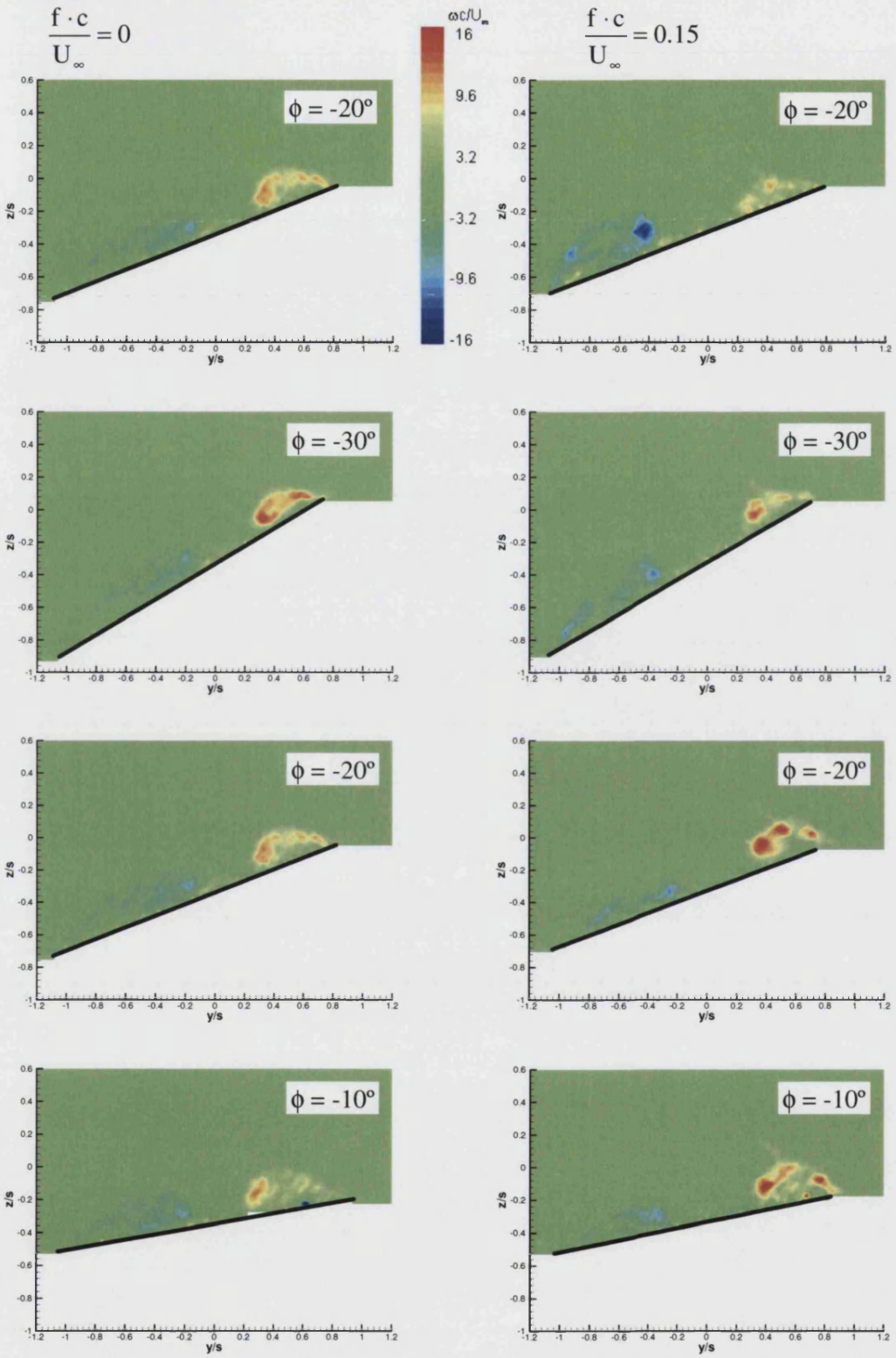

Figure 7.14: continued

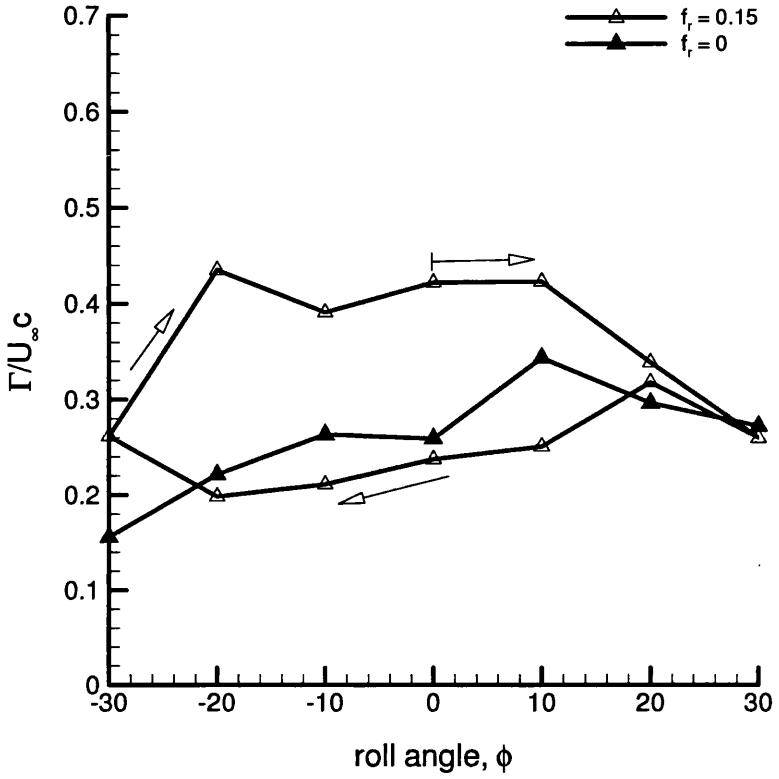

Figure 7.15: Variation of normalised circulation with the roll angle for the counter-clockwise vortex over a cycle , for the static and dynamic case at $\alpha = 20°$ and $x/c = 0.8$.

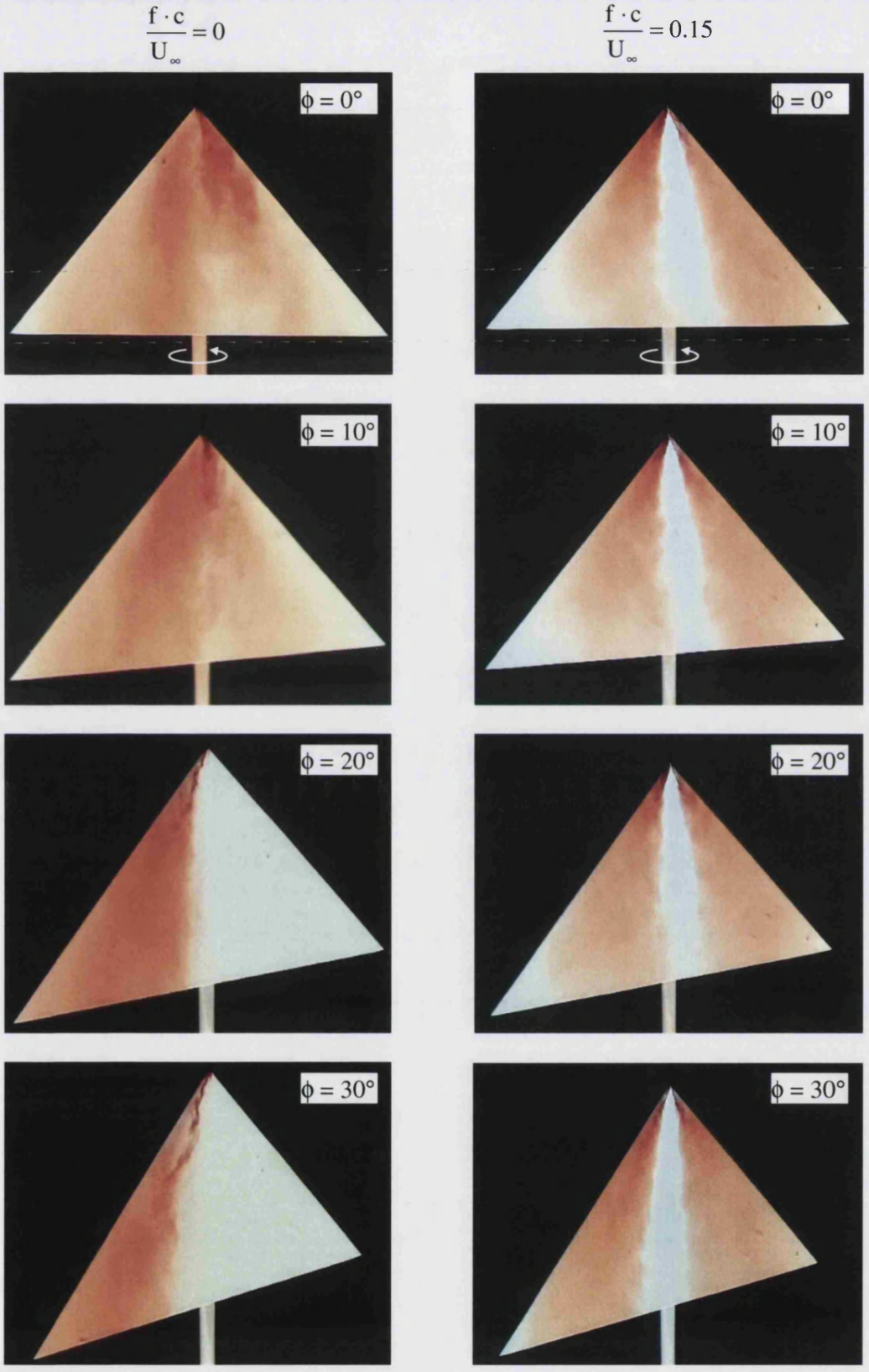

Figure 7.16: Comparison between static (*left side*) and dynamic case (*right side*) flow visualisation images at $\alpha = 25°$ for $\phi_{max} = 30°$.

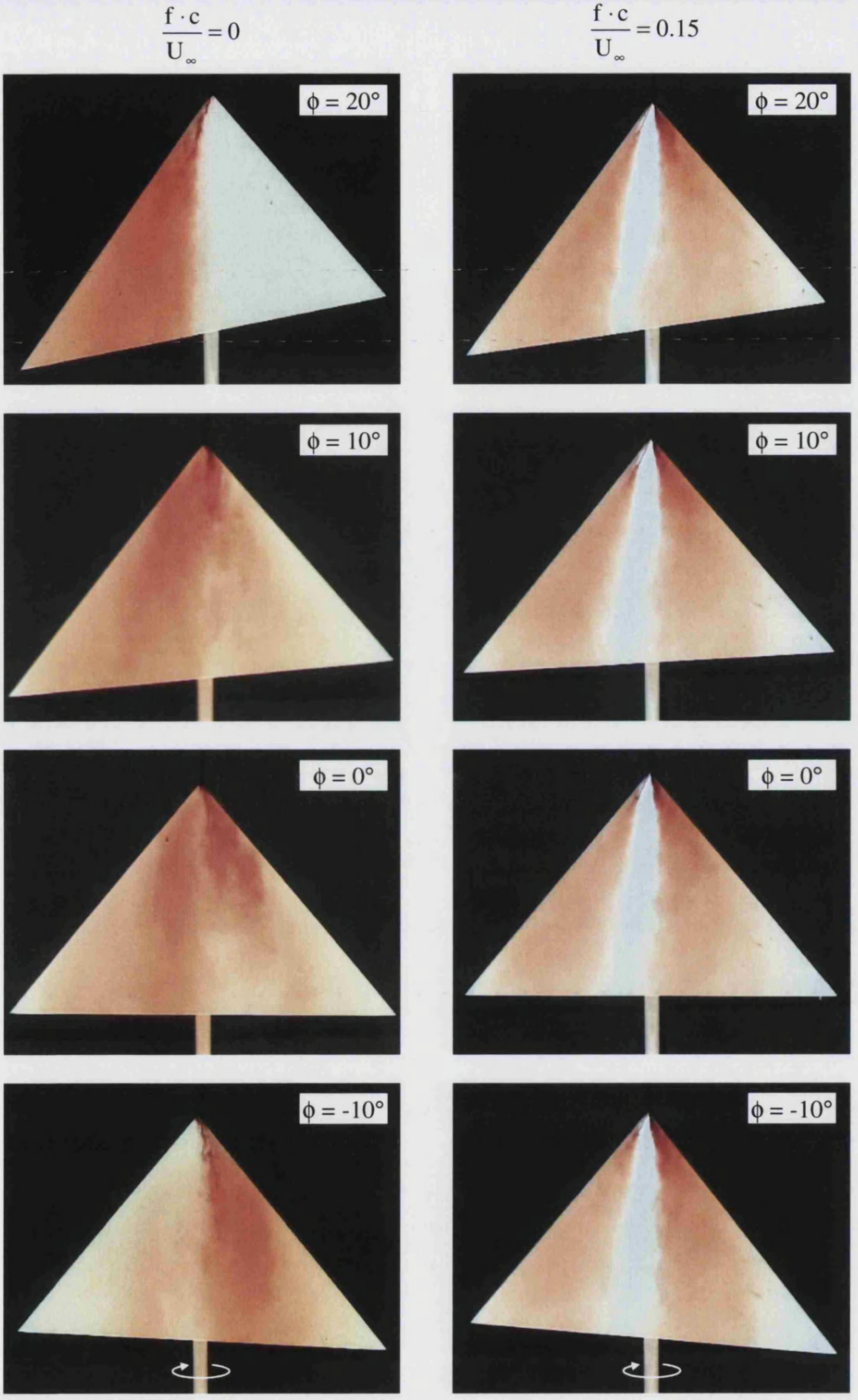

Figure 7.16: continued

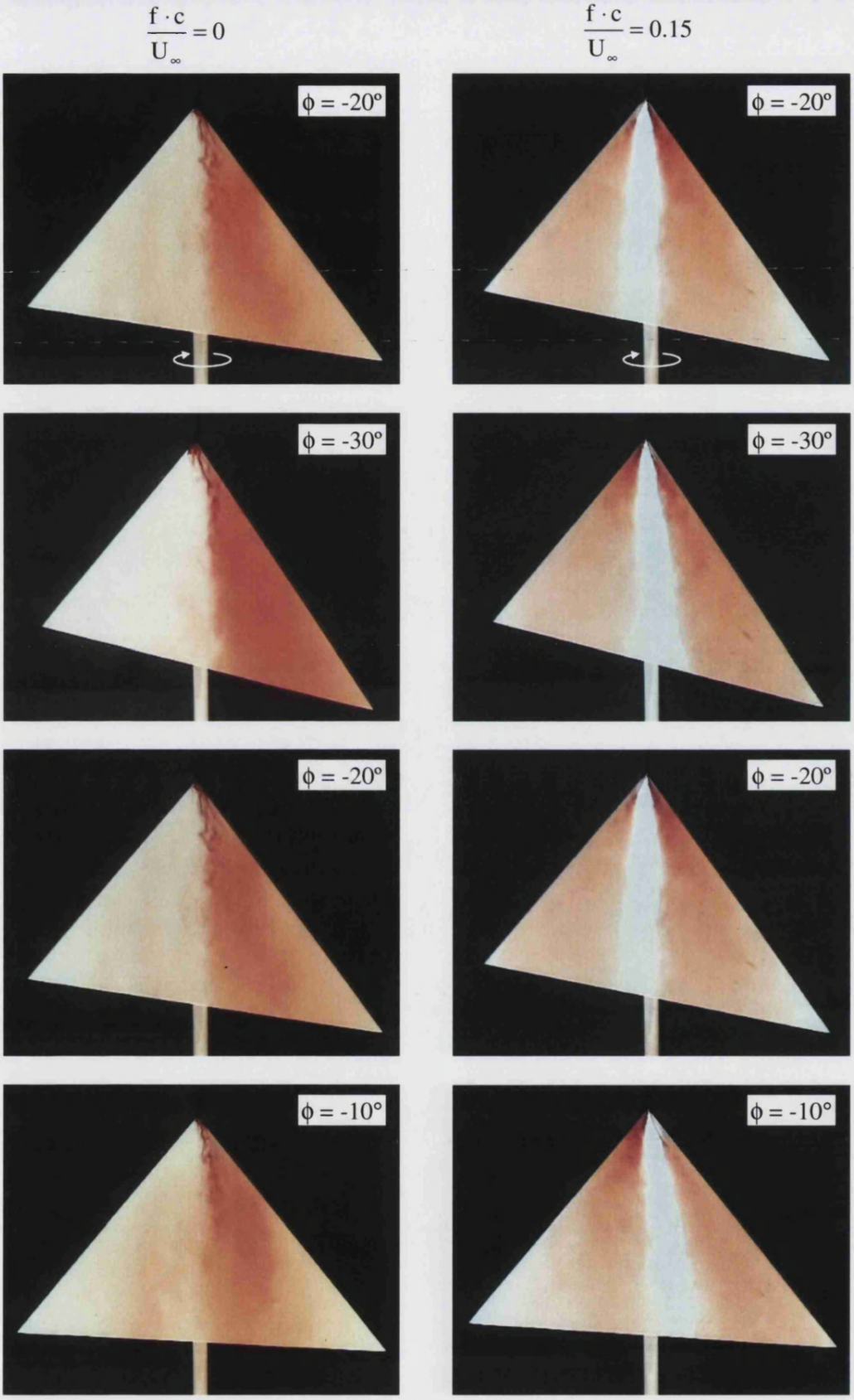

Figure 7.16: continued

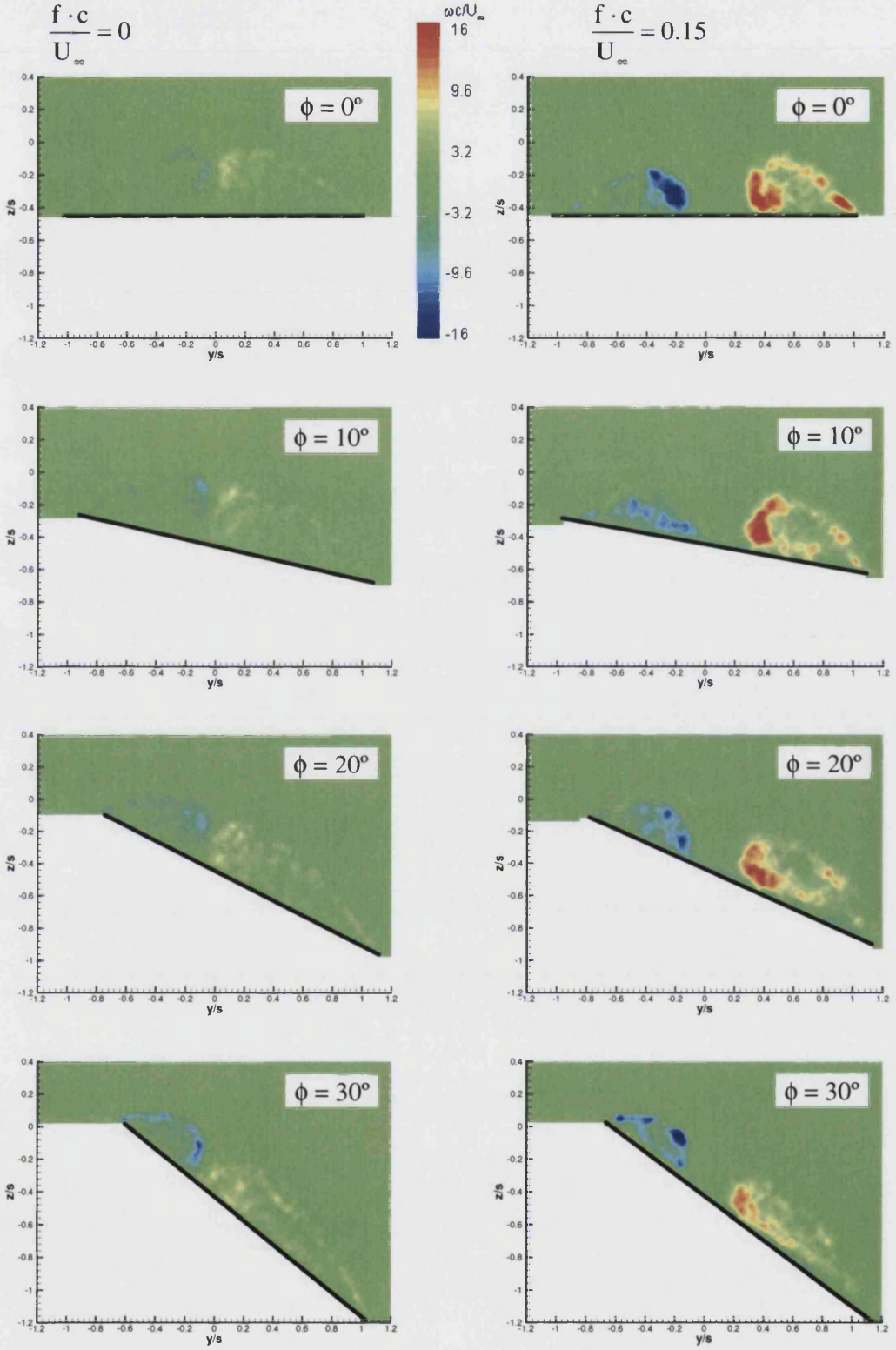

Figure 7.17: Comparison between static and dynamic vorticity in crossflow plane at $x/c = 0.8$ and $\alpha = 25°$ over a cycle.

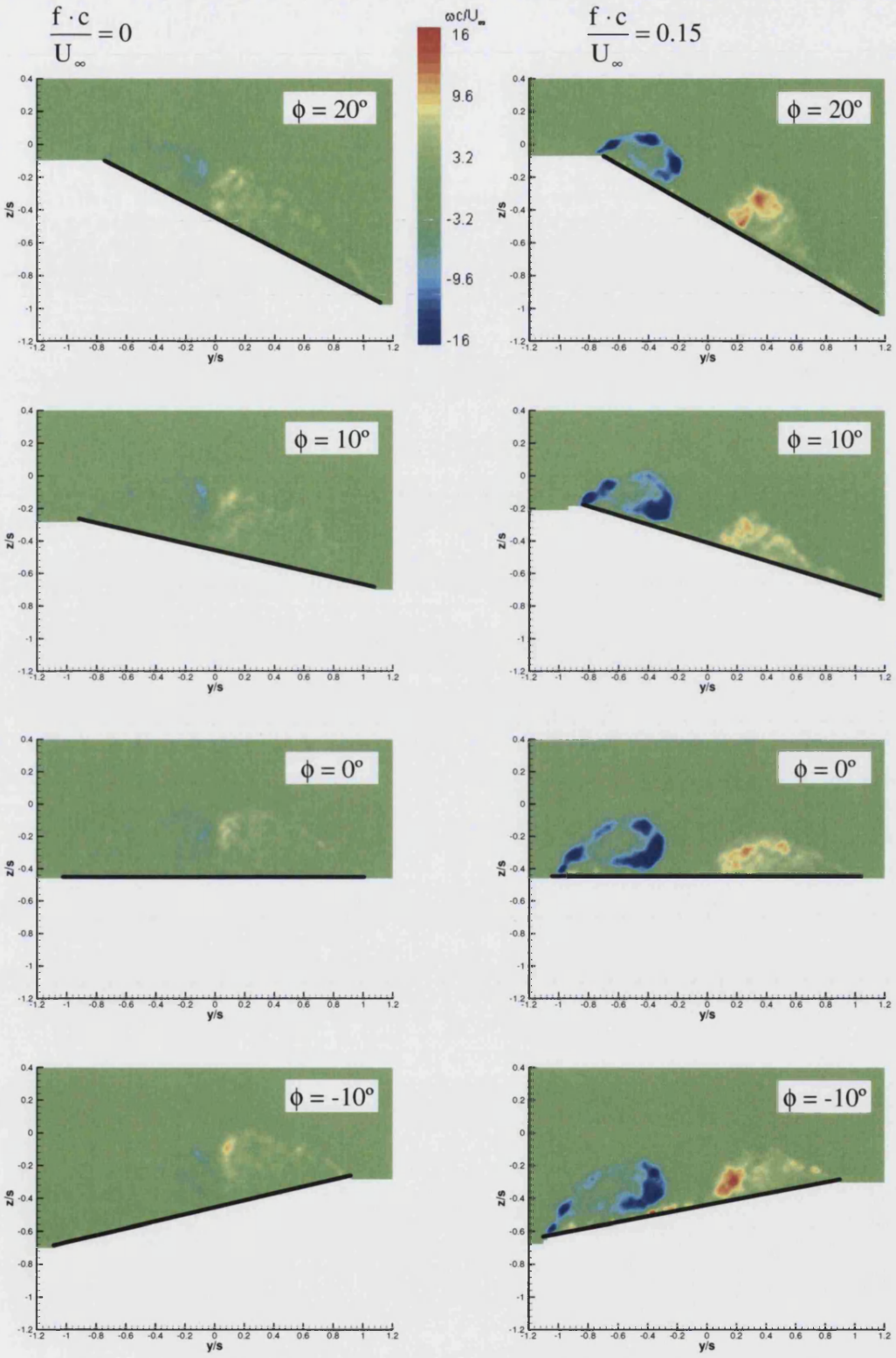

Figure 7.17: continued

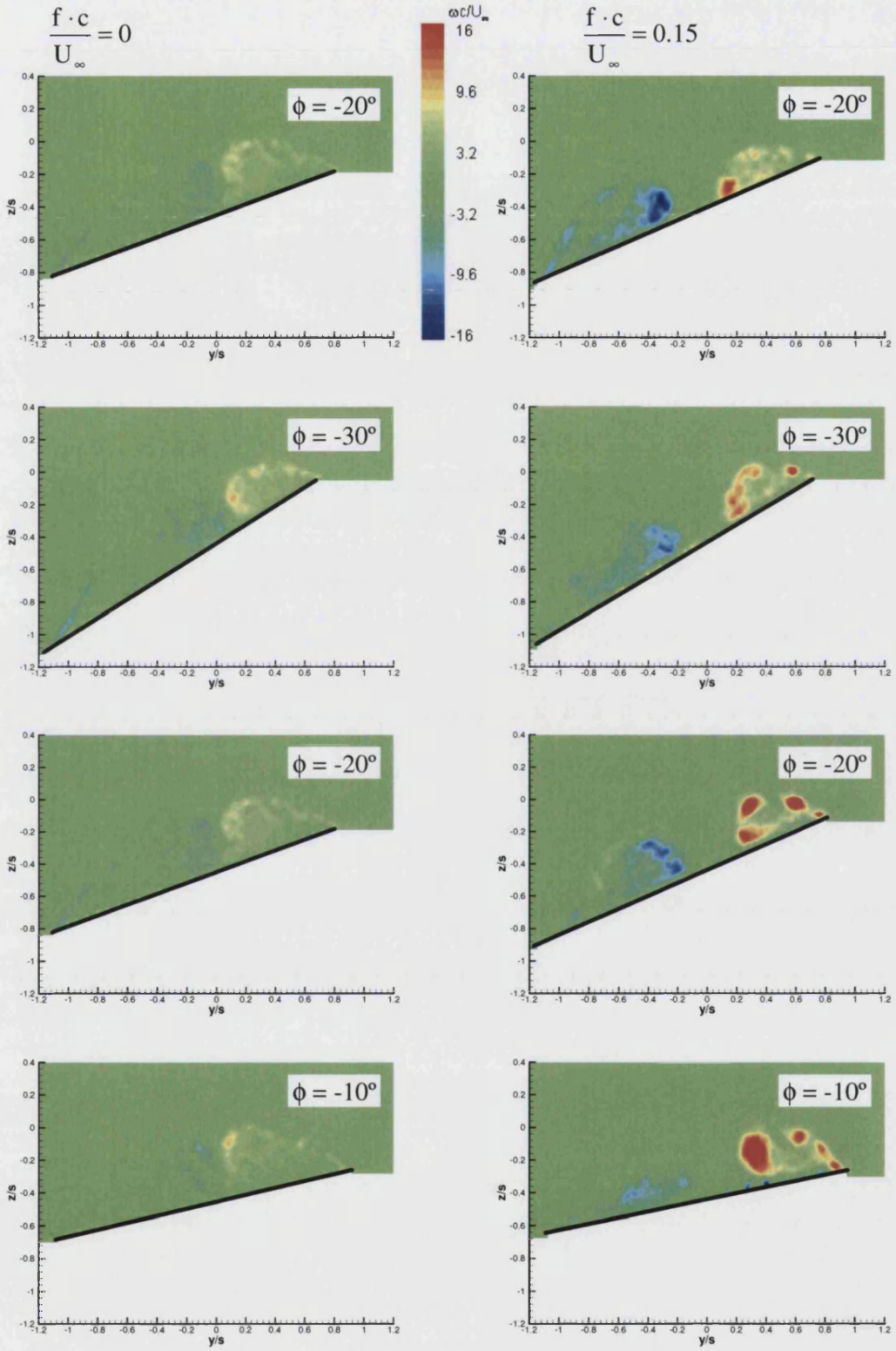

Figure 7.17: continued

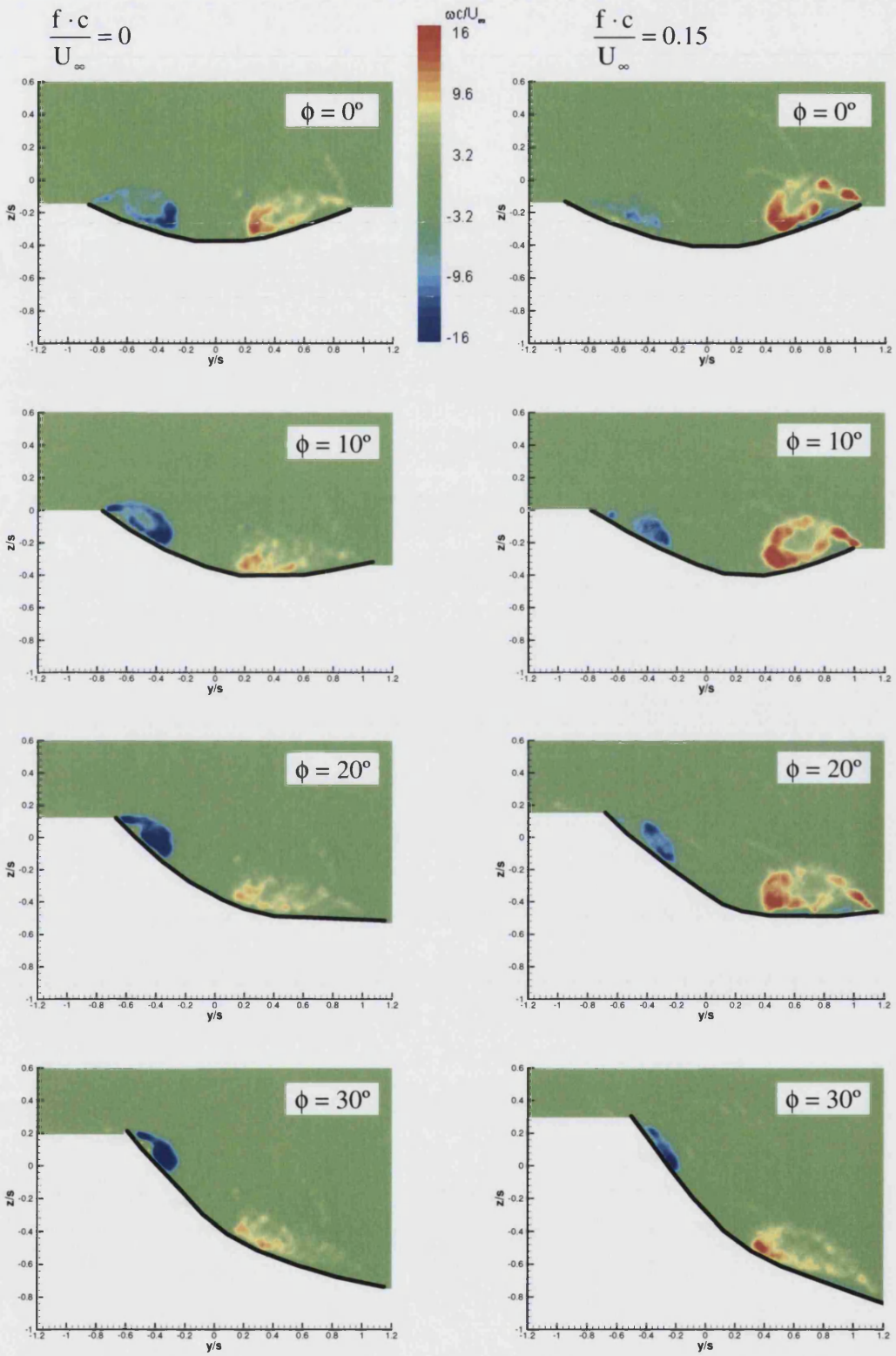

Figure 7.18: Comparison between static and dynamic vorticity in crossflow plane at $x/c = 0.8$ and $\alpha = 20°$ over a cycle for $\lambda = 9$.

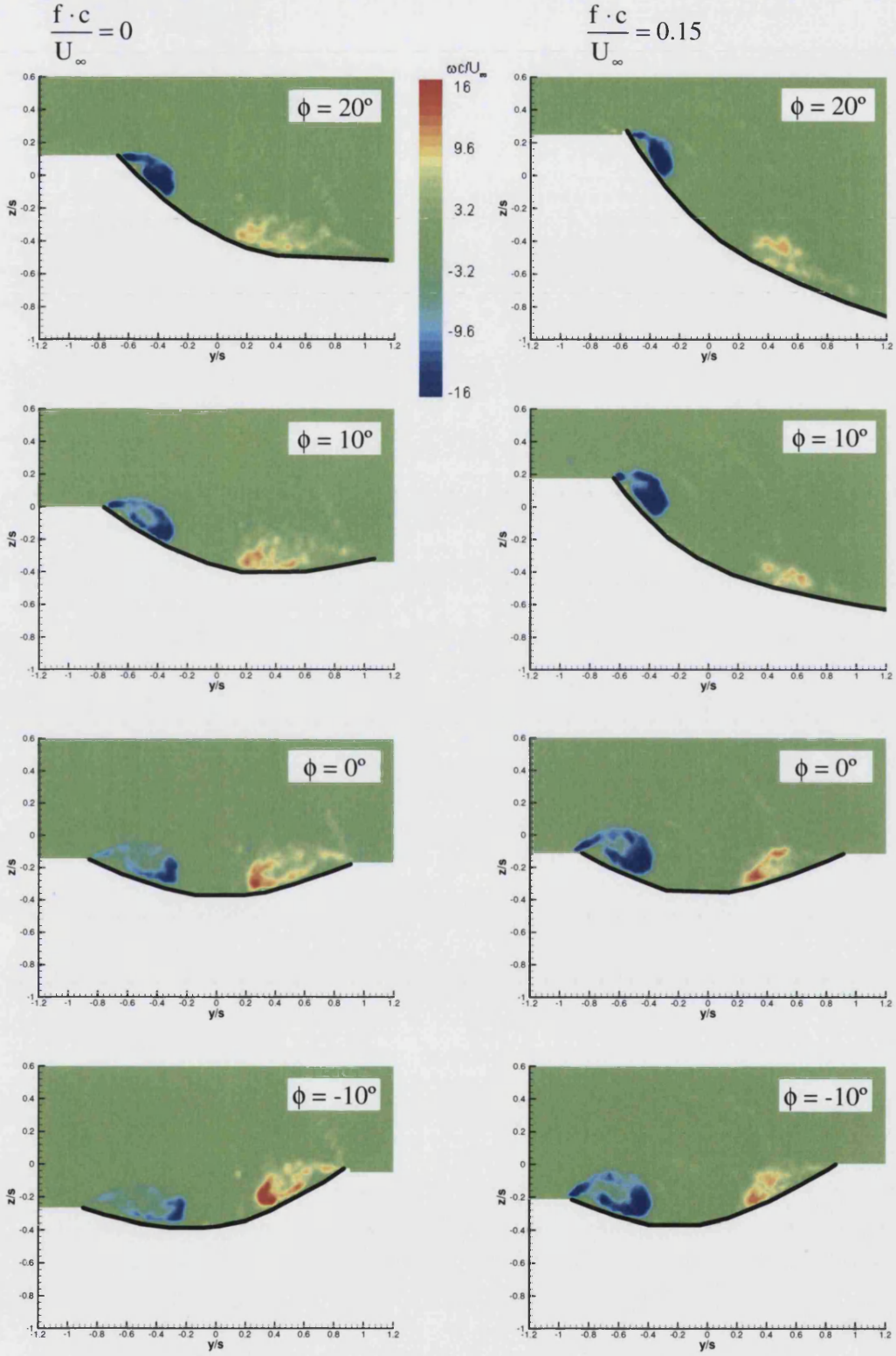

Figure 7.18: continued

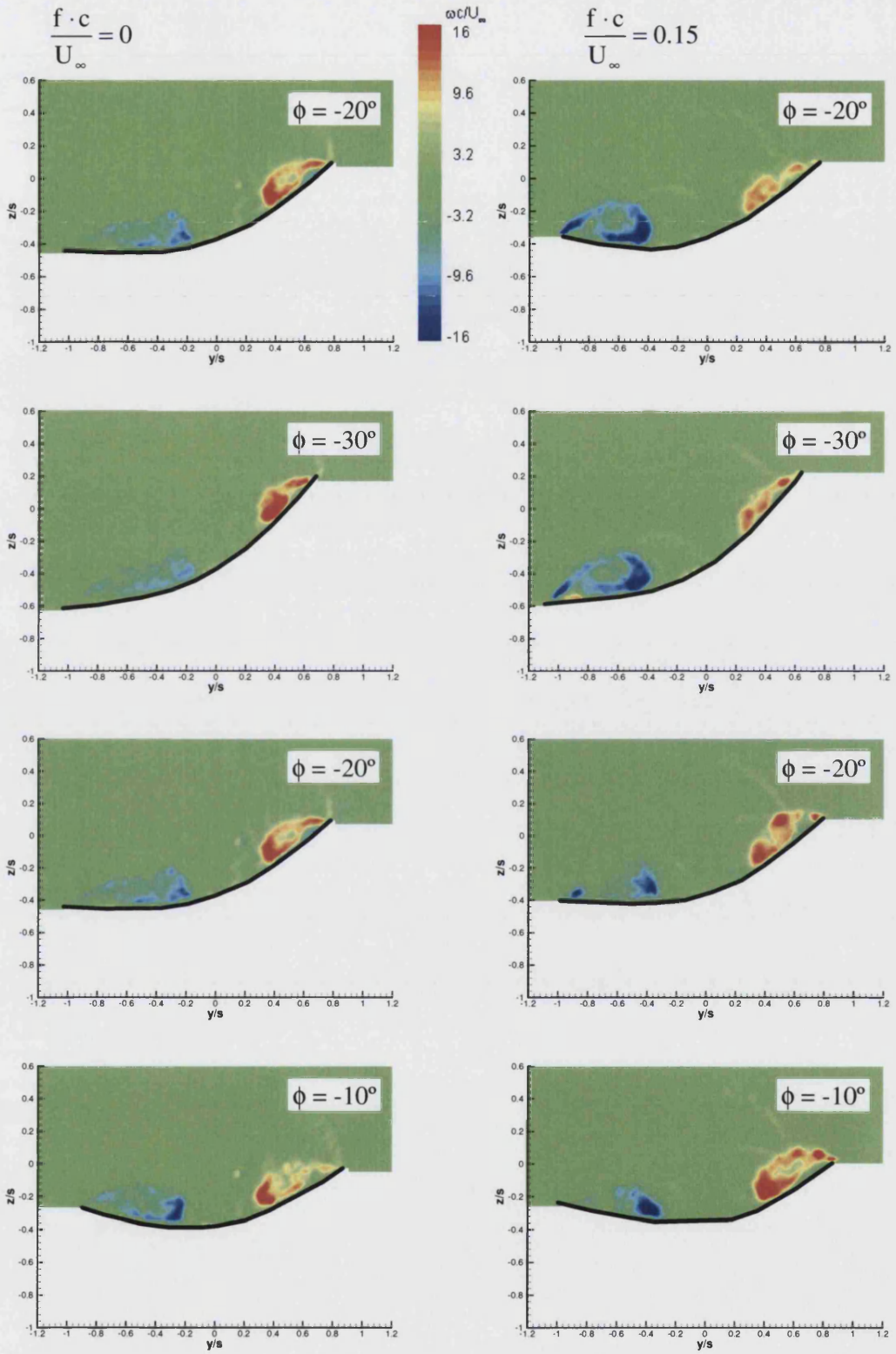

Figure 7.18: continued

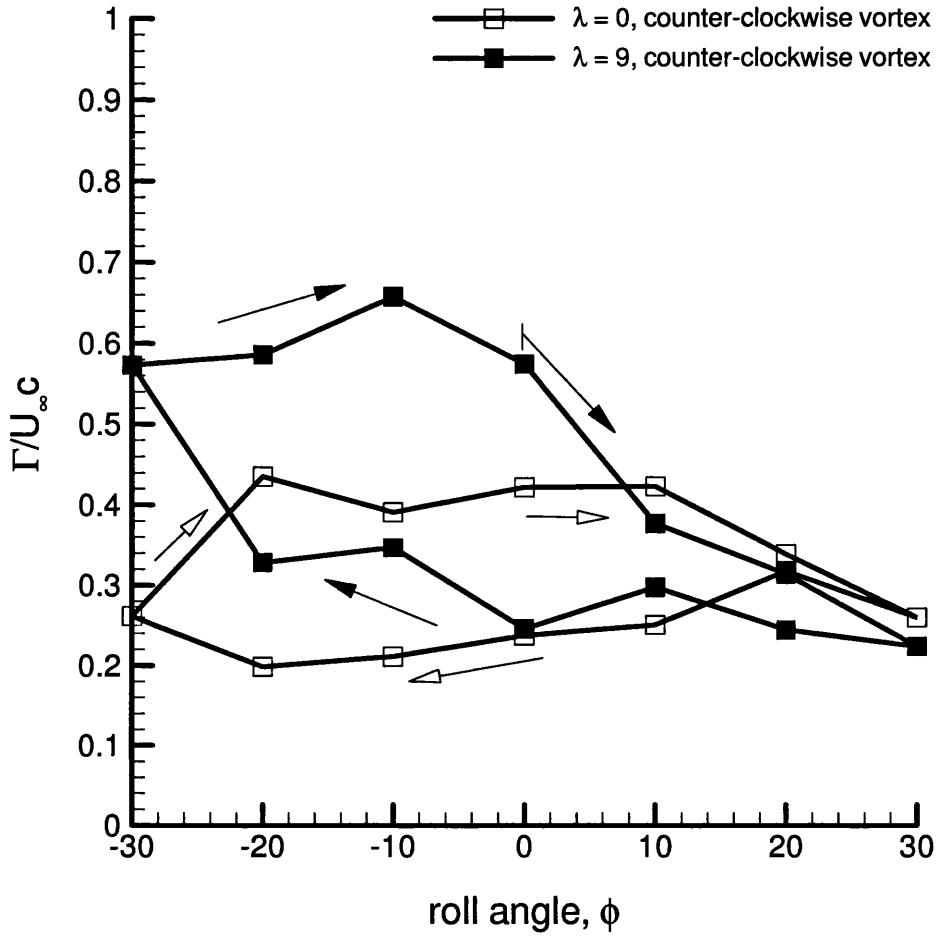

Figure 7.19: Variation of normalised circulation with the roll angle for the counter-clockwise vortex over a cycle , for the dynamic case, $f_r = 0.15$, at $\alpha = 20°$ and $x/c = 0.8$ for the rigid and a flexible wing.

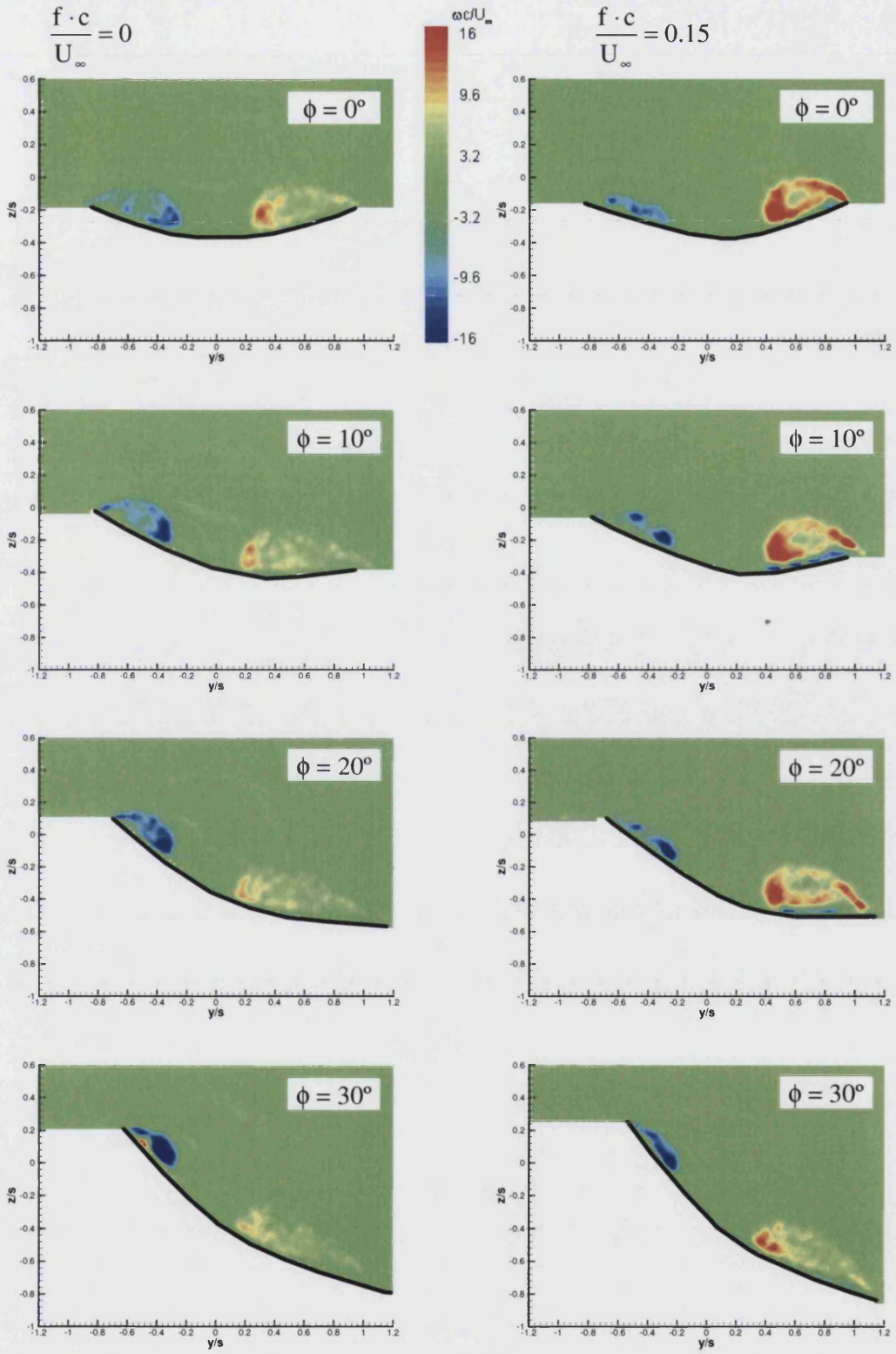

Figure 7.20: Comparison between static and dynamic vorticity in crossflow plane at $x/c = 0.8$ and $\alpha = 20°$ over a cycle for $\lambda = 21.3$.

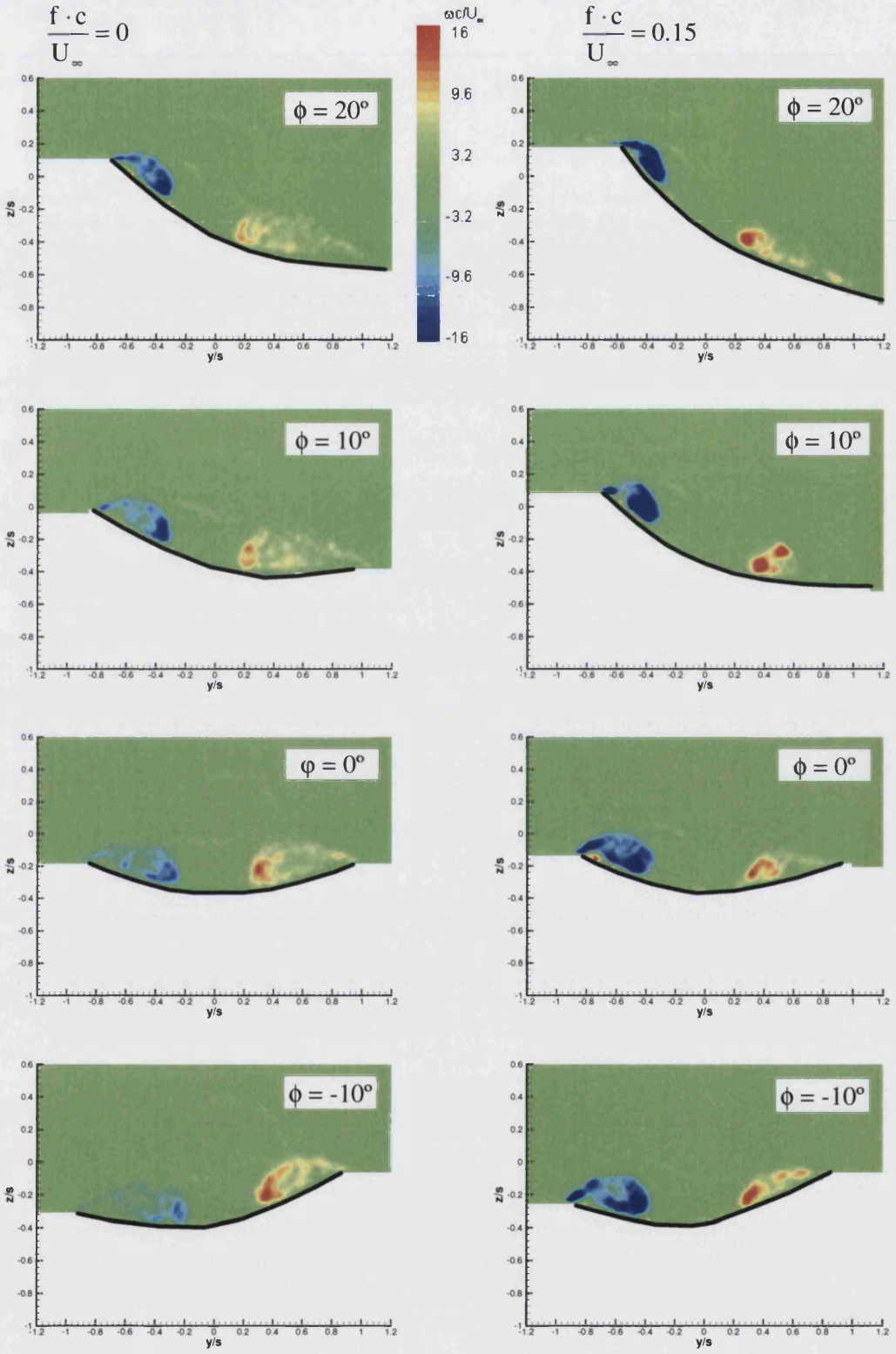

Figure 7.20: continued

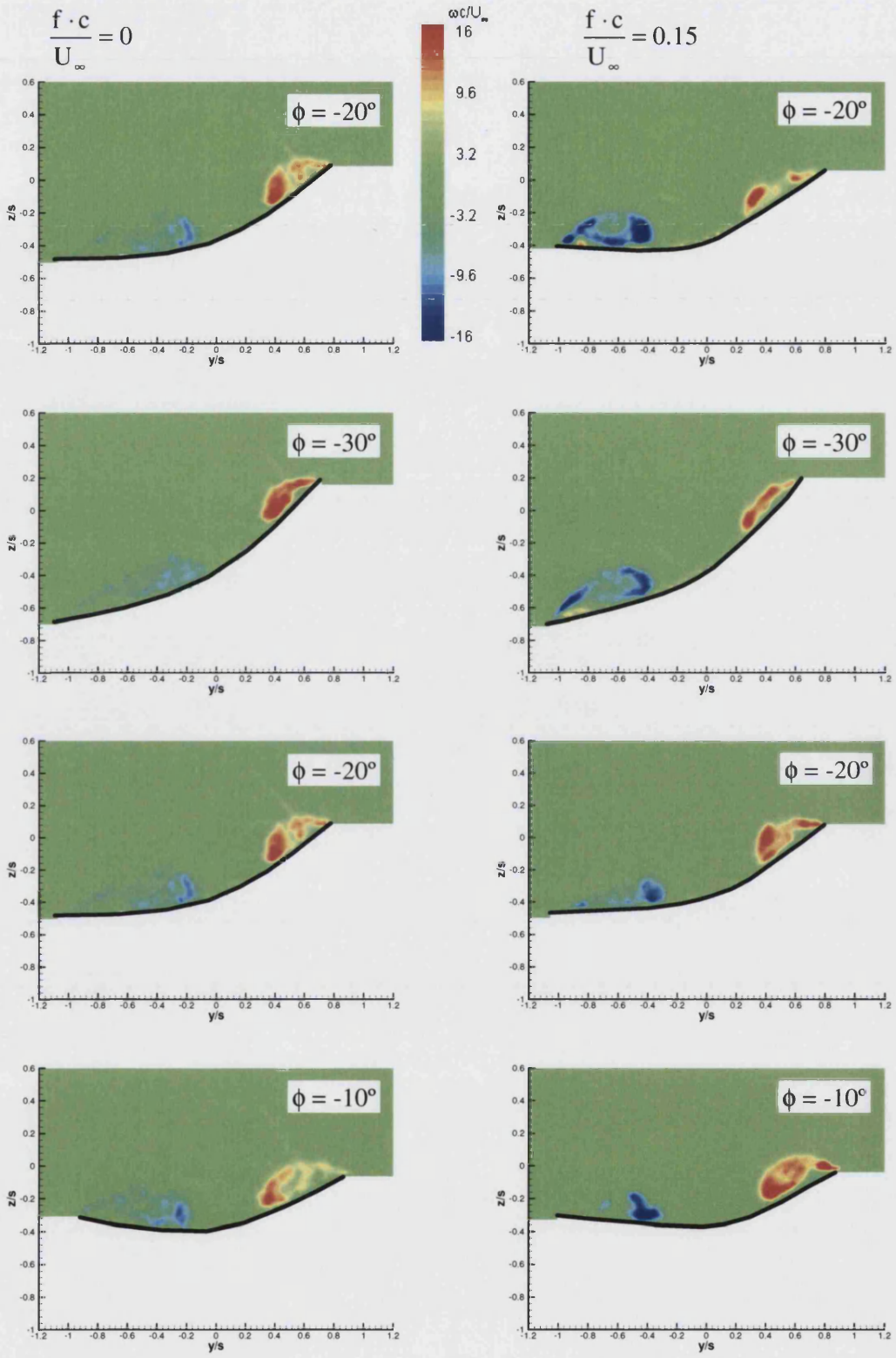

Figure 7.20: continued

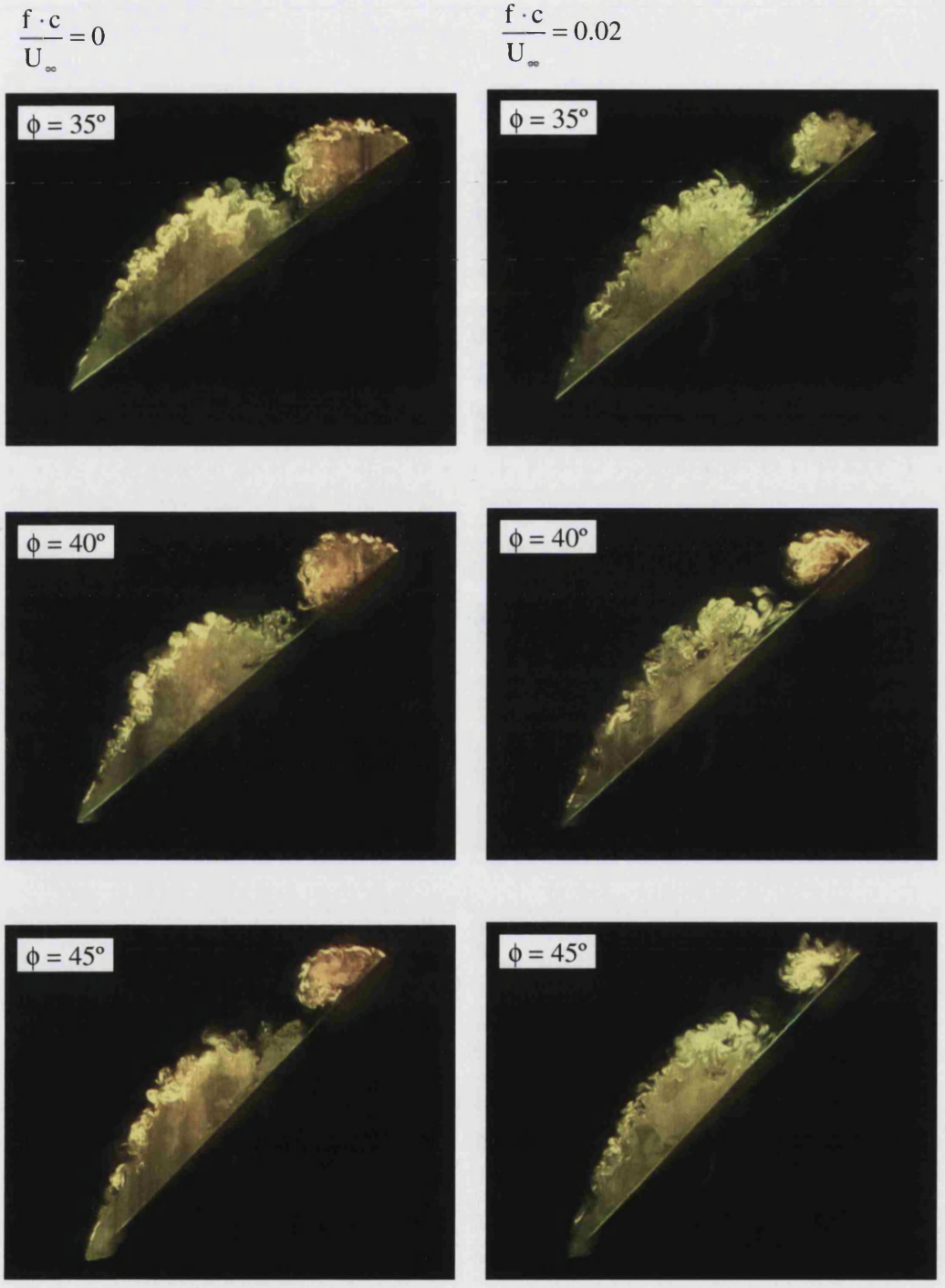

Figure 7.21: Instantaneous laser induced flow visualisation images in crossflow plane for different roll angles at $x/c = 0.8$, for stationary (*left side*) and dynamic case (*right side*) at $\alpha = 22.5°$.

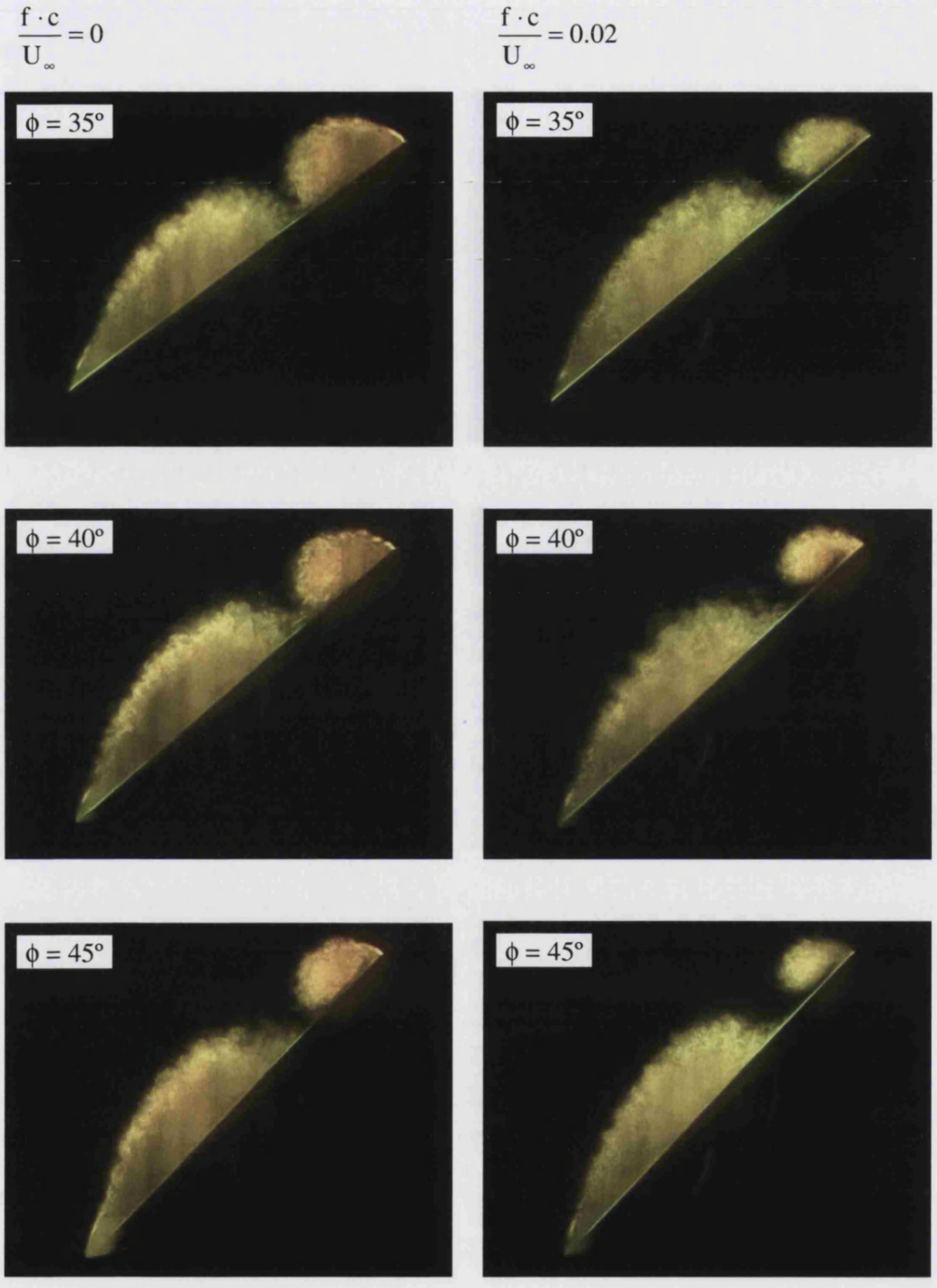

Figure 7.22: Time average laser induced flow visualisation images in crossflow plane for different roll angles at $x/c = 0.8$, for stationary (*left side*) and dynamic case (*right side*) at $\alpha = 22.5°$.

CHAPTER 8: CONCLUSIONS

8.1 Introduction

The aim of this chapter is to give the reader a final overview of the project, along with the main conclusions obtained after this three year long experimental project on the unsteady aerodynamics of nonslender delta wings. An objective overview of the project will be given. The chapter ends with recommendations for future work to be undertaken to extend the knowledge on the unsteady aerodynamics of nonslender delta wings.

8.2 Review and Concluding Remarks

The aerodynamics of nonslender delta wings has been investigated, covering a wide range of unsteady phenomena. Every possible effort was made to obtain accurate experimental results by ensuring the correct approach in the methods used to acquire the results presented in the previous four chapters.

Initially, the effect of flexibility on a 50° sweep angle was tested against a rigid delta wing. The flowfield was studied thoroughly using various measurement techniques over a range of flexibilities. Three different regimes were identified, which depended on the angle of attack and on the breakdown location. Flexibility was found to be capable of delaying the breakdown location by moving it closer to the trailing edge, at incidences where breakdown occurred on the wing surface. Earlier reattachment, vortex reformation, followed by the existence of a breakdown location on the wing surface has been demonstrated to take place in the presence of flexibility, when the vortices on the rigid equivalent had already broken down at the apex. Finally, in angles of attack where no vortices are present, and completely stalled, separated flow is the main characteristic of the flowfield, flexibility seemed to promote reattachment. Vortex reformation however, was not observed in the last regime. In conclusion, flexibility was found to have a beneficial effect on the flowfield of a nonslender delta wing with a strong dependence on the incidence.

The results obtained on the flexible wings led to the conclusion that it cannot be the static deflection of the wing tips, and thus the spanwise curvature, that is responsible for the changes in the flowfield, but some form of self-induced vibration. In an attempt to simulate these vibrations a set of experiments were undertaken on the 50° sweep angle delta wing undergoing a small amplitude and high frequency oscillatory motion. It was shown that in the presence of a small amplitude oscillatory motion, a stalled, separated flow becomes reattached, and the vortices are regenerated with the consequent appearance of breakdown. Notice that a minimum dimensionless frequency had to be applied for the reformation of the flowfield to occur. Increasing the oscillating frequency seemed to improve the flowfield by further delaying vortex breakdown. However, an upper limit was found, after which deterioration followed. Consequently, a range of optimum frequencies was identified $(f_r = 1-2)$. This range compares well with the dominant frequencies of the shear layer instabilities. Since the vortices on delta wings are the main source of lift generation, their reformation in the stall region can be seen as a potential lift enhancement. This clearly suggests that the main mechanism of lift enhancement is the excitation of shear layer instabilities, and promotion of reattachment of the separated flow. The oscillating leading edge is an unsteady source of vorticity, which leads to an increase in the vorticity flux and circulation. Despite the increasing strength of the vortical flow, reformation of the leading edge vortices with axial flow was observed, which suggested that the streamwise pressure gradient might have been modified favourably due to the wing motion.

Given the encouraging results obtained from the oscillations of a 50° simple delta wing, it was deemed vital to investigate the response of the same oscillations on wings with lower sweep angles and different planform shapes. A 40° and 30° sweep angle simple delta wing along with a series of cropped delta wings ranging from 50° sweep angle to 20°, were tested under the same oscillatory conditions. Interestingly, the same range of dominant frequencies was identified $(f_r = 1-2)$, for which reattachment or vortex reformation could be controlled best. For this range of frequencies, the breakdown location (measured from the apex) or the distance between the broken down wakes (a rough measure of the reattachment), were found to be maximum. The results also suggested that the lower limit of sweep angle below which the beneficial effect of wing sweep diminishes, is around $\Lambda = 20°$. Additionally, symmetric perturbations in the form of small amplitude pitching oscillations (1° amplitude) were studied for a $\Lambda = 50°$ simple delta wing. The results show that symmetric perturbations also promote reattachment and vortex reformation. If the results obtained in this project were to be implemented for active control of the leading edge vortices, both symmetric and antisymmetric excitations would be considered as potentially effective, for promoting earlier reattachment and vortex reformation. However, passive control for a flexible wing occurs only in the antisymmetric mode.

Finally, large amplitude and low frequency rolling manoeuvres of both flexible and rigid wings were studied. Different flow regimes were identified in this case as well. When vortex breakdown was present over the wing at zero roll angle, its variation was little affected at static or dynamic roll angles. However, relatively large

variations in maximum vorticity and vortex size were identified in the crossflow plane. In the static case, when vortex breakdown was at the apex of the wing at zero roll angle, a coherent vortex was formed and vortex breakdown could be observed over the wing for large roll angles. In the dynamic case, even for small dimensionless frequencies, coherent leading edge vortices were observed on both sides of the wing throughout the whole cycle, rather than partially or completely stalled flow as in the static case. However, the variation of breakdown location over a cycle was much smaller. When the dimensionless frequency of the rolling motion was substantially increased, the amplitude of cyclic variations in breakdown location decreased. In addition, hysteresis increased with frequency, and was mostly noticeable at a zero roll angle. The existence of multiple vortices with the same sign of vorticity as the primary vortices was apparent at some roll angles. The variation of circulation also showed hysteresis, and had certain similarities to the variations in breakdown location, although the magnitudes of these were much larger.

The structure of the flowfield noticeably changed when flexible delta wings were tested undergoing the same large amplitude manoeuvres. Vortices were seen on both sides of the wing for a zero roll angle in the stationary case. The magnitude of vorticity was considerably increased, and the breakdown location for the vortex on the side where the effective sweep angle was increased, moved closer to the trailing edge. The dynamic motion seemed to act adversely on the flowfield by weakening both vortices, even in the presence of high roll angles. The magnitudes of circulation of the counter-clockwise vortex calculated for the dynamic case, for both rigid and flexible delta wings, proved to be of the same order, during positive roll angles throughout the cycle. Hence, the biggest differences are observed in the negative roll angles for the counter-clockwise vortex. This indicates an asymmetry between the two vortices, a feature also observed for the different manoeuvres of the rigid wing, and therefore suggests that it is a characteristic of large amplitude manoeuvres on nonslender delta wings. A large hysteresis loop was observed in both cases, with the average circulation being higher for the flexible wing. This is expected and is possibly attributed to the increased vorticity flux as a result of the oscillations of the leading edge. Additional rolling manoeuvres starting from a nonzero roll angle, using the 50° sweep angle delta wing simulating a forced wing rock manoeuvre, presented interesting findings. Small scale vortical structures occupied the outline of the shear layer and earlier reattachment was promoted due to the wing motion. An interaction was observed in the reattachment lines, which can potentially play an important role in the self-excited roll oscillations that describe the wing rock phenomenon.

8.3 Recommendations for Future Work

An area of particular interest in which the author is particularly keen to see progress on, is that of flexible nonslender delta wings. Previous findings, as well as the encouraging results obtained in the present research, can provide a starting point for the investigation of the complex mechanisms occurring on flexible nonslender wings. More extensive data and further studies (and therefore time and resources) are required in order to understand the self-excited vibrations and consequential lift enhancement.

One recommendation is the utilisation of a high frame rate PIV system which can support an in depth spectral analysis of the flow. It is expected that such a system would provide information on the frequencies observed in flexible wings, and thus lead to a more accurate calculation of the range detected in the present study. The spectra of frequencies are calculated on a 2D plane, such that the frequencies can be calculated in both the streamwise and cross-flow directions, and their phase be deduced. Information on the turbulence levels of the flowfield can also be extracted from a high frame rate PIV system, giving a clear idea of the variation of the velocity magnitude in the vortex and the surrounding areas. This can be computed by the standard deviation of the velocity vectors. Valuable information could also be extracted from instantaneous images of the flowfield. For example, small vortical structures, essential to the formation of the leading edge vortices, could be captured and measurements on their wavelength can be preformed. The aforementioned results in combination with the accumulation of time-averaged flowfield data in both streamwise and the crossflow can give a complete overview of the phenomena observed in flexible nonslender delta wings. In general, the implementation of a high frame rate PIV system can shed light on the physical mechanisms leading to the reformation of the vortices in the stall region by careful examination of instantaneous images, evaluation of the time-averaged flowfields and collection of accurate information on the frequencies of the self-excited vibrations.

The rolling manoeuvre of nonslender delta wings has not been covered extensively in the literature. This fact creates a need for additional studies in this area to take place. Computational studies can provide additional information on the flowfield, as well as further the understanding on how the vortices are developed and destroyed over a manoeuvring wing. On the other hand, more experimental data is needed both for improving the understanding of the aerodynamics of manoeuvring wings, as well as to be used as a basis for the aforementioned computational studies. One area that specifically requires attention, for example, is the determination of lift forces and moments on a rolling wing. Hence, force measurements could provide valuable information on how the lift changes with respect to the roll angle and the angle of attack. These measurements could then subsequently be refined by determining the lift distribution over the wing throughout these manoeuvres. Additionally, calculation of the rolling moment can enhance our understanding of hysteresis effects and time lags observed in the rolling manoeuvre. The vortices undergo a number of changes during the rolling manoeuvre, including promotion and delay of breakdown location, thus continuously affecting the lift distribution over the wing, and consequently also the moments. This can have severe consequences on the flight envelope of a manoeuvring aircraft, and hence a thorough investigation into the rolling manoeuvre can constructively improve its lift utilisation. A possible starting point could involve experiments using a number of pressure tappings, uniformly placed throughout the suction surface of the wing thus providing detailed information on the lift distribution over the wing for a range of roll angles.

CHAPTER 9: REFERENCES

Adrian, R. J., (1997), "Dynamic Ranges of Velocity and Spatial Resolution of Particle Image Velocimetry", Measurements Science and Technology, Vol. 8, pp. 1393-1398.

Algieri, A., Bova, S., and De Bartolo, C., (2005), "Experimental and Numerical Investigation on the Effects of the Seeding Properties on LDA Measurements", ASME, Journal of Fluid Engineering, Vol. 127, pp. 514-522.

Anderson, Jr. J. D., (2001), "Fundamentals of Aerodynamics", 3rd Edition, New York: McGraw-Hill International Edition.

Arena, Jr. A. S., and Nelson, R. C., (1994), "Experimental Investigations on Limit Cycle Wing Rock of Slender Wings", Journal of Aircraft, Vol., 31, No. 5, pp. 1148-1155.

Attar, P. J., Gordnier, R. E., and Visbal, M. R., (2006), "Numerical Simulation of the Buffet of a Full Span Delta Wing at High Angle of Attack", AIAA-2006-2075, 47th AIAA/ASME/ASCE/AHS/ASC Structures, Structural Dynamics and Material Conference, 1-4 May, Newport, RI.

Benjamin, T. B., (1967), "Some Developments in the Theory of the Vortex Breakdown" Journal of Fluid Mechanics, Vol. 28, part 1, pp. 65-84.

Benjamin, T. B., (1962), "Theory of the Vortex Breakdown Phenomenon", Journal of Fluid Mechanics, Vol. 14, part 1, pp. 593-629.

Cipolla, K. M., and Rockwell, D., (1998), "Instantaneous Crossflow Topology on a Delta Wing in Presence of Vortex Breakdown", Journal of Aircraft, Vol.35, No. 2, pp. 218-223.

Cummings, R. M., Morton, S. A., Siegel, S. G., and Bosscher, S., (2003), "Numerical Prediction and Wind Tunnel Experiment for a Pitching Unmanned Combat Air Vehicle", AIAA-2003-0417, 41st Aerospace Sciences Meeting, 6-9 January 2003, Reno, NV.

Delery, J. M., (1994), "Aspects of Vortex Breakdown", Progress in Aerospace Sciences, Vol. 30, pp. 1-59.

Earnshaw, P. B., and Lawford, J. A., (1964), "Low-Speed Wind-Tunnel Experiments on a Series of Sharp-Edged Delta Wings", ARC Reports and Memoranda No. 3424.

Erickson, G. E., (1982), "Water-Tunnel Studies of Leading-Edge Vortices", Journal of Aircraft, Vol. 19, No. 6, pp. 442-448.

Ericsson, L. E., (2001), "Wing rock of Nonslender Delta Wings", Journal of Aircraft, Vol. 38, No. 1, pp. 36-41.

Escudier, M., (1988), "Vortex Breakdown: Observations and Explanations", Progress in Aerospace Sciences, Vol. 25, pp. 189-229.

Fisher, D. F., Del Frate, J. H., and Richwine, D. M., (1990), "In-Flight Flow Visualization Characteristics of the NASA F-18 High Alpha Research Vehicle at High Angles of Attack", NASA TM 4193.

Gad-el-Hak, M., and Blackwelder, R. F., (1985), "The Discrete Vortices from a Delta Wing", Technical Note, AIAA Journal, Vol. 23, No. 6, pp. 961-962.

Gordnier, R. E., (1997), "Numerical Simulation of a 65-Degree Delta-Wing Flowfield", Journal of Aircraft, Vol. 34, No. 4, pp. 492-499.

Gordnier, R. E., and Visbal, M. R., (2004), "Computation of the Aeroelastic Response of a Flexible Delta wing at High Angles of Attack", Journal of Fluids and Structures, Vol. 19, pp. 785-800.

Gordnier, R. E., and Visbal, M. R., (2003), "Higher-Order Compact Difference Scheme Applied to the Simulation of a Low sweep Delta Wing Flow", AIAA-2003-0620, 41st AIAA Aerospace Sciences Meeting and Exhibit, 6-9 January 2003, Reno, NV.

Gordnier, R. E., and Visbal, M. R., (1998) "Numerical Simulation of Delta-Wing Roll", Aerospace Science and Technology, No. 6, pp. 347-357.

Gordnier, R. E., and Visbal, M. R., (1994), "Unsteady Vortex Structure over a Delta Wing", Journal of Aircraft, Vol.31, No. 1, pp. 243-248.

Greenwell, D. I., and Nangia, R. K., (2003), "Lift Loss Due to Vortex Breakdown", Royal Aeronautical Society, CEAS Aerospace Aerodynamics Research Conference 10-12 June 2003, London, UK, Vortical Flows, Paper 28, pp. 1-13.

Grismer, D. S., and Jenkins, J. E., (1997), "Critical-State Transients for a Rolling 65-Degree Delta Wing", Journal of Aircraft, Vol. 34, No. 3, pp. 380-386.

Gursul, I., (2005), "Review of Unsteady Vortex Flows over Slender Delta Wings", Journal of Aircraft, Vol. 42, No. 2, pp. 299-319.

Gursul, I., (2004), "Vortex Flows on UAVs: Issues and Challenges", The Aeronautical Journal, vol. 108, No. 1090, pp. 597-610.

Gursul, I., (2003), "Review of Unsteady Vortex Flows over Delta Wings", AIAA-2003-3942, 21st AIAA Applied Aerodynamics Conference, 23-26 June, Orlando, FL.

Gursul, I., (1995), "Criteria for Location of Vortex Breakdown over Delta wings", The Aeronautical Journal of the Royal Aeronautical Society, Technical Note, pp.194-196.

Gursul, I., (1994), "Unsteady Flow Phenomena over Delta Wings at High Angle of Attack", AIAA Journal, Vol. 32, No. 2, pp. 225-231.

Gursul, I., and Yang, H., (1995), "Vortex Breakdown over a Pitching Delta Wing", Journal of Fluids and Structures, Vol. 9, pp. 571-583.

Gursul, I., Vardaki, E., and Wang, Z., (2006), "Active and Passive Control of Reattachment on Various Low-Sweep Wings", AIAA-2006-0506, 44th AIAA Aerospace Sciences Meeting and Exhibit, 9-12 January 2006, Reno, NV.

Gursul, I., Gordnier, R., and Visbal, M., (2005), "Unsteady Aerodynamics on Nonslender Delta Wings", Progress in Aerospace Sciences, Vol. 41, pp. 515-557.

Gursul, I., Taylor, G. S., and Wooding, C. L., (2002), "Vortex Flows over Fixed-Wing Micro Air Vehicles," AIAA Paper 2002-0698, 40th AIAA Aerospace Sciences Meeting & Exhibit, 14-17 January 2002, Reno, NV.

Hall, M. G., (1972), "Vortex Breakdown", Annual Review of Fluid Mechanics, Vol. 4, pp. 195-218.

Hanff, E. S., and Huang, X. Z., (1991), "Roll-Induced Cross-Loads on a Delta Wing at High Incidence", AIAA-91-3223, 9th AIAA Applied Aerodynamics Conference, 23-25 September 1991, Baltimore, MD.

Hart, D. P., (1998), "The Elimination of Correlation Errors in PIV Processing", 9th International Symposium on Applications of Laser Techniques to Fluid Mechanics, Lisbon, Portugal, July.

Harvey, J. K., (1962), "Some Observations of the Vortex Breakdown Phenomenon", Journal of Fluid Mechanics, Vol. 14, Part 4, pp. 585-592.

Hemsch, M. J., and Luckring, J. M., (1990), "Connection Between Leading-Edge Sweep, Vortex Lift and Vortex Strength for Delta Wings", Engineering Notes, Journal of Aircraft, Vol. 27, No. 5, pp. 473-475.

Honkan, A., and Andreopoulos, J., (1997), "Instantaneous Three-Dimensional Vorticity Measurements in Vortical Flow over a Delta Wing", AIAA Journal, Vol. 35, No. 10, pp. 1612-1620.

Huang, H., Dabiri, D., and Gharib, M., (1997), "On Errors of Digital Particle Image Velocimetry", Measurements Science and Technology, Vol. 8, pp.1427-1440.

Hummel, D., and Srinivasan, P. S., (1967), "Vortex Breakdown Effects on the Low-Speed Aerodynamic Characteristics of Slender Delta Wings in Symmetrical Flow", Technical Notes, Journal of the Royal Aeronautical Society, Vol. 71, pp. 319-321.

Hüschler, S., (2003), "Wing Rock of Nonslender Delta Wings", Thesis (MEng), University of Bath.

Instruction Manual Particle Image Velocimetry Software, (2001), TSI Incorporated., Version 6.0, St. Paul, MN 55164, USA.

Iowa State University e-Library, (2000), Ames, IA 50011, Alexander M. Lippisch, Available from: http://www.lib.iastate.edu/spcl/manuscripts/MS243.html [Accessed 26 August 2005].

Jaworski, A. J., (1996), "A Study of Pressure Fluctuations Caused by Vortex Breakdown", PhD thesis, Imperial College of Science, Technology and Medicine, London.

Jenkins, J. E., Myatt, J. H., and Hanff, E. S., (1996), "Body-Axis Rolling Motion Critical States of a 65-Degree Delta Wing", Journal of Aircraft, Vol. 33, No. 2, pp. 268-278.

Kegelman, J., and Roos, F., (1989), "Effects of Leading-Edge Shape and Vortex Burst on the Flowfield of a 70 Degree Sweep Delta-Wing", AIAA-89-0086, 27th Aerospace Sciences Meeting, 9-12 January 1989, Reno, NV.

Klute, S. M., Vlachos, P. P., and Telionis D. P., (2005), "High-Speed Digital-Particle-Image-Velocimetry Study of Vortex Breakdown", AIAA Journal, Vol. 43, No. 3, pp. 642-650.

Kumar, A., (1998), "On the structure of vortex breakdown on a delta wing", Proceedings Of The Royal Society, London, A Vol. 454, pp. 89-110.

Lambourne, N. C., and Bryer, D. W., (1961), "The Bursting of Leading-Edge Vortices-Some Observations and Discussion of the Phenomenon", Aeronautical Research Council, R&M, No. 3282.

Lee, M., and Ho, C., (1990), "Lift Force of Delta Wings", Applied Mechanics Reviews, Vol. 43, No. 9, pp. 209-221.

Leibovich, S., (1984), "Vortex stability and Breakdown: Survey and Extension", AIAA Journal, Vol. 22, No. 9, pp. 1992-1206.

Leibovich, S., (1978), "The Structure of Vortex Breakdown", Annual Review in Fluid Mechanics, No. 10, pp. 221-246.

Lowson, M. V., (1991), "Visualization Measurements of Vortex Flows", Journal of Aircraft, Vol.28, No.5, pp. 320-327.

Lowson, M. V., (1964), "Some Experiments with Vortex Breakdown", Technical Notes, Journal of the Royal Aeronautical Society, Vol. 68, pp. 343-346.

Lowson, M. V., and Riley, A. J., (1995), "Vortex Breakdown Control by Delta Wing Geometry", Journal of Aircraft, Vol. 32, No. 4, pp. 832-838.

Lucca-Negro, O., and O'Doherty, T., (2001), "Vortex Breakdown: a Review", Progress in Energy and Combustion Science, No. 27, pp. 431-481.

Luckring, J. M., (2002), "An Overview of the RTO Symposium on Vortex Flow and High Angle of Attack Aerodynamics", ICAS 2002 Congress.

Ludwieg, H., (1970), "Vortex Breakdown", Deutsche Luft-und Raumfahrt, Rep, 70-40.

McClain, A., (2004), "Aerodynamics of Nonslender Delta Wings", MPhil Thesis, University of Bath, Department of Mechanical Engineering.

McClain, A., Wang, Z., Vardaki, E., and Gursul, I., (2007), "Unsteady Aerodynamics of Free-to-Roll Nonslender Delta Wings", Extended Abstract submitted for the 45th AIAA Aerospace Sciences Meeting and Exhibit, 8-11 January, 2007, Reno, NV.

Megson, TH. G., (1999), "Aircraft Structures for Engineering Students", 3rd Edition, Oxford: Butterworth-Heinemann.

Melling, A., (1997), "Tracer Particles and Seeding for Particle Image Velocimetry", Measurements Science and Technology, Vol. 8, pp. 1406-1416.

Menke, M., and Gursul, I., (1997), "Unsteady Nature of Leading Edge Vortices", Physics of Fluids, American Institute of Physics.

Menke, M., Yang, H., and Gursul, I., (1999), "Experiments on the Unsteady Nature of Vortex Breakdown over Delta Wings", Experiments in Fluids, Vol. 27, pp. 262-272.

Miau, J. J., Kuo, K. T., Liu, W. H., Hsieh, S. J., Chou, J. H., and Lin, C. K., (1995), "Flow Developments Above 50-Deg Sweep Delta Wings with Different Leading-Edge Profiles", Journal of Aircraft, Vol. 32, No. 4, pp. 787-794.

Mitchell, A. M., and Molton, P., (2002), "Vortical Substructures in the Shear Layers Forming Leading-Edge Vortices", Technical Notes, AIAA Journal, Vol. 40, No. 8, pp. 1689-1692.

Nelson, R. C., and Pelletier, A., (2003), "The Unsteady Aerodynamics of Slender Wings and Aircraft Undergoing Large Amplitude Maneuvers", Progress in Aerospace Sciences, No 39, pp. 185-248.

Nelson, R. C., and Visser, K. D., (1990), "Breaking Down the Delta Wing Vortex", AGARD Symposium on Vortex Flow Aerodynamics, 1-4 October 1990, Scheveningen, The Netherlands.

Nogueira, J., Lecuona, A., and Rodríguez, P. A., (1997), "Data Validation, False Vectors Correction and Derived Magnitudes Calculation on PIV Data", Measurements Science and Technology, Vol. 8, pp.1493-1501.

Ol, M. V., (2001), "An Experimental Investigation of Leading Edge Vortices and Passage to Stall of Nonslender Delta Wings", Symposium on Advanced Flow Management, RTO AVT-072, May 2001, Paper 2.

Ol, M. V., and Gharib, M., (2003), "Leading-Edge Vortex Structure of Nonslender Delta Wings at Low Reynolds Number", AIAA Journal, Vol. 41, No. 1, pp. 16-26.

Ol, M. V., and Gharib, M., (2001), "The Passage Toward Stall of Nonslender Delta Wings at Low Reynolds Number", AIAA-2001-2843, 31st AIAA Fluid Dynamics Conference and Exhibit, 11-14 June 2001, Anaheim, CA.

Operations Manual for the Phase Doppler Particle Analyzer (PDPA)/Laser Doppler Velocimetry (LDV), (2001), TSI Incorporated., St. Paul, MN 55164,USA.

Operator's Manual for the Coherent Innova 70 Series Ion Laser, (1989), Coherent Incorporated., Palo Alto, CA 94303,USA.

Oxford Advanced Learner's Dictionary, (1993), Fourth Edition, Oxford, Oxford University Press.

Ozgoren, M., Sahin, B., and Rockwell, D., (2002), "Vortex Structure on a Delta Wing at High Angle of Attack", AIAA Journal, Vol. 40, No. 2, pp. 285-292.

Payne, F. M., Nelson, R. C., and Schiff, L. B., (1988), "Visualization and Wake surveys of Vortical Flow over a Delta Wing", AIAA Journal, Vol. 26, No. 2, pp. 137-143.

Pelletier, A., and Nelson, R. C., (2000), "Prediction of Vortex Breakdown Location on a Banked Delta Wing", Engineering Notes, Journal of Aircraft, Vol. 37, No. 4, pp. 738-739.

Polhamus, E. C., (1971), "Predictions of Vortex-Lift Characteristics by a Leading-Edge Suction Analogy", Journal of Aircraft, Vol. 8, No. 4, pp. 193-199.

Rediniotis, O. K., Stapountzis, H., and Telionis, D. P., (1993), "Periodic Vortex Shedding over Delta Wings", AIAA Journal, Vol. 31, No. 9, pp. 1555-1562.

Riley, A. J., and Lowson, M. V., (1998), "Development of a Three-Dimensional Free Shear Layer", Journal of Fluid Mechanics, Vol. 369, pp. 49-89.

Rolling Hills Research Corporation, (2002), "Available from: http://www.rollinghillsresearch.com/Water_Tunnels/Model_1520.html [Accessed 26 August 2005].

Rusak, Z., and Lamb, D., (1999), "Prediction of Vortex Breakdown in Leading-Edge Vortices Above Slender Delta Wings" Journal of Aircraft, Vol. 36, No. 4, pp. 659-667.

Sarpkaya, T., (1971a), "On Stationary and Travelling Vortex Breakdowns", Journal of Fluid Mechanics, Vol. 45, Part. 3, pp. 545-559.

Sarpkaya, T., (1971b), "Vortex breakdown in Swirling Conical Flows", AIAA Journal, Vol. 9, No. 9, pp. 1792-1799.

Shih, C., and Ding, Z., (2002), "Vortex Interaction of a Delta-Wing Flowfield", Technical Notes, AIAA Journal, Vol. 41, No. 2.

Stanislas, M., and Monnier, J. C., (1997), "Practical Aspects of Image Recording in Particle Image Velocimetry", Measurements Science and Technology, Vol. 8, pp. 1417-1426.

Taylor, G. S., and Gursul, I., (2004a), "Lift Enhancement over a Flexible Delta Wing", AIAA-2004-2618, 2nd Flow Control Conference, 28-1 July 2004, Portland, Oregon.

Taylor, G. S., and Gursul, I., (2004b), "Unsteady Vortex Flows and Buffeting of a Low Sweep Delta Wing", AIAA-2004-1066, 42nd Aerospace Sciences Meeting & Exhibit, 5–9 January 2004, Reno, NV.

Taylor, G. S., and Gursul, I., (2004c), "Buffeting Flows over a Low Sweep Delta Wing", AIAA Journal, 42nd Vol. 42, No. 9, pp. 1737-1745.

Taylor, G. S., Kroker, A., and Gursul, I., (2005), "Passive Flow Control over Flexible Non-Slender Delta Wings", AIAA-2005-0865, 43rd Aerospace Sciences Meeting and Exhibit, 10-13 January 2005, Reno, NV.

Taylor, G. S., Schnorbus, T., and Gursul, I., (2003), "An Investigation of Vortex Flow over Low Sweep Delta Wings", AIAA-2003-4021, 33rd AIAA Fluid Dynamics Conference and Exhibit, 23-26 June 2003, Orlando, FL.

The Engineering Tool Box, (2002), Fluid Mechanics, Absolute or dynamic viscosity of water, Available from: http://www.engineeringtoolbox.com/water-dynamic-kinematic-viscosity-d_596.html, [Accessed 10 December 2002].

Traub, L. W., (2000a), "Aerodynamic Characteristics of Spanwise Cambered Delta Wings", Journal of Aircraft, Vol. 37, No. 4, pp. 714-724.

Traub, L. W., (2000b), "Effects of Anhedral and Dihedral on a 75-deg Sweep Delta wings", Journal of Aircraft, Vol. 37, No. 2, pp. 302-312.

Traub, L. W., (1999), "Lift Prediction of Spanwise Cambered Delta wings", Journal of Aircraft, Vol. 36, No. 3, pp. 515-522.

Traub, L. W., (1997a), "Prediction of Delta Wing Leading-Edge Vortex Circulation and Lift-Curve Slope", Engineering Notes, Journal of Aircraft, Vol. 34, No. 3, pp. 450-452.

Traub, L. W., (1997b), "Prediction of Vortex Breakdown and Longitudinal Characteristics of Swept Slender Planforms", Journal of Aircraft, Vol. 34, No. 3, pp. 353-359.

Traub, L. W., (1996), "Simple Prediction Method for Location of Vortex Breakdown on Delta Wings", Engineering Notes, Journal of Aircraft, Vol. 33, No. 2.

Traub, L. W., Moeller, B., and Rediniotis, O., (1998), "Low-Reynolds-Number Effects on Delta-Wing Aerodynamics", Engineering Notes, Journal of Aircraft, Vol. 35, No. 4, pp. 653-656.

Ueno, M., Matsuno, T., and Nakamura, Y., (1998), "Unsteady Aerodynamics of Rolling Thick Delta Wing with High Aspect Ratio", AIAA-98-2520, 16th Applied Aerodynamics Conference Meeting and Exhibit, June 15-18 1998, Albuquerque, NM.

Vardaki, E., Gursul, I., and Taylor, G. S., (2005), "Physical Mechanisms of Lift Enhancement for Flexible Delta Wings", AIAA-2005-0867, 43rd AIAA Aerospace Sciences Meeting and Exhibit, 10-13 January 2005, Reno, NV.

Verhaagen, N. G., and Jobe, C. E., (2003), "Wind Tunnel Study on a 65-deg Delta Wing at Sideslip", Journal of Aircraft, Vol. 40, No. 2, pp. 290-296.

Visbal, M. R., and Gordnier, R. E., (2003), "On the Structure of the Shear Layer Emanating from a Swept Leading Edge at Angle of Attack", AIAA-2003-4016, 33rd Fluid Dynamics Conference and Exhibit, 23-26 June 2003, Orlando, FL.

Visser, K. D., and Nelson, R. C., (1993), "Measurements of Circulation and Vorticity in the Leading-Edge Vortex of a Delta Wing", AIAA Journal, Vol. 31, No. 1, pp. 104-111.

Visser, K. D., and Washburn, A. E., (1994), "Transition Behaviour on Flat Plate Delta Wings", AIAA-94-1850, 12th Applied Aerodynamics Conference, June 20-23 1994, Colorado Springs, CO.

Washburn, A. E., and Visser, K. D., (1994), "Evolution of Vortical Structures in the Shear Layer of Delta Wings", AIAA-94-2317, 25th Fluid Dynamic Conference, June 20-23 1994, Colorado Springs, CO.

Wentz, Jr. W. H., and Kohlman, D. L., (1971), "Vortex Breakdown on Slender Sharp-Edged Wings", Journal of Aircraft, Vol. 8, No. 3, pp. 156-161.

Werle, H., (1960), "Sur l'eclatement des tourbillons d'apex d'une aile delta aux faibles vitesses", La Recherche Aeronautique, no. 74.

Westerweel, J., (1997), "Fundamentals of Digital Particle Image Velocimetry", Measurements Science and Technology, Vol. 8, pp. 1379-1392.

Willert, C. E., and Gharib, M., (1991), "Digital Particle Image Velocimetry", Experiments in Fluids, Vol. 10, pp. 181-193.

World Scientific Publishing Co., Bookshop, Engineering, (2005), "FLOW VISUALIZATION Techniques and Examples", pp. 408, Available from: http://www.worldscibooks.com/engineering/p167.html [Accessed 26 August 2005].

Yaniktepe, B., and Rockwell, D., (2004), "Flow Structure on a Delta Wing of Low Sweep Angle", AIAA Journal, Vol. 42, No. 3, pp. 513-523.

Yavuz, M. M., Elkhoury, M., and Rockwell, D., (2004), "Near-Surface Topology and Flow Structure on a Delta Wing", AIAA Journal, Vol. 42, No. 2, pp. 332-340.

CHAPTER 10: LIST OF PUBLICATIONS

McClain, A., Wang, Z., Vardaki, E., and Gursul, I., (2007), "Unsteady Aerodynamics of Free-to-Roll Nonslender Delta Wings", AIAA-2007-1074, 45th AIAA Aerospace Sciences Meeting and Exhibit, 8-11 January, 2007, Reno, NV.

Gursul, I., Vardaki, E., Margaris, P., and Wang, Z., (2006), "Control of Wing Vortices", Conference on Active Flow Control, 2006, 27-29 September, 2006, Berlin, Germany. Also to be published in "Notes on Numerical Fluid Mechanics and Multidisciplinary Design (NNFM)", Springer-Verlag.

Gursul, I., Wang, Z., and Vardaki, E., (2006), "Review of Flow Control Mechanisms of Leading-Edge Vortices", AIAA-2006-3508, 3rd AIAA Flow Control Conference, 5-8 June, 2006, San Francisco, CA.

Gursul, I., Vardaki, E., and Wang, Z., (2006), "Active and Passive Control of Reattachment on Various Low- Sweep Wings", AIAA-2006-0506, 44th AIAA Aerospace Sciences Meeting and Exhibit, 9-12 January, 2006, Reno, NV.

Vardaki, E., Gursul, I., and Taylor, G. S., (2005) "Physical Mechanisms of Lift Enhancement for Flexible Delta Wings", AIAA-2005-0867, 43rd AIAA Aerospace Sciences Meeting and Exhibit, 10-13 January, 2005, Reno, NV.

Gursul, I., Vardaki, E., and Taylor, G. S., (2004), "Flow Control with Wing Flexibility", Oral Presentation, 1st European Forum on Flow Control, 11-14 October, 2004, Poitiers, France.

Vardaki, E., and Gursul, I., (2004), "Vortex Flows on a Rolling Nonslender Delta Wing," AIAA–2004-4729, 22nd Applied Aerodynamics Conference and Exhibit, 16-19 August 2004, Providence, RI.